Magda Sofia Gonçalves da Silva

A new approach for ligament regeneration based on graphene nanocomposites

A new approach for ligament regeneration based on graphene nanocomposites

Magda Sofia Gonçalves da Silva

UMinho | 2023

outubro de 2023

Universidade do Minho

Escola de Engenharia

Magda Sofia Gonçalves da Silva

A new approach for ligament regeneration based on graphene nanocomposites

Doctoral Thesis in
Science and Engineering of Polymers and Composites

Work accomplished under the supervision of
Dr. Maria da Conceição de Jesus Rêgo Paiva
and
Dr. Natália Maria Araújo Alves

October 2023

DECLARAÇÃO

DIREITOS DE AUTOR E CONDIÇÕES DE UTILIZAÇÃO DO TRABALHO POR TERCEIROS

Este é um trabalho académico que pode ser utilizado por terceiros desde que respeitadas as regras e boas práticas internacionalmente aceites, no que concerne aos direitos de autor e direitos conexos.

Assim, o presente trabalho pode ser utilizado nos termos previstos na licença abaixo indicada.

Caso o utilizador necessite de permissão para poder fazer um uso do trabalho em condições não previstas no licenciamento indicado, deverá contactar o autor, através do RepositóriUM da Universidade do Minho.

Licença concedida aos utilizadores deste trabalho

ACKNOWLEDGEMENTS

friendship, valuable advices and availability for helping me during this entire journey.

A special thanks to Dr. Paulo Rodrigues for the motivation, encouragement and support throughout the years.

Finally, I would like to express my eternal gratitude from the bottom of my heart to my family, parents, brother, grandmother, and fiancé, for all important values transmitted, and their constant love, patience and unconditional support. None of this would have been possible if it was not for their effort.

STATEMENT OF INTEGRITY

I hereby declare having conducted this academic work with integrity. I confirm that I have not used plagiarism or any form of undue use of information or falsification of results along the process leading to its elaboration.

I further declare that I have fully acknowledged the Code of Ethical Conduct of the University of Minho.

University of Minho, October 13th 2023

Magda Sofia Gonçalves da Silva

ABSTRACT

A new approach for ligament regeneration based on graphene nanocomposites

Ligament injuries are frequent and often require surgical reconstruction with auto-/ allografts, with severe limitations that have prompted a growing interest in the development of tissue-engineered scaffolds for ligament regeneration. Polylactic acid (PLA) is a biocompatible/biodegradable polymer with acceptable mechanical properties and routinely used for several medical applications. It may be reinforced with nanoparticles such as few-layer graphene to enhance the mechanical performance and provide other functionalities. Micronized graphite nanoplatelets (EG) may be covalently functionalized (f-EG) maintaining the excellent mechanical properties and providing adequate chemistry to bond with PLA, establishing strong interfaces that will enhance stress-transfer from polymer to reinforcement. Anchoring on f-EG a controlled concentration of silver nanoparticles ((f-EG)+Ag) may be beneficial for tissue regeneration by preventing bacterial adhesion and accelerating the healing process.

The present work targeted the production of novel biodegradable and biocompatible graphene-based scaffolds, with controlled dimensions, as well as mechanical properties that match the requirements of the native human ligaments. Two alternative manufacturing techniques were investigated, one based on braiding, the other using 3D printing. To reach this goal, composite filaments of PLA reinforced with (f-EG)+Ag were produced by twin screw extrusion and melt-drawing, with enhanced mechanical performance for textile-engineered and 3D-printed ligament scaffolds. The composite filaments and scaffolds were extensively characterized by relevant techniques, being suitable for tendon/ligament tissue engineering applications. Scaffolds based on a medical grade PLA containing 0.5 wt.% of (f-EG)+Ag were produced by 3D printing. (f-EG)+Ag exhibited antibacterial properties against *Staphylococcus aureus* and *Escherichia coli*, an important feature for the healing process and prevention of bacterial infections. The scaffolds' structure, biodegradation, and mechanical properties confirm their suitability for tendon and ligament regeneration. The PLA+[(f-EG)+Ag] scaffolds were non-toxic, and showed the ability to maintain the tenogenic commitment of human tendon-derived cells, with an increase in the gene expression of specific tendon/ligament-related markers. The results demonstrate the possibility for easy, cost-effective and personalized 3D-printed scaffolds with great potential applications for tendon and ligament regeneration.

Keywords: 3D printing; graphite; ligaments; PLA

RESUMO

Nova abordagem para regeneração de ligamento à base de nanocompósitos de grafeno

As lesões do ligamento são frequentes e envolvem muitas vezes reconstruções cirúrgicas com auto/alo-enxertos. Esta estratégia apresenta várias limitações potenciando o desenvolvimento de *scaffolds* que propiciem a regeneração do ligamento. O poliácido láctico (PLA) é um polímero biocompatível e biodegradável, com razoáveis propriedades mecânicas e amplamente usado na área médica. Este polímero pode ser reforçado com nanopartículas como grafeno multi-camada para melhorar a *performance* mecânica e conferir outras funcionalidades. As nanoplaquetas de grafite micronizada (EG) podem ser funcionalizadas covalentemente (f-EG) mantendo as excelentes propriedades mecânicas, providenciando uma química adequada para uma ligação com o PLA e assim, estabelecer interfaces fortes que irão melhorar a transferência de carga do polímero para o material de reforço. A ancoragem a f-EG de uma concentração controlada de nanopartículas de prata ((f-EG)+Ag) pode ser benéfica para a regeneração de tecidos, prevenindo a adesão bacteriana e acelerando o processo de cicatrização.

Este trabalho tem como objetivo a produção de *scaffolds* à base de grafeno, biodegradáveis e biocompatíveis, com dimensões controladas e propriedades mecânicas que cumpram os requisitos dos ligamentos humanos nativos. Foram investigados dois métodos alternativos de produção, entrançado e impressão 3D. Assim, foram produzidos por extrusão e estiramento filamentos compósitos de PLA+[(f-EG)+Ag], com *performance* mecânica melhorada, para a produção de *scaffolds*. Os filamentos e os *scaffolds* compósitos foram extensamente caracterizados, sendo adequados para regeneração de ligamento/tendão. Foram também produzidos *scaffolds* de PLA de grau médico reforçado com 0.5 wt.% de (f-EG)+Ag, por impressão 3D. (f-EG)+Ag exibiu propriedades antibacterianas em relação a *Staphylococcus aureus* e *Escherichia coli*, uma importante caraterística para a prevenção de infeções bacterianas e para o processo de cura. A estrutura, biodegradação e propriedades mecânicas dos *scaffolds* confirmam a sua adequabilidade para regenerar ligamentos e tendões. Os *scaffolds* de PLA+[(f-EG)+Ag] não são tóxicos, e mostraram capacidade de manter a predisposição tenogénica de células humanas derivadas do tendão, com aumento da expressão genética de marcadores específicos de tendão/ligamento. Os resultados demostram a possibilidade de obter scaffolds por impressão 3D de forma fácil, económica e personalizada com grande potencial para regeneração de tendão/ligamento.

Palavras-chave: grafite; impressão 3D; ligamentos; PLA

TABLE OF CONTENTS

LIST OF FIGURES

LIST OF TABLES

LIST OF ABBREVIATIONS AND SYMBOLS

Abbreviations

AA	Ascorbic acid
A/A	Antibiotic-Antimycotic
ABS	Acrylonitrile-Butadiene-Styrene
ACL	Anterior cruciate ligament
AMSCs	Adipose-tissue-derived mesenchymal stem cells
ADSCs	Human adipose -derived stem cells
AgNPs	Silver nanoparticles
ALG	Alginate
AM	Additive manufacturing
AMB	Anteromedial band
α-MEM	Medium essential alpha
AT	Achilles tendon
bFGF	Basic fibroblast growth factor
BMSCs	Bone marrow mesenchymal stem cells
BS	Bone surface
BSA	Bovine serum albumin
βTCP	β-tricalcium phosphate
BV	Bone volume
CAD	Computer aided Design
CB	Carbon black
CHI	Chitosan
CLSM	Confocal laser scanning microscopy
CNT-COOH	COOH functionalized carbon nanotubes
CNTs	Carbon Nanotubes
Col	Collagen
COL1	Collagen type 1
C_s	Compressive strength

DAPI	4',6-diami-dino-2-phenylindole
DCA	Dipolar cycloaddition
DIW	Direct ink writing
DMA	Dynamic Mechanical Analysis
DMEM	Dulbecco's modified minimum essential medium
DMF	*N,N*-dimethylformamide
DNA	Deoxyribonucleic acid
DPBS	Dulbecco's phosphate buffered saline
DSC	Differential Scanning Calorimetry
3D	Three-dimensional
ECM	Extracellular Matrix
E. coli	*Escherichia coli*
EDS	Energy-dispersive X-ray spectroscopy
EG	Micronized graphite nanoplatelets
EMA	European Medicines Agency
ES	Electrical stimulation
EU	European Union
FBS	Fetal bovine serum
FDA	Food and Drug Administration
FDM	Fused deposition modeling
f-EG	Functionalized graphite
(f-EG)+Ag	Functionalized graphite decorated with silver nanoparticles
FFE	Free Form Extrusion
FFF	Fused filament fabrication
FilText	Filaments for braided scaffold
Fil3D	Filaments for 3D printing
FLG	Few layer graphene
Fn	Fibronectin
GAPDH	Glyceraldehyde-3-phosphate dehydrogenase
GelMa	Gelatin-methacrylate
GICs	Graphite intercalation compounds
GNPs	Graphene/graphite nanoplatelets

GO	Graphene oxide
HA	Hyaluronic acid
Hap	Hydroxyapatite
HDF	Human dermal fibroblasts
HD-KFM	High-definition Kelvin force microscopy
HFF-1	Human fibroblasts
HRP	Horseradish Peroxidase
hTDCs	Human tendon-derived cells
hTSCs	Human tendon stem cells
iGF-I	Growth factor
iGO	Isocyanate treated graphene oxide
IL-1β	Interleukin-1-beta
iPSC	Induced pluripotent stem cells
LARS	Ligament Augmentation and Reconstruction System
lCL	Lateral collateral ligament
LOD	Limit of detection
LPE	Liquid phase exfoliation
MBC	Minimal bactericidal concentration
mCL	Medial collateral ligament
MFI	Melt Flow Index
MHA	Mueller Hinton agar
Micro-CT	Computed micro-tomography
MSCs	Mesenchymal stem cells
NRS	Nanoyarns
NBR	Natural bone regeneration
PA	Polyamide
PANI	Polyaniline
PBS	Phosphate Buffered Saline
PC	Polycarbonate
PCL	Poly(ε-caprolactone)
pCL	Posterior cruciate ligament
PCLF	Polycaprolactone Fumarate

PD	Polydioxanone
PDMS	Polydimethylsiloxane
PE	Polyethylene
PEG	Poly(ethylene glycol)
PEGDA	Polyethylene glycol diacrylate
PEEK	Polyether ether ketone
PET	Poly(ethylene terephthalate)
PGA	Poly(glycolic) acid
P3HB	Poly(3-hydroxybutyrate)
PI	Propidium Iodide
PLA	Polylactic acid
PLGA	Poly (lactide-co-glycolide
PLLA	Poly (L-lactic) acid
PLB	Posterolateral band
PLCL	Poly(L-lactide- co-ε-caprolactone)
Pluronic®	Poly(ethylene oxide–propylene oxide) co polymers
PMMA	Poly(methyl metacrylate)
PPy	Polypyrrole
PS	Polystyrene
PT	Patellar tendon
PTMC	Poly (trimethylene carbonate)
PU	Polyurethane
PVA	Poly(vinyl alcohol)
QDs	Quantum dots
qPCR	Quantitative polymerase chain reaction
Ra	Arithmetic average height
rGO	Reduced graphene oxide
RMS	Root mean square
RNA	Ribonucleic acid
S.aureus	*Staphylococcus aureus*
SCX	Scleraxis
SD	Standard Deviation

SEM	Scanning electron microscopy
SLA	Stereolithography
SLS	Selective laser sintering
STL	Standard Tessellation Language
TCPS	Tissue culture polystyrene
TE	Tissue engineering
TGA	Thermogravimetric analysis
TGF-β	Growth factor-β
TNF-α	Necrosis factor-alpha
TNMD	Tenomodulin
UA	Uric acid
USA	United States of America
UTS	Ultimate tensile strength
UV	Ultraviolet radiation
VPR	Vanillin-based porphyrin
WJ-MSCs	Wharton's jelly mesenchymal stem cells

SYMBOLS

%	Percentage
E'	Storage Modulus
ΔH_{cc}	Cold crystallization enthalpy
ΔH_m	Melting enthalpy
L/L	Length-to-diameter ratio
Tan δ	Loss factor
T_c	Cold crystallization temperature
T_g	Glass transition temperature
T_m	Melting temperature
χ_c	Degree of crystallinity

CHAPTER 1

Introduction

1 Introduction

1.1 Motivation

Ligaments are fibrous tissue connecting two or more bones (1, 2) that present poor vascularity and limited regeneration capacity (3). Particularly, the anterior cruciate ligament (ACL) plays an essential role in the smooth motion and stability of the knee joint and is one of the most commonly injured ligaments (3, 4).

Currently, a ligament injury often lead to surgical procedure using auto- or allografts (5). Despite the ongoing success of these biological grafts in terms of short-term results, 5-year studies show that patients have instability and pain (6). The inherent inadequacies of autografts such as the need of additional surgery with potential donor harvest site infection and limited graft availability or even potential for infectious disease transfer and unreliable graft incorporation, in the case of allografts, led to the development of new approaches for ACL ligament repair (4, 7).

Indeed, since early 1970s, attempts to use non-biodegradable synthetic materials for ACL repair included polyaramid fibers and ethylene (Proplast), carbon fibers, polyethylene terephthalate (Leeds-Keio ligament), polypropylene (Kennedy Ligament Augmentation Device), and polytetrafluoroethylene (Gore-Tex®). Although these synthetic implants initially supply the function of the ligaments, they fail over time and some of them were removed from the market by FDA due to stress shielding of new tissue formed, long-term rupture because of fatigue, creep and production of wear debris with particulate-induced synovitis (8-10).

Such unsolved questions associated with both biological and synthetic grafts have prompted the interest in tissue-engineered solutions to ACL rupture.

Textile technologies have been suggested as a strategy to produce fibrous scaffolds for musculo-skeletal tissue by using different methods such as knitting, twisting, cabling, weaving, and braiding since they could mimic the hierarchical structure of native ligament (1, 4, 11).

Three dimensional (3D) printing or additive manufacturing of medical devices and TE scaffolds have generated a great interest since it offers a better control over the architecture and physical properties of the scaffolds. Some of these devices have already received the FDA clearance (12, 13). The major capabilities of 3D printing are the consistency of reproduction, property predictability and large geometric design freedom (14) which are great advantages over the conventional scaffold fabrication methods (15).

1.2 Objectives

The aim of this work is the production of novel biodegradable scaffolds for ligament regeneration.

To achieve this, composite filaments of functionalized graphene decorated with silver nanoparticles and polylactic acid matrix have been produced. The main purposes are to take advantage of the outstanding mechanical properties of graphene to reinforce polylactic acid (PLA), and the antibacterial properties of silver nanoparticles to benefit wound healing and ligament regeneration. Two alternative scaffold production techniques are presented, one based on conventional braiding, the other using 3D printing technology.

To demonstrate the potential use of 3D printed scaffolds for tendon and ligament regeneration, their biocompatibility is assessed. The knowledge built up in this work will hopefully widen the application of 3D printed graphene-based PLA composite scaffolds.

1.3 Thesis outline

This thesis is organized in six chapters:

Chapter 1 presents a review about the main topic of this thesis, describing the motivation and the main objectives, as well as the thesis outline.

Chapter 2 is divided in two sub-sections with relevant information for the production of new ligament scaffolds, focusing on the state of the art about this topic. The first section emphasizes the current approaches for the healing of tendon/ligament injuries as well as the latest developments regarding the production of tendon/ligament scaffolds based on biodegradable polymer composites. The second section is focused on the graphene-based polymer nanocomposites and provides an overview of the additive manufacturing techniques of these composites for different biomedical applications, including scaffolds and biosensors.

Chapter 3 presents the successful production of composite filaments with different diameters by melt mixing/melt drawing, on a twin-screw extruder, for textile-engineered and 3D-printed scaffolds. An extensive study was performed in order to evaluate the properties of composite filaments based on PLA reinforced with different concentrations of micronized graphite nanoplatelets (EG), functionalized EG (f-EG) and f-EG decorated with silver nanoparticles ((f-EG)+Ag). The filaments' characterization was performed using optical microscopy and scanning electron microscopy for cross sectional analysis, electrical resistivity tests, dynamic mechanical, thermogravimetric and differential scanning calorimetry

analysis for thermomechanical behavior and glass transition temperature measurement.

Chapter 4 describes the production of braided and 3D-printed scaffolds using the PLA/graphite nanoplatelet composite filaments. Braided scaffolds benefit from the tailorable structures that may be obtained by conventional textile techniques to mimic the native ligament morphology. 3D printing also allows the production of a suitable scaffold for tendon/ligament regeneration and is a simple, fast, and cost-effective technique. A systematic study was performed in order to evaluate the mechanical and viscoelastic properties of the scaffolds. Micro-CT was used to assess their structure and porosity.

Chapter 5 presents the production and characterization of composite filaments based on medical-grade PLA+[(f-EG)+Ag] as well as the development of biocompatible 3D-printed scaffolds. The antibacterial efficiency of (f-EG)+Ag against Gram-positive and Gram-negative bacteria was investigated. The mechanical performance and biodegradation of 3D-printed scaffolds were evaluated under physiological conditions. The scaffolds' biocompatibility was assessed using L929 cells. To investigate the tenogenic commitment and to analyze the gene expression of specific tendon/ligament-related markers, the scaffolds were loaded with human tendon-derived stem cells.

Finally, **Chapter 6** presents the general conclusions concerning the production of composite scaffolds for tendon/ligament regeneration, as well as considerations for future work.

1.4 Author contributions

This section lists the publications that resulted from the thesis work.

1.4.1 International journal publications

Silva M, Ferreira FN, Alves NM, Paiva MC. Biodegradable Polymer Nanocomposites for Ligament/Tendon Tissue Engineering. *J Nanobiotechnol*. 2020, 18, 23.

Silva M, Pinho I, Covas JA, Alves NM, Paiva MC. 3D printing of graphene-based polymeric nanocomposites for biomedical applications. *Functional Composite Materials*. 2021, 2, 8, 1-21.

Silva M, Gomes C, Pinho I, Gonçalves H, Vale AC, Covas JA, Alves NM, Paiva MC. Poly(Lactic Acid)/Graphite Nanoplatelet Nanocomposite Filaments for Ligament Scaffolds. *Nanomaterials*. 2021, 11, 2796.

Silva M, Pinho I, Gonçalves H, Vale AC, Paiva MC, Alves NM, Covas JA. Engineering Ligament Scaffolds Based on PLA/Graphite Nanoplatelet Composites by 3D Printing or Braiding. *J Compos Sci*. 2023, 7, 104.

Silva M, Gomes S, Correia C, Peixoto D, Vinhas A, Rodrigues MT, Gomes ME, Covas JA, Paiva MC, Alves NM. Biocompatible 3D-Printed Tendon/Ligament Scaffolds Based on Polylactic Acid/Graphite Nanoplatelet Composites. *Nanomaterials*. 2023, 13 (18), 2518.

1.4.2 International conference proceedings books

Oral communications

Silva M, Gomes C, Lopes PE, Alves N, Covas J, Paiva MC. "Composite Fibers of PLA and Functionalized Few-Layer Graphene for Ligament Regeneration", CNPComp2019 – 8th International Conference on Carbon NanoParticle based Composites, London, UK, 17–19 July 2019.

Silva M, Pinho I, Gonçalves H, Vale AC, Paiva MC, Alves NM, Covas JA, "Ligament Scaffolds Based On PLA/Graphite Nanoplatelet Composites", International Conference on Nanomaterials and Nanotechnology, Paris, France, 27–28 March 2023.

Silva M, Pinho I, Gonçalves H, Vale AC, Paiva MC, Alves NM, Covas JA, "Ligament Scaffolds Based On PLA/Graphite Nanoplatelet Composites", Materiais 2023, Guimarães, Portugal, 3–6 April 2023.

Poster communication

Silva M, Gomes C, Gonçalves H, Pinho I, Vale AC, Alves NM, Paiva MC, "Poly(lactic acid)/Graphene-based Nanocomposite Filaments for Ligament Scaffolds", DCE21- 4th Doctoral Congress in Engineering, Porto, Portugal, 28–29 June 2021.

CHAPTER **2**

Current progress on materials and processes for

ligament/tendon tissue engineering

This chapter in based on the articles:

Silva M, Ferreira FN, Alves NM, Paiva MC. Biodegradable polymer nanocomposites for ligament/tendon tissue engineering. J. Nanobiotechnol. 2020, 18, 23. https://doi.org/10.1186/s12951-019-0556-1

Silva M, Pinho IS, Covas JA, Alves, NM, Paiva MC. 3D printing of graphene-based polymeric nanocomposites for biomedical applications. Functional Composite Mater. 2021, 2, 8, 1-21. https://doi.org/10.1186/s42252-021-00020-6

2 Current progress on materials and processes for ligament/tendon tissue engineering

2.1 Biodegradable polymer nanocomposites for ligament/tendon tissue engineering

Ligaments and tendons are fibrous tissues with poor vascularity and limited regeneration capacity. Currently, a ligament/tendon injury often require a surgical procedure using auto- or allografts that present some limitations. These inadequacies combined with the significant economic and health impact have prompted the development of tissue engineering approaches. Several natural and synthetic biodegradable polymers as well as composites, blends and hybrids based on such materials have been used to produce tendon and ligament scaffolds. Given the complex structure of native tissues, the production of fiber-based scaffolds has been the preferred option for tendon/ligament tissue engineering. Electrospinning and several textile methods such as twisting, braiding, and knitting have been used to produce these scaffolds. This review focuses on the developments achieved in the preparation of tendon/ligament scaffolds based on different biodegradable polymers. Several examples are overviewed and their processing methodologies, as well as their biological and mechanical performances, are discussed.

2.1.1 Introduction

Tendons and ligaments have poor regeneration capacity with low cell density and low nutrient and oxygen requirements (2). Injuries in these tissues such as in ACL are frequent in athletes and in elder and active working people, which cause joint instability accompanied by pain, disability, progressing of degenerative diseases and often, surgical interventions (16).

Current surgical reparative techniques rely on tissue replacement with auto- or allografts (5). Despite excellent outcomes in terms of short-term results, serious complications are related to their usage and 5-year studies show that patients have instability and pain (6). The main problems about the use of autografts include the need of additional surgery with potential donor harvest site infection and pain. On the other hand, concerns about using allografts are limited graft availability or even the risk of disease transmission, bacterial infection and the possibility of immunogenic response elicited in the host (4, 7, 9). The need to address the shortcomings of existing strategies has prompted the investigation of synthetic and non-degradable substitutes.

The development of non-degradable synthetic ACL substitutes has emerged since the early 1970s and offer advantages over autograft or allograft (9). They allowed a rapid rehabilitation, avoid donor tissue morbidity, and provide improved knee stability, not losing their strength during tissue revascularization (17, 18). Thus, in 1973, Proplast, a combination of polyaramid fibers and ethylene polymers allowed cellular ingrowth and received Food and Drug Administration (FDA) approval for use as a ligament substitute (9). Other commercial devices have emerged and have received the FDA approval as permanent prosthetic devices (17), such as a Gore-Tex device made with woven polytetrafluoroethylene fibers (17, 19) that was used between the mid 1980s and mid 1990s. In the early 1980s, the use of a polypropylene braid as a ligament augmentation device was proposed-Kennedy LAD device. Other devices were produced with polyester composites such as a polyester mesh in the case of the Leeds-Keio device. A second-generation of the Leeds-Keio device was made available in 2003. Distinct Polyethylene terephthalate devices were produced including Trevira-Hochfest, Proflex device, ProPivot and Ligament Augmentation and Reconstruction System (LARS) (19). Initial enthusiasm for these devices was later faded by reports of complications and are not currently recommended for ACL repair (8). They supply enough initial tensile strength, but all fail over time, with several limitations specific to their use: device creep, mechanical failure or mechanical mismatch with native tissue, problems with synovitis, chronic effusions, recurrent instability and early knee osteoarthritis (8, 18, 19). Because of these complications, FDA has since removed these synthetic ACL grafts from the market. Thus, no synthetic replacements for ACL reconstruction are unconditionally approved for medical use in the United States (9). The deficiencies of current approaches combined with the significant impact of these injuries on the community in terms of social, economic and health have prompted the research of tissue engineering (TE) approaches for tendon/ligament regeneration (9, 16, 18). Thus, TE proposes alternative approaches combining cells with 3D scaffolds to mimic the mechanical and chemical cues of native extracellular matrix (ECM), and/or bioactive molecules to biochemically stimulate cells growth (18).

Specific cell types are incorporated into the scaffold which will be implanted into the host and interact with native cells and growth factors (20). Interactions between cells and material's scaffold are very important since materials could interfere with cells' adhesion, proliferation and differentiation (17). Ideally, cells should be readily available and have potential to proliferate and elaborate an ECM similar to native ligaments/tendons (21). Resident tendon and ligament fibroblasts are the logical candidates for their regeneration. However, accessing them is difficult due to their intrasynovial location and exhibited a limited quantity and modest proliferative potential, which have restricted their usage. With the

advancement of stem cell technology, pluripotent and multipotent stem cells for ligament/tendon tissue engineering have been more and more used (9) and include embryonic stem cells (ESCs), induced pluripotent stem cells (iPSC), bone marrow mesenchymal stem cells (BMSCs) and adipose-tissue-derived mesenchymal stem cells (AMSCs) (18).

The scaffold acts as a temporary engineered replacement of the native ECM with similar mechanical and functional characteristics (22, 23) and will gradually degrade, being slowly resorbed by the surrounding tissue, and replaced while a new natural tissue is resynthesized (5, 9, 20, 24).

The scaffold should mimic the properties of the native tissue, not only in terms of mechanical function (25), but also proper topography, geometry and porosity to recreate the native microenvironment and aid the cell adhesion, growth (22) and differentiation of the populating cells (25).

By labelling cells with Quantum dots (QDs), it is possible to analyze variations in terms of number of cell populations adherent on different topographical regions, by counting cells labeled with QDs of the respective color. These QDs are readily incorporated by most cells' lines and, at moderate concentrations and incubation times, do not cause acute cytotoxicity (26). Besides, it has been found that the interaction between these nanoparticles and mesenchymal stem cells (MSCs) may influence their self-renewal, function and differentiation. Graphene-QDs, within a nontoxic concentration, promoted an osteogenic differentiation of MSCs, with gene activation and protein expression. Moreover, Graphene-QDs also promoted adipogenic differentiation of MSCs, which confirms that the pluripotency ability of MSCs was preserved (27).

Pore interconnectivity throughout an implant favors the distribution of nutrients, cell migration, metabolic waste removal and the tissue ingrowth, enhancing its regenerative properties (7, 28). The long-term clinical success of scaffold also requires biocompatibility (7, 22) which is the ability of a material to perform with an appropriate host response in a desired application. It is not only dependent on the material characteristics but also on the situation in which the material is used and the toxicity of the degradation products (29, 30). To improve biocompatibility and biofunctionality, extracellular matrix proteins and growth factors such as insulin like growth factor I (IGF-I),transforming growth factor-β (TGF-β) or basic fibroblast growth factor (bFGF) (9) have been incorporated into scaffolds to promote ligament/tendon regeneration (31).

Regarding the regulatory aspects of these TE scaffolds, they are generally under the category of medical devices. Medical devices are products or equipment generally intended for medical use. In European Union (EU), they are strictly regulated by both national competent authorities and by the

European Medicines Agency (EMA). The adopted regulation in EU for such devices is Regulation 2017/745 on Medical Devices. In USA, the extensive regulatory requirements are defined by FDA. Moreover, when TE scaffolds are combined with cells, the classification of their category is not straightforward, depending on the cell type, and varying with the Regulatory Agency, e.g. FDA and EMA have distinct regulatory aspects. Also, their approval would be more complex: in fact, an acellular scaffold should face less regulatory scrutiny than approaches utilizing allogeneic or xenogeneic cells, iPSC, ESCs, or even significant *ex vivo* manipulation of autologous cells. The introduction of cells as a component in TE introduces attendant risks associated with possible immunogenicity, teratoma formation, cell culture adaptation/morphogenesis, or contamination which must be addressed to assure safety. In summary, the regulation of TE products is time-consuming, with an average time from pre-clinical/clinical studies to the market of about 15 years, and extremely high cost. There are already several papers/book chapters in the literature just devoted to the clinical translation of TE constructs and the associated regulatory aspects (32).

Despite the variety of TE solutions and biodegradable polymers proposed for ligament/tendon TE, they haven't yet reached the clinic or even pre-clinics because they still exhibited problems related to the inadequacy of mechanical properties, degradation rate and biological response that are necessary to overcome (2). For instance, there appears to be no consensus in the literature as to the nature of the scaffold material that is most suitable for clinical trials. So, further research is required to optimize tissue engineered ligament/tendon scaffolds before clinical application.

Thus, the selection of biodegradable and biocompatible materials with adequate degradation rate, structural and mechanical properties that mimic the organization of the ligaments/tendons represents a critical feature in the development of a successful scaffold.

2.1.2 Biodegradable polymers for ligament/tendon tissue engineering

Biomaterials are natural or synthetic materials designed to interact with the biological systems, with an intended function in the body or to treat, augment or replace any tissue or organ (33, 34). Successful scaffolds should be biocompatible and maintain the mechanical properties until it is replaced by native tissue, disintegrating into smaller fragments along the replacement process, being absorbed and excreted by the body (35). Understanding the scaffold's materials degradation behavior is very important when designing a new scaffold since it may alter its physicochemical properties and hence, its

functionality or even its biological response (36). Thus, the scaffolds' biocompatibility is intimately related to the scaffolds' composition, which should not cause any significant systemic inflammation or local reaction (37), but also to its biodegradation, since the degradation products should be nontoxic and metabolized by the body (25, 37). Scaffold's polymer degradation rate plays an important role in the cellular vitality and growth and should be similar to the rate of new tissue formation, allowing the occupation of the scaffolds' space by the new tissue formed (37).

When in contact with surrounding fluids, polymers degrade by chain scission yielding low molecular weight species, oligomers and monomers (38). All biodegradable polymers contain hydrolysable bonds making them prone to chemical degradation via hydrolysis or enzyme-catalyzed hydrolysis (37, 39, 40). Synthetic polymers, in contrast to natural polymers, are less susceptible to enzymatic hydrolysis, and so tend to degrade by simple hydrolysis (10). As a consequence of the water soluble degradation products (chemical phenomena), erosion of the material can occur (physical phenomena) (37).

Several natural polymers such as collagen (Col), silk, chitosan (CHI), hyaluronic acid (HA) and synthetic biodegradable polymers such as PLA, Polyglycolic acid (PGA), poly(lactic-co-glycolic acid (PLGA), poly(ε-caprolactone) (PCL), as well as biodegradable based polymeric composites have been used to produce scaffolds for tendon and ligament TE (2, 4, 5, 12, 22), in the form of gels, membranes, or 3D fibrous scaffolds.

PLA, PGA and PLGA are considered biocompatible, causing just minimal or mild foreign body reaction, since their hydrolytic degradation products (lactic and glycolic acids) are normally present in the metabolic pathways of the human body (38). However, their bulk degradation may occasionally lead to local inflammation due to accumulation of acidic degradation products that cannot be easily disposed. PCL is also biocompatible and degrades at a much lower rate than PLA, PGA, and PLGA, making it attractive for long-term scaffolds such as tendon/ligament scaffolds (38). For instance, ACL regeneration and subsequent functionality usually requires at least 6 months (41). For such applications materials with a slower degradation should be selected (10, 41).

The polymer degradation rate is strongly influenced by several parameters such as the morphology, molecular weight and its distribution, crystallinity degree, glass transition temperature and environmental conditions (medium, temperature, and pH) (42). It can be controlled by varying composition, molecular weight, processing conditions or even blending with biodegradable polymers with different characteristics (10, 20). For example, several degradation profiles and mechanical properties

are possible to obtain just by using different fibers, composed of materials with different degradation rates, and varying their diameter or architecture (10).

Most degradation experiments are performed *in vitro* by incubating the scaffold in phosphate buffered saline (PBS) at body temperature (37°C). However, *in vivo* degradation is significantly different and occurs faster than *in vitro* degradation due to the tissue response. Once implanted, the scaffold is identified as a foreign body creating an inflammatory response. This induces the migration of leucocytes and macrophages to the implant site, forming reactive products as hydrogen peroxide that oxidize the polymer. The degradation products will be removed from the implantation site by the lymphatic system and subsequently secreted from the body. The *in vivo* mass loss can be also increased by mechanical stimulations and cellular activity. Besides, the size and the shape of the scaffold influence its degradation rate. Larger implants require longer degradation times (38).

Most of the research for tendon tissue regeneration proposes the use of Col alone or mixed with other molecules, such as proteoglycans, to produce scaffolds in form of sponges, aligned extruded Col fibers or electrochemically-aligned Col (43). Regarding ligament regeneration and specifically tissue-engineered ACLs, Col and the L enantiomer of PLA, Poly (L-lactic) acid (PLLA), have been the most used materials to produce biodegradable scaffolds, although some of them do not achieve more than 20% of the ultimate tensile strength of native ACL (17). PLLA has demonstrated reasonable properties in terms of material strength and resorption rate (44), as well as it does not cause a permanent foreign body reaction (8).

All the referred biodegradable polymers can be easily processed into fibers and fibrous scaffolds. However, each of these polymers has exhibited some inadequacies for tendon/ligament applications, such as inadequate mechanical properties and degradation rate (38). Also, despite the variety of approaches on ligament tissue-engineering, only a few of them were tested *in vivo,* using dogs, rabbits, goats and sheep (17).

2.1.2.1 Natural polymers

Natural polymers such as Col, alginate (ALG), CHI, HA, silk, fibrin and cellulose are attractive materials for biomedical applications due to their biocompatibility and capacity to structurally mimic the native ECM (45). These polymers are capable of hydrolytic or enzymatic degradation (20), since they have a similar composition to macromolecular substances which are recognized by the biological environment and metabolized (46). For that reason, the common problems caused by synthetic polymers

are frequently avoided, such as stimulation of chronic immunological reactions and toxicity, as well as lack of cell recognition (33). Natural polymers contain functional groups that allow a chemical conjugation with other molecules, such as growth factors (20, 47). This feature may be beneficial for their further application in tendon/ligament scaffolds, as described in Table 1.

Table 1 – Natural biodegradable polymers commonly used in tendon/ligament regeneration.

Natural Biomaterial	Advantages	Disadvantages
Collagen	Biocompatible; major component of ligaments (9); reasonable mechanical properties (18)	Poor mechanical strength (9); risk of immunogenicity (35); fast degradation (48)
Silk	Good mechanical properties; slow rate biodegradation (18); loses its strength after 1 year, *in vivo* (10)	Limited cell adhesion (9)
Alginate	Biocompatible ECM component; can be in sponge or hydrogel form (9); proper substrate for fibroblasts growth and collagen type I production (18)	Lacks mechanical properties (9)
Hyaluronic acid	Biocompatible; can be in sponge or hydrogel form (9)	Natural form with very short degradation time (49)
Chitosan	Biocompatible; can be in sponge or hydrogel form (9); proper substrate for fibroblasts growth and Col type I production (18)	Lacks mechanical properties (9)

In spite of various advantages, natural polymers typically have relatively poor mechanical properties (50) and present low processing ability when compared to the synthetic ones, which limit their application (25, 33). Besides, these polymers often suffer batch-to-batch variability in molecular weight and purity, which represent low reproducibility amongst different samples of the same material (20, 25).

Collagen

The most obvious and common choice for ligament and tendon TE is Col type I because of its prevalence in the native tissues (5, 51-54). It forms the connective tissue on which the fibroblasts adhere and proliferate (2, 45). For that reason, Col was the first natural scaffold's material to be used in ligament reconstruction (2). Purified Col derived from animal tissue requires crosslinking to remove foreign antigen,

14

avoid potential disease transmission, improve its mechanical strength and slow down its degradation rate (10). However, even after physical or chemical crosslinking of Col, the collagenous scaffolds fail to reproduce the mechanical properties of native collagenous tissues, the support of mechanical loading decreases over time (21, 22) and suffer relatively fast *in vivo* degradation (10).

Dunn et al. (52) extruded Col fibers and crosslinked them to produce collagen fibrous scaffolds. Rabbit ACL and patellar tendon (PT) fibroblasts were seeded onto Col scaffolds and adherence and viability *in vitro* was found in both cases (52). Bellincampi and co-workers (53) determined the *in vivo* fate of autogenous ACL and skin fibroblasts-seeded onto collagenous scaffold as a function of fibroblast source, implantation site and time. The cultured cells were seeded onto Col fiber scaffolds and implanted in rabbits. The seeded skin and ACL fibroblasts survived for at least 4–6 weeks after implantation and the fibroblast type seemed to have no influence on the viability. However, they verified a complete resorption of the scaffolds after 6 weeks (53).

Concerns about the Col mechanical performance, immunogenicity and leaching of chemical crosslinking agents have led to explore alternative scaffold materials (9, 21), such as silk, polysaccharides or synthetic polymers. Nevertheless, new crosslinking strategies as well as scaffolds with a braid-twist design (9) or even decellularized ECM-derived Col scaffolds (22) are still being explored to achieve Col scaffolds with more favorable properties for ligament regeneration. Walters et al. (54) have recently developed Col type I fiber-based scaffolds for ACL ligament with a braid-twist design and evaluated the effect of crosslinking method and the addition of gelatin on the mechanical properties. Although the crosslinked scaffolds without gelatin exhibit lower ultimate tensile strength (UTS) than native human ACL but with a similar Young's Modulus, improvements are still desired (54). According to Noyes and Grood (55), ACLs from younger human donors (16–26 years of age) exhibited a UTS of 37.8 ± 9.3 MPa and a Young's modulus of 111 ± 26 MPa.

Silk

Like Col, silk has been effectively used in ligament regeneration approaches (16, 24, 56-62) being easily fabricated into gels, films and braided or knitted fibers (5).

Its main advantage is its remarkable tensile strength and toughness compared to most natural materials although being lower than native human ACL (2). Silk fibers lose their tensile strength in 1 year and undergo complete proteolytic degradation within 2 years *in vivo* (9). This allows a gradual transfer of mechanical load from the scaffold to the neoligament (63).

In addition, silk biomaterials are biocompatible *in vitro* and *in vivo*.(64) Silk scaffolds have supported attachment and proliferation of several primary cells and cell lines (64), such as human BMSCs and fibroblast (61) as well as synthesis of fibroblastic markers with the application of mechanical stimulation (9, 24).

Recently, Teuschl et al. (59) reported the braiding of silk fibers into wire rope–like structures to produce scaffolds that were boiled in borate buffer to remove sericin. The resulting silk ACL grafts were seeded with autologous stem cells and were able to stimulate ACL regeneration under *in vivo* conditions, using mountain sheep models. The seeded scaffolds exhibited UTS and elasticity values comparable to native ovine ACL (59). Several textile methods such as twisting or cabling have been used to design TE scaffolds – see Figure 1 (58). Similarly, Chen et al. (61) and Altman et al. (24) showed that silk fibroin, is nonantigenic, biocompatible, and allow the BMSCs attachment, proliferation and differentiation toward ligament lineage – Figure 2.
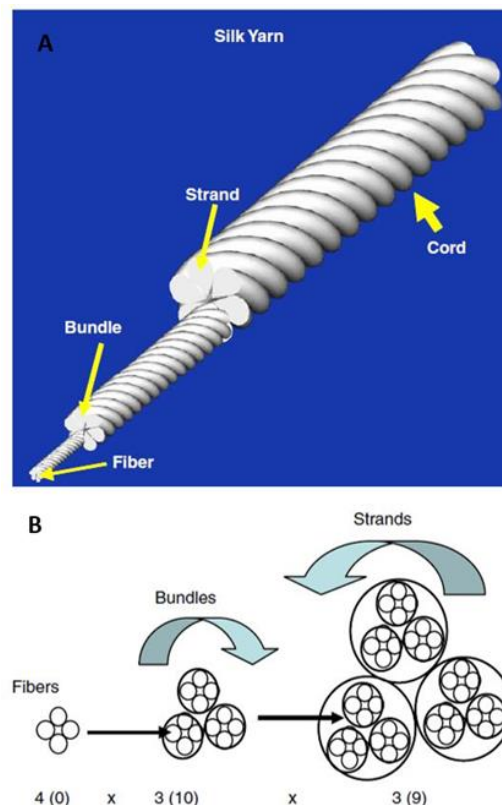
Figure 1 – (**A** and **B**) Structure of a twisted or cabled yarn. Fibers are combined to form bundles, bundles to form strands, and strands to form cords. Yarns were labeled: A(a) x B(b) x C(c), where A, B, C represent, the number of fibers/bundles/strands in the final structure, respectively and a, b, c is the number of turns per inch on each of the hierarchical levels (58).
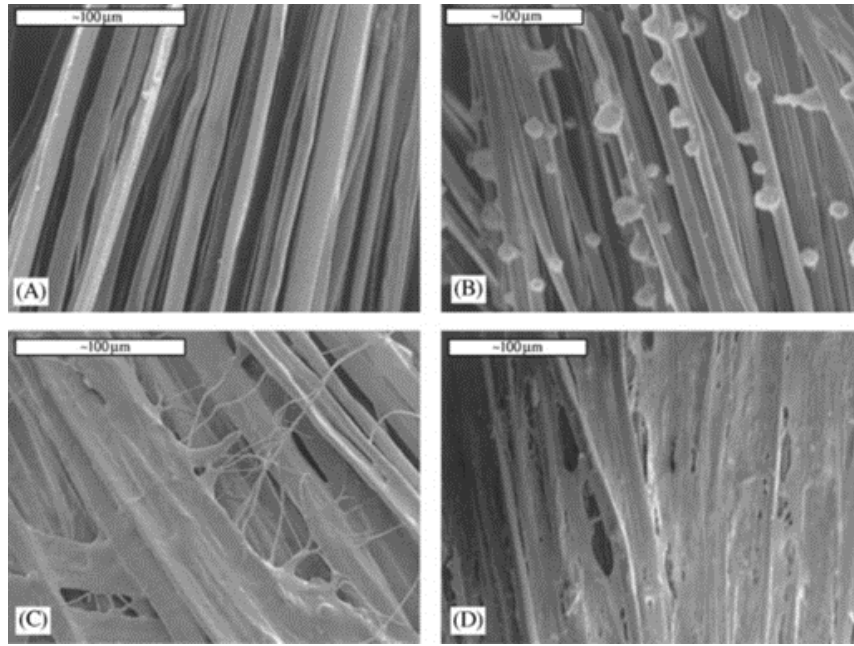
Figure 2 – Scanning electron microscopy (SEM) showing adherence, proliferation and cell sheet formation by human BMSCs on the silk cord matrix prior to seeding (**A**), time 0 following seeding (**B**), 1 day (**C**), and 14 days (**D**). Scale bars=100 mm. Reprinted with permission from (24).

In their study, Chen *et al.* (61) studied wire-rope silk matrices and silk films, modified with a short polypeptide. Modified silk matrices improved human BMSCs and ACL fibroblasts adhesion and showed higher cell density and Col production, over 14 days in culture when compared with the non -modified matrices (61). The 6-cord silk wire-rope scaffold produced by Altman et al. (24) not only supported the aforementioned attachment, expansion and differentiation of BMSCs but also presented slow degradability and mechanical properties similar to those of the native human ACL (24). Fan and co-workers (56) prepared a scaffold by rolling a knitted microporous silk mesh around a braided silk cord. MSCs seeded on these scaffolds (56) proliferated and differentiated into fibroblast-like cells by expressing collagen I, collagen III and tenascin-C genes in mRNA level. MSCs seeded scaffolds were implanted in a pig to regenerate the ACL. A remarkable scaffold degradation was observed, but the maximum tensile load of regenerated ligament was be maintained after 24 weeks of implantation. The tensile loss caused by the degradation of scaffold was compensated by the new tissue formed. MSCs showed robust proliferation and fibroblast differentiation, at 24 weeks postoperatively (56).

Liu et al. (62) proposed a combined scaffold that incorporates microporous silk sponges into a knitted silk scaffold for ACL tissue engineering. BMSCs and ACL fibroblasts were seeded onto the scaffolds and cultured *in vitro* for two weeks. To evaluate the *in vivo* survivability, BMSCs or ACL fibroblasts seeded

17

on each silk scaffold and implanted in rabbits were examined at 4 weeks post implantation. BMSCs presented advantages over ACL fibroblasts, in terms of cell proliferation, glycosaminoglycan excretion, gene and protein expression for ligament-related ECM markers, and *in vivo* viability – Figure 3 (62).
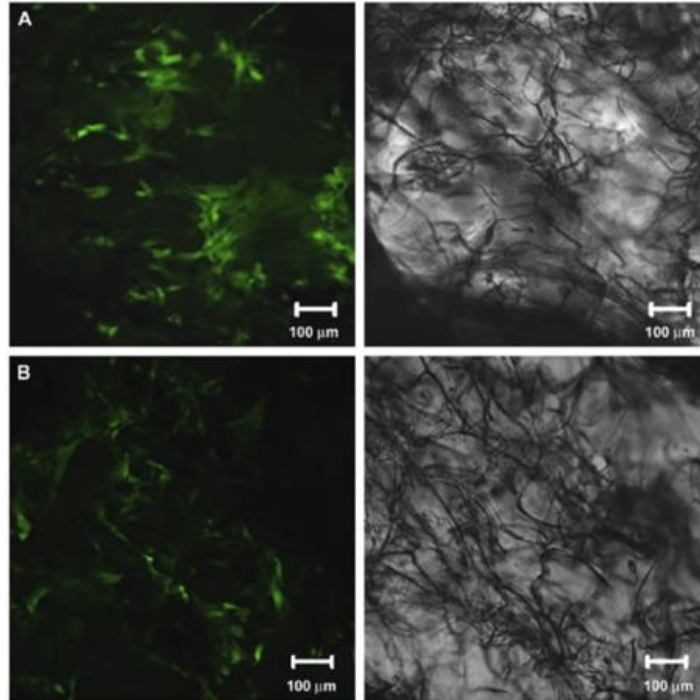
Figure 3 – Fluorescence images of implants with silk scaffolds-with BMSCs (**A**) and ACL fibroblasts (**B**) at 4 weeks post implantation. Scale bars = 100 mm. Reprinted with permission from (62).

Polysaccharides

HA fibers are another natural-origin alternative for ACL replacement (49, 65). HA is an anionic polysaccharide naturally present in all soft tissues, being responsible for the maintenance of the normal extracellular matrix structure (49). It is not immunogenic (49), being the main component of glycosaminoglycans, known for stimulating various *in vitro* tissue regenerative processes. The natural form of HA is in gel and has a very short degradation time. For that reason, some chemical modifications have been proposed to improve its processability and biodegradation (49). The biological effects of HA, such as the improvement of cellular adhesion and proliferation as well as anti-inflammatory character, could enhance ligament tissue regeneration (66). For example, Cristino et al. (49) seeded MSCs into the HA-based prototype ligament scaffold, and verified that MSCs cells completely wrapped the scaffold fibers and expressed CD44, a receptor important for scaffold interaction, and typical ligamentous markers, such as collagen type I, type III, fibronectin, laminin, and actin (49).

CHI is a cationic polysaccharide with excellent adhesive properties and biocompatibility which has led to its application as a scaffold material in the field of musculoskeletal tissue engineering (66). Due to their opposite charges, HA and ALG are usually combined with CHI to form polyionic complexes effective for scaffolds and with excellent adhesive properties (66, 67).

Table 2 summarizes the main studies that have used natural biodegradable polymers for ligament/tendon tissue engineering and highlights the major outcomes for the proposed scaffolds in terms of mechanical and *in vitro/ in vivo* properties.

2.1.2.2 Synthetic polymers

Owing to their availability, ease of processability and reproducibility, synthetic polymers have been widely used to produce tendon/ligament scaffolds (22, 25). Contrasting to the natural ones, synthetic polymers present low immunogenicity potential and are more versatile, enabling tailoring and controlling the chemical and physical properties (16).

Polyesters such as PCL and PGA, PLLA, poly(L-lactide-co-ε-caprolactone) (PLCL) and PLGA have been effectively used to produce mechanically strong and biodegradable scaffolds for tendon/ligament applications – Table 3 (22, 41). These polymers are well characterized and have been approved by the FDA for certain human uses (43). However, one of the disadvantages of synthetic polymers is the lack of biological cues for promoting cell adhesion and proliferation, which has to be overcome by, for example, applying a specific coating (43).

Table 2 – Performance of natural biodegradable polymers in ligament/tendon TE ([a]Maximum tensile load; [b]Human foreskin fibroblasts)

Material	Scaffold	Tissue	*In vivo /in vitro*	Mechanical Response				Biological Response	Ref
				Young's Modulus (MPa)	Stiffness (N/mm)	Max. Strength (MPa)	Max. Load [a] (N)		
Collagen	Aligned parallel 200 extruded-crosslinked Col fibers; Coating with Col	Ligament	*In vitro* (ACL and PT fibroblasts)	ND			ND	Cells adhesion, proliferation; ACL cells: ovoid shape; no alignment; PT cells: elongation	(52)
	Aligned parallel 200 extruded-crosslinked Col fibers		*In vivo*, rabbit model	ND			ND	Skin/ACL fibroblasts survived 4-6 weeks, after implantation; Scaffold resorption after 8 weeks	(53)
	i) Extruded-crosslinked Col fibers from bovine Achilles tendon; ii) Extruded-crosslinked Col fibers from rat tail tendon; iii) Fiber-embedded gel scaffolds		*In vitro* (Fibroblasts)	i)359.6± 28.4; ii) 995.1± 144; iii) 83.4± 10.8	ND	i)36.0±5.40; ii)106.1± 13.90; iii) 5.4±0.4	ND	Non-uniform cells distribution	(51)
	Braid-twist scaffold of extruded-crosslinked Col fiber i) with or ii) without gelatin		*In vitro* (Primary rat ligament fibroblasts)	i) 6.32±0.95; ii) 148± 170	ND	i) 1.07± 0.06; ii) 19.3± 3.10	ND	Cell adhesion, proliferation; Only ii) exhibited increased cellular activity after 21 days of culture	(54)

Material	Scaffold	Tissue	*In vivo /in vitro*	Mechanical Response				Biological Response	Ref
				Young's Modulus (MPa)	Stiffness (N/mm)	Max. Strength (MPa)	Max. Load ˑ (N)		
	Woven scaffold by electrochemically aligned Col threads (yarns)	Tendon	*In vitro* (MSCs)	~520	ND	~65	ND	MSCs adhesion, proliferation, elongation after 35 days in culture; Tendon-specific/related markers	(68)
	Sponges (L/W/T= 23/9/3 mm) i)Non-stimulated scaffolds; ii)Mechanically stimulated scaffolds		*In vitro* (rabbit MSCs) / *In vivo*, rabbit model	i) 343.2± 21.2; ii)441.2± 26.3	ND	i) 50.2±9.2; ii) 72.1±11.1	i)271.5±17.5 ii)339±11.4	MSCs adhesion and alignment; i)and ii) excellent cellular alignment, after 12 weeks of culture; Tendon-related ECM components	(69)
Silk	Knitted microporous silk mesh rolled up around a braided silk cord	Ligament	*In vitro* (MSCs) / *In vivo*, pig model	ND	58.5±17	ND	398±70	MSCs adhesion, proliferation, differentiation; Ligament-specific ECM markers at 24 weeks post-operatively	(56)
	Wire rope–like scaffolds i) Cell seeded-scaffold ii) Non-seeded scaffold		*In vivo* (autologous stem cells), sheep model	ND	194±27	ND	1450±65	i) Higher cell content in the inner part, after 6 months i), ii) Silk fiber degradation after 12 months	(59)
	i)Wire rope of multifiber; ii)Parallel multifiber (theoretical)		*In vitro* (BMSCs)	ND	i) 354 ± 26; ii) 1740	ND	i) 2337±72; ii) 2214	i) BMSCs adhesion, proliferation, differentiation Ligament-specific markers, after 14 days of culture ii) ND	(24)
	Knitted silk mesh integrated:		*In vitro* (MSCs)	ND	i) 22.12± 1.2; ii)19.21± 0.9;	ND	i)129±7.4; ii)106±6.2; iii)93.2±5.6	i) MSCs proliferation, elongation, orientation along the fibers; Ligament-related proteins increased when compared to ii) scaffolds	(57)

21

Material	Scaffold	Tissue	*In vivo /in vitro*	Mechanical Response				Biological Response	Ref
				Young's Modulus (MPa)	Stiffness (N/mm)	Max. Strength (MPa)	Max. Load ᵃ (N)		
	i) Aligned electrospun fibers; ii) Random electrospun fibers iii) Without fibers				iii)16.24±0.8				
	Microporous silk sponges incorporated into a knitted silk scaffold		*In vitro* (BMSCs and ACL fibroblasts) / *In vivo*, rabbit model	ND			ND	BMSCs with higher proliferation, ligament-related ECM markers and *in vivo* viability, comparing to ACL fibroblasts	(62)
			In vitro (MSCs)	ND	50±4 (after 14 days of cell culture)	ND	257±7 (after 14 days of cell culture)	MSCs adhesion, proliferation; Ligament- specific ECM markers, after 15 days of culture	(70)
	i) Wired ii) Braided		*In vitro* (hFFᵇ)	ND	i) ˜280; ii) ˜240 (wet)	ND	i)˜1560; ii)˜1610(wet)	Inconclusive cell invasion, proliferation	(71)
i) Silk; ii) PBS	Extruded fibers in knitted scaffolds (weft knitting)	Tendon/ Ligament	*In vitro* (L929 fibroblasts)	i) 31.6; ii) 7.9	ND	i) 17.4; ii) 8.2	ND	i), ii): L929 adhesion, proliferation; i) Differentiation, after 14 days of culture; ii) Cells with rounder shape	(11)
HA (HYAFF 11 ®)	Multilayered knitted cylindrical array of fibers	Ligament	*In vitro* (MSCs)	ND			ND	MSCs adhesion, proliferation, differentiation; Ligament-specific ECM markers	(49)

Table 3 – Synthetic biodegradable polymers commonly used in tendon/ligament regeneration

Synthetic Biomaterial	Advantages	Disadvantages
PLLA	Slow degradation rate (10 months to 4 years) (10), better cell adhesion than PGA or PLGA. Easily manufactured (9)	Acidic degradation (9)
PCL	Easily manufactured; FDA approved material (9); (over 3 years *in vivo*) (72)	Very slow degradation rate (9)
PGA	Easily manufactured; FDA approved material (9)	Rapid (6–12 months) (73) and acidic degradation (9); lack of signaling molecules (67)
PLGA	Half-life of 1.5 months (73); Degradation rate can be tailored by changing the ratio of PLA:PGA. Easily manufactured (9)	Acidic degradation (9)
PLCL	Properties can be tailored by changing the ratio of PLA:PCL. Good biocompatibility and mechanical properties; easily manufactured (74)	Excessively elastic for tendon regeneration (74)

Poly-α-hydroxyesters

PLGA is a linear aliphatic polyester that contains lactide and glycolide as its monomers (45). It has been considered an attractive choice for ligament/tendon regeneration mainly due to its design flexibility and complete *in vivo* bioresorption (7, 22, 75-77). Moffat et al. (75) produced a PLGA nanofiber-based scaffold for rotator cuff tendon tissue engineering. The influence of design in the attachment, alignment and gene expression of human rotator cuff fibroblasts on aligned and unaligned PLGA nanofiber scaffolds was evaluated. Aligned nanofiber scaffolds presented significantly better mechanical properties than those of the unaligned. The tensile modulus of the unaligned and aligned scaffolds averaged 107 MPa and 341 MPa, respectively, with mean ultimate tensile strength ranging from 3.7 to 12.0 MPa. The human rotator cuff fibroblasts exhibited a phenotypic morphology and attached preferentially along the nanofiber axis of the aligned scaffolds, whereas only random cell attachment was observed on the unaligned scaffold.

Cooper et al. (7) proposed 3D braided scaffolds based on PLGA fibers, using a 3D circular braiding system and a rectangular braiding system for comparison. The 3D circular fibrous scaffold has

the highest tensile loads of 907 ± 132 N, which was greater than the level for normal human physical activity. The stress–strain profile was found to be similar to that of natural ligament tissue. The scaffold porosity (175–233 mm) was adequate for tissue ingrowth. An example of the scaffold design for 3D rectangular braid and the corresponding load–deformation curves of the 3D rectangular braids is shown in Figure 4 and 5, respectively. Primary rabbit ACL cells and BALB/C mouse fibroblasts adhered and spread on scaffolds. Both types of cells grew on the rectangular braided scaffold but only the ACL cells grew on the 3D circular braids (7).
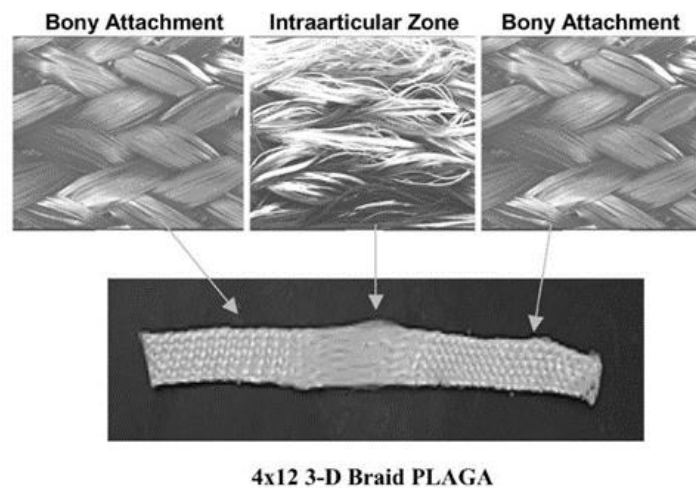
Figure 4 – General configuration of ligament scaffold design for 3D rectangular braid, with 3 regions: femoral tunnel attachment site, ligament region, and tibial tunnel attachment site. Reprinted with permission from (7).
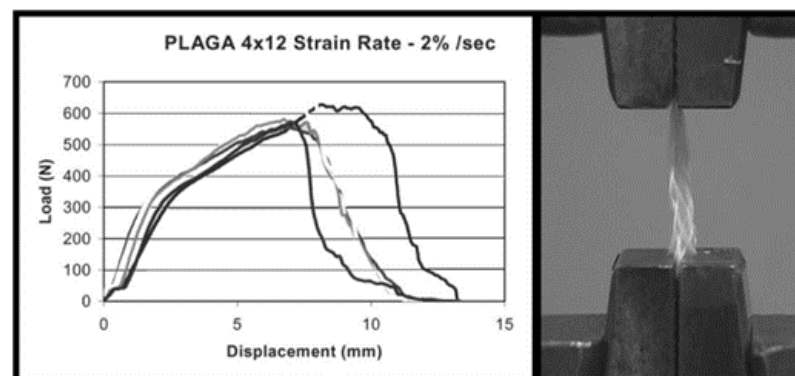
Figure 5 – Load-deformation curve and photomicrograph of mechanical failure of the 4 x12 PLGA 3D rectangular braids at a strain rate of 2%/s. Reprinted with permission from (7).

Braided and knitted scaffolds often require a gel system for cell seeding. In order to overcome this limitation, Sahoo et al. (76) proposed a biodegradable scaffold produced by electrospinning PLGA nanofibers onto a knitted PLGA scaffold. BMSCs were seeded on these scaffolds and on knitted PLGA

scaffolds by immobilizing in fibrin gel. BMSCs produced abundant ECM with a higher expression of collagen-I, decorin, and biglycan on the scaffold with nanofibers demonstrating their potential to differentiate into tendon/ligament tissue.

The biodegradation of PLGA occurs mainly via chemical hydrolysis of the hydrolytically unstable ester bonds into lactic acid and glycolic acid, which are non-toxic and removed from the body by normal metabolic pathways (42). However, its biodegradation occurs within weeks, which results in complete loss of mechanical strength and compromise the integrity of PLGA-based scaffolds throughout the ligament healing period that generally extends to months (22, 78). For that reason, PLGA is usually combined with other polymers, such as PLA (41).

Regarding PLA, it is a linear aliphatic polyester, an homopolymer containing only lactide subunits as monomer (45). It has a slow degradation rate(10) being widely suggested for several tendon-ligament scaffolds (1, 8, 79-81). It undergoes hydrolytic scission into lactic acid and is eliminated from the body mainly through respiration by the lungs, as CO_2 (82). This degradation occurs within a period between 10 months to 4 years depending on its molecular weight, crystallinity, shape and site of the implant (83).

Cooper et al. (79) cultured, *in vitro* different types of cells derived from the ACL, medial collateral ligament (MCL), Achilles tendon (AT), and PT of rabbits on 3D braided PLLA scaffolds. This study revealed that all the primary connective tissue fibroblasts expressed genes associated with ligament differentiation but only PT and AT cells had the greatest *in vitro* proliferation on 3D braided scaffolds – Figure 6. The 3D braiding geometry affected the matrix production of ACL cells, favoring the production of a filamentous matrix (79). Lu et al. (77) and Laurencin *et al.*(8) reported an affinity of ACL fibroblasts to PLLA scaffolds. According to Cooper et al. (7) PLGA scaffolds produced by a circular braiding achieved higher tensile loads. For that reason, Lu et al. (77) also developed 3D braided PLLA scaffolds in a circular system. They verified that ACL fibroblasts conformed to the geometry of these PLLA scaffolds, being the cell attachment and proliferation increased when the scaffolds were coated with fibronectin (Fn). Fn is an important protein which is upregulated during ligament healing (77).

Concerning PCL, it is a hydrophobic polyester with semi-crystalline structure, containing caprolactone subunits (45). It exhibits favorable biocompatibility, adequate mechanical strength, high elasticity as well as long degradation time which has prompted its application in tissue engineering (84). Comparing to PLLA, PCL presents a slower degradation rate. However, its hydrophobicity may results in poor cell attachment and proliferation (85). For that reason, when aiming tendon/ligament regeneration, PCL and derivatives are usually combined with other polymers such as CHI (86, 87), or simply coated

25

with Col (84, 88). In a study, electrospun PCL fibers were implanted in a rodent model for wound healing, showing evidences that PCL is nonimmunogenic, being integrated into local tissue without adverse reactions (89).
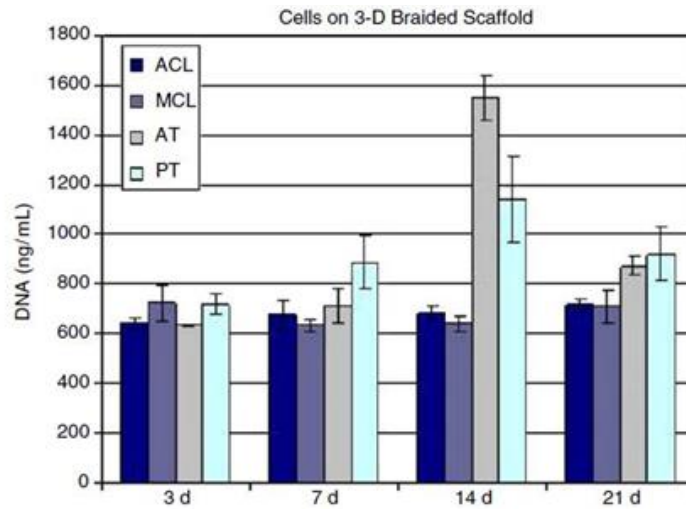
Figure 6 – The cellular proliferation after culturing for 3, 7, 14 and 21 days on 5x5 PLLA 3-D square braided scaffolds. The temporal cell growth of the ligament cells was slower as compared to the tendon cells (79).

In order to compare these three biomaterials, in addition to braided PLLA scaffolds, Lu et al. (77) also produced braided scaffolds made of PGA and PLGA to evaluate the effect of fiber composition on the mechanical properties and biodegradation. The scaffolds were coated with Fn before the culturing with primary rabbit ACL cells. Although PGA presented the highest tensile strength, the rapid degradation conducted to scaffold failure. Pre-coating the scaffold surfaces led to an increase in cell attachment efficiency and overall cell proliferation. Based on the overall cellular response, with highest rates of ACL fibroblast proliferation, and its superior mechanical and *in vitro* slow degradation properties, the PLLA braided scaffold coated with Fn was considered to be the most appropriate scaffold for ACL tissue engineering – Figure 7 (77).

Wagner et al. (90) produced 3D porous polycaprolactone fumarate (PCLF) scaffolds to mimic the anterior cruciate ligament. Porous scaffold molds were designed using SolidWorks CAD software and 3D-printed. The scaffolds were produced by ultraviolet radiation (UV) cross-linking of the PCLF solution and then seeded with human AMSCs in human platelet lysate. AMSCs proliferated, filling the pores and exhibited a collagen-rich extracellular matrix. At day 14, the cells remained viable and continued to increase in number, completely covering the surface and channels of the PCLF scaffold.
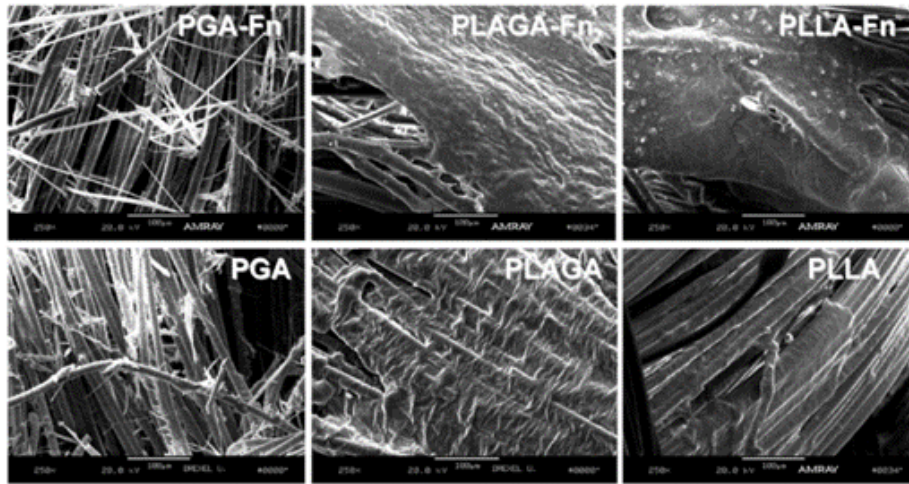
Figure 7 – ACL fibroblast on braided scaffolds after 14 days of culture. Cells grown on braided scaffolds pre-coated with Fn elaborates a great amount of matrix compared to PLGA or PLLA scaffolds without Fn. Degradation of the PGA scaffold after two weeks of culture resulted in extensive cell loss and matrix depletion. Reprinted with permission (77).

Table 4 presents a summary of the main studies that have used synthetic biodegradable polymers for ligament/tendon tissue engineering and the outcomes for the proposed scaffolds in terms of mechanical and *in vitro/in vivo* properties.

2.1.2.3 Materials for ligament/tendon scaffolds

The difficulty of satisfying all the ideal scaffold requirements by using a single class of materials is a recurrent problem (45). Advanced composite biomaterials have been fabricated to synergistically combine the beneficial properties of the constituents (45) and thus, achieving scaffolds that mimic complex structures of tendon/ligaments (91) and exhibit improved biological, biophysical and mechanical properties (9, 16, 20).

In the last years, the use of nanofillers (length < 100nm) for the production of polymer nanocomposites has received great attention in academic research and industry. Even with low nanofiller content, nanocomposites exhibited unique properties compared to conventional composites (92, 93). The significant higher surface-to-volume ratio of nanoparticles and their extremely higher characteristic ratio increase ductility with no decrease of strength and scratching resistance (94). Besides, with the incorporation of nanoparticles in the polymer matrix, new properties may arise, which would not be possible when using macrosized particles (92).

Table 4 – Performance of synthetic biodegradable polymers in ligament/tendon.

Material	Scaffold	Tissue	*In vivo / in vitro*	Mechanical Response				Biological Response	Ref
				Young's Modulus(MPa)	Stiffness (N/mm)	Max. Strength (MPa)	Max. Load (N)		
PLGA	i) Electrospun PLGA fibers onto knitted PLGA; ii) Knitted PLGA scaffold	Ligament/ Tendon	*In vitro* (porcine BMSCs)		i)0.85±0.2 ii)0.64±0.2(at 14 days of culture)	ND		i) Higher BMSCs attachment, proliferation, ECM deposition compared to ii)	(76)
	Electrospun Aligned i) Nanofiber diameter (320,680 nm); ii) Microfiber diameter (1.8 μm)		*In vitro* (Human rotator cuff fibroblast)	i) 421 ± 23; ii) 510 ±32 (for 1.8 μm)	ND	i) ~13; ii) ~14 (for 1.8 μm)	ND	i) Higher cells proliferation; ii) Higher tendon-related ECM markers, after 14 days of culture	(95)
	Electrospun i) Aligned nanofibers; ii) Random nanofibers	Tendon	*In vitro* (Human rotator cuff fibroblast)	i) 341±30; ii) 107±23	ND	i)12.0±1.5; ii)3.7± 0.2	ND	Cellular adhesion, proliferation; i) Elongated morphology and orientation along the fibers; ii) Polygonal shape, random orientation	(75)
	i) Rectangular braid; ii) Circular braid (scaffold with 3 regions)	Ligament	*In vitro* (fibroblasts: rabbit ACL; mouse BALB/C)	ND		i)217±11; ii)212±25	i)705±36; ii)907 ±132	Cellular adhesion and proliferation; i) ACL and BALB/C spread along the fibers ii) Only ACL proliferate along the fibers	(7)

Material	Scaffold	Tissue	In vivo / in vitro	Mechanical Response				Biological Response	Ref
				Young's Modulus(MPa)	Stiffness (N/mm)	Max. Strength (MPa)	Max. Load (N)		
PLLA	Rectangular braid (scaffold with 3 regions)	Ligament/ Tendon	*In vitro* (rabbit ACL; MCL;AT; PT fibroblast)			ND		Cellular adhesion, proliferation, elongation along the fibers; ACL with higher matrix production	(8, 79)
	Braided scaffolds of i) 3, ii) 4; iii) 5 aligned electrospun nanofibers		*In vitro* (human MSCs)	i) 55.0±2.8; ii) 47.8±7.5; iii)47.6±2.8	ND	i)7.62±0.2; ii)6.57±0.5; iii)6.67±0.4	ND	i)human MSCs adhesion and proliferation, orientation along the fibers; Expression of pluripotency genes ii), iii) ND	(96)
	i) Braided scaffold; ii) Twisted fiber scaffold; iii) Braid-twist scaffold	Ligament	*In vitro* (rabbit PT fibroblasts)	i) 810.2±233.5; ii) 888.2±60.7; iii) 428.2±60.7	ND	i) ~52.3±7.7; ii) 80.9±6.9; iii) 81.6±1.6	ND	i), iii) Comparable cellular adhesion, proliferation. Production of ECM, after 7 days of culture; ii) ND	(1, 97)
	5x5 Square braid: i) Scaffold before implantation ii)Seeded iii)Unseeded (i),ii) 4 weeks post-surgery)		*In vivo* (after seeded with primary rabbit ACL cells) rabbit model	i) 354.4± 68.5; ii)108.4± 27.7; iii)103.0± 53.9		ND	i) 332.2±19.6 ii) 239.0±43; iii) 209.0±73.5	i) ND ii)After 12 weeks, vascularization and greater tissue ingrowth and alignment of collagen fibers compared to iii) Mild inflammatory response observed in i) and ii)	(80)
	Electrospun i) Aligned; ii) Random nanofibers	Tendon	*In vitro/In vivo*, (human tendon stem cells (hTSCs)) mouse model	i)22.76±5.63; ii) 0.63± 0.56		ND		hTSCs adhesion, proliferation; *In vitro /In vivo* i) Cells with spindle-shaped and well orientated; teno-lineage differentiation	(98)

Material	Scaffold	Tissue	*In vivo /* *in vitro*	Mechanical Response				Biological Response	Ref
				Young's Modulus(MPa)	Stiffness (N/mm)	Max. Strength (MPa)	Max. Load (N)		
								ii) Cells with round shapes; random distribution	
i)PLLA; ii) PLGA; iii) PGA; iv) Fn pre-coated: i)-iii)	Circular Braid (multi-filament yarns-3 regions)	Ligament	*In vitro* (rabbit ACL fibroblasts)	ND		i) 165±33; ii)117±12; iii)378±18; iv) ND	i) 298±59; ii) 215±23; iii)502±24 iv) ND	ACL adhesion, proliferation; i) Cells with spindle-like morphology; ii) Cells with a form of spiked rods; iii) Cells form large globular aggregates; iv) Higher ECM production; Fn improved cellular proliferation mainly on i)	(77)
PCLF	UV-crosslinked PCLF solution injected over 3D printed mold - square porous: i) 500×500 μm; ii) 750×750 μm (Mold designed by SolidWorks CAD software)	Ligament	*In vitro* (AMSCs)		ND			i),ii)AMSCs adhesion and proliferation, filling the pores, after 14 days of culture; Expression of ligament-ECM in the presence of growth factors	(90)
PCL	Twisted electrospun fibers	Tendon	*In vitro* (human MSCs)	i)~34±6.8; ii) ~27±6.8	ND	i)~13±0.7; ii) ~12±1.4	ND	Cellular adhesion/proliferation; Elongated cells along the fiber direction;	

Material	Scaffold	Tissue	*In vivo /* *in vitro*	Mechanical Response				Biological Response	Ref
				Young's Modulus(MPa)	Stiffness (N/mm)	Max. Strength (MPa)	Max. Load (N)		
	i) Under static conditions; ii) Dynamic Loading			(acellular, after 21days)		(acellular, after 21days)		ii) Textured/round cells; Higher cell proliferation, comparing to i); i) Cells flatter and fused together; ii) Up-regulation of tendon genes, after 21 days	(99)

Several nanocomposites with biodegradable polymer matrices have been developed specifically for various biomedical purposes such as drug delivery, tissue engineering, wound dressings, stem cell therapy and cancer therapy (93, 94). The specific use of biodegradable polymer matrices for the production of the nanocomposites offers great advantages and include the ability to tailor mechanical properties and degradation kinetics to suit various applications (100). Other advantages of using biodegradable matrices in TE approaches are their potential to fully restore the tendon or ligament tissues, with a simple surgical technique and minimal patient morbidity and risk of infection or disease transmission as well as rapid return to preinjury functions, by using biodegradable biomaterials scaffolds (2, 16, 20, 101).

Composites, blends and hybrid materials based on natural polymers

Scaffolds have been produced using collagen and sericin-extracted silk to improve scaffold properties for tendon/ligament applications and then seeded with cells (2, 102-106). Chen and co-workers (60, 102) embedded MSCs derived from human embryonic stem cells within a knitted silk-Col sponge scaffold and achieved an enhancement of tendon tissue regeneration. They demonstrated through *in vivo* tests that dynamic mechanical stimulation is beneficial to tissue-engineered tendons, not only in terms of histology but also for the mechanical performance (102). A similar silk-Col scaffold for MCL regeneration, seeded with MSCs had higher mechanical properties than a silk scaffold. The silk scaffold elicited a mild inflammatory reaction and degraded slowly after subcutaneous implantation in a mouse model (60). Similarly, Shen et al. (103), Zheng et al. (104), Ran et al. (105) and Bi et al. (106) used scaffolds produced with Col micro-sponges in a knitted silk sponge matrix and all of them revealed efficient for tendon/ligament regeneration.

Bi et al. (106) evaluated the biomechanical performance of these silk-Col scaffolds and compared their performance with an autograft – Figure 8. Scaffolds were sterilized and implanted *in vivo*, in 20 rabbits, and autologous semitendinosus tendons were used to recover the ACL in the autograft control group. At 4 and 16 weeks after surgery, grafts were retrieved and analyzed. After 4 weeks of surgery, the failure load in the scaffold group was significantly higher than that in the autograft group (autograft, 17.33±3.43 vs. scaffold, 25.63±4.17 N; P<0.05, n = 5). After 16 weeks, there was no significant difference in the failure load between the two groups (autograft,27.64±5.56 vs. scaffold, 31.85±4.74 N, P>0.05, n = 5; Figure 8A). Regarding the stiffness, at 4 weeks postoperatively, there was no significant

difference between the two groups (autograft, 3.72±1.19 N/mm vs. scaffold, 5.78±2.04 N/mm; P>0.05, n = 5). However, at week 16, the stiffness in scaffold group was significantly greater than that of the autograft group (autograft, 3.63±1.01 N/mm vs. scaffold, 7.09±1.25 N/mm; P<0.05, n = 5; Figure 8B). Thus, the scaffold provided enough mechanical strength to resist the daily activities of the experimental rabbits (106).
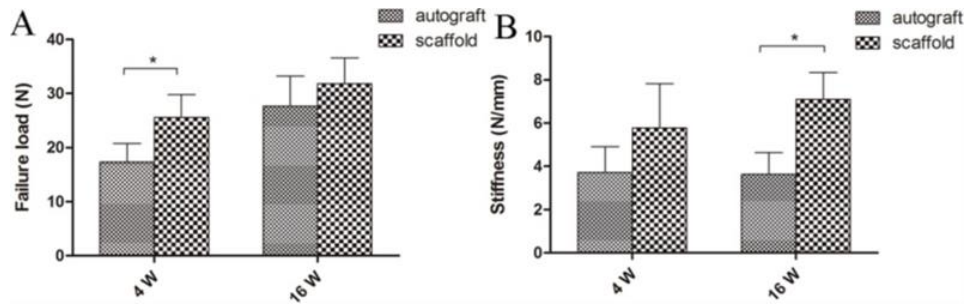
Figure 8 – Statistical evaluation of differences in failure load (**A**) and stiffness (**B**) between the autograft group and scaffold group at 4 and 16 weeks postoperatively. * Significant difference between groups (106).

ALG is an anionic polysaccharide. Its combination with CHI was reported by Majima et al. (67) and improves its biocompatibility and cell adhesive potential as well as decreases its degradation rate. This *in vitro* study using rabbit patellar tendon fibroblasts showed that ALG-0.1% CHI polyionic complex fibers had significantly higher cell attachment compared to ALG-only and polyglactin controls (67, 91).

In another study of Majima et al. (66), a biocompatible braided scaffold was produced from melt spun fibers of CHI and 0.1%HA. The scaffold presents adequate biodegradability and biocompatibility, with intense collagen type I production. The reduction in the strength of the composite fibers, due to water absorption, was measured after incubation for 0 h, 2 h, and 28 days in the standard culture medium. The tensile strength decreased after 2h of incubation and then remained constant until 28 days-Table 5. *In vivo* animal experiments with fibroblasts of Achilles tendon of a rabbit seeded on the CHI–0.1% HA hybrid-polymer fiber scaffold, showed that the mechanical properties of the scaffold had the possibility to stabilize the joint (66).

A natural composite scaffold that combines silk, Col and HA was produced by Seo et al. (107) for ligament regeneration. In that study, a silk scaffold was knitted by hand and dry coated with collagen-HA followed by freeze drying. The initial attachment and proliferation of human ACL cells on the composite silk scaffold was higher than the observed on the silk scaffold. The Col-HA substrate on the silk scaffold enhances new blood vessel and cell migration *in vivo* (107).

Table 5 – Tensile strength of CHI-0.1% HA fiber after 0h, 2h and 28 days in the standard medium (Dulbecco's modified Eagle's medium). Adapted from (66).

Incubation Time	Tensile strength (MPa)
0 h	213.3 ± 10.0
2 h	60.0 ± 6.7
28 days	65.1 ± 6.6

n=45 in each samle (mean±standard deviation)

Composites, blends and hybrid materials based on natural and synthetic polymers

Natural materials have the advantage of being biocompatible, recognizable by cells, favoring the cell adhesion and proliferation. However, their quick degradability and low- mechanical properties may limit their application in tissue engineering, while synthetic polymers present low bioactivity and higher mechanical properties (43). Thus, the combination both types of materials is expected to yield a synergetic effect between natural and synthetic polymers (43), and has been proposed as a good compromise between biological and mechanical performance for tendon and ligament regeneration (87, 108).

A hybrid scaffold comprised of degummed knitted silk microfibers coated with bioactive bFGF-releasing electrospun PLGA fibers was produced by Sahoo et al. (109) and its feasibility for use in ligament/tendon was evaluated *in vitro*. Rabbit BMSCs grew on PLGA fibers and silk microfibers and exhibited good viability. The release of bFGF stimulated cell proliferation and the gene expression of ligament/tendon-specific ECM proteins increased the collagen production and hence, the mechanical properties of the scaffold (109).

Three types of electrospun scaffolds of PLCL and silk fibroin, random nanofibrous scaffold, aligned nanofibrous scaffold and aligned nanoyarns (NRS), were studied by Yang and co-workers (110). The Young's modulus value of the NRS was lower than that of the aligned nanofibrous scaffold but was approximately two times higher than the one of the random nanofibrous scaffold. However, random and aligned nanofibrous scaffolds presented limitations in terms of cell infiltration due to the dense fiber packing. NRS configuration provided larger pores and enough space for cell infiltration which yielded improved cell proliferation for up to 28 days of culture as it can be observed in Figure 9. NRS are used to achieve a balance between the porosity and mechanical properties of electrospun scaffolds (110).
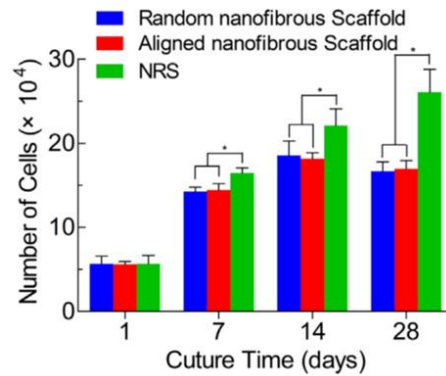
Figure 9 – Commercially available Cell Counting Kit-8 (CCK-8) result of MSCs cultured on the random nanofibrous scaffolds, aligned nanofibrous and NRSs for up to 28 days. The data are expressed as the mean ±SD. The samples marked with (*) has a significant difference between the two groups($p<0.05$). Reprinted with permission from (110).

Col has been widely combined with various polymers, often as a coating to stimulate tendon/ligament regeneration (84, 85, 91, 111). Similarly to the previously reported work of Yang et al.(110), Xu et al. (111) studied three morphologies (random nanofiber, aligned nanofibers and aligned nanoyarn) of electrospun scaffolds composed by PLCL and in this case, collagen type I, for tendon tissue engineering. Nanoyarn scaffolds displayed desirable properties for tendon tissue engineering. Besides, tendon cells exhibited enhanced proliferation and expression of tendon-ECM genes on the nanoyarn scaffold, compared to random and aligned nanofiber scaffold (111).

Leong and co-workers (84) evaluated electrospun PCL grafts coated with Col, with and without the addition of bFGF and hFF, using an athymic rat model of ACL reconstruction. The histological and mechanical evaluation of PCL scaffolds demonstrated excellent healing and regenerative potential. After 16 weeks of implantation, Col + bFGF grafts presented the highest stiffness, achieving 58.8% of the stiffness and 40.7% of the peak load of healthy native ACL. The implantation of cells on the scaffolds does not appear to be beneficial for ligament regeneration while the implantation of bFGF had a beneficial effect on the graft cellularity and mechanical properties (84).

Similarly, Petrigliano et al. (88) used bFGF to treat PCL scaffolds (pre-coated with Col). Scaffolds were then seeded with BMSCs. Scaffolds treated with the growth factor and subjected to mechanical stimulation demonstrated cellular adherence and spreading at 21 days.

Electrospun bundles containing PLLA and collagen type I in different percentages, PLLA/Col-75/25 and PLLA/Col-50/50, were tested by Sensini et al. (108) to evaluate its potential for human Achille tendon regeneration. Human tenocytes were cultured over the same time range on the bundles and cell morphology was assessed. The mechanical properties (stiffness and strength) achieved are comparable

to those of natural tendon. The PLLA/Col-75/25 blend was the most promising blend, with a Young modulus of 98.6 ± 12.4 MPa (as-spun), similar to that of native ligament and 205.1 ± 73.0 MPa, after 14 days in PBS. A good cell attachment and viability after 14 days of culture was observed. However, cells exhibited a better adhesion on PLLA/Coll-50/50 bundles and a more elongated morphology in comparison to PLLA/Coll-75/25 one (108).

A co-electrospun scaffold with 3 regions containing PCL-Col, a mixture of PLLA/Col and PCL/Col fibers and PLLA-Col was studied by Ladd et al. (112) for tendon-muscle junction tissue engineering. The scaffolds exhibited a randomly oriented nanofiber architecture in every region. The PLLA side had smaller fiber sizes on average, while the PCL side had larger fibers, and the center region, was a mixture of PLLA/Col and PCL/Col fibers with a fiber size in between. The scaffold was cytocompatible and accommodated cell attachment and myotube formation. Figure 10 shows the mechanical properties of this scaffold (112).
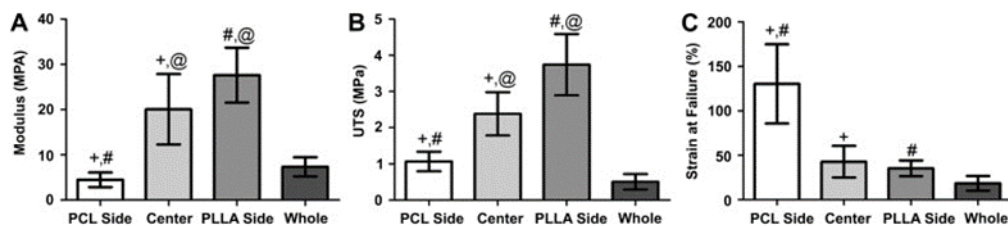
Figure 10 – Average parameters obtained from tensile testing to failure of each region (n = 9) and the whole scaffold (n = 10). (**A**) Young's modulus. (**B**) Ultimate tensile strength. (**C**) Strain at failure. +, #, @ indicate statistical significance with $p < 0.05$ (112).

Sahoo et al. (85) reported the use of coating over PLLA and PLGA scaffolds, with PCL, PLGA nanofibers or collagen type I. They verified that collagen type I coating over both the PLGA or PLLA scaffolds offers a very favorable surface for MSCs attachment and proliferation. PLLA scaffolds exhibited reduced cell proliferation due to its hydrophobic character (85).

In order to study the ability to use nanomaterials to effectively reinforce collagen, Green *et al.* (113) produced gel-spun collagen type I and carbon nanofibers composite scaffolds, with 0.5% and 5% of filling load, for tendon tissue engineering. Fibers were subjected to fiber elongation and were crosslinked with glutaraldehyde. Wet-state tensile testing indicates that the structure and mechanical behavior are comparable to the native materials.

Other natural polymers such as CHI, ALG and HA have been combined with synthetic polymers (86). For instance, Leung et al. (86) investigated aligned CHI–PCL nanofibers with TGF-b3 growth factor for tendon regeneration and they concluded that it led to a rapid and effective BMSCs differentiation into

tenogenic progenitors (86). Domingues et al. (87) reported the use of cellulose nanocrystals as reinforcing agents in aligned electrospun scaffolds containing PCL and CHI. The nanocomposite fibrous scaffolds fulfill the mechanical requirements for tendon TE applications and the aligned morphology promoted a remarkable uniaxial cell orientation and induced elongated cell morphology (87). A PLCL (lactic acid/ε-caprolactone proportion of 85/15) multilayered braided scaffold was produced by Liu et al. (74) A layer-by-layer coating was introduced by immersing the scaffolds into poly-L-lysine solution (polycation) and subsequently into HA solution (polyanion) to promote MSCs growth, differentiation, and migration. The braided PLCL scaffold with one-layer of poly-L-lysine and HA modification shows biocompatibility and satisfying mechanical properties that may constitute a promising scaffold for ligament tissue engineering (74).

Composites, blends and hybrid materials based on synthetic polymers

The combination of different synthetic polymers has also been a strategic design for achieving hybrid scaffolds for ligament/tendon regeneration. For instance, although PLGA exhibits good cell affinity, it also presents a rapid degradation which limits its application in tissue engineering. For that reason, PLGA may be combined with another material with slower degradation rate, such as PLLA to ensure the scaffolds' integrity and adequate mechanical properties for a longer time. A PLLA-PLGA knitted scaffold was studied for ligament tissue engineering by Ge and co-workers (41). To understand the degradability of the biomaterial, *in vitro* degradation tests were performed, by immersing the knitted scaffolds in cell-culture medium for 20 weeks. As can be seen in Figure 11, there was obvious mass loss at initial 4 week. This is possibility attributed to relatively quick degradation of PLGA, which may be important to promote potential tissue in-growth, at the initial stage of implantation.

Figure 11 – Mass loss of knitted structure during 20 weeks (41).

Comparing to PLLA yarns, PLGA yarns degraded more quickly and were not visible at 8 weeks. PLLA yarns kept their integrity for at least 20 weeks (41). They found that this scaffold can fulfill most of

the requirements in terms of porosity, degradation rate and mechanical properties (41). When seeded onto these scaffolds, MSCs proliferated and increased the synthesis of collagen type I and type III (114).

Pinto et al. (115) reported the production of nanocomposite thin films containing PLA/COOH functionalized carbon nanotubes (CNTs-COOH) and PLA–graphene/graphite nanoplatelets (GNPs). *In vitro* tests were performed by seeding human dermal fibroblasts (HDF) onto PLA, PLA/GNPs and PLA/CNT-COOH films and all formulations exhibited no cytotoxic responses and supported cell proliferation up to 3 days in culture. After 72 hours of *in vitro* culture, HDF exhibited higher proliferation on the nanocomposite materials with PLA/CNTs 0.3% and PLA/CNTs 0.5%, when compared to PLA. Besides, increasing percentages of CNTs-COOH within PLA matrix did not affect cultured fibroblasts – Figure 12. *In vivo* tests performed by subcutaneous implantation of nanocomposites in mice showed no severe inflammatory response, as observed 1 and 2 weeks after implantation, which supports that the use of carbon-based nanofillers in PLA-based structures has potential for ACL reinforcement (115).
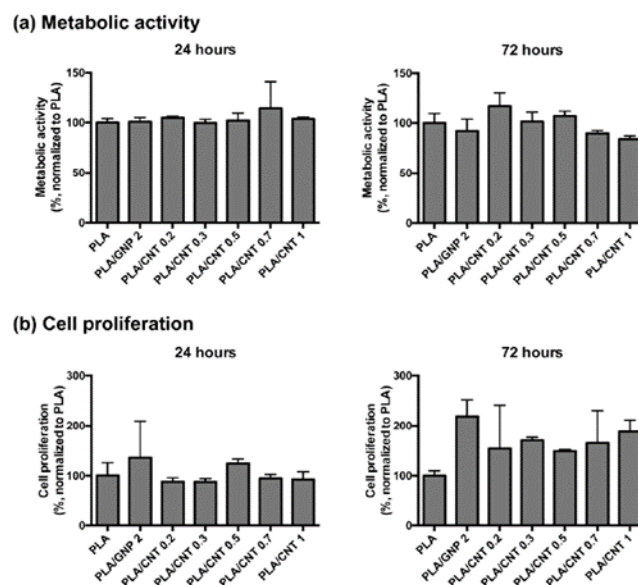
Figure 12 – Viability (**a**) and proliferation (**b**) of fibroblasts seeded in different composites after 24 and 72 hours in culture. Results are normalized with respect to the values for cells cultured in PLA control. Reprinted with permission from (115).

In a previous study Pinto et al. (116) reported that the carbon nanostructures improved the mechanical properties of the PLA composites, approaching the range of natural tendons and ligaments: tensile strength in the range of 5–100 MPa and Young's modulus from 20 MPa to 1200 MPa (117). The composite with 0.7 wt.% CNTs-COOH presented enhanced tensile strength relative to PLA (from 59.90 ± 4.93 MPa to 72.22 ± 1.52 MPa), as well as elongation at break (from 1.86 ± 0.06 % to 2.25 ± 0.40 %).(116) Besides, the composites with 0.7 wt.% CNTs-COOH and 2 wt.% GNPs showed a considerable

increase (>20%) in the Young's modulus relative to PLA, from 3.99 ± 0.42 GPa to 4.86 ± 0.47 GPa and 4.92 ± 0.15 GPa, for PLA-CNTs-COOH and PLA-GNPs, respectively. The composite scaffolds were cytocompatible, supporting fibroblasts metabolic activity and proliferation up to 72hours (116).

Liu et al. (118) produced a 3D biodegradable PLA screw-like scaffold coated with hydroxyapatite for ACL regeneration. The scaffold presented adequate size porosity and the pores were interconnected in regular patterns with orthogonal structure. MSCs were seeded on PLA scaffold, PLA-hydroxyapatite scaffold, and suspended in Pluronic F-127 hydrogel on PLA-hydroxyapatite scaffold. The last group showed the highest *in vitro* cell proliferation and osteogenesis. For the histological examination, PLA, PLA-hydroxyapatite, and PLA-hydroxyapatite loaded MSCs screw-like scaffolds were implanted into the femoral tunnel of rabbits. The histological results revealed that PLA-hydroxyapatite scaffolds with MSCs seeded presented increased new bone formation at the interface between the bone tunnel and graft after 12 weeks. Hydroxyapatite surface modification not only enhanced new bone ingrowth but also the proliferation and migration of MSCs and osteoblasts with excellent vascularization (118).

Sahoo et al. (85) reported that coating PLLA or PLGA scaffolds with collagen type I also offers a very favorable surface for MSCs attachment and proliferation. However, they verified that compared to Col, a PCL coating on PLLA or PLGA scaffolds resulted in a reduced cell attachment and higher mechanical strength (85).

A composite tendon scaffold composed of an inner part of PGA unwoven fibers and an outer part of knitted PGA/PLA fibers, to provide mechanical strength, was produced by Deng et al. (119) – Figure 13.
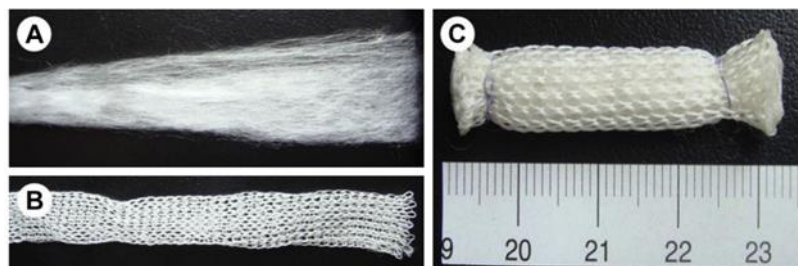
Figure 13 – Preparation of a composite tendon scaffold. The scaffold was composed of an inner part of PGA unwoven fibers (**A**) and an outer part of a net knitted with PGA/PLA fibers in a ratio of 4:2 (**B**). The outcome of assembled two parts (**C**). Reprinted with permission from (119).

AMSCs were seeded onto these scaffolds (119). Cytocompatibility between cells and PGA fibers was found since short-term *in vitro* culture enabled AMSCs proliferation and the production of extracellular matrix on the PGA fibers. The scaffolds exhibited a tensile strength around 50 MPa (119). The *in vitro*

cultured scaffolds were then subjected to an *in vivo* transplantation on rabbits. Cell-seeded scaffold was integrated within the native tissue and with the increase of implantation time, cells gradually form neo-tendon. The diameter of collagen fibrils significantly increased which is related to the role of seeded AMSCs in the formation of engineered tendon *in vivo* – Figure 14. After 45 weeks of implantation, there was no obvious remaining scaffold-base material and the formed tendon exhibited a cord-like shape with a smooth surface, comparable to the normal tendon (119).
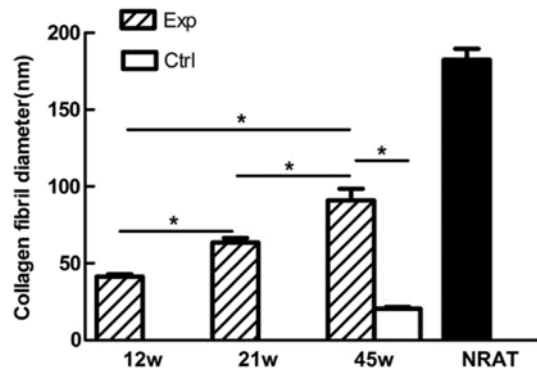
Figure 14 – Quantification of collagen fibril diameter of *in vivo* engineered tendons with native tendon as a control. Collagen fibril diameter of *in vivo* engineered tendons increased with time. There was significant difference between 12 and 21 weeks, between 21 and 45 weeks and between 12 and 45 weeks of the AMSCs seeded group (*, $p < 0.001$). There was significant difference between two groups at 45 weeks post implantation (*, $p < 0.001$). Abbreviation: Exp: experimental group; Ctrl: control group; w: week; NRAT: normal rabbit tendon. Reprinted with permission from (119).

A summary of the studies that have used composites, blends and hybrid materials based on natural or synthetic polymers for tendon/ligament TE are presented in Tables 6 and 7, respectively. A review about composites, blends and hybrid materials based on the combination of natural and synthetic polymers for tendon/ligament TE is presented in Table 8. These tables include, for each combination of materials, the proposed scaffold and the reported mechanical and *in vitro/ in vivo* properties.

2.1.3 Processing techniques of ligament/tendon scaffolds

The architecture of the scaffold is an important design concern since it can modulate the mechanical and biological response and hence, determine the long-term clinical success of the scaffold (10). Literature has reported several methods to produce tendon/ligament scaffolds including gas foaming, phase separation, emulsion freeze-drying and porogen leaching (11). However, their ability to precisely control the pore size and interconnectivity as well as scaffolds' structure and mechanical properties is often limited (120).

Table 6 – Performance of composites, blends and hybrid materials based on natural polymers for ligament/tendon TE

Material	Scaffold	Tissue	*In vivo/ in vitro*	Mechanical Response				Biological Response	Ref
				Young's Modulus(MPa)	Stiffness (N/mm)	Max. Strength(MPa)	Max. Load(N)		
Silk-Col	Col -sponge incorporated into a freeze-dried knitted silk mesh i) addition of rhSDF[a]-1 alpha; ii) no rhSDF-1 alpha	Ligament	*In vivo*, rabbit model	ND	7.02±1.25 (at 16 weeks after surgery)	ND		Fibroblasts distribution throughout the scaffold, at 4 weeks post-implantation; At 16 weeks postoperatively, host cells had invaded the core of the scaffold	(106)
				49.49±10.14 (at 16 weeks post surgery)	ND		~25±12	At 2 weeks post-reconstruction, spindle tendon-like cells and vascularization; At 12 weeks, ligament-ECM deposition	(105)
		Ligament/ Tendon	*In vitro* (BMSCs); *In vivo*, rabbit model	ND	24.3±2.9	ND	47.0±7.4	At 15-360 days after implantation, tissue ingrowth by fibroblasts between the fibers; At 4 weeks, denser ECM, larger number of cells, spindle-shaped morphology; Rarely vascularity; no evident inflammation	(60)
			In vitro (MSCs) *In vivo,* mouse model i) Dynamic mechanical stress; ii) No mechanical stress	24.44 ± 10.03 (unseeded)		ND		*In vitro:* MSCs adhesion and proliferation i)After 14 days, cells elongation, aligned along the direction of mechanical stress; *In vivo:* i) Aligned cells and larger collagen fibers comparing to ii)After 4 weeks post-surgery, tendon-related ECM, indicating tenocyte-lineage	(102)

41

Material	Scaffold	Tissue	*In vivo/ in vitro*	Mechanical Response				Biological Response	Ref
				Young's Modulus(MPa)	Stiffness (N/mm)	Max. Strength(MPa)	Max. Load(N)		
		Tendon	*In vitro* (BMSCs, HDF), Achilles tendon fibroblasts (ATFs); *In vivo*, rat model	i) 45.3±10.4 ii)32.6± 3.9		ND	i)68.5± 18.0 ii)65.7± 10.3	i),ii) At 4 days post-surgery neo-tendons appeared with cord-like shape; i) Migratory BMSCs/ HDF; Vascularization; At 1 week post-surgery more fibroblasts and ECM; At 4 weeks, organized bundles of collagen fibers	(103)
CHI-HA	Braid with wetspun fibers	Ligament/ Tendon	*In vitro* (fibroblast rabbit PT) i)static; ii)stretch; iii) rotation; iv)stretch+ rotation			ND		Cell adhesion and proliferation; iv)Higher cell proliferation after 21 days of culture and ECM production after 14 days of culture, comparing to i-iii); iii)Higher cell proliferation than i) and ii)	(121)
Silk coated with Col-HA	i) Knitted silk; ii)Freeze-dried silk coated with Col-HA	Ligament	*In vitro* (Human ACL fibroblasts); *In vivo*, dog model			ND		*In vitro:* ii) Higher cell attachment, proliferation and ECM synthesis than i); *In vivo:* i),ii) Synovitis;ii) Induced angiogenesis, new collagen formation and higher vascularity than i)	(107)

[a]rhSDF-1 alpha(exogenous recombinant human SDF): cytokine that regulates stem cell homing

Table 7– Performance of composites, blends and hybrid materials based on synthetic polymers for ligament/tendon TE. ([a] Polyethylene glycol diacrylate (PEGDA))

Material	Scaffold	Tissue	*In vivo / in vitro*	Mechanical Performance			Biological Performance	Ref
				Young's Modulus(MPa)	Max. Strength(MPa)	Max. Load (N)		
PGA-PLA	Two ends cord: Inner part: PGA unwoven fibers Outer part: knitted PGA and PLA fibers	Tendon	*In vitro* (AMSCs); *In vivo*, rabbit model	ND	53.71 ± 22.32	ND	AMSCs adhesion and proliferation, At 12 weeks post-repair, middle part with organized Col pattern and host inflammatory cells; At 45 weeks, mature elongated tendons, aligned Col fibers; Scaffold completely degraded	(119)
PLA-GNPs; PLA-(CNT-COOH)	Melt-blended films of: i)PLA/CNT-COOH; ii) PLA/GNPs	Ligament/ Tendon	*In vitro* (HDF), *In vivo*, mice model	i) 4860± 470; ii) 4920 ±150	i) 72.22±1.52 ii) 58.56±3.99	ND	*In vitro:* Cell adhesion, proliferation; i) Higher proliferation compared to ii) *In vivo:* Localized inflammatory response; Livers with no toxicity for i),ii)	(115, 116)
PLLA-PLGA	i)PLLA yarns; ii)PLGA yarns; iii) Two ends Knitted (PLLA-PLGA)		ND	iii)~287	iii)~60	iii)72	ND	(41)
	Two ends Knitted (PLLA-PLGA): i) no cells, no fascia lata wrap; ii)MSCs seeded; iii) MSCs seeded+fascia wrap iv) fascia lata wrap	Ligament	*In vivo*, rabbit model	ND	ND	i) 14.0±7.8 ii) 14.9± 6.6 iii) 20.9± 4.5 iv) 15.8± 6.8 (at 20 weeks post-surgery)	i-iv) Cellular spread and elongation; few macrophages; ECM synthesis i),ii) Non parallel fibroblasts; iii),iv)Higher Col type I and type III	(114)

Material	Scaffold	Tissue	*In vivo / in vitro*	Mechanical Performance			Biological Performance	Ref
				Young's Modulus(MPa)	Max. Strength(MPa)	Max. Load (N)		
PLLA-PEGDA[a]	i) Braid-twist fibrous PLLA and crosslinked PEGDA [a] hydrogel ii) Braid twist (no hydrogel)		*In vitro* (primary rabbit PT fibroblasts)	i)437±38 ii) ND	i)36±3 ii) ND	ND	i) Higher cell proliferation than ii), at day 14 of culture; i),ii) Comparable cell proliferation, at day 21 and 28 of culture	(122)
PLA-Hydroxyapatite	3D printed PLA scaffold: i) No coating; ii) Coated with hydroxyapatite; iii) Coated with hydroxyapatite + MSCs suspended in hydrogel	Ligament	*In vitro* (rabbit MSCs); *In vivo*, rabbit model		ND		*In vitro*: iii) Higher cell proliferation and osteogenic markers, compared to i),ii); *In vivo*: iii) After 4 weeks post-surgery, more chondrocytes and cartilage matrix in the interface with the bone; Higher Col fibers, after 12 weeks	(118)

44

Table 8 – Performance of composites, blends and hybrid materials based on natural and synthetic polymers for ligament/tendon TE. ([a] Polydioxanone(PD); [b] Single walled nanotubes (SWNTs); [c] poly(3-hydroxybutyrate) (P3HB); [d] Wharton's jelly mesenchymal stem cells (WJ-MSCs); *16 weeks post-surgery).

Material	Scaffold	Tissue	*In vivo/ in vitro*	Mechanical Performance				Biological Performance	Ref
				Young's Modulus (MPa)	Stiffness (N/mm)	Max. Strength (MPa)	Max. Load (N)		
CHI-PCL-cellulose	Electrospun CHI-PCL nanofibers + cellulose nanocrystals: i)Aligned nanofibers; ii)Random nanofibers	Tendon	*In vitro* (human tenocytes)	i) 540.5± 83.7; ii) ND	ND	i) 39.3 ±1.9; ii) ND	ND	Cellular adhesion/ spread; i) Cells elongated/ aligned along the nanofibers; ii)Cells with random shape and orientation; Synthesis of tendon-specific markers	(87)
Silk-PLCL	Electrospun i) Aligned nanoyarn- reinforced random fibers (NRS); ii) Random nanofibers; iii) Aligned nanofibers		*In vitro* (primary rat BMSCs)	i) 288.95 ± 13.26; ii) 186.65 ± 8.87; iii) 433.56 ± 48.06	ND	i) 24.25 ± 0.76; ii) 9.70 ± 0.51; iii) 39.10 ± 2.89	ND	BMSCs adhesion/spread; i) Higher cell spread than ii),iii); Cells elongation/ random distribution; ii) Cells with random distribution, pyramidal shape; iii) Cellular elongation	(110)
Col-PLCL	Electrospun i) Nanoyarn; ii) Random nanofibers; iii) Aligned nanofibers		*In vitro* (primary rabbit tendon cells)	i) ~2.1; ii)~3.9; iii) ~4.5	ND	i) ~3.3; ii)~5.6; iii)~6.2	ND	Cell adhesion, spread; i) Higher cell growth; i),ii) Elongation along the nanofibers/nanoyarn; iii) Cells with random spread; i) Higher tendon-ECM genes, compared to ii),iii), after 14 days	(111)

Material	Scaffold	Tissue	*In vivo/ in vitro*	Mechanical Performance				Biological Performance	Ref
				Young's Modulus (MPa)	Stiffness (N/mm)	Max. Strength (MPa)	Max. Load (N)		
Col-PD[a]	Electrospun i) Col nanofibers; ii) Col microfibers coated with PD		*In vivo*, rabbit model	i) 0.549; ii) 0.754 (60 days post surgery)	i) 20.37; ii) 29.87 (60 days post surgery)	i) 10.44; ii) 11.37 (60 days post surgery)	i) 52.72; ii) 74.02 (60 days post surgery)	i),ii) Some inflammatory response, after surgery; ii) Cells with better alignment and higher mature tenoblasts and macrophages, compared to i), 60 days post-surgery; Scaffold partially degraded	(123)
Col-Carbon nanofibers	Elongated Gel-spun fibers: i) Col/ 0.5carbon nanochips crosslinked with glutaraldehyde; ii) Col/ 0.5carbon nanochips; iii) Col/ 0.5SWNTs [b], crosslinked with glutaraldehyde; iv) Col/ 0.5SWNTs	Tendon	ND	i) 590±50; ii) 46±4; iii) 840±40; iv) 92±35 (wet-state)	ND	i) 75±15; ii) 5±2; iii) 70±8; iv) 9±1 (wet-state)	ND	ND	(113)
(PLLA-Col)-(PCL-Col)	Co-electrospun onto opposite ends: PLLA-Col; PCL-Col (3 regions)		*In vitro* (myoblasts and fibroblasts)	7.34±2.13	ND	0.51±0.21	ND	Myoblasts and fibroblasts adhesion and proliferation onto the 3 regions; Myoblasts differentiation into myotubes	(112)
	Random electrospun PLGA nanofibers			ND	4.8±0.52	ND		Cellular adhesion, proliferation; Production of ECM between the nanofibers	(124)

Material	Scaffold		Tissue	In vivo/ in vitro	Mechanical Performance				Biological Performance	Ref
					Young's Modulus (MPa)	Stiffness (N/mm)	Max. Strength (MPa)	Max. Load (N)		
Silk coated with PLGA	Knitted silk microfibers coated with	i) bFGF-releasing electrospun PLGA nanofibers; ii)Electrospun PLGA nanofibers	Ligament/ Tendon	*In vitro* (rabbit BMSCs)	ND	i)4.3±0.3; ii)ND	ND	ND	Cell adhesion/spread; i)Higher cell proliferation, viability; Higher Col production, ligament/tendon-specific ECM, from day 7 to 14, comparing to ii)	(109)
Silk coated with PCL or P3HB[c]	Twisted nanofiber-coated silk yarn Nanofiber coating: i) PCL; ii)P3HB; iii) No coating			*In vitro* (L929 murine fibroblasts)		ND		i)110.5±6.6; ii)97.6±11.4; iii)92.6 ±8.2	Cell adhesion/spread; Cell viability decreased from the 1st to 3rd day of culture; i),ii) Higher cell viability than iii), after 3 days of culture	(125)
PCL coated with Col	Electrospun PCL scaffold coated with: i) Col; ii) Col+bFGF iii) Col+hFF; iv) Col+bFGF+hFF		Ligament	*In vivo*, rat model	ND	* i) 12.4±3.8; ii) 23.3±8.1; iii) 4.4±1.2; iv) 10.1±2.1	ND	* i) 16.0± 3.4; ii) 23.1± 6.1; iii)17±6.9; iv) 15.1± 4.9	Cell proliferation and alignment along the fibers; Col deposition; ii) Higher cell proliferation than i), (*) iii), iv) No beneficial effect of hFF for regeneration	(84)
PLCL (85/15)-poly-L-lysine-HA	Multilayer braid: i)PLCL; ii) PLCL+Poly-L-lysine; iii)PLCL+ poly-L-lysine+HA			*In vitro* (human BMSCs and WJ-MSCs[d])	i) 1616±643; ii) 1608±156; iii)1758± 470		ND		Cell adhesion, proliferation, elongation and alignment; ECM synthesis on day 14; Metabolic activities decreased from i) to ii) and iii); iii) Higher MSCs migration	(74)

47

Material	Scaffold	Tissue	*In vivo/ in vitro*	Mechanical Performance				Biological Performance	Ref
				Young's Modulus (MPa)	Stiffness (N/mm)	Max. Strength (MPa)	Max. Load (N)		
		Ligament							
PLLA-gelatin-Col	Gelatin-bFGF hydrogel sandwiched by Fn-coated PLLA braided scaffold, and wrapped with a Col membrane, reinforced with PLLA microspheres		*In vivo*, rabbit model	ND	~30	ND		At 8 weeks post-surgery, great cell spread/migration; Vascularization induced by bFGF; Great Col and ECM synthesis	(44)

Since both tendons and ligaments are fibrous tissues, the production of fiber-based scaffolds has been the preferred option for tendon/ligament TE and has proven to promote cellular proliferation and collagenous matrix deposition (10, 18). The main factor is the way that fibers are organized. Parallel align of fibers/yarns is the simplest way to organize fibers (18) and has been widely reported for tendon TE approaches (17, 22, 87, 110, 111). These fibers are commonly achieved through electrospinning (87, 110, 111) or electrochemical alignment (68, 126). Figure 15 illustrates scanning electron micrographs of (A) random and (B) aligned nanofiber scaffolds proposed by Domingues et al. (87) for tendon regeneration. However, the lack of interaction between the fibers usually restrict its application (17). Attending to the complexity of the ligament/tendon, the most common approach adopted by researchers relies on complex structures produced by textile techniques (120), in which fibers are engineered into braided, knitted, twisted or woven structures to obtain hierarchical scaffolds (17, 18, 22).
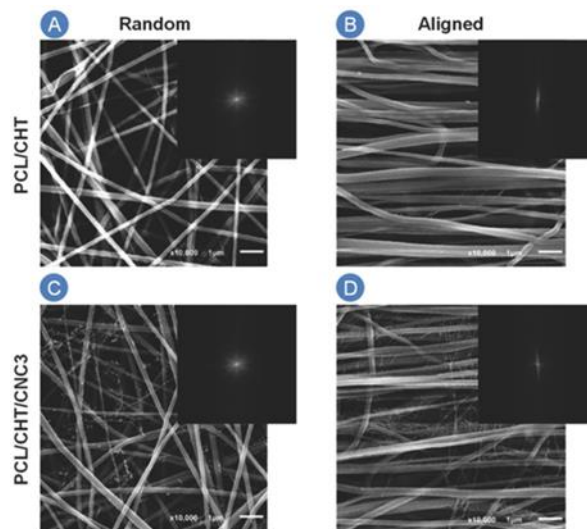
Figure 15 – SEM images of random nanofiber meshes and aligned nanofiber bundles of (**A, B**) PCL/CHI and (**C, D**) PCL/CHI/ cellulose nanocrystals (3wt.%) with the respective 2D-fast Fourier transform frequency plots. Scale bar 1 μm (87).

Electrospinning allows the production of long continuous fibers with controlled diameter ranging from nanometers to microns, mimicking the nanoscale structure of tendon and ligament ECM (18). It allows the production of fibers from several natural and synthetic polymers including Col, CHI, HA, silk fibroin (18) or PCL (99), PLGA (76), PLA (98), as well as combinations of natural and synthetic fibers (84, 87). However, the weak mechanical properties of the electrospun scaffolds produced for tendon/ligament TE limit the successful translation to the clinic (12). Additionally, electrospinning typically produces 2D fiber mats, limiting the production of 3D hierarchical structures. For that reason, electrospun nanofibers have been twisted or rolled using standard textile techniques such as e.g. weaving or braiding, to produce

3D hierarchical structures with proper mechanical properties (12). Yarns made of aligned fibers can be formed by electrospinning and then intertwined to form braided(96) or knitted scaffolds as can be observed in Figure 16 (109).

Figure 16 – BMSCs-seeded (7 days of culture) scaffold produced by electrospinning bFGF-PLGA fibers onto the surface of knitted microfibrous silk scaffolds (109).

Textile technologies allow the production of complex 3D constructs from monofilaments and multifilament threads, for various TE applications, being extensively applied in tendon/ligament regeneration (120). These scaffolds are produced by several textile methods such as braiding, twisting, wire-rope, weaving and knitting (58) that enable tailoring the scaffolds' architecture by controlling the fiber size/orientation, pore size and interconnectivity, surface topography, mechanical properties and the cellular distribution that scaffold provides (120).

Twisted scaffolds are formed with multilevel yarns that combine multiple ends at a single point and twisting the structure together (58). Twisted structures ensure interaction between fibers, unlike parallel aligned fibers, and are morphologically closer to native ligament, as depicted in Figure 17(B) (17).

Knitting allows the production of complex structures from a yarn that is interlaced in a previous loop to form interconnected loops. Knitted scaffolds present different mechanical and physical properties depending on the type of stitches and the yarn material. While the production of knitted structures with adjustable properties in different directions is difficult, it is possible to produce 3D structures with precise microstructure control by combining knitting machines with computer-aided design (CAD) systems (120). Knitted scaffolds for tendon/ligament tissue engineering (18, 107, 114) have demonstrated good mechanical properties and adequate porosity for tissue ingrowth – Figure 17(C) (76).
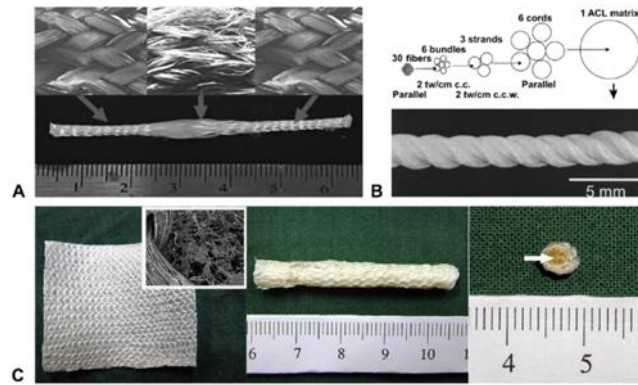
Figure 17 – Scaffolds for ligament tissue engineering. (**A**) Braided scaffold with a fibrous intra-articular zone terminated at each end by a less porous bony attachment zones in a single braid; (**B**) Twisted fibrous scaffold; (**C**) Silk scaffold produced by rolling up the porous knitted silk mesh around a silk cord. Reprinted with permission from (12).

Braiding technique comprises three or more yarns intertwined in overlapping patterns (120). In general, braided scaffolds are dimensionally very stable, having good flexibility, high strength and fatigue resistance (17). These enhanced mechanical properties promoted their extensive application in tendon and ligament scaffolds with biomimetic characteristics (120). The morphology of the braided scaffolds made of PLCL and modified PLCL developed by Liu et al. (74) are illustrated in Figure 18 (A) as well as the global structure of the multilayer braided scaffolds (B). The mechanical and biological properties of these scaffolds were reported above.
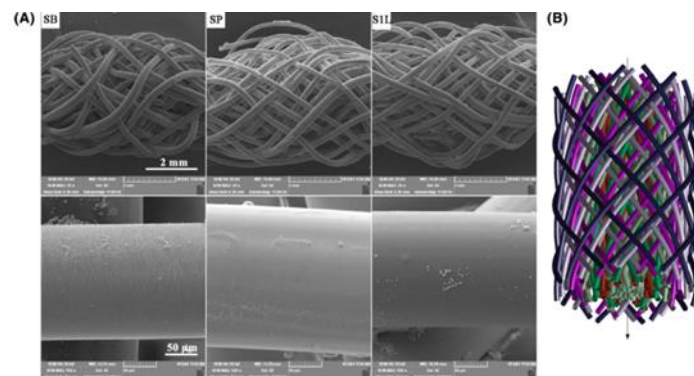
Figure 18 – (**A**) Morphology of PLCL scaffold and PLCL scaffold modified with poly-L-lysine and HA by scanning electron microscopy (SB: scaffold blank; SP: PLCL- poly-L-lysine; S1L: PLCL- poly-L-lysine/HA- PLCL- poly-L-lysine). (**B**) Global structure of the multi-layer braided scaffold. The six different constitutive layers, made of 16 fibers/layer, are represented with different colors. Reprinted with permission from (74).

Braided structures present low porosity which restricts the tissue ingrowth (17), as compared to the highly porous knitted structures that favor tissue ingrowth and the deposition of collagenous connective tissue, which is crucial for tendon/ligament reconstruction (17, 76). The pore size of braided

structures may be controlled by varying the yarn size and braiding angle, which may also develop anisotropic mechanical properties with adjustable gradient along any desired direction (120). Laurencin et al. (8) proposed a braided scaffold for ACL regeneration that comprised three regions: femoral tunnel attachment site (bony attachment end), ligament region (intra-articular zone), and tibial tunnel attachment site (bony attachment end) as illustrated in Figure 17(A). The attachment sites exhibit a high-angle fiber orientation and smaller pore size to improve the quality of anchorage in bone tunnels and provide resistance to wear within it. The intra-articular zone (central region with larger pore size) has a lower-angle fiber orientation. A minimum pore diameter of 150 μm is suggested for bone and 200–250 μm for soft tissue ingrowth (8).

Researchers have reported the production of yarns made of twisted fibers combined by the braiding process (1) in order to withstand it, since the degree of twisting as well as the direction affect the yarn strength, abrasion resistance, and flexibility (10). Table 9 presents the braiding and twisting angles associated to each braided scaffold, braided-twisted scaffold and twisted scaffold (1).

Table 9 – The braiding and twisting angles associated to each braided scaffold, braided-twisted scaffold and twisted scaffold. Reprinted with permission from (1).

Scaffold levels	Twisting angles[a] (degrees)		
Fiber twisted to form fiber bundles	78±3.4	69±4.0	60±4.5
Fiber bundles twisted to form yarns	83±2.1	72±2.3	62±4.5
Yarns twisted to form scaffolds	79±1.4	68±3.8	62±4.5
Scaffold	2 braid	4 braid	6 braid
Braiding angle (degrees)	78±1.8	69±2.7	61±3.4

[a]The twisting angles are arranged into structures (fiber bundles, yarns and scaffolds)

An optical microscopy of a braided-twisted scaffold for ligament regeneration developed by Leroy et al. (127), made of PLA combined with Pluronic or Tetronic (poly(ethylene oxide–propylene oxide co polymers), is illustrated in Figure 19. Both types of scaffolds presented stress at failure compatible with that of ACL. Besides, *in vitro* tests with MSCs revealed cytocompatibility of both scaffolds, suggesting that the twisted-braided shape did not cause any significant loss of cell viability and enhanced cell proliferation (127).

Figure 19 – Optical microscopy picture of the ligament tissue engineering scaffold (127). Reproduced by permission of The Royal Society of Chemistry.

Other common approaches for ligament/tendon regeneration combine fibrous or spongy scaffolds with gels of fibrin, Col or HA, for cell seeding, attempting to improve their biocompatibility, but these exhibited lack of mechanical properties and are unstable in a dynamic situation, such as in the knee joint (10, 76).

Coating of scaffolds with Col, HA or nanofibers, as well as the addition of growth factors, has been reported (84, 85, 107) as favoring cell attachment and proliferation, and ECM deposition (10). The architecture of the scaffold can be modified in terms of pore diameter, porosity, surface area, by varying the fiber composition, diameter, braiding and twisting angles as well as yarn density (10).

Most of conventional methods used to produce TE scaffolds lack the ability to obtain highly repeatable designs with precise, well-defined micro- and nanoscale structures (128). 3D printing enables the production of scaffolds with patient-specific requirements (128) and it has recently been suggested for the production of screw-like scaffolds for tendon/ligament scaffolds (118, 129). This kind of scaffold could fix the tendon/ligament graft, and provide adequate space for bone ingrowth around the graft (118). 3D printing offers control over the architecture of the scaffold, such as porosity, thus controlling physical properties (13). It follows a procedure based on the layer-by-layer deposition of the material, from bottom to top, to build a 3D product directly from a CAD model (14, 130). 3D processes provide increased speed, customization and efficiency, not involving toxic solvents (14, 131, 132). Figure 20 illustrates a 3D printed PLA screw-like scaffold developed by Liu et al. (118) for ligament applications, whose mechanical and biological properties were reported above.

Advances in 3D printing have increased feasibility towards the synthesis of living tissues - bioprinting (133). This technology is based on a precise deposition of biomaterials, either encapsulating cells or loaded with cells later on, and growth factors, in micrometer scale to produce a bioidentical tissue (133, 134). Several research groups have bioprinted materials and cells for musculoskeletal applications

including bone, cartilage, muscle, tendon and ligament tissues. However, there are significant challenges to be resolved in terms of technological progresses (135, 136).
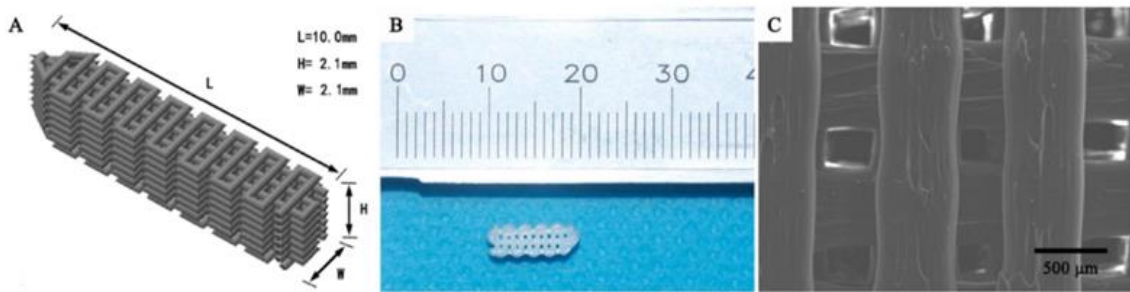
Figure 20 – (**A**) 3D view of the theoretical designed PLA screw-like scaffold structure. (**B**) The prepared PLA screw-like scaffold. (**C**) The SEM image of the PLA scaffold surface with well-defined orthogonal structure. Reprinted with permission from (118).

2.1.4 Conclusions

Tissue engineering is a promising alternative approach to the current surgery procedures for tendon/ligament repair. Its goal is to provide a complete regeneration of the damaged tissue, recovering its native architecture and functionality. A wide variety of biodegradable polymers and composites has been proposed for that purpose. Col and PLLA are the most used materials to produce biodegradable scaffolds. Given the complex structure of native tissues, the production of fiber-based scaffolds has been the preferred option for tendon/ligament scaffolds. Despite the remarkable progress made in this field, the current TE approaches still present limitations in terms of mechanical properties, degradation rate and biological response that are necessary to overcome. In the future, new strategies such as 3D printing may provide a rapid and promising solution for the production of tendon/ligament scaffolds.

2.2 3D printing of graphene-based polymeric nanocomposites for biomedical applications

Additive manufacturing techniques established a new paradigm in the manufacture of composite materials providing a simple solution to build complex, custom designed shapes. In the biomedical field, 3D printing enabled the production of scaffolds with patient-specific requirements, controlling product architecture and microstructure, and have been proposed to regenerate a variety of tissues such as bone, cartilage, or the nervous system. Polymers reinforced with graphene or graphene derivatives have demonstrated potential interest for applications that require electrical and mechanical properties as well as enhanced cell response, presenting increasing interest for applications in the biomedical field. The present review focuses on graphene-based polymer nanocomposites developed for additive manufacturing fabrication, provides an overview of the manufacturing techniques available to reach the different biomedical applications, and summarizes relevant results obtained with 3D printed graphene/polymer scaffolds and biosensors.

2.2.1 Introduction

Graphene, a one-atom thick two-dimensional carbon material, has remarkable mechanical, thermal, electrical, and physicochemical properties. However, practical applications of graphene are still limited. As a nanofiller for polymer-based composites, graphene can significantly improve the properties at low incorporation levels. These composites are potentially suitable for a wide range of applications in electronics, energy storage, thermal engineering, automotive and healthcare (137).

The biomedical device industry is vast and expected to be valued at 409.5 billion dollars by 2023 (138). Graphene-based composites are mostly used for the fabrication of 3D structures such as scaffolds for tissue engineering (139) and also for biosensing (140, 141). Suitable scaffolds have been developed using conventional fabrication methods such as solvent casting, freeze-drying and salt leaching (142-144). However, control over the scaffold geometry is limited (139) and the production of multifunctional, multi-material scaffold structures is challenging (138). The recent advancements in additive manufacturing brought about new and exciting possibilities for the fabrication of complex architectures for biomedical applications (139).

Additive manufacturing (AM), also known as 3D printing or rapid prototyping, denotes a group of techniques where a CAD model is converted into a 3D object, which is successively built layer-by-layer.

This contrasts obviously with the conventional formative (e.g., injection moulding, casting) and subtractive methods (e.g, turning, drilling). AM techniques can fabricate complex structures (eventually not possible to obtain by the other methods) in a relatively short time and with low cost, since they do not require a shaping mold and generate minimal waste. These unique features induced revolutionary applications of AM in healthcare, aerospace, automotive, electronics and civil construction (138, 145, 146). In the medical/biomedical field, AM has been applied in tissue engineering to design personalized scaffolds or artificial tissues and organs for transplants, drug delivery systems, probes and tools to detect specific medical parameters, orthoses, prostheses and implants, anatomical models and medical instruments for diagnostics and surgery (147, 148).

It is estimated that biomedical applications share about 11% of the AM technology market and this percentage is steadily increasing (149). Indeed, AM is suited to manufacture small quantities of customized prototypes or products, which is particularly useful as patient-customized products are frequently required (150). The availability of 3D printed prototypes of a patient unique anatomy can improve surgery planning, implant design, and provide specialized medical procedure training. The ability to 3D print not only biomaterials, but also living cells and/or other biological components (e.g. distinct proteins, growth factors), known as bioprinting, enables the creation of biological constructs that can regenerate or augment lost/damaged tissues and organs (138).

The use of polymer nanocomposites combined with the versatility of AM provide great potential to meet the demands of a wide range of clinical needs (138, 139) by creating personalized implants, organ printing, drug delivery devices as well as regenerative scaffolds. In particular, the incorporation of graphene and its derivatives can improve the dimensional accuracy as well as the mechanical, electrical and biological properties of novel biomedical devices (138).

This review discusses the recent advances of using AM techniques and graphene-based polymer nanocomposites to manufacture biomedical products and devices, with emphasis on scaffolds and biosensors. The main 3D printing techniques used with polymers are first introduced. Then, the main preparation methods of graphene-based polymer nanocomposites are reviewed. Finally, representative examples of 3D printed graphene-based scaffolds and biosensors are discussed.

2.2.2 3D printing techniques for polymers

AM techniques use computer files describing the 3D geometry of the part or prototype to be produced, to successively build a series of horizontal 2D layers in the vertical direction, usually from the bottom to the top. The techniques vary in terms of the material deposition procedure, the physical form of the material (liquid, solid or powder-based) and the nature of the material (e.g., thermoplastics, thermosets, nanocomposites, fiber composites). The length-scale, dimensional accuracy and surface finish of the printed object will also depend on the AM technique utilized. Moreover, some techniques are better suited to industrial production than others (130, 149).

Generally, the printing process involves the following steps (see Figure 21):

a) Definition of the geometry and dimensions of the 3D structure to be manufactured, using CAD software;

b) Conversion of the design into a digital approximation (using triangulations) as a Standard Tessellation Language (STL) file format;

c) Slicing of the 3D model into layers of specified thickness, using dedicated software;

d) Use of G-code commands (often via a user-friendly interface) to define how the printer will work during the printing sequence. For example, the in-fill density will determine the porosity of a part;

e) Transfer of the files to the actual 3D printer;

f) Layer-by-layer manufacturing of the part, eventually followed by post-processing operations (such as removing support material, sintering, or polishing the surface) (151).
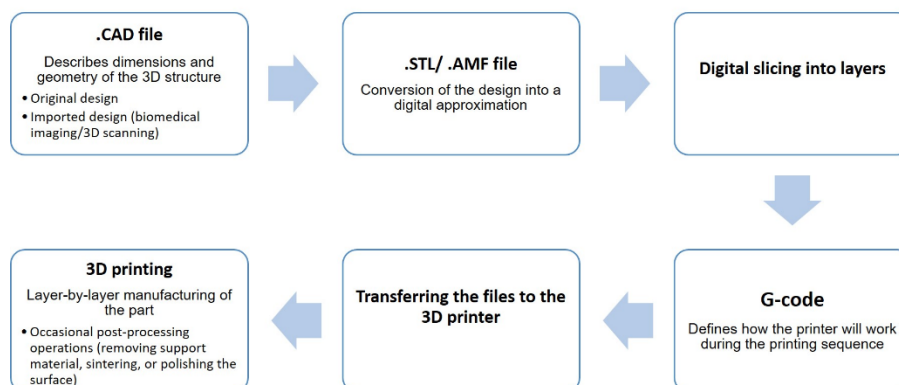
Figure 21 – 3D Printing process. Adapted from (151).

Figure 22 presents three major families of AM techniques used for graphene-based composites. 3D printing of polymer/graphene composite parts has been mainly carried out using extrusion-based and powder-based techniques such as fused deposition modeling (FDM), direct ink writing (DIW) and selective laser sintering (SLS), as well as stereolithography (SLA) (152).
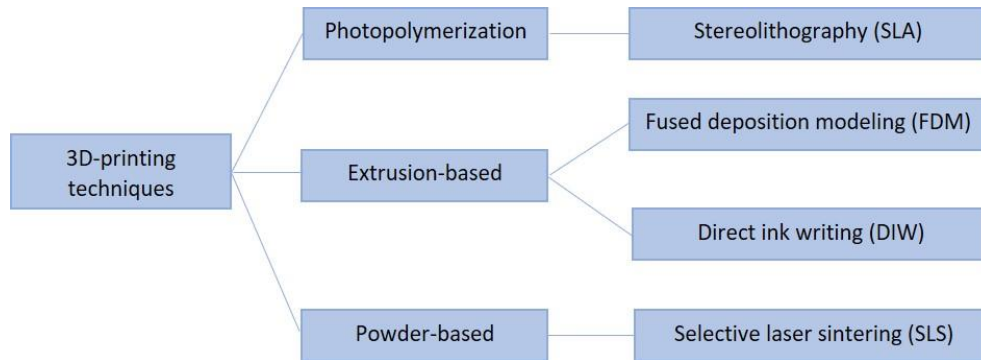
Figure 22 – 3D Printing techniques used for graphene-based composites. Adapted from (152).

2.2.2.1 Fused deposition modeling

FDM involves the deposition of thin filaments of thermoplastic polymers or composites onto a support, to create a vertical series of horizontal 2D layers of the part under manufacture (see Figure 23a). The 3D printer is fed with a spool of a previously extruded filament with standard diameter of 1.75mm or 3mm, which is pushed into a heated nozzle - generally by means of a pair of counter-rotating gears - where it melts and is extruded as a thinner filament (diameter of approximately 0.1 – 0.2 mm), which is deposited to fabricate the 3D part. The nozzle moves in the XY direction to build each layer, and vertically (Z-axis) to create other layers (132). An interesting variant of FDM is Free Form Extrusion (FFE), where a screw extruder replaces the nozzle to produce the thin filament. The extruder can be directly fed by polymers/composites in pellet/powder form, thus widening quite significantly the range of materials that can be printed, considering the relatively limited scope of commercial materials in filament form available for printing. FDM/FFE is by far the most used 3D printing technology (153). Currently, many 3D printers can handle simultaneously two or more materials. This brings about several advantages:

- the production of parts with specific geometrical features; in the case of a geometry consisting of a vertical cylindrical column with a wide disk on top, it is necessary to deposit two materials; one generates the column, while the other will serve as support when printing the disk above; the support material is subsequently removed during post-processing;

- the production of parts with gradient of particular local properties (e.g., soft vs. rigid zones);

- obtaining aesthetical effects, for example by mixing filaments with different colors and in varying proportions in a single nozzle.

Despite of its apparent simplicity, FDM/FFE is governed by a large number of process parameters, which creates requirements in terms of materials properties, particularly rheological and thermal (154). Operating parameters include extrusion velocity and temperature, printing velocity, build orientation (the rotation of the part in the manufacturing space around the axes of the machine's coordinate system), deposition sequence (the path taken by the filament during deposition, for example, unidirectional and aligned, unidirectional and skewed, or perpendicular), infill % (0% is hollow while 100% is solid), environment temperature, and support temperature. Flow in the nozzle depends on the melt viscosity of the polymer/composite, which is a function of temperature and shear rate, i.e., extrusion velocity and temperature. Upon exiting the nozzle, the molten filament swells, but is simultaneously stretched axially by the printing head (the filament diameter resulting from these two conflicting effects depends on the viscoelastic response of the material). Deposition involves filament deformation and bonding with contacting filaments that were previously deposited. Therefore, once deposited, each filament should solidify quickly to minimize its deformation due to its own weight and/or the weight of the material that will be deposited above it, thus preserving dimensional accuracy. Conversely, the new filament should remain sufficiently hot during enough time, to ensure adequate bonding (i.e., molecular diffusion) with the neighboring filament(s) (155).

Therefore, process parameters and material properties influence the morphology and properties of printed parts. These are usually significantly anisotropic and may exhibit warping and eventual delamination due to differences in local shrinkage. Adequate bonding between filaments and good porosity control are key factors to obtain quality parts (131, 132). Fiber and nanofiller matrix reinforcement usually cause improvements in the mechanical properties (131).

2.2.2.2 Direct ink writing

DIW uses a printing mechanism similar to that of Fused Deposition Modelling but focuses on meso- and micro-scale parts, and generally handles materials with viscosities lower than those of typical polymer melts. The material(s) is (are) supplied under controlled flow rate using a piston (e.g. a syringe), an Archimedes-type screw, or pneumatic force (156) and are heated, so that the nozzle extrudes a liquid "ink" or a "paste" filament that is subsequently printed (Figure 23b). The pneumatic force system is easy to install and enables pressure adjustment, whereas the screw system is more appropriate for high

viscosity materials (157). If a low heating temperature is used, cells and bacteria can survive during printing, making DIW suitable for biomedical applications. Biopolymers (158-160), thermoplastics (161), hydrogels (162-165), organic/inorganic monomers (43) or graphene-based nanocomposites (166-168) have been printed. Several DIW printers designed for healthcare and food research are currently available in the market, many having a temperature-controlled building platform (152).

As in FDM, the printability of a given material is related to its rheological response. The ink is extruded as liquid, but its viscosity should immediately increase thereafter, so that the printed structure holds without significant dimensional distortion. Hence, rheofluidifying materials, whose viscosity decreases with increasing shear rate, as well as fluids with a yield stress, are recommended. This increase in viscosity can also be induced by cooling, via phase change, or achieved through chemical reactions (169). Low viscosity (often Newtonian) fluids can also be used in DIW, by extruding into a coagulation liquid where they form a gel. High viscosity inks are thus easier to print, but they tend to clog the nozzle. Proper ink formulation is a key issue in DIW (152).
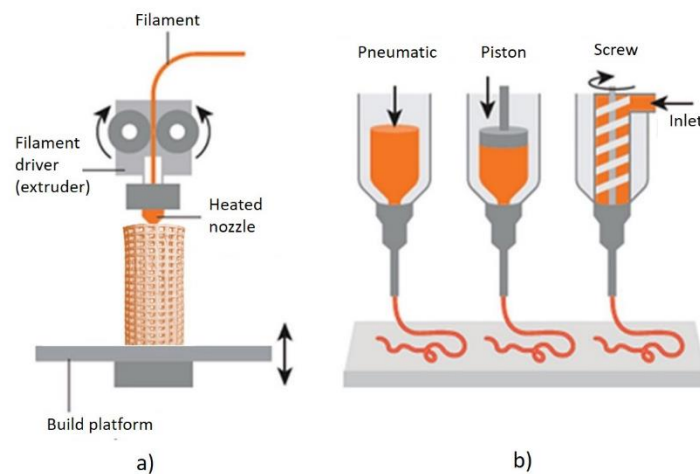
Figure 23 – Schematic representation of extrusion-based techniques, namely (**a**) FDM method; (**b**) DIW method. Adapted from (157).

2.2.2.3 Stereolithography

SLA consists on the layer-by-layer deposition of a photo-curable liquid resin/monomer, which cures/polymerizes and solidifies by irradiation with a spatially controlled UV light or laser beam, forming the desired pattern (see Figure 24a). Quick solidification is important in order to hold subsequent layers. After printing, the unreacted resin is removed. The thickness of each layer is controlled by the energy of

the light source and exposure time. Post-processing may involve heating or further photo-curing, in order to achieve higher mechanical performance (152).

SLA is one of the earliest additive manufacturing techniques. Although relatively slow, expensive and displaying a limited range of materials for printing, it produces high quality parts, and higher resolution that those produced by extrusion-based techniques, with an accuracy as low as 10 μm (170).

Materials and nanocomposites for SLA must fulfill two important requirements: i) fast response to the light irradiation (i.e., rapid initiated polymerization) in order to assure swift solidification; ii) sufficient low viscosity, to allow for the dipping of the resin layer. The latter usually limits the level of filler incorporation and demands a homogeneous filler dispersion (152).

2.2.2.4 Selective laser sintering

SLS employs a laser to progressively sinter thin layers of powdered polymer/composite on top of a platform, to create a 3D part. The manufacturing cycle may start by preheating the powder to a temperature just below the formation of a melt. Then, the laser scans one horizontal slice of the geometry, sintering the particles together to create one solid layer. Next, the platform lowers vertically the equivalent to the thickness of one layer. A roller applies a new layer of powder material on top, and the above steps are repeated until printing is completed. The part cools down inside the printer and then is removed and cleaned (171, 172). Generally, SLS parts exhibit a slightly rough surface, hence post-processing operations are often carried out (173). Unlike most other AM techniques, SLS does not require the use of support material to generate parts with overhanging features, since the unfused powder supports the part during printing, and thus facilitating the production of particularly complex structures (174). SLS is widely used for advanced applications, such as scaffolds for tissue engineering. Powder particle size and particle distribution determine the density of the printed part. Normally, powder particles with diameters in the range of 10 – 100 μm are used to facilitate spreading, as well as play efficiently the role of support material if unfused (175). Nevertheless, the porosity of the part can also be controlled through a post-treatment by infiltration (176). A low melting/sintering material temperature also facilitates the use of the laser.
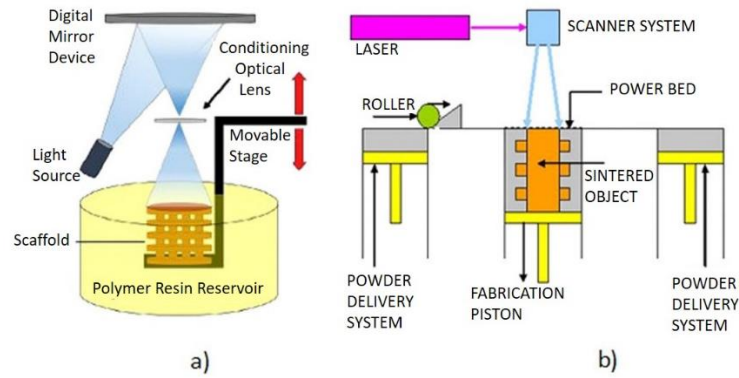
Figure 24 – Schematic representation of laser technologies: (**a**) SLA and (**b**) SLS. Reproduced with permission from (177).

For the 3D printing techniques most used for biomedical applications, Table 10 identifies the most common polymers and applications, together with the main advantages and limitations.

Table 10 – Types of AM in biomedical applications. Adapted from (178).

AM TECHNIQUE	POLYMER	RESOLUTION	BIOMEDICAL APPLICATIONS	ADVANTAGES	DISADVANTAGES
FDM	PLA; Acrylonitrile butadiene styrene (ABS); Polycarbonate (PC); Nylon	100–200 μm	Scaffolds for cell culture, and tissue engineering	Low cost, high strength, composite materials, not using toxic solvents	Nozzle clogging, anisotropy, lower resolution, thermal degradation of polymer
DIW	ALG; CHI; collagen; gelatin; silk	1–100 μm	Tissue regeneration, wound healing, drug delivery	Structures with different geometries, sizes, and materials	Formulation of inks
SLA	Photocurable resin (epoxy or acrylate-based resin)	1.2–200 μm	Scaffolds for cell culture, tissue, and organ	High resolution, fast, good cell viability, nozzle free	Cytotoxicity, high cost, material limitation, possible harm to deoxyribonucleic acid (DNA) by UV
SLS	PCL, Polyamide (PA) power	100–200 μm	Temporary and degradable rigid implants	Good strength, easy removal of support, no solvents required	High cost, medium resolution, post-processing required

2.2.3 Graphene-based polymer nanocomposites

2.2.3.1 Graphene and graphene derivative particles

Graphene consists of a single 2D sheet of sp^2-hybridized carbon atoms arranged in a crystalline hexagonal lattice. Its properties are estimated to be similar or even higher than those of carbon nanotubes (179). Graphene is not permeable to gases, has high flexibility and an optical transmittance of 97.7% of the total incident light over a wide range of wavelengths (180). Yet, graphene has found limited practical applications due to the difficulty and cost to obtain at a commercial production scale, in the form of a single defect-free carbon sheet. A good method to produce graphene derivatives at large scale has been the exfoliation of graphite, using different procedures, such as depicted in Figure 5a. The most significant methods have been: i) thermal expansion of graphite intercalation compounds (GICs), ii) chemical oxidation of graphite to obtain graphene oxide (GO) (156), and iii) liquid phase exfoliation (LPE) of graphite using liquids of appropriate surface tension and application of high shear forces (181).

GICs are formed by the insertion of atomic or molecular layers of different chemical species (alkali metal, metal oxide, metal halogenate, etc.) within the graphene layers, which receive or donate electrons to the intercalated species. The graphite obtained with intercalation compounds presents increased interlayer spacing and weakening of the van der Waals interactions between graphene layers. Subjecting GIGs to sufficiently high temperature or microwave radiation, they will further expand due to vaporization of the intercalate, forming expanded graphite flakes with nano-size thickness (180, 182).

GO is prepared by treatment of graphite flakes with oxidizing agents, bonding oxygen containing functional groups at the graphite surface and edge carbons. In this process the hybridization of part of the graphene carbon changes from sp^2 to sp^3, expanding the spacing between the graphene layers and facilitating the exfoliation of GO single layers in the liquid phase, aided by the application of mechanical forces. GO is electrically insulating, the electrical resistivity varying with the degree of oxidation attained (182), and is stable in aqueous solution due to the polar nature of the oxidizing groups. The subsequent reduction of GO produces reduced graphene oxide (rGO) which can partially recover the electrical conductivity, but a high oxygen content and physical damage remains in the rGO structure. GO and rGO are less performing than graphene, but the oxygen containing functional groups at the GO or rGO surface potentiate covalent bonding and strengthen the interface with the polymers, or provide reactivity with biomolecules (156).

LPE of graphite is a cost-effective process that can be up-scaled to mass-production of few layer graphene (FLG), typically based on the application of high shear to graphite suspensions in organic

solvents with surface tension near 40 mJ m^{-2} (181), ionic liquids, or water-surfactant solutions (183). The use of organic solvents and ionic liquids is not suited for most biomedical applications, thus LPE of graphite in water solutions of amphiphilic molecules has been favored in this field. LPE produces mainly FLG, with possible formation of a low concentration of monolayer graphene, however requiring the application of high shear rates, larger than 10^4 s^{-1}.

GNPs can be obtained from graphite through liquid phase exfoliation processes, exposure of acid-intercalated graphite to microwave radiation, ball milling and shear exfoliation. These techniques produce GNPs with varying morphology, within a range of thicknesses, lateral sizes, aspect ratios and concentration of defects (184, 185). Commercially available GNPs are typically formed by a combination of single layer, few layer and nano-sized graphite platelets. Thus, its thickness can vary from 0.34 to 100 nm within the same production batch (184).

GNPs exhibit interesting properties such as low density, high aspect ratio, 2D morphology, high electrical and thermal conductivity, mechanical toughness, at low cost. Typical mechanical and physical properties (electrical and thermal conductivity) of graphene and graphene derivatives are presented in Table 11. In this way, GNPs have potential for application in several fields, including thermal interface materials, gas barriers, flame retardants, composites with sensing ability and in the biomedical area (184).

Table 11 – Mechanical and physical properties of graphene-based materials.

Properties	Graphene-based materials				
	Graphene	GO	rGO	Graphite	GNPs
Thermal conductivity [W m^{-1} K^{-1}]	~ 5000 (186)	3000 (187)	30 – 250 (188)	3000 (182)	5000 (189)
Young's Modulus [GPa]	~1000 (186)	200 (190)	250 (190)	20 (191)	1000 (192)
Electrical conductivity [S m^{-1}]	~10^6 (193)	Insulator (190)	~667(188)	Insulator	10^5 (189)

GNPs and FLG are often used as reinforcement in polymer composites. These nanoparticles are typically produced before composite preparation, and then mixed in the resin or polymer melt using adequate techniques that ensure dispersion of the nanoparticle agglomerates. Only the composites produced in the liquid phase (polymer dilute solutions, monomers for *in situ* polymerization) may allow the simultaneous LPE of graphite while mixing with the solution.

With the growing interest in graphene-based materials for applications in the medical field, the issue of biocompatibility has gained importance and the studies concerning its cytotoxicity and biocompatibility have multiplied, however there is no scientific consensus on this topic yet (194). To date, *in vitro* studies have been performed with bacterial and mammalian cell models, and *in vivo* studies performed with animals and embryos (195). The inherent hydrophobic nature of graphene may be responsible for cellular toxicity, since it interferes with the hydrophobic protein-protein interaction in the membrane, interrupting the cell's metabolism, leading to cell mortality (196). Functionalized graphene-based nanomaterials have shown reduced cellular toxicity (197) since it can help in pacifying the strong hydrophobic interaction of graphene/GO with cells and tissues (194). Dextran-functionalized GO was found to accumulate in the reticuloendothelial system of mouse such as the liver and spleen after intravenous injection, and could be cleared from its body within a week without significant toxicity (198). Besides, rGO has greater cellular toxicity than GO, due to the different surface functional group density and oxidation status (197).

However, it is not possible to make general statements on graphene–based materials safety or toxicity in eukaryotic cells, since they are strongly influenced by several factors such as the production methods, concentration, shape, distribution, surface area, number of layers, lateral dimensions, hydrophobicity, purity, particulate state, surface functionalization (199-201) and even to the type of cells that graphene was exposed to (202). For instance, Wei et al. (203) reported that pristine GO inhibited the proliferation of BMSCs at a high concentration of 10 μg/mL, but enhanced their proliferation at a low concentration of 0.1 μg/mL (203). Similarly, Zhang et. al.(204) investigated the toxic effects of GO nanosheets on BMSCs. A high concentration of GO inhibited cell viability and membrane integrity. It was observed that the toxic effects of GO on BMSCs occur in a dose-dependent manner through the mitochondrial apoptotic pathway and autophagy. Exposure of BMSCs to GO at 0.1, 0.5 and 2.5 μg/ml for 24 hours resulted in a slight increase in apoptosis by 5, 7 and 8% (204).

In addition, the *in vivo* effect of graphene-based materials is also dependent on the dose/time exposure, administration route, and the characteristics of the animals used in the experiment (195, 205).

Thus, conflicting results on the toxicity/biocompatibility of graphene derivatives have been reported. Some studies suggested that graphene-based materials are beneficial (206-211) and others mention adverse responses including cytotoxicity (212, 213), tissue fibrosis (214), and inflammatory cell recruitment, usually in lung and liver (212, 215-217).

2.2.3.2 Nanocomposites preparation methods

Most preparation methods of commercial graphene-derivatives are based on the bulk exfoliation of graphite. Given the atomically flat surface of graphene, those materials may be obtained as cohesive agglomerates of individual nanoparticles, stabilized by non-covalent interactions through Van der Waals forces (218). To fully explore the reinforcing effect and the functional properties resulting from the incorporation of graphene-derivatives into polymer matrices, it is essential to guarantee the uniform dispersion and distribution of the individual nanoparticles, in order to generate a large interfacial area between the composite components (219).

There are three main routes economically viable and scalable to produce well-dispersed polymer composites, as summarized in Figure 25b. Solution and melt mixing are essentially based on the mechanical action and physical interactions between the polymer and nanoparticles, while *in situ* polymerization also uses a chemical approach (220).
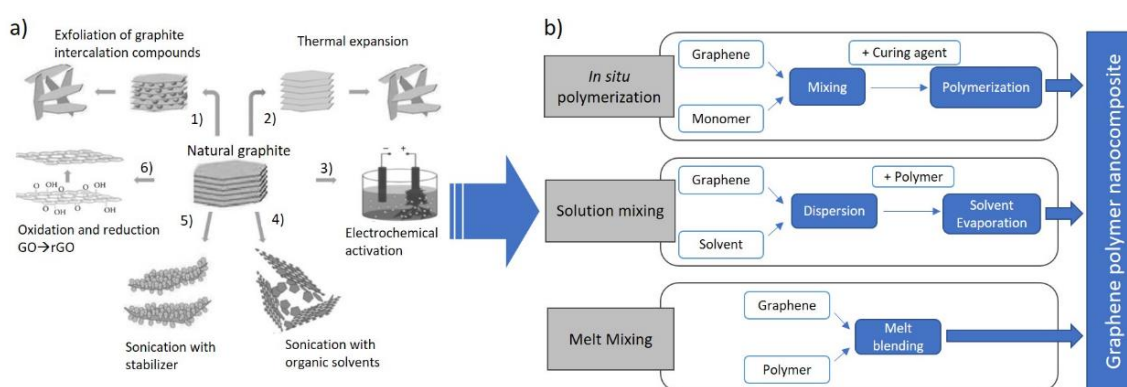
Figure 25 – Schematic representation of graphene nanocomposite production: (**a**) preparing graphene by 1) exfoliation of graphite intercalation materials; (2) solvothermal exfoliation; (3) electrochemical activation uses an applied potential to drive exfoliation; (4) sonication in organic solvents uses direct sonication in various solvents, but without auxiliary stabilizer present; (5) sonication with stabilizer; (6) chemical oxidation to graphene oxide followed by chemical reduction back to reduced single-sheet graphene oxide; (**b**) dispersion of graphene in the polymer matrix by melt mixing, solution mixing or in situ polymerization. Adapted from (221, 222).

Solution mixing is especially used for the small-scale manufacture of polymer composites whenever they are soluble in aqueous or organic solvents (223). The technique entails the dispersion of the nanoparticles in a solvent by mechanical mixing, magnetic stirring, or sonication, followed by the addition of the polymer solution and mixing again by the same methods. The composite is obtained by removing the solvent by precipitation in a non-solvent or by direct solvent evaporation (224). During mixing, the nanoparticles further separate/expand due to diffusion of the low viscosity polymer solution, and may adsorb polymer molecules at their surface, which helps preventing reagglomeration when the solvent is evaporated.

Melt mixing uses polymer processing equipment, typically internal mixers, or twin-screw extruders, to subject the flowing polymer melt and the graphene-based reinforcement to high hydrodynamic (shear and extensional) forces and complex flow fields. Processing parameters such as temperature, mixing speed, residence time and mixer geometry need to be adequately selected to obtain good dispersion levels (225). Nevertheless, melt mixing generally attains lower dispersion levels than the remaining methods, although it exhibits strong advantages, such as avoiding the use of solvents, easily scaling to industrial production and high yield. The composite can be readily processed into a final product, or used as a masterbatch, i.e., diluted into the polymer using the same processing method to obtain the desired filler incorporation level.

In situ polymerization involves the preparation of a stable dispersion/suspension of the graphene-derivative particles in the liquid monomer, followed by polymerization. The latter may be initiated by heat, radiation, or by the addition of a catalyst. If the nanoparticles are functionalized with the adequate chemical functions, reaction may occur with the growing polymer chains during polymerization, enhancing interfacial strength and avoiding nanoparticle reagglomeration (218, 223).

For each of the above methods, Table 12 presents a list of polymers used for the manufacture of graphene-based composites, together with their advantages and limitations.

Kim et al. (226) compared the performance of PU/graphene-based nanocomposites produced by different methods using the procedure represented in Figure 26. Solvent-based methods yielded the best dispersion, improving the composite properties. Indeed, composites obtained by *in situ* polymerization exhibited a slightly higher percolation threshold when compared to those prepared by solution mixing. The electrical conductivity of the composites produced by *in situ* polymerization and solvent mixing was higher relative to that of materials produced by melting mixing, at similar reinforcement concentration (226).

Table 12 – Preparation methods of graphene-based composites. ([a] Polymethylmethacrylate (PMMA); [b] Polyvinyl alcohol (PVA); [c] Polystyrene (PS); [d] Polyurethane (PU); [e] Polyethylene terephthalate (PET); [f] Polyethylene (PE); [g] Polypyrrole (PPy)).

Preparation method	Polymer matrix	Advantages	Disadvantages	Reference
Solution Mixing	PC; PMMA[a]; PVA[b]; PS[c]; PU[d]	Inexpensive; Homogeneous dispersion.	Need to remove solvents	(139, 218, 220, 227)
Melt Mixing	PU; PET[e]; PLA; PC	Applicable to polar and non-polar polymers; does not use solvents; adequate for both small and large-scale production.	Less effective in dispersion; possible buckling, rolling, or shortening of graphene sheets.	(220, 223, 228)
***In Situ* Polymerization**	PA; PE[f]; PPy[g]; PMMA	Applicable to insoluble or thermally unstable polymers.	Need to remove solvents.	(218, 224, 228)
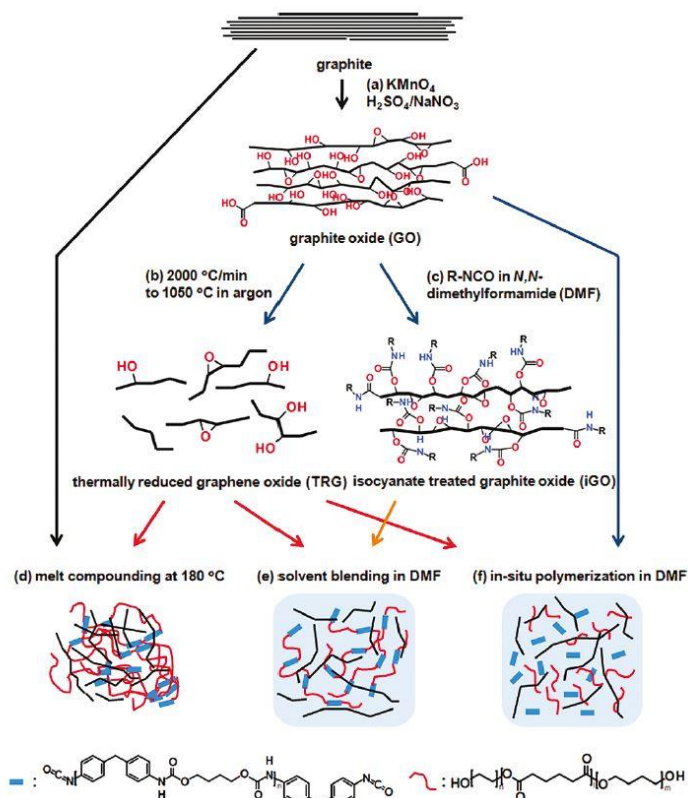
Figure 26 – Schematic representation of TPU/Graphene Composite Preparation: (**a**) After oxidation of graphite functionalized layers of graphene can be obtained by (**b**) Rapid Thermal Expansion or (**c**) Organic Modification with Isocyanate in dimethylformamide (iGO); (**d**) Graphite can be mixed with TPU via Melt mixing, or (**e**) Solvent mixing, followed by solvent removal; (**f**) In opposite, composites can be produced monomers using In situ polymerization. Black lines represent graphitic reinforcements. TPU hard and soft segments are represented by short blue blocks and thin red curves, respectively (226).

2.2.3.3 Properties of 3D printed graphene-based nanocomposites

3D printing of graphene-based nanocomposites has been the focus of extensive research, aiming to explore the potential to develop components for advanced applications in electronics, healthcare, energy storage, among others. Table 13 compares results obtained for the properties of 3D printed composites produced with different polymers and using different AM techniques. Despite the advantages of these technologies, some practical issues such as efficiency, cost, feasibility of mass production, still prevents the large-scale adoption of this solution (229).

Table 13 – Properties of 3D printed graphene-based composites.

Technique	Matrix	Filler	Properties	Ref.
SLA	Photopolymer (Envision TEC PIC 100 resin)	GO	0.2 wt.%GO increased 62.2% and 12.8% the tensile strength and ductility, respectively of the printed composite.	(185)
DIW	Polyaniline (PANI)	GO	Specific capacitance of the printed supercapacitor: 1329 mF cm^{-2}.	(186)
	Polydimethylsilo xane (PDMS)		The printed device exhibited a resistivity of 1660 Ω.cm at a low GO percolation threshold (0.83 vol.%)	(187)
	Epoxy	Graphene	Printed composites with 10 wt.% of graphene presented flexural modulus of 3.2 GPa and bulk resistivity of 1x10^3 Ω.m, i.e., five orders of magnitude lower than that of the neat epoxy.	(188)
SLS	PA		Tensile modulus for PA-rGO compared to PA (221 ± 17 vs 149 ± 26 MPa) and similar tensile strength.	(189)
FDM	ABS		Electrical conductivity increased to 1.78 x 10^{-7} and 1.05 x 10^{-3} S.m^{-1} with the addition of 0.4 and 5.6 wt% of graphene, respectively	(190)

2.2.4 3D printing of graphene-based Polymer composites for biomedical applications

2.2.4.1 Scaffolds for tissue engineering

The development of scaffolds with higher mechanical properties suitable for *in vivo* application requires sophisticated manufacturing methods. Additive manufacturing techniques brought the possibility

to process composite scaffolds with fine control of geometry and size, enabling the development of complex and personalized shapes with vast potential to regenerate distinct tissues (230).

With the advances of 3D printing, the production of 3D biological constructs that mimic the structure and function of native tissues with precise control over the positioning of both cells or other biological components (proteins, growth factors...) and biomaterials, called biofabrication, is now possible (231, 232). Bioprinting such constructs comprises several technologies such as SLS, SLA, FDM or inkjet bioprinting, as already addressed in section 2.2.2. Most of them were originally developed as AM technologies for rapid prototyping, but are included as biofabrication strategies when used for biomedical applications (232, 233).

The bioprinting process can be performed by two different approaches designated as pre-seeding, or direct, and post-seeding, or indirect (234). The former involves the simultaneous printing of materials and cells combined, while the latter consists of initially printing the material and then co-culturing it with the proper cells. The studies found in literature related with graphene-based 3D-printed scaffolds, which will be overviewed in this section, fall under the category of post-seeding bioprinting.

Recently, Belaid and co-workers (235) developed a 3D-printed scaffold of PLA reinforced by the incorporation of GO at different concentrations (0.1, 0.2 and 0.3 wt %). A composite polymer solution of GO and PLA was cast to form a film that was cut into pieces and introduced into a single-screw extruder, at 200 °C. A filament with a diameter of 1.75 mm was obtained and used to print 3D-scaffolds by FDM. To facilitate bone regeneration, the authors generated scaffolds with a porous interconnected network and a pore size around 300 µm, corresponding to an infill of 70%. With the incorporation of GO, the scaffolds revealed a rougher and hydrophilic surface, when compared to control PLA scaffolds. Tensile tests showed that the mechanical properties were improved with the GO incorporation (30% increase of the Young's modulus with 0.3% GO) – Figure 27. Composite scaffolds were also biocompatible as the cell viability, attachment, proliferation, and differentiation assays using MG-63 osteosarcoma cells showed. They promoted cell proliferation and mineralization more efficiently than pure PLA scaffolds which potentially allow bone formation (235).

The need for conductive and mechanically robust, biocompatible, and biodegradable materials in TE is constantly increasing. The advantages of electrical conductivity and electrical stimulation (ES) have been recognized and explored in the biomedical field (236), since cell adhesion and differentiation are affected by a residual permanent charge on the materials surface. Therefore, it is expected that the use of ES after biomaterial implantation would induce osteointegration.
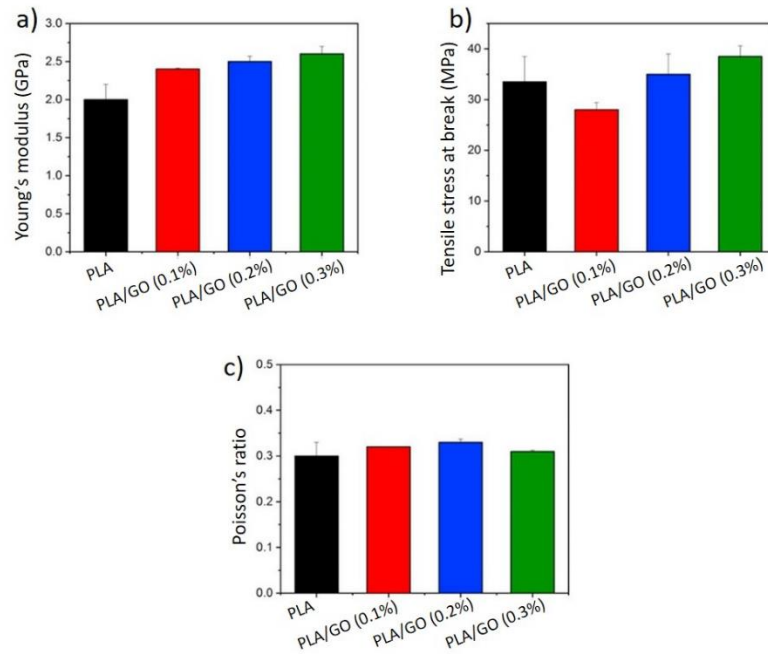
Figure 27 – Mechanical properties of PLA and PLA/GO scaffolds produced by FDM: (**a**) Young's modulus, (**b**) Tensile stress at break, and (**c**) Poisson's ratio. Reproduced with permission from (235).

Graphene-based materials have been proposed as additives to produce electrically conducting composites demonstrating that the simple presence of the electrical stimuli of the materials will contribute to improve cellular functions (236, 237). However, as mentioned above, there is no consensus about graphene cytotoxicity and some authors still mention some risks (238). Wang and colleagues (238) printed PCL-graphene scaffolds loaded with 0.13 wt.%, 0.50 wt.% and 0.78 wt.% of graphene and associated a non-invasive microcurrent therapy to treat rat calvaria critical size bone defects. The blended composite material was cut into small pellets for processing. The melt processing temperature was 90 °C, 220 μm of slice thickness, 22 rpm of screw speed, and 20 mm/s of deposition velocity. The fabrication process was performed at room temperature. A 0°/90° lay-down pattern was used to obtain pores with a regular geometry, a constant filament diameter of 330 μm, and a filament distance of 680 μm. Thereafter, MC3T3 pre-osteoblastic cells were seeded on the scaffolds – Figure 28. These results showed that cell proliferation was stimulated by the increase of graphene concentration and no significant cytotoxicity was found. Printed scaffolds with 0.78 wt.% induced an acceptable level of immune response, revealed by the low levels of tumor necrosis factor-alpha (TNFα) and interleukin-1-beta (IL-1β), suggesting high potential for *in vivo* applications. The incorporation of graphene and the application of electrical stimulation (10 μA) led to an increase in cell migration, leading to new tissue formation, well-organized tissue deposition and bone remodeling, as can be seen in Figure 29 (238).
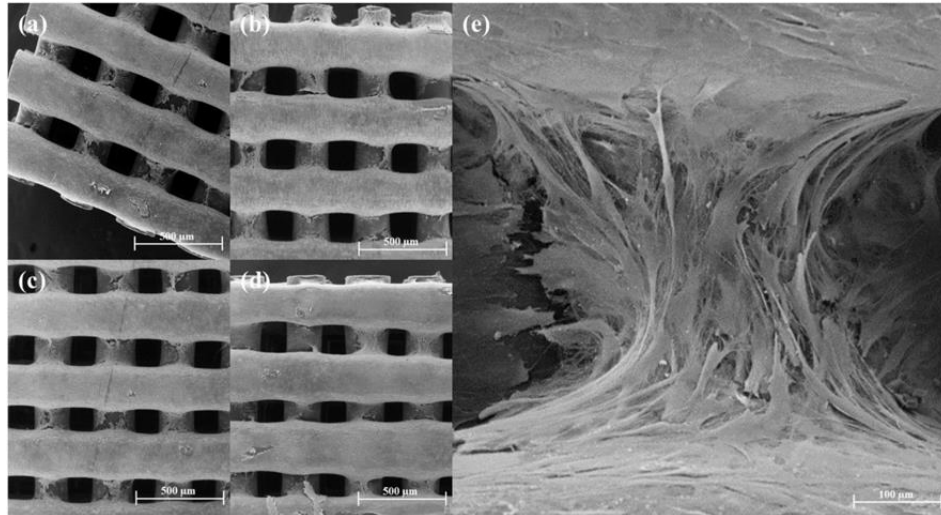
Figure 28 – SEM images of cell seeded scaffolds after 14 days. (**a**) PCL; (**b**) PCL/graphene (0.13 wt.%); (**c**) PCL/graphene (0.50 wt.%); (**d**) PCL/graphene (0.78 wt.%); (**e**) zoom up image for cell bridging. Reproduced with permission from (238).
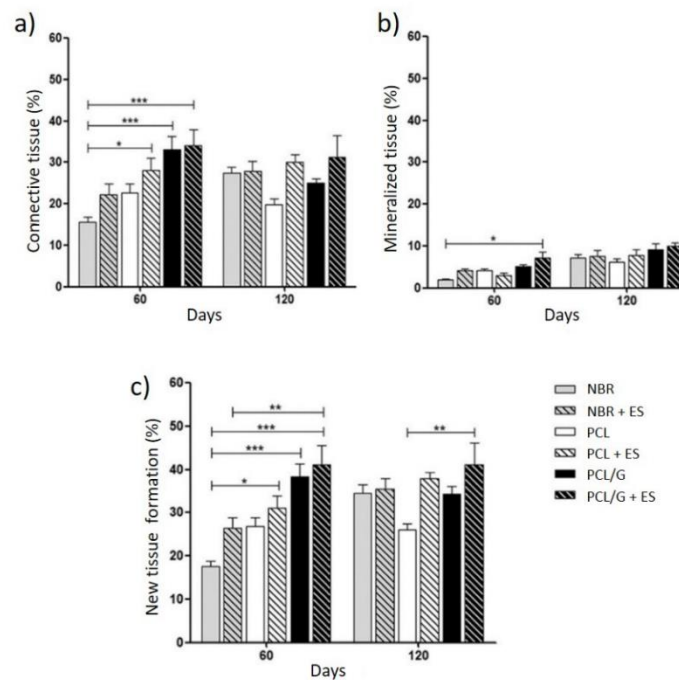
Figure 29 – Evolution in time of the formation of (**a**) connective tissue; (**b**) mineralized bone tissue; and (**c**) cumulative tissue formation (connective + bone tissues) on the PCL and PCL/0.78 wt.% of graphene (G) scaffolds, with and without electrical stimulation. NBR stands for "natural bone regeneration" or control group. Reproduced with permission from (238).

In another study, Jakus et al. (239) developed 3D-printable graphene inks and used them to produce electrically conductive, mechanically resilient, and biocompatible scaffolds with high graphene content (20 and 60 vol % of solid). The ink contained graphene flakes and PLGA and was produced by combining a solution of PLGA and dichloromethane with a graphene dispersion, followed by solvent

evaporation. The authors used this ink via extrusion-based 3D printing to create mechanically robust graphene scaffolds. The retained electrical conductivity was greater than 800 S/m. These composite scaffolds supported cells adhesion/proliferation, as well as neurogenic differentiation, as illustrated in Figure 10. On day 14, a distinct difference in cell morphology was observed, where human mesenchymal stem cells (hMSC) on 20 vol % graphene scaffold exhibited a sheet-like morphology, characteristic of adherent cell types such as fibroblasts. In contrast, cells on 60 vol % graphene scaffold presented highly elongated morphologies similar to uni- or multipolar neurons – Figure 30. *In vivo* experiments of 30 days in mice showed promising biocompatibility with no evidence for the accumulation of graphene flakes in the kidney, liver, or spleen. Besides, the scaffolds present exceptional handling characteristics being able to apply in fine surgical procedures (239).
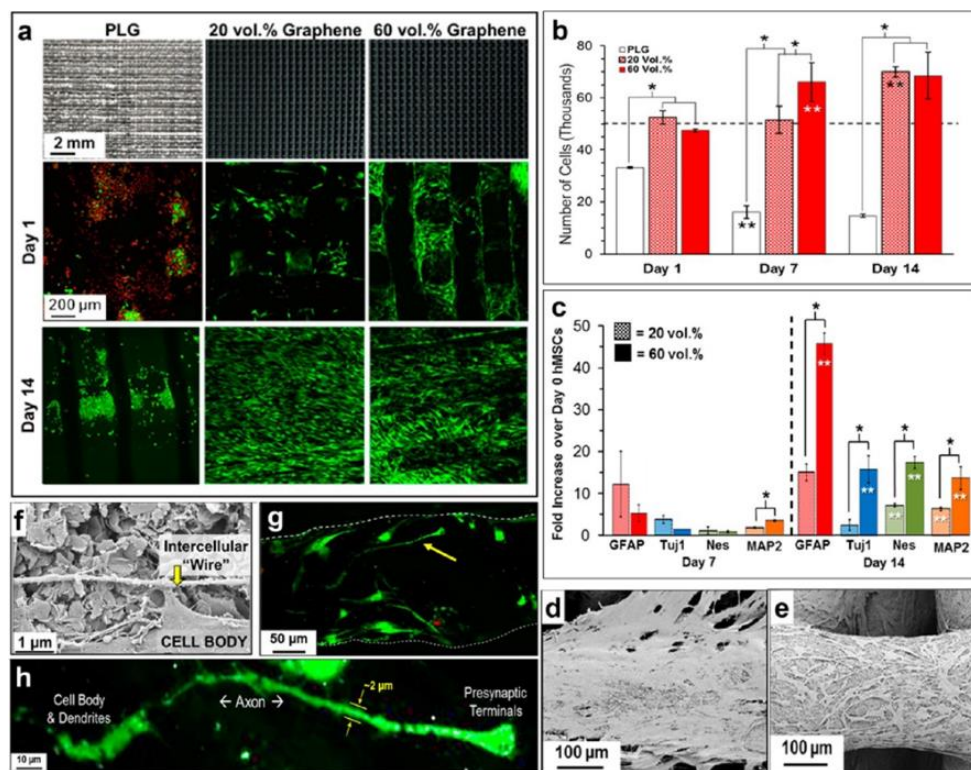
Figure 30 – (**a**) Images and scanning laser confocal 3D reconstruction projections of live stained (green) and dead stained (red) human MSCs on different scaffolds after 1, 7 and 14 days of seeding. (**b**) Number of human MSCs present on scaffolds as a function of composition and days after seeding, according to DNA quantification. Dotted line represents initial cell seeding number. (**c**) Neurogenic relevant gene expression of cells on scaffolds with 20 and 60 vol% graphene after 7 and 14 days of seeding, normalized to expression of day 0 (unseeded human MSCs). SEM micrographs of human MSCs on (**d**) 20 and (**e**) 60 vol % graphene scaffolds 7 days after seeding. (**f**) High-magnification SEM micrograph of cells on day 7, 60 vol % graphene scaffolds, revealing human MSCs connecting via a small "intercellular" wire. (**g**) Scanning laser confocal 3D reconstruction of live (green) and dead (red) cells on day 14 for 60 vol % graphene scaffolds and (**h**) detail of cell indicated by yellow arrow in

(**f**). For panels (**b**) and (**c**), "*" indicates significance of $p < 0.05$ between compared groups (n = 4); "**" indicates significant ($p < 0.05$) difference over previous time point for the same material group. Reproduced with permission from (239).

Sayyar et al. (240) used different percentages of rGO to reinforce a CHI-lactic acid matrix and produce conductive hydrogels. These composites were easily processed into 3D scaffolds by extrusion-printing. Scaffolds with 30 layers of each graphene/CHI dispersion were printed from a 200 μm diameter nozzle, at 0°/90° orientation, a feed rate of 150 mm.min^{-1} and with a strand spacing of 0.6 mm. The addition of graphene led to significant improvements in terms of mechanical strength. An addition of 3wt.% of graphene caused an increase over 200% in tensile strength. The resulting structures were seeded with fibroblast (L929) cells that adhered and proliferated on several layers of the 3D scaffold. These scaffolds revealed to be excellent conducting substrates for the growth of electro-responsive cells (240).

Zhou and co-workers (104) combined GO in different concentrations (0, 0.05, 0.1, 0.25, 0.5 and 1 mg/mL) with a gelatin-methacrylate (GelMA) and poly (ethylene glycol) diacrylate (PEGDA) solution to produce a biocompatible photopolymerizable ink and then 3D-printed scaffolds. GelMA-PEGDA inks with and without GO were placed on the z-control movable platform and printed by SLA, using a table-top stereolithography-based printer that applied UV laser. The printing parameters were: 200μm diameter laser beam, 25 μJ intensity output of 20 kHz emitted UV, and 10 mm/s printing speed. Human MSCs spread and extended on these scaffolds, after 5 days of culture. The results showed that the optimal combination was 15% GelMA+PEGDA with GO incorporated at 0.1 mg/mL, as seen in Figure 31. Moreover, the authors showed that these GelMA-PEGDA-GO scaffolds induced chondrogenic differentiation of human MSCs and promoted the glycosaminoglycan and collagen levels. Collagen II, SOX 9 and Aggrecan gene expressions associated with chondrogenesis were also greatly promoted on the scaffolds. Such scaffolds are excellent candidates for cartilage regenerative applications (104).

Composite scaffolds of polyether ether ketone (PEEK)/PVA reinforced with GO was developed by Feng and co-workers using a SLS system envisaging bone regeneration (241). The resulting scaffolds presented good hydrophilicity and degradability. For a GO loading of 1 wt.%, the strength and modulus of PEEK/PVA scaffolds increased by 97.16% and 147.06%, respectively. *In vitro* tests with MG63 cells revealed that the scaffolds promoted cell attachment and proliferation as well as osteogenic differentiation and bone regeneration *in vivo*, with rabbits (241).
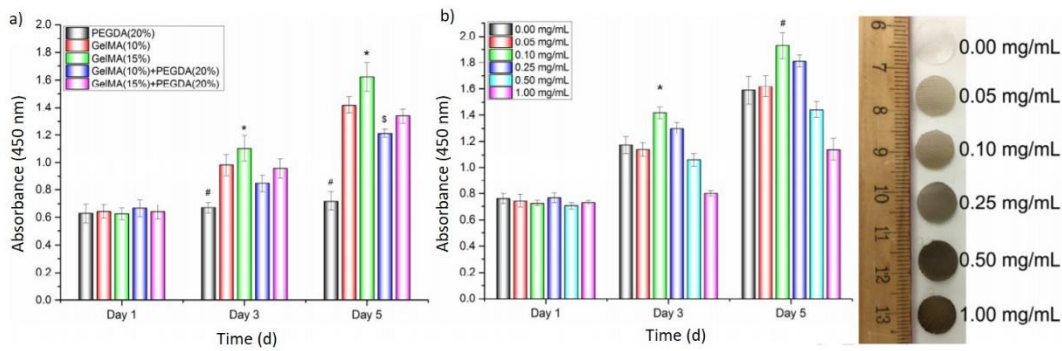
Figure 31 – (**a**) Evolution along 5 days of MSCs proliferation on hydrogels with different compositions. (**b**) MSCs proliferation on scaffolds with GelMA-PEGDA and different concentrations of GO for 5 days. The photographs represent the corresponding scaffolds. Reproduced with permission from (104).

In addition to all outstanding mechanical and electrical properties, graphene can be exploited in the medical field because of its antibacterial activity. Angulo-Pineda et al. (242) explored this property and developed SLA composite scaffolds of PCL filled with conductive thermally reduced graphene oxide nanoparticles at concentrations above the percolation threshold. By applying a voltage along their surface, a bactericidal effect was observed. Moreover, under the same regime of ES, the adhesion and viability of human stem cells were further enhanced when compared with pure PCL scaffolds with and without ES (242). The antibacterial activity was also observed by Zhang and co-workers in 3D printed Ag-GO nanocomposite scaffolds (243) as well as by Cabral et al. (244) who produced tricalcium phosphate/gelatin/chitosan scaffolds reinforced with rGO displaying antimicrobial activity without compromising the osteoblasts' viability and proliferation (244).

Cryogenic 3D printing is a recently developed biofabrication process that allows the production of scaffolds with a predesigned shape, controllable architecture, and suitable mechanical strength at the relatively low temperature of $-32°C$. It allows the incorporation of a large quantity of biomolecules/drugs into scaffolds and the retention of a high level of the biomolecule's biological activity. It does not require UV light and post-sintering use of a high-power laser, avoiding some typical 3D printing's disadvantages. Despite being barely explored, the *in situ* incorporation of GO-loaded drugs/biomolecules into scaffolds by this method shows great potential in TE (245). A recent and novel bioactive PLGA/β-tricalcium phosphate (β-TCP) composite scaffold, in which GO and a bone morphogenetic protein were loaded *in situ*, was produced by Zhang et al. (246) using the cryogenic 3D printing method. The composites were produced at various GO concentrations (0, 0.025, 0.05, and 0.1 wt.% with respect to the final mixture) and were designated as 'PT/P', '0.025PTG/P', '0.05PTG/P', and '0.1PTG/P', respectively. The PLGA/β-TCP scaffold without peptide was generated as the negative control and denoted as 'PT'. Critical-sized

calvarial defects were successfully created in rats (Figure 32). Scaffolds with a diameter of 5 mm were implanted in these animal models to evaluate *in vivo* bone regeneration. When the implantation time was extended to 12 weeks, more bone formation was observed in the groups with scaffolds than in the control group, particularly in the graphene-based scaffolds. The bone volume (BV) and bone surface (BS) were quantitatively analyzed to confirm the bone regeneration ability – Figure 32. The scaffolds presented a customized shape with hierarchical porosity and were mechanically comparable to the human cancellous bone. GO improved the scaffold's wettability and mechanical strength as well as controlled the peptide release, promoting bone marrow – derived mesenchymal stem cells ingrowth into the scaffold, enhancing the osteogenic differentiation in a critical bone defect (246).
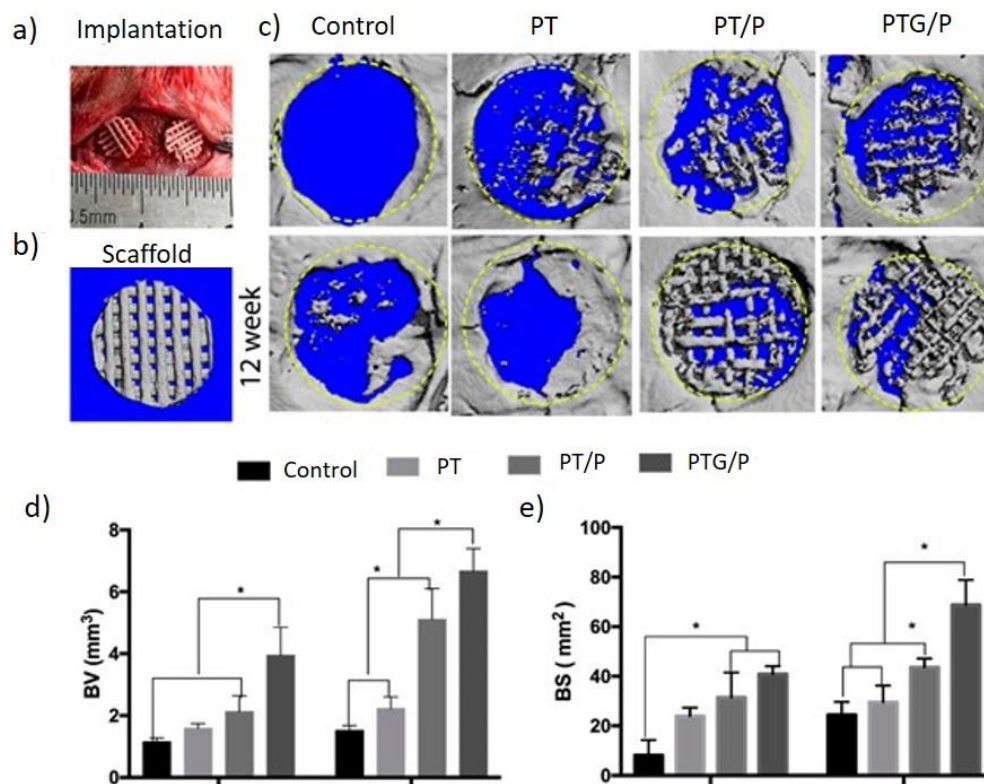
Figure 32 – Bone volume and bone surface results obtained by Micro-CT for the *in vivo* animal tests: (**a**) Implantation process; (**b**) Micro-CT image of the scaffold; (**c**) 3D reconstructed images of the control, PT, PT/P, and PTG/P scaffolds 4 weeks after the implantation (top row) and 12 weeks after the implantation (boot row); (**d**) Bone volume and (**e**) bone surface of the newly formed bone in the critical-size defects (p < 0.05). Reproduced with permission from (246).

In summary, several graphene-based composites have been processed by 3D printing to manufacture scaffolds with enhanced biological, mechanical and electrical performance, to regenerate a variety of tissues such as bone, cartilage, or the nervous system. A summary of relevant examples of such scaffolds, as well as their main processing details and properties, is presented in Table 14.

Table 14 – Graphene-based 3D-printed scaffolds. [a]Compressive strength

AM technique	Scaffold	Printing parameters	Cellular behavior	Mechanical properties	Ref
Extrusion-based 3D printing	PCL + Graphene (0.13 and 0.78wt.%) Coating with P1-latex protein	Pattern:0/90 lay down; 90°C; slice thickness: 220 μm; 22 rpm; speed: 20 mm/ s	Human adipose -derived stem cells (ADSCs) adhered/spread and presented a spindle-like morphology; osteogenic differentiation; Scaffolds(0.78wt.%): higher viability/spread	C_s^a (0.13wt.%): 80MPa; C_s (0.78wt.%): 130 MPa	(247)
	PCL + Graphene (0.5 and 0.78 wt.%)		ADSCs adhered and proliferated. After 7 and 14 days, scaffolds with graphene exhibited better biological performance over the neat PCL scaffolds.	_____	(248)
	PCL + Modified graphene nanoplatelets (0.5 wt.%)	Pattern: 3 layers arranged in at 90° Layers height: 0.15 mm; 190°C; Bed: 50°C; Speed: 15 mm/s	Adhesion and proliferation of human chondrocytes; Higher cell proliferation in 3D scaffold comparing to polystyrene positive control; Graphene did not increase the cellular toxicity	No mechanical results for scaffolds Composite filaments (0.5 wt.% graphene): Young's modulus=271± 29 MPa Tensile strength: 16.35±0.28	(249)
	PCL + GO (0.1 and 0.5wt.%)	Cuboidal shape 22 layers Layer thickness: 2.2 mm; 100°C; 80-100 PSI; Speed:1 mm/s	Murine preosteoblast cells with higher proliferation and osteogenic differentiation in scaffolds with 0.5wt.% GO)	C_s (PCL):75.36 ± 4.07 MPa C_s (PCL+GO) without any statistical significance	(250)

AM technique	Scaffold	Printing parameters	Cellular behavior	Mechanical properties	Ref
	Thermoplastic PU /PLA + GO (0.5, 2, 5wt.%)	Cuboid shape printing in height/width direction; Layer thickness: 0.1 mm; 210°C; Bed: 60°C; Speed: 20 mm/s	NIH/3T3 mouse fibroblast cells with higher adhesion and proliferation in scaffolds with 0.5wt.%GO.	Printing-lying specimen (0.5 wt.%) : Tensile modulus and yield point increased by 75.50% ($\simeq$80 MPa) and 69.17%, respectively.	(251)
Extrusion-based 3D printing	Poly(trimethylene carbonate) (PTMC) +Graphene sheets from rGO (3 wt.%)	7 layers; 1x1 cm 60−150°C; nitrogen pressure: 100−200 kPa; cross-linking by UV irradiation for 10−15 min	MSCs with good attachment and viability Addition of graphene did not alter cell number; Electrical stimulation did not compromise MSCs and the osteogenic markers were upregulated	Tensile strength: 7.4 ± 0.3 MPa Young's Modulus: 19.1 ± 0.5 MPa Elongation at break: 420 ± 11 %	(236)
	Chondroitin sulfate/ALG/gelatin+GO (1 mg ml^{-1})	30 × 30 × 1 mm^3; mesh-like inner pattern:1.5 mm of thread spacing; Speed:50 mm s^{-1}; Pressure: 1 bar; extrusion needle tip:25 G; Petri dish at 2 °C; UV : 9 mW cm^{-2} for 5 min	Human MSCs cells adhered and spread; Composites presented cells with great proliferation, alignment and distribution; Chondrogenic differentiation	C_s: ~100 kPa	(252)

AM technique	Scaffold	Printing parameters	Cellular behavior	Mechanical properties	Ref
SLA	Commercial polyurethane: triethylene glycol dimethacrylate (TEGDMA) / PLA-PUA + few-layer graphene (0.5 wt.%)	UV light: 20 W Speed: 0.020 m.h^{-1} XY resolution: 47 μm, Z resolution: 1.25 μm Layer thickness 0.02 mm	_____	Resin: Tensile strength: 68 MPa Flexural strength: 115 MPa Tensile strength: 41.8 MPa (Direct casting specimens) 62% higher (3D-printed specimens)	(253)
SLS	PVA+GO (2.5 wt.%)	Laser power: 5W scan speed:400 mm.min^{-1} spot diameter: 1.6 mm scan spacing/ layer thickness, 2.7/0.1–0.2 mm, respectively	Human osteoblast like- MG-63 adhered and spread; The addition of GO to PVA led to higher cell growth and proliferation comparing to pure PVA scaffold.	C$_s$: 240.49 kPa Young's Modulus: 2.47 MPa Maximum tensile strength: 929.54 kPa Elongation at break: 164.6%	(254)

2.2.4.2 Biosensors

The incorporation of conductive materials such as graphene derivatives into polymers to form conductive composites allows the printing of electrodes and circuits, which can be integrated into complex structures, permitting the electrochemical detection of organic compounds and biologically active molecules. Graphene-based composites can be combined with biological receptors such as enzymes, antibodies, and single-stranded DNA. Printed graphene-based biosensors have good reliability and great potential for numerous applications (255).

Palenzuela et al. (256) fabricated ring-shaped electrodes by FDM using graphene/PLA composite filaments, for the electrochemical sensing of picric acid and ascorbic acid. The activation of the graphene-based 3D-printed electrodes consisted of the DMF-assisted partial dissolution of the insulating PLA. Different activation times (1, 10, 20, and 60 min) were studied, but immersing the 3D printed electrodes in DMF for 10 min was the optimum time. Picric acid and ascorbic acid could be detected with these electrodes in a wide range of concentrations, from 5 to 350 ppm for the former and 10 to 500 μM for the latter (256).

Cardoso et al. (257) used FDM to produce biosensing platforms from graphene-PLA filaments. The enzymatic biosensor was fabricated on the PLA-graphene surface and used for glucose sensing in blood plasma. The biosensor presented a limit of detection (LOD) of 15 μM L^{-1}, inter-day, and intra-day precision lower than 5 %, and adequate recovery values (90–105 %) for the analysis of plasma. At the same time, after a surface treatment of the 3D-printed sensor, it also exhibited improved electrochemical properties for the direct detection of nitrite and uric acid (257).

Marzo and co-workers (258) developed 3D-printed enzymatic graphene-PLA electrodes to immobilize horseradish peroxidase (HRP) creating a direct electron transfer biosensor for hydrogen peroxide (H_2O_2) detection. 3D electrodes were first printed by FDM using graphene/PLA filaments and then exposed to a chemical and electrochemical treatment for activation. Electrodes modified with gold nanoparticles enhanced the direct electron transfer between the HRP and the biosensors. Figure 33A depicts the good selectivity to H_2O_2 of DMF-EC/ AuNPs/HRP. The response of these biosensors with and without gold nanoparticles (DMF-EC/HRP and DMF-EC/ AuNPs/HRP, respectively) in human serum was also evaluated (Figure 13B) as well as their long-term stability up to seven days, in the presence of 25 (Figure 33C) and 50 μM of H_2O_2 (Figure 33D). This work opens possibilities for 3D-printed enzymatic systems to detect other biomarkers without the use of electron mediators and binder polymers (258).
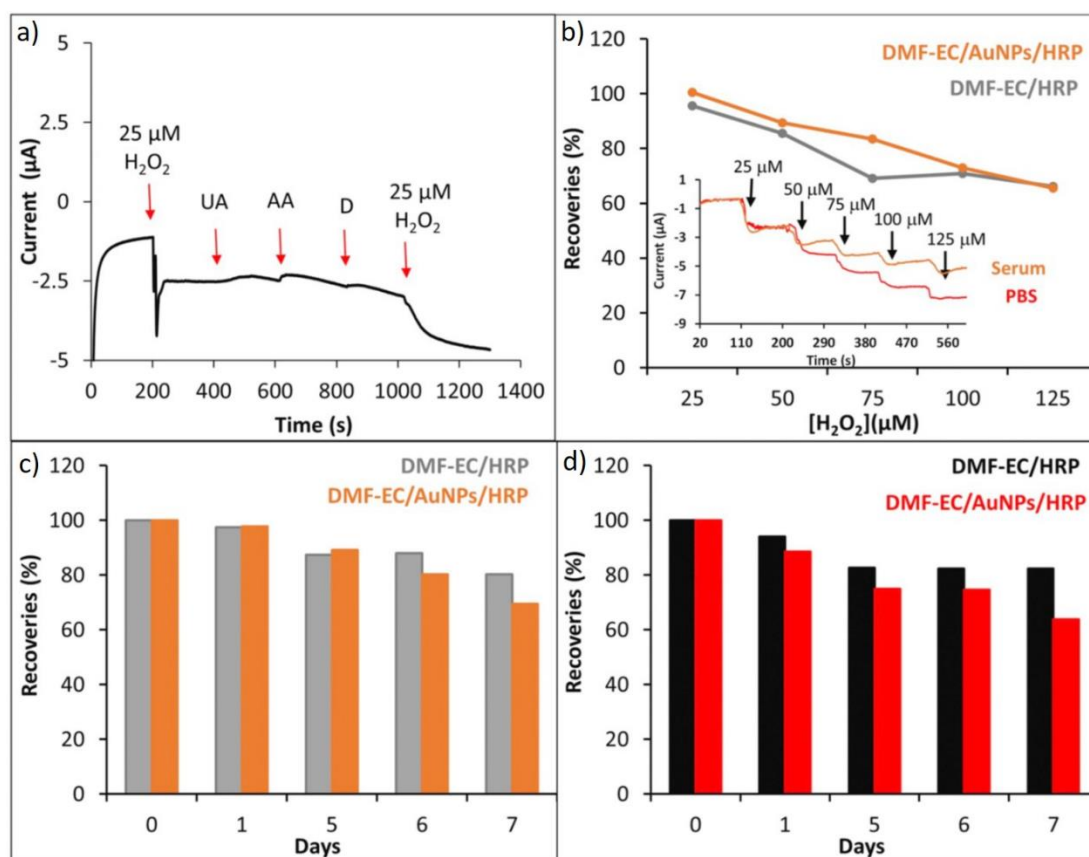
Figure 33 – (**a**) Selectivity assay of DMF-EC/AuNPs/HRP for H_2O_2 analysis in the presence of 50 µM of uric acid (UA), ascorbic acid (AA), and dopamine (D). (**b**) Accuracy assay of DMF-EC/AuNPs/HRP and DMF-EC/HRP) for H_2O_2 detection. Long-term stability response of 3D DMF-EC/HRP and 3D DMF-EC/AuNPs/HRP biosensors for 25 (**c**) and 50 (**d**) µM H_2O_2 detection. Reproduced with permission from (258).

Leigh et al. (259) used a PCL/carbon black (CB) composite filament to manufacture electronic sensors capable of detecting mechanical flexing and capacitance changes, using a low-cost 3D printer. The filler ratio was defined considering the percolation threshold and the melt viscosity of the composite, the final chosen loading of CB was 15 wt.%. Through resistivity tests, the authors verified the existence of a piezoresistive behaviour, enabling its use in the field of biomechanics. The sensors also have a capacitive behaviour when printed as part of an interface device or embedded inside a "smart" vessel, making it possible to detect the presence and quantity of a liquid inside (259).

Kadimisetty and co-workers (260) produced PCL/graphene (10 wt.%) electrodes using a KIMM SPS1000 bioplotter extrusion printing system. These electrodes presented robustness, flexibility, biodegradability, and conductivity required for the electrochemical studies. Before the electrochemical experiment, the electrode was immersed in DMF solvent for 10 min to remove the PCL that blocked the graphene layer, allowing an ideal contact between the graphene and the electrolytes. Biocompatibility

was demonstrated by the electrochemical response derived from the diatom microalgae grown on the PCL/graphene substrate. The produced electrode offers a great potential in electrical stimulation to promote tissue formation, as well as in bioelectronic applications (260).

2.2.5 Conclusions

The manufacture of 3D printed devices is an emerging multidisciplinary field, namely in the biomedical area. In this review, the whole 3D printing process was presented, from the preparation of composites to the most used techniques for printing graphene-based polymer composites for biomedical applications. The properties of the reported graphene-based composite structures have shown significant improvement over polymer matrices without reinforcement, and enhancement of cell response.

3D printing demonstrated the versatility to build complex shapes and custom designed parts, revolutionizing the development of complex structures with target properties, as compared to conventional manufacturing methods. The processing of graphene-based polymer composites with the recent AM technologies has enormous potential for several biomedical applications, namely, to engineer distinct tissues such as bone, cartilage, or the nervous system, as demonstrated by the examples discussed in section 2.2.4, and also other tissues such as tendon, ligament, spinal cord or cardiac tissue, which could potentially benefit from the electrical properties conferred by graphene. The development and integration of biosensors is also a growing application of such 3D printed graphene-based nanocomposites, with promising results, as shown in this review.

CHAPTER **3**

Poly (Lactic Acid)/Graphite Nanoplatelet

Nanocomposite Filaments for Ligament Scaffolds

This chapter in based on the article:

Silva M, Gomes C, Pinho I, Gonçalves H, Vale AC, Covas JA, Alves NM, Paiva MC. Poly(Lactic Acid)/Graphite Nanoplatelet Nanocomposite Filaments for Ligament Scaffolds. Nanomaterials. 2021, **11**, 2796. https://doi.org/10.3390/nano11112796

3 Polylactic Acid/Graphite Nanoplatelet Nanocomposite Filaments for Ligament Scaffolds

The anterior cruciate ligament is one of the most prone to injury in the human body. Due to its insufficient vascularization and low regenerative capacity, surgery is often required when it is ruptured. Most of the current TE strategies are based on scaffolds produced with fibers due to the natural ligament's fibrous structure. In the present work, composite filaments based on PLA reinforced with graphite nanoplatelets (PLA+EG) as received, chemically functionalized (PLA+f-EG), or functionalized and decorated with silver nanoparticles (PLA+[(f-EG)+Ag]) were produced by melt mixing, ensuring good filler dispersion. These filaments were produced with diameters of 0.25 mm and 1.75 mm for textile-engineered and 3D-printed ligament scaffolds, respectively. The resulting composite filaments are thermally stable, and the incorporation of graphite increases the stiffness of the composites and decreases the electrical resistivity, as compared to PLA. None of the filaments suffered significant degradation after 27 days. The composite filaments were processed into 3D scaffolds with finely controlled dimensions and porosity by textile-engineered and additive fabrication techniques, demonstrating their potential for ligament TE applications.

3.1 Introduction

Ligaments are formed by dense collagenous tissues that connect bones, allowing body motion and assuring joint stability, and are constantly exposed to mechanical loadings (85, 115). Adult ligaments exhibit poor healing capacity and limited vascularization (115). In particular, injuries of the ACL are common and particularly frequent in the young and physically active population (7, 85), and often require surgical intervention (7). The recurring complications of current grafts have prompted a growing interest in the development of novel materials and TE solutions for ACL reconstruction (77).

Most current scaffolds are essentially composed of fibers (85), mimicking the architecture and the biomechanical properties of native ligament tissue (12). The major variations between scaffolds relate to the fiber geometrical organization (17), most of them being produced by textile techniques such as braiding, twisting or knitting (17, 18, 22). The current demands for easier, faster and customizable solutions prompted the search for 3D printing approaches (118, 129).

PLA and its derivatives are accepted as safe for humans, several PLA-based formulations being already approved by the FDA for clinical applications such as sutures, scaffolds, cell carriers and drug

delivery systems (261). PLA has low immunogenicity and may cause only a slight or mild reaction to the foreign body (38, 82, 83). However, its mechanical response is poor, making it difficult to mimic the ligaments properties. Thus, PLA-based hybrid composites have been widely adopted to produce fibers and fibrous scaffolds with enhanced properties (45, 91).

Graphene presents outstanding mechanical, thermal and electrical properties (228). The use of graphene-based materials such as GNPs, carbon nanotubes (CNTs), or graphite nanoflakes, has been effective to reinforce PLA and other polymer matrices (116, 262). The resulting composites are expected to exhibit enhanced mechanical, electrical and thermal properties (228, 263), increasing their potential use in different biomedical applications, such as biosensing, drug delivery and tissue engineering (264, 265). For example, Pinto *et al* (116) produced nanocomposites containing PLA/COOH functionalized carbon nanotubes (CNTs-COOH) and PLA/GNPs and reported that the carbon nanostructures improved the mechanical properties of the corresponding PLA composites, approaching the range of ligament properties (116).

The functionalization of graphene is a suitable strategy to enhance its compatibility with a polymeric matrix (266). A covalent functionalization based on 1,3-dipolar cycloaddition reaction of an azomethine ylide (DCA) has been successfully applied to graphene, preserving its inherent structure (267-269). For example, CNTs were functionalized by DCA reaction forming pyrrolidine groups at their surface that reacted with the ester groups of PLA, forming covalent bonds with the polymer. The resulting composites presented higher tensile properties and lower electrical resistivity (263).

The possibility of incorporating antibacterial components into scaffolds may ensure proper healing and postoperative regeneration of the scaffold implantation site (249, 270, 271). Silver nanoparticles have shown to be particularly beneficial for tissue regeneration, not only by preventing the bacterial adhesion and infection, but also by accelerating the healing process and production of extracellular matrix components (270, 272, 273). Functionalized graphene surfaces can be decorated with silver nanoparticles through a reaction based on the reduction of silver ions by N, N-dimethylformamide. This decoration was successfully applied by Silva et al. (274) to amine-functionalized single-walled CNTs.

The aim of this work is the production by melt processing of composite filaments based on PLA reinforced with graphite nanoplatelets, as received, chemically functionalized, and decorated with silver nanoparticles, whilst ensuring good dispersion of the various fillers. All filaments were produced with diameters of approximately 0.25 and 1.75 mm, for the subsequent preparation of textile-engineered and 3D printed scaffolds, respectively. The thermal and mechanical properties, morphology, biodegradation

and structure, as well as suitability for the production of tissue engineering scaffolds by textile-fabrication and additive manufacturing, were assessed.

3.2 Materials and methods

3.2.1 Production of Functionalized Micronized Graphite

Micrograf HC11 (hereafter designated as EG), a graphite subjected to grinding and exfoliation, with a purity of 99.5%, nominal equivalent diameter of approximately 10 μm and few tens of nanometers of thickness, was obtained from Nacional de Grafite Lda (Brazil). The functionalized EG (f-EG) was obtained by using the solvent-free DCA reaction, adapted from the procedure described for CNTs (267). The reagents used were α-amino acid *N*-benzyloxycarbonylglycin (Z-gly-OH, 99%, from Aldrich) and paraformaldehyde, from Sigma-Aldrich, St. Louis, MO, USA, and a small amount of diethyl ether (Fisher Scientific Loughborough, UK) to aid homogenization. The solid mixture was heated for 3 h at 250 °C. The functionalized products were washed with absolute ethanol, hexane (95% n-hexane) and acetone (all from Fisher Scientific, Loughborough, UK), and drying was performed for 2 h at 150 °C in vacuum.

3.2.2 Anchoring of silver nanoparticles onto functionalized exfoliated graphite

The procedure of anchoring silver nanoparticles onto f-EG was adapted from a method described for CNTs (274) consisting on the reduction reaction of silver ions (Ag^+) using N, N-dimethylformamide (DMF, from Panreac, Barcelona, Spain), obtaining (f-EG) + Ag. A total of 140 mg of silver nitrate was mixed with 8 ml of absolute ethanol (both from Fisher Scientific, Loughborough, UK) and left under magnetic stirring, at room temperature, for 15 min. At the same time, 280 mg f-EG was mixed with 16 ml DMF and magnetically stirring, at room temperature, for 15 min. These two suspensions were then mixed together and stirred for 72 h, protected from light, being subjected to ultrasounds for 15 min every 24h. Finally, the product was filtered and washed with diethyl ether and hexane (95% n-hexane) (from Fisher Scientific, Loughborough, UK) and then dried for 2h at 150 °C in vacuum.

3.2.3 Characterization of Functionalized Graphite

Thermogravimetric analysis (TGA) was performed on a Q500 equipment (TA Instruments®, New Castle, DE, USA). EG, f-EG, and (f-EG)+Ag were placed in a platinum crucible and heated from 40–800 °C at 10 °C min^{-1} under a nitrogen atmosphere of 50 mL min^{-1}.

Raman spectra were acquired using a LabRAM HR Evolution Raman spectrometer with a microscope (Horiba Scientific, Piscataway, NJ, USA) using a laser with wavelength of 532 nm and a grating of 600 gr mm^{-1}. The results were analyzed with the Horiba Scientific's Labspec 6 (version 6.4.4) Spectroscopy Suite Software (Horiba France SAS, Longjumeau, France) and the peak positions were determined by applying a baseline (in LabSpec 6).

Scanning electron microscopy (SEM) and energy-dispersive X-ray spectroscopy (EDS) were carried out using a FEI Nova 200 FEG-SEM/EDS (FEI Europe Company, Hillsboro, OR, USA). The samples were previously sputtered with a gold layer, using a sputter coater 108A (Cressington,Watford, UK).

3.2.4 Production of filaments

PLA with a melt flow index of 3 g/10 min (Luminy LX175 from Total Corbion, Gorinchem, The Netherlands) was used as matrix of the composites. Filaments of PLA and PLA with 0.25, 0.5, 1, and 2 wt.% of EG, f-EG, and (f-EG)+Ag were produced with diameters of circa 0.25 mm (FilText) and 1.75 mm (Fil3D), using an intermeshing co-rotating twin-screw extruder (Rondol Microlab, Nancy, France) with a screw diameter of 10 mm and a length-to-diameter ratio (L/D) of 25 (Figure 34), coupled to an extrusion rod die with 2 mm of diameter and two pulling rolls (see Figure 35). The screws comprised three mixing zones separated by conveying elements. The polymer was fed upstream by a volumetric feeder (Piovan MDP1, S. Maria di Sala, VE, Italy) at the rate of 2.81 g.min^{-1} or 0.62 g.min^{-1} for the production of Fil3D and FilText, respectively. The fillers were added manually at the same location, at a rate adjusted according to the desired concentration. The speed of the puling rolls was adjusted to obtain filament diameters of 1.75 and 0.25 mm. The operating parameters used for the production of the filaments Fil3D and FilText are presented in Supplementary Materials Table 18. The PLA was dried for 8 h at 70 °C and 3 h at 100 °C before processing.

Figure 34 – Screw profile used for the production of the composite filaments. The screws comprise three mixing zones separated by conveying elements. Polymer and fillers are fed at the conveying zone upstream. The polymer melts at the first mixing section. The remaining two mixing zones promote dispersive and distributive mixing.
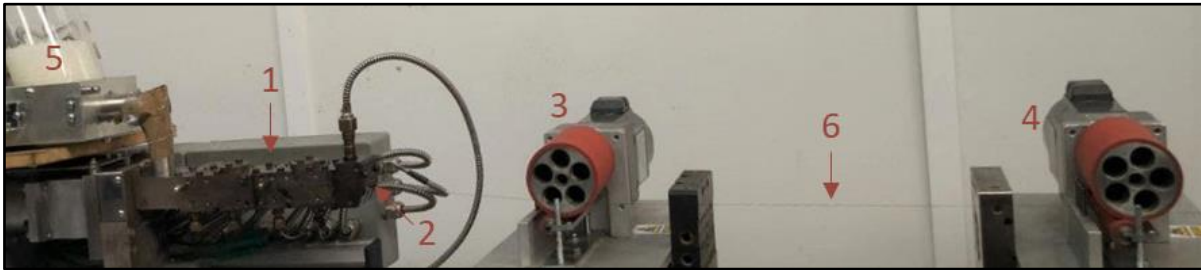
Figure 35 – Extrusion setup: 1–Twin-screw extruder; 2–Extrusion die; 3–Drawing roll 1; 4–Drawing roll 2; 5–feeder; 6–filament

3.2.5 Characterization of the composite filaments

The filaments were analyzed on a LabRAM HR Evolution Raman spectrometer (Horiba Scientific, Piscataway, NJ, USA) equipped with a laser with wavelength of 532 nm and a grating of 600 gr mm^{-1}. The results were analyzed with the LabSpec6 (version 6.4.4) software.

TGA analysis was carried out on Q500 equipment (TA Instruments®, New Castle, DE, USA). The samples were placed in a platinum crucible and heated from 40–800 °C at 10 °C min^{-1} under a nitrogen atmosphere of 50 mL min^{-1}. The filaments' cross-sections were analyzed by SEM, using a FEI Nova 200 FEGSEM/EDS (FEI Europe Company, Hillsboro, OR, USA). Composite filaments with (f-EG)+Ag were also analyzed by EDS, using the same equipment.

Cross-sections with 3 μm thickness of each type of filament were cut with a Leica EMUC6 ultramicrotome and placed over a glass coverslip with Canada balm. Due to the reduced diameter, FilText filaments were embedded in epoxy to facilitate sample microtoming. Then, the cross-sections were analyzed on an Olympus BH-2 optical microscope using a 40× objective, in transmission mode. The images obtained from OM were then analyzed with the ImageJ software for statistical analysis.

Differential scanning calorimetry (DSC) measurements were performed on a DSC 200 F3 Maia (Netzsch-Gerätebau GmbH, Selb, Germany) under a constant flow of nitrogen. The samples were heated from 30–190 °C at 5 °C min^{-1}, cooled and then reheated up to 190 °C, at the same rate. The results were analyzed using the Netzsch Proteus software. The degree of crystallinity (χ_c) of PLA and composite filaments was calculated by:

$$\chi_c\ (\%) = \frac{\Delta H_m}{\varphi_{PLA} \times \Delta H_m{}^0} \times 100 \qquad (1)$$

where, ΔH_m is the enthalpy of fusion (J g^{-1}), φ_{PLA} is the weight fraction of PLA in the composites, and $\Delta H_m{}^0$ is the standard enthalpy of PLA for 100% crystallinity, considered equal to 93.7 J g^1(275).

Dynamic mechanical analysis (DMA) tests were carried out using Tritec 2000 B equipment (Triton Technology, Grantham, UK), equipped with the tensile mode and a grip distance of 15 mm. Filament samples were cut with a length of approximately 30 mm. The diameter of each sample was measured on three different places along the filament length, using a micrometer (Mitutoyo, Kawasaki, Japan). The tests were carried out between 10 °C and 70 °C, with a step of 2 °C. A static pre-load of 1 N was used and the measurements were made at a frequency of 1Hz, which corresponds to the physiological loading frequency defined as an ASTM standard frequency to determine T_g (ASTM E1640–07) (276). At least three specimens were tested for each composition.

The electrical resistivity of the composite filaments was measured on a Keithley SMU 2635B SourceMeter® (Keithley Instruments Inc., Cleveland, OH, USA). The test specimens were cut with 20 mm length and their diameter was measured on three different places along the filament length, using a micrometer (Mitutoyo, Kawasaki, Japan). Each sample was clamped by the electrodes and the current across the test specimen was measured with the application of a 10 V potential.

To assess the biodegradation, composite filaments with 0.25 and 0.5 wt.% of fillers, previously dried and weighed, were immersed in PBS and stored in an incubator at 37 °C for 7, 14, 21, and 28 days. Every two days the PBS solutions were replaced by fresh solutions; the filaments were removed from the PBS, washed with distilled water, dried, and weighed. The weight loss was calculated by:

$$Weight\ loss\ (\%) = \frac{m_i - m_f}{m_i} \times 100 \qquad (2)$$

where m_i is the weight of the filament before immersion in PBS and m_f is the dry weight of the filament at each time. Each experiment was repeated three times.

3.2.6 Scaffold production and characterization

Braided and 3D-printed scaffolds were manufactured using FilText and Fil3D reinforced with 0.5 and 2 wt.% of fillers to evaluate their potential usefulness for scaffold production.

Three-dimensional-printed scaffolds were designed using the Ultimaker Cura software and produced by an Ender-3 3D Printer adopting the following parameters: infill density of 50%, infill linear pattern (0 and 90 °C), and a layer height of 0.15 mm. The build platform was set to 80 °C, the nozzle temperature to 185 °C, and the printing speed to 45 mm.s^{-1}. The textile-engineered scaffold was produced through a *kumihimo* hand braiding technique, with a circular stand. The scaffold is formed by an exterior braided structure formed by 8 FilText and an inner part containing 4 pairs of bundles. The bundles were aligned in parallel and tied together with a suture of the same material and each was formed by 8 braided FilText. Both scaffolds exhibit approximately 32 mm of length and 9 mm of diameter, similar to the dimensions of the native ACL.

The scaffolds were analyzed using the Digital Microscope Leica DMS1000 in order to identify their morphology and qualitatively estimate the shape, size, and distribution of the pores. Images were collected with a magnification of 1.6x.

3.3 Results and Discussion

3.3.1 Functionalization of Graphite

The functionalization of EG to form f-EG was carried out using a 1,3 dipolar cycloaddition reaction of an azomethine ylide. This reaction is expected to functionalize the EG surface by covalent bonding pyrrolidine (cyclic amine) groups without structural damage to the EG (267). The cyclic amine may react with PLA under melt processing conditions, establishing a strong interface that enhances stress transfer from the polymer to the reinforcement (263). This process is represented in Figure 36.

Silver nanoparticles were anchored onto f-EG through a reaction based on the reduction of silver ions by DMF (274). At the end of this step, silver decorated f-EG ((f-EG)+Ag) was obtained, as represented in Figure 37.
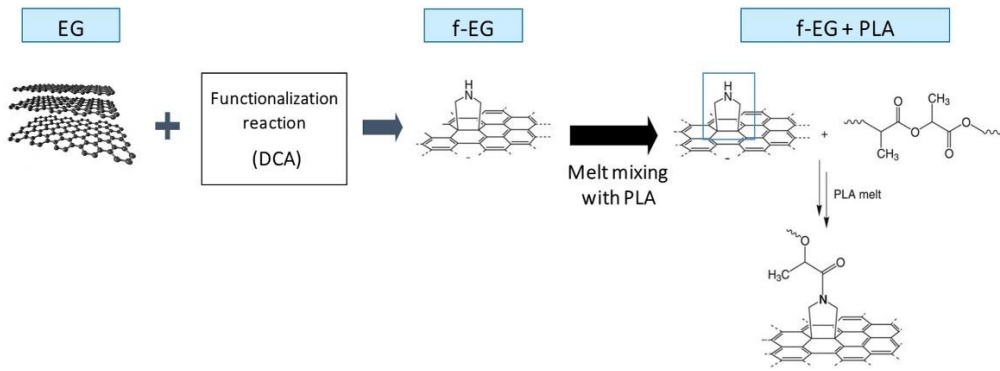
Figure 36 – Schematic representation of the EG functionalization by the DCA reaction, obtaining f-EG as well as its further interaction with PLA under melt processing conditions.
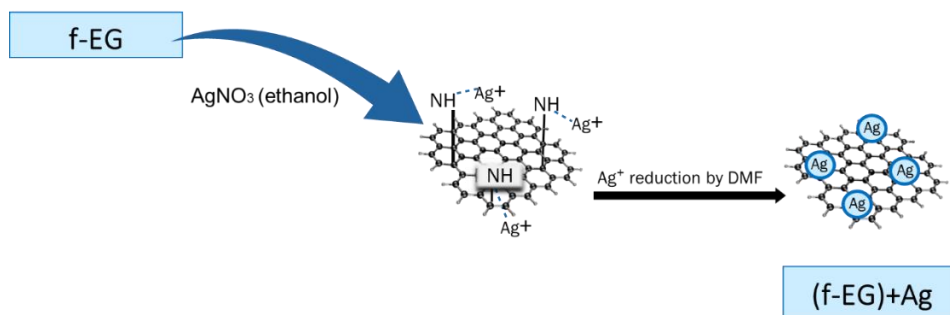
Figure 37 – Schematic representation of the decoration of f-EG with silver nanoparticles, obtaining (f-EG)+Ag.

3.3.2 Characterization of Functionalized Graphite

3.3.2.1 Thermogravimetry

The effect of functionalization on the thermal stability of graphite was assessed by TGA, performed on EG, f-EG and (f-EG)+Ag. The results are presented in Figure 38.
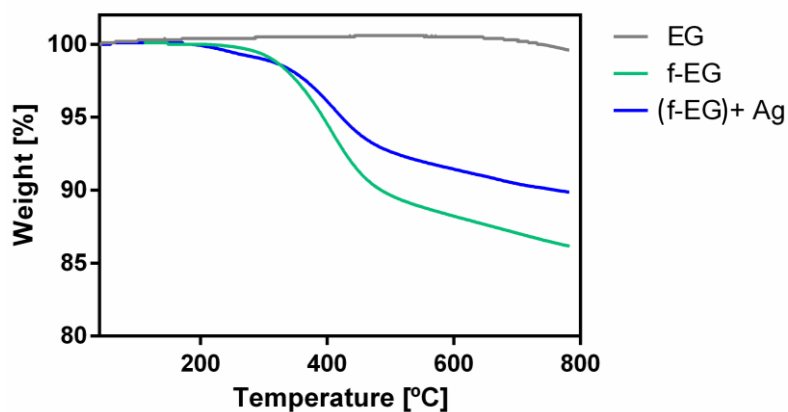
Figure 38 – TGA curves for pristine EG, f-EG and (f-EG)+Ag

The TGA curves of f-EG and (f-EG)+Ag exhibit similar shape. The beginning of thermal degradation is observed at a lower temperature for (f-EG)+Ag, but their weight loss at 800°C is lower than hat observed for f-EG. As shown by Silva et al. (266), pristine EG is thermally stable in the analyzed temperature range, as expected for pristine materials with low contamination level. Thus, the weight loss observed is due to the thermal degradation of the organic moieties bonded to EG through the DCA reaction. Since (f-EG)+Ag was expected to have the same organic groups that were bonded in f-EG, the weight loss difference between f-EG and (f-EG)+Ag results from the silver nanoparticle residue that remains stable within the temperature range of the TGA tests. This indicates a successful functionalization of EG and addition of Ag nanoparticles. The weight loss of EG, f-EG, and (f-EG)+Ag was 0.4, 13.8, and 10.1, respectively. The functionalization yield was 13.4 wt.% and silver nanoparticle content was 3.7 wt.%.

3.3.2.2 Raman Spectroscopy

The Raman spectra of graphite and graphene derivatives typically exhibits three characteristic bands designated by D, G and 2D (Figure 39) (180). The D band, located at 1350 cm^{-1}, indicates the presence of sp^3 carbon atoms, demonstrating the existence of defects in the sp^2 hybridized carbon lattice. The G band, near 1580 cm^{-1}, results from in-plane vibration of the ordered sp^2 bonded carbon atoms (277, 278). The normalized Raman spectra of EG, f-EG and (f-EG)+Ag allowed the measurement of the intensity ratio of D and G bands (I_D/I_G) (see Table 16).
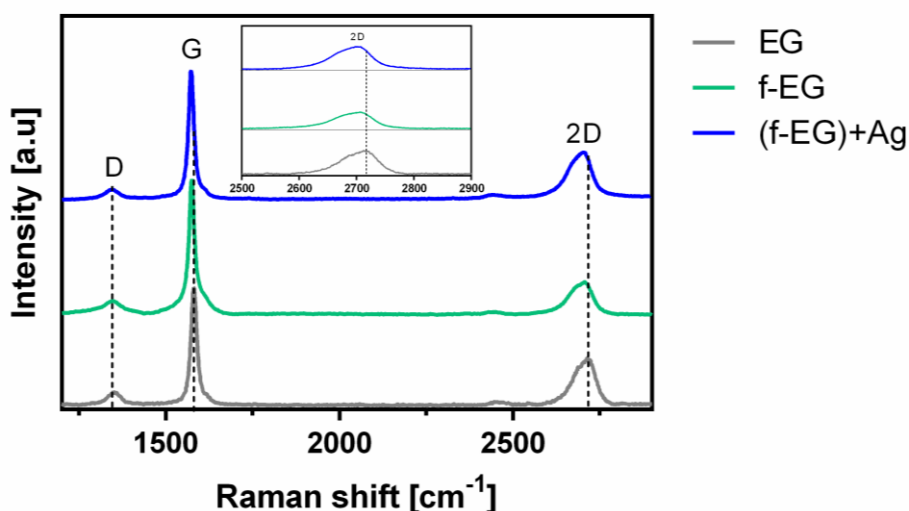
Figure 39 – Raman spectra of pristine EG, f-EG and (f-EG)+Ag

The I_D/I_G ratio is 0.24, 0.10, and 0.13 for EG, f-EG, and (f-EG)+Ag, respectively. The low I_D/I_G ratio is indicative of few defects in the pristine graphite structure. Moreover, the I_D/I_G ratio decreased from 0.24 to 0.10 after functionalization, indicating fewer defects present in the f-EG compared to the pristine EG. This may result from the functionalization method, consisting of the cycloaddition reaction to the graphite C–C double bonds, which may lead to the selection of the less defective graphite flakes (279). Additionally, although sp^3 carbon is generated by functionalization, the reaction does not damage the graphene structure, keeping the hexagonal lattice. Finally, the EG material remaining with a low degree of functionalization, or not functionalized, may be separated during the washing and sonication procedures, leaving mostly the functionalized material (f-EG). With the addition of silver nanoparticles, the I_D/I_G intensity ratio between f-EG and (f-EG)+Ag was maintained or slightly increased, which may indicate incipient disturbance of the in-plane sp_2 carbon lattice (266) due to the addition of Ag nanoparticles to the graphene layers. Nevertheless, this is a negligible variation.

Table 15 – Data obtained from the Raman spectra of the composite filaments

	I_D/I_G	2D-band [cm^{-1}]
EG	0.24	2717
f-EG	0.10	2706
(f-EG)+Ag	0.13	2698

The 2D band observed near 2700 cm^{-1} correlates with the quality of graphene and with the number of layers of graphene by the shape, width, and position of the peak (180). This band is at double the frequency of the D band (223). As Zhu et al. (180) and Ferrari et al. (280) reported in their studies, with an increasing number of layers the 2D peak moves to higher wavenumbers and becomes broader, while pure graphene exhibits a single sharp 2D peak with higher intensity relative to the G peak (280). In Figure 39, a shift of the 2D peak wavenumber is observed, decreasing from 2717 cm^{-1}, for EG, to 2706 and 2698 cm^{-1}, for f-EG and (f-EG)+Ag, respectively. This observation is consistent with the selective functionalization of the thinner and structurally more perfect pristine EG flakes. Besides, the deposition of silver nanoparticles on functionalized graphite also shifted the 2D band towards lower wavenumbers, which may suggest a charge-transfer process and chemical interaction between the Ag nanoparticles and the graphene surface after the deposition process, as reported in previous works (281).

3.3.2.3 Scanning Electron Microscopy

The graphite morphology was characterized by SEM, the images of (a) pristine EG, (b) f-EG and (c) (f-EG)+Ag, being displayed in Figure 40, evidencing that the graphite morphology was maintained after functionalization. EDS tests were performed for (f-EG)+Ag and are presented in Figure 51 (Supplementary Materials), showing the presence of Ag on the graphite surface.
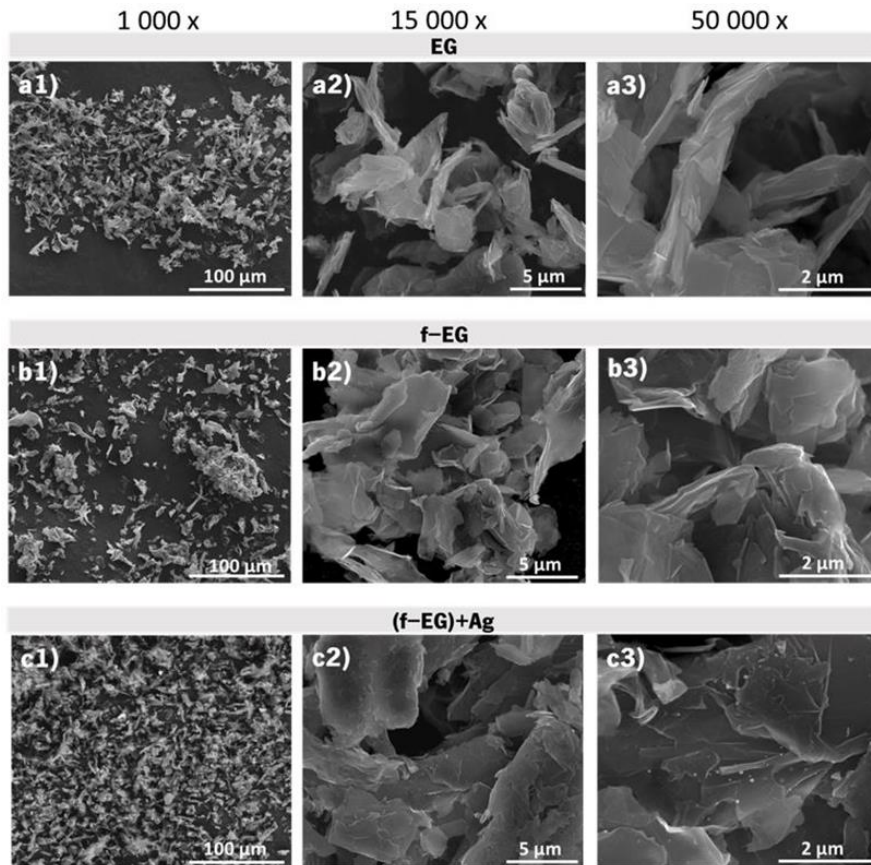
Figure 40 – SEM images for pristine EG at different magnifications: (**a1−a3**); f-EG: (**b1−b3**) and (f-EG) + Ag: (**c1−c3**).

3.3.3 Characterization of the composite filaments

3.3.3.1 Macroscopic characterization

Figure 41 presents the filaments produced by melt-mixing, namely of PLA, PLA+0.5[(f-EG)+Ag] and PLA+2[(f-EG)+Ag] of FilText (Figure 41: a1– a3, respectively) with an average diameter of 0.26±0.03 mm and Fil3D (Figure 41: b1– b3, respectively), with an average diameter of 1.71±0.07 mm. All filaments exhibited good filler dispersion and a flexibility suited to the intended application. Their thermal, mechanical and electrical properties are presented and discussed below.
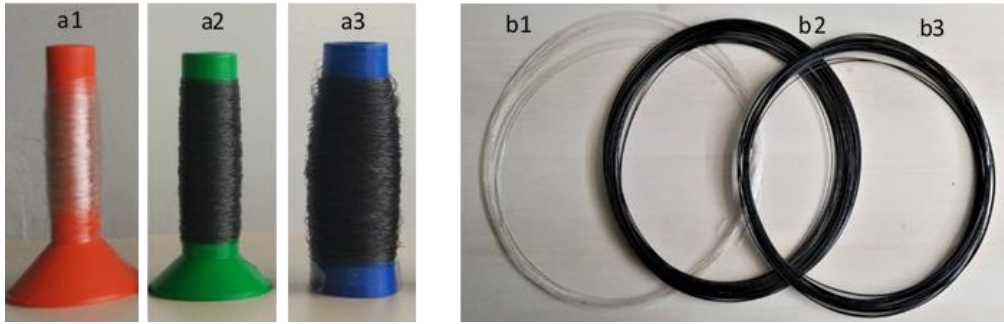
Figure 41 – Composite filaments: FilText (**a1** – PLA; **a2** – PLA+0.5[(f-EG)+Ag]; **a3** – PLA+2[(f-EG)+Ag]) and Fil3D (**b1** – PLA; **b2** – PLA+0.5[(f-EG)+Ag]; **b3** – PLA+2[(f-EG)+Ag]).

3.3.3.2 Thermogravimetric Analysis

The thermal stability of Fil3D and FilText as well as their nanoparticle weight composition were assessed by TGA. Thermal stability is an important factor due to its impact on melt processing, as well as on the end-use applications. The analysis of the thermograms of Fil3D and FilText presented in Figure 42a,b shows a single step degradation for all the compositions in the range of 300–400 °C, which occurs due to the decomposition of the PLA and functional organic groups of f-EG and (f-EG)+Ag.

Above 400 °C the weight loss stabilizes, reaching a plateau, and showing a higher residual weight of the composite filaments as compared to the PLA filament. Graphene-based materials are known for their high thermal stability under inert atmosphere, thus allowing the estimation of the filler composition by residual weight analysis.

Table 16 presents the temperature at the onset of thermal degradation, as well as the residual weight measured at 800 °C. It is observed that PLA and composites present similar thermal stability, in agreement with results reported before by Paiva et al. (267) for composites with PLA and CNTs.

The residual weight percent increases with increasing reinforcement concentration and is within the nominal range, except for the composition of PLA+2EG for Fil3D and PLA+2[(f-EG)+Ag] for FilText, where the effective composition is considerably lower than the nominal value. More than five TGA tests were carried out for each composition, showing a significant variation in the final residue values. This variation is possibly due to the manual feeding of the extruder during composite preparation by melt mixing.
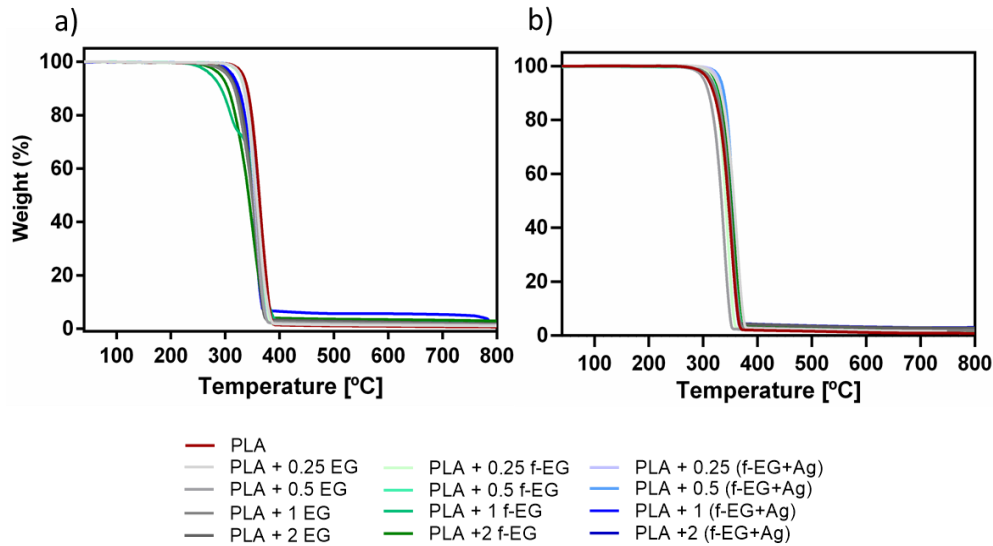
Figure 42 – TGA thermograms of (**a**) Fil3D and (**b**) FilText

Table 16 – Initial degradation temperatures of composite filaments

Filament		Fil3D		FilText	
		T_{onset} (°C)	Residue (wt.%)	T_{onset} (°C)	Residue (wt.%)
PLA		351	-	301.6	-
PLA+0.25	EG	347	0.43 ± 0.21	318	0.20 ± 0.25
PLA+0.5		342	0.74 ± 0.22	295	0.39 ± 0.31
PLA+1		342	1.02 ± 0.88	307	1.14 ± 1.30
PLA+2		328	1.44 ± 0.37	301	2.34 ± 1.74
PLA+0.25	f-EG	342	0.23 ± 0.25	310	0.48 ± 0.74
PLA+0.5		339	0.73 ± 0.16	310	0.36 ± 0.58
PLA+1		342	1.13 ± 1.17	307	1.15 ± 0.26
PLA+2		328	2.00 ± 0.96	312	2.18 ± 1.72
PLA+0.25	(f-EG)+Ag	343	0.26 ± 0.14	323	0.21 ± 0.85
PLA+0.5		344	0.55 ± 0.27	327	0.53 ± 0.44
PLA+1		330	1.43 ± 1.40	309	1.06 ± 1.10
PLA+2		338	2.04 ± 0.85	304	1.02 ± 0.22

3.3.3.3 Scanning Electron Microscopy

The morphology of all filaments and the dispersion of the reinforcement in the polymeric matrix were analyzed by SEM. The images of the cross-sections of composite filaments reinforced with 2wt.% of fillers are presented in Figure 43 and are complemented in the Supplementary Materials Figures 52 and 53. A good dispersion of nanoparticles across the composite and a good interface between PLA and graphite are observed, especially for the smaller particles. The incorporation of Ag nanoparticles does not

significantly affect the filament morphology. SEM images highlighting the presence of silver nanoparticles and EDS analysis confirming their presence in Fil3D and FilText reinforced with (f-EG)+Ag are shown in the Supplementary Materials Figure 54.
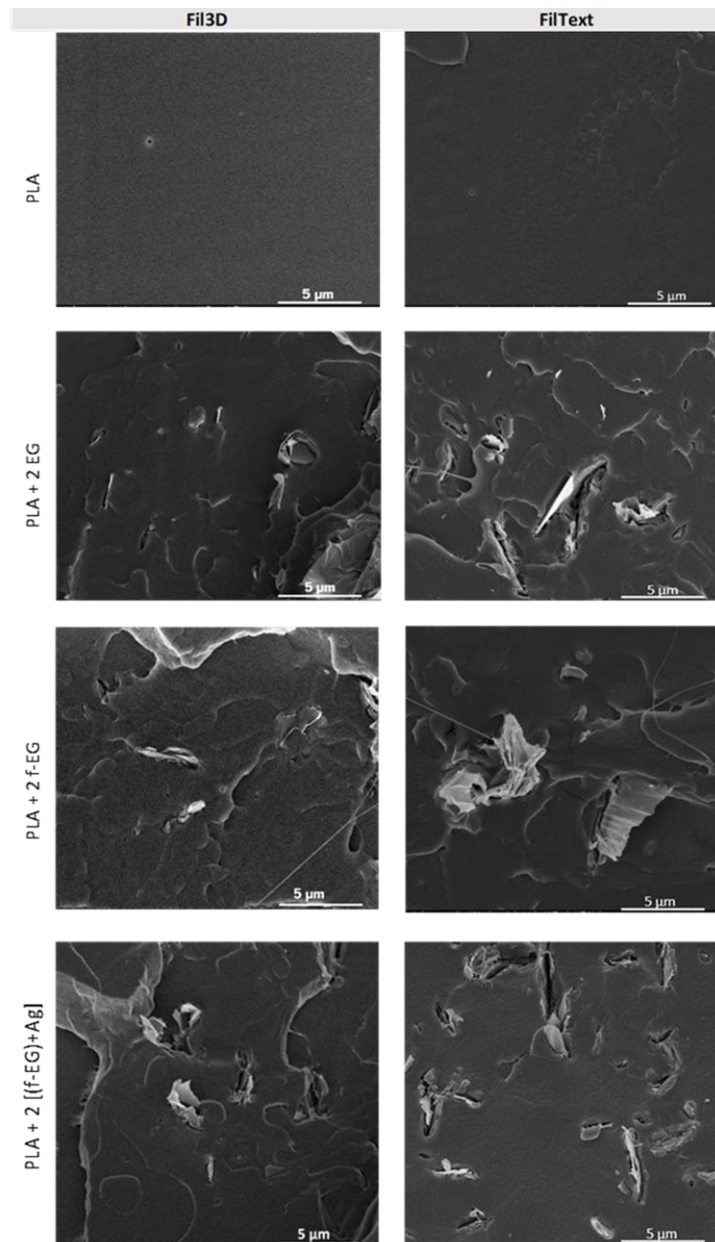
Figure 43 – SEM images of Fil3D and FilText: PLA; PLA+2EG; PLA+2f-EG; PLA+2[(f-EG)+Ag].

3.3.3.4 Optical Microscopy

Figure 44 shows the OM images of the composite filament cross-sections containing 0.5 and 2wt.% of fillers. Images of the composite filament cross-sections at all the compositions of EG, f-EG, and (f-EG)+Ag are displayed in the Supplementary Materials Figures 55 and 56. The statistical analysis of the

average particle size, as well as the number of particles per unit composite area, measured for the composite filaments, is presented in Table 17.

Table 17 – Characterization of Fil3D and FilText's cross-section by optical microscopy

Filament		Average Agglomerate Size (µm²)		Number of Agglomerates (mm⁻²)	
		Fil3D	FilText	Fil3D	FilText
PLA + 0.25		2.97	1.37	2757	11,025
PLA + 0.5		2.34	0.72	6691	11,675
PLA + 1	EG	5.90	7.35	6032	27,244
PLA + 2		6.53	4.92	6223	29,534
PLA + 0.25		5.30	3.52	2390	6523
PLA + 0.5		2.67	1.83	7735	7806
PLA + 1	f-EG	6.95	8.76	3378	12,045
PLA + 2		10.91	3.64	4378	14,813
PLA + 0.25		2.53	3.38	6671	9132
PLA + 0.5	(f-EG) + Ag	4.06	0.60	5154	9749
PLA + 1		11.83	3.66	2992	12,170
PLA + 2		6.69	4.66	6118	20,430

The average agglomerate size is slightly higher for the composites with 1 and 2 wt.% of reinforcement. Generally, filaments with functionalized graphite present a smaller number of agglomerates, except for Fil3D with 0.5 wt.% f-EG and 0.25 wt.% (f-EG)+Ag. However, they also present slightly larger particles, which may result from higher nanoparticle cohesion after functionalization, as observed in SEM images for f-EG. In general, the average agglomerate size tends to be smaller for FilTex filaments, which is a consequence of the higher draw ratio applied during filament production, inducing the alignment of the EG flakes along the filament length, thus showing mainly the thinner flake side on the filament cross-sections. A rough estimate for the lateral size and thickness of one flake, considering a circular flake with 10 µm diameter and 30 nm thickness, is 80 µm² and 0.3 µm², respectively. The average agglomerate areas obtained (Table 17) are much lower than the flat surface area of an average EG flake, which is indicative of considerable flake alignment along the filament axis, in particular for FilTex, and good EG dispersion.
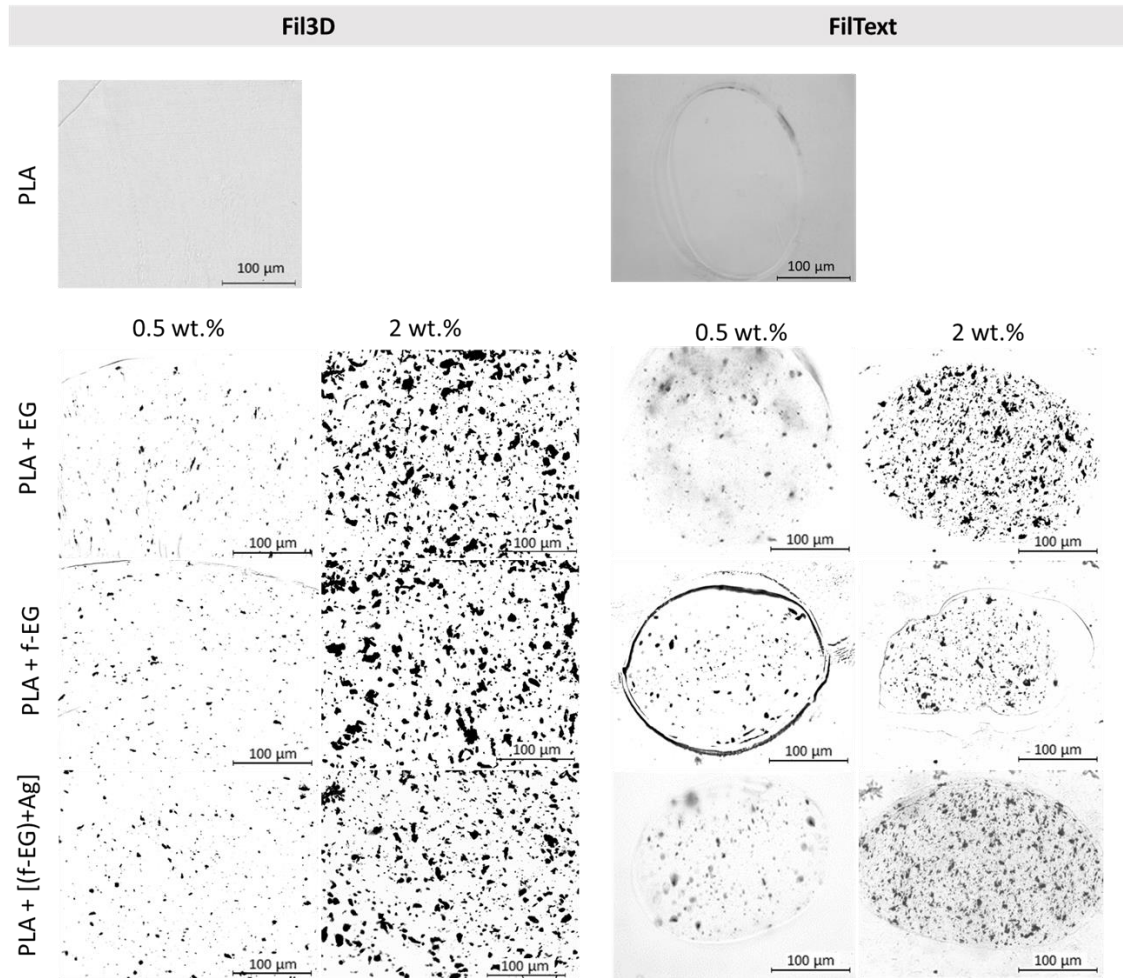
Figure 44 – Optical microscopy images of the filaments' cross-section, namely PLA and PLA reinforced with 0.5wt.% and 2wt.% of EG, f-EG and (f-EG)+Ag.

3.3.3.5 Raman Spectroscopy

Raman spectroscopy was performed on the filaments to further observe the graphite nanoparticles in the composite filaments. As mentioned before, all carbon-based materials show characteristic bands at a specific wavenumber in the Raman spectrum, namely D, G, and 2D bands (278). All Raman spectra of Fil3D and FilText are similar and exhibited these three characteristics bands. Figure 45 presents the Raman spectra of filaments reinforced with 0.5 wt.% of EG, f-EG, and (f-EG)+Ag. PLA also presents prominent bands in the Raman spectrum, thus the wavenumbers of the D, G, and 2D bands of EG, f-EG, and (f-EG)+Ag were highlighted in the spectra. PLA does not show scattering in the region of the G band, and thus the corresponding wavenumber may be used to monitor the presence of graphite in composite filaments.
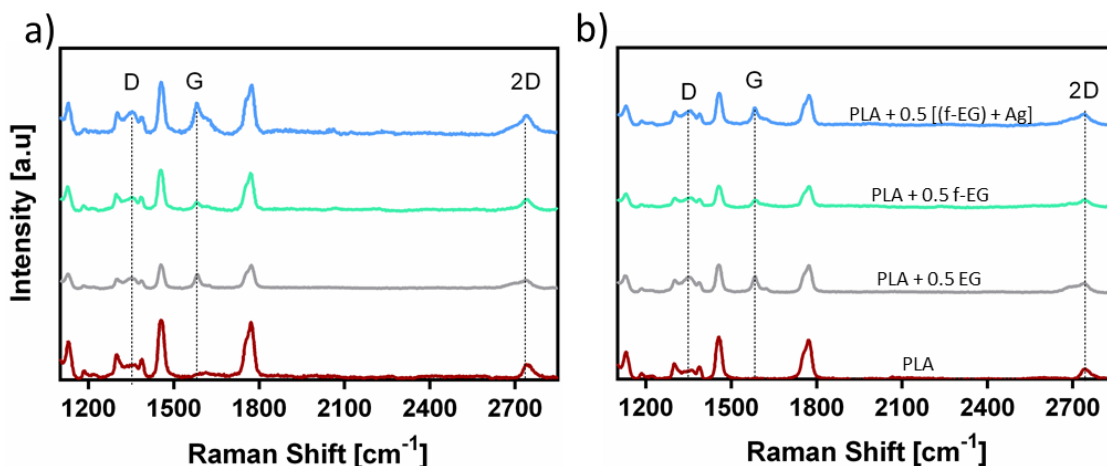
Figure 45 – Raman spectra obtained for (**a**) Fil3D and (**b**) FilText with 0.5wt% of EG, f-EG and (f-EG)+Ag

3.3.3.6 Differential Scanning Calorimetry

The analysis of the DSC results allows the characterization of the thermal behavior of PLA and the influence of filler addition. The relevant thermal characteristics (glass transition temperature, T_g, cold crystallization temperature, T_c, melting temperature, T_m, melting enthalpy, ΔH_m, cold crystallization enthalpy, ΔH_c, and degree of crystallinity, χ_c) of each composition obtained for the first and second heating scans are reported in Supplementary Materials Tables 19 and 20, respectively. Since the Fil3D will be used in additive manufacturing to produce 3D-printed scaffolds involving filament melting, the analysis of the second heating scan has particular interest. It can be seen in Figure 46 that the T_g of the composites for the second heating does not vary significantly compared to PLA and it is approximately 60 °C. Additionally, all compositions exhibited a similar T_m of approximately 158 °C and the double-melting peak, as was observed in PLA composites by other authors (282, 283). Conversely, FilText filaments are used as-produced to manufacture textile-based scaffolds without further heating and thus the analysis of the first heating scan is more relevant. For FilText, the T_g of the first and second heating is approximately 58.3 °C and 58.6 °C, respectively, and it is not significantly affected by the presence of reinforcement. All FilText filaments presented a similar T_m of approximately 160 °C and a double-melting peak. The cold crystallization temperature measured on the second heating scan is shifted to a higher temperature, presenting lower values for the PLA filaments compared to the composite filaments, either Fil3D and FilText. This observation suggests that PLA crystallization is delayed by the presence of the graphite nano-particles, with and without functionalization, as reported in previous works (275). Filaments

101

exhibited low crystallinity, slightly increasing in the second heating with the incorporation of graphite, as was observed by other authors for PLA composites (284).
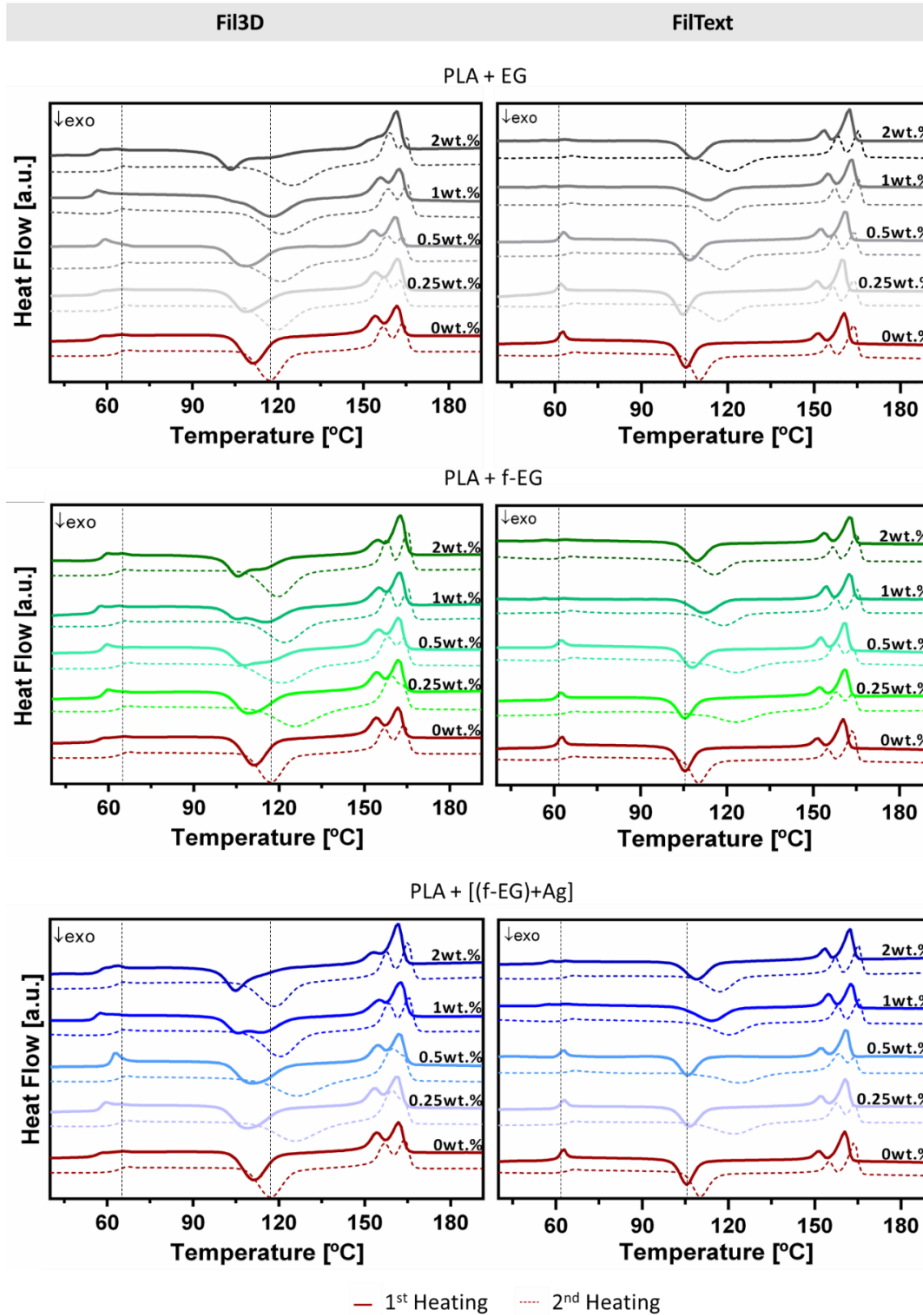
Figure 46 – DSC scans of Fil3D and FilText, namely first and second heating, represented by continuous and dashed lines, respectively. Black dashed vertical lines mark the T_g and T_c of PLA, during the second heating scan of Fil3D and first heating scan of FilText.

3.3.3.7 Mechanical characterization

DMA was used to evaluate the effect of the incorporation of EG, f-EG, and (f-EG)+Ag on the mechanical and viscoelastic properties of the filaments. Figure 47 shows the DMA results obtained as a

function of temperature, at 1Hz (physiological frequency), with (a1) and (a2) representing the storage modulus of Fil3D and FilText, respectively, and (b1) and (b2) the loss factor of Fil3D and FilText, respectively.

As the temperature increases, all compositions show a gradual decrease in the storage modulus (E'), followed by a drop when T_g is reached. The drop in modulus is related to the material transition from the glassy to the rubbery state (285). As expected, the composite filaments present higher E' values compared to PLA (275), and may indicate good interfacial properties allowing the stress transfer at low deformations (285).

The loss factor, or tan δ, expressed as the ratio of the loss modulus to the storage modulus, is a measure of energy loss and provides information about the damping properties of the composites (286). In Figure 47 b1,b2, the tan δ peak observed at about 63–68°C is related to the T_g of the nanocomposites. Except for PLA+0.25[(f-EG)+Ag] of FilText, all composite filaments exhibited higher tan δ values compared to PLA, indicating that they have a higher capacity to dissipate energy and damping. The viscoelastic character of these filaments has particular relevance for the application, since ligaments also exhibit a viscoelastic behavior (287).
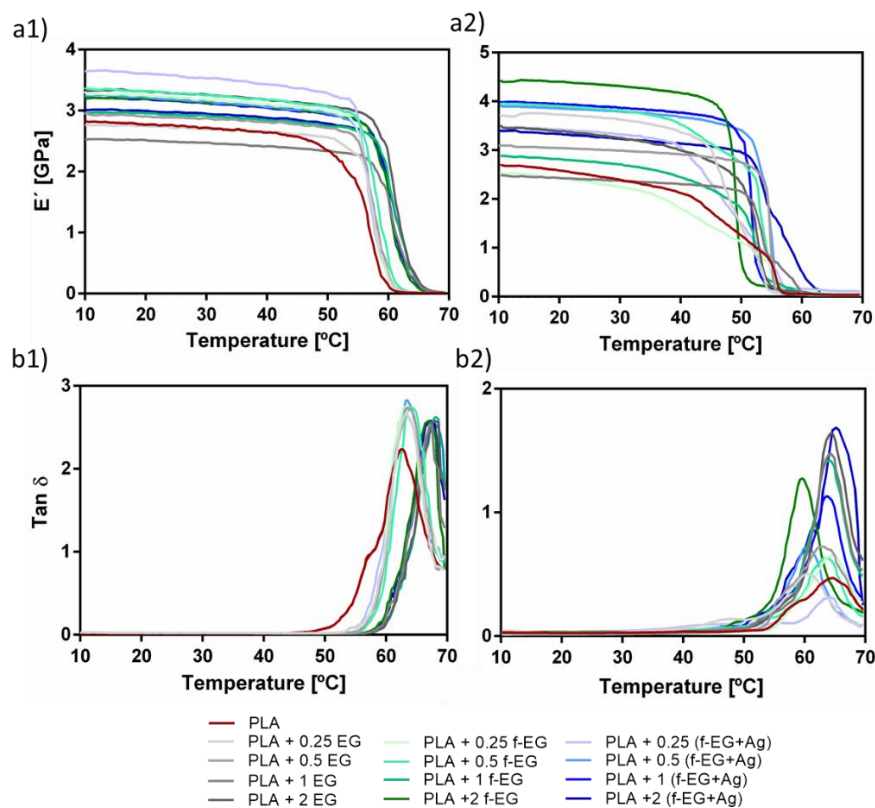
Figure 47 – DMA spectra for the E' of (**a1**) Fil3D and (**a2**) FilText, and tan δ of (**b1**) Fil3D and (**b2**) FilText, as a function of the temperature, ranging from 10–70 °C.

The analysis of E' at body temperature is presented in Figure 48, showing that most of the composite filaments present higher E' compared to PLA.
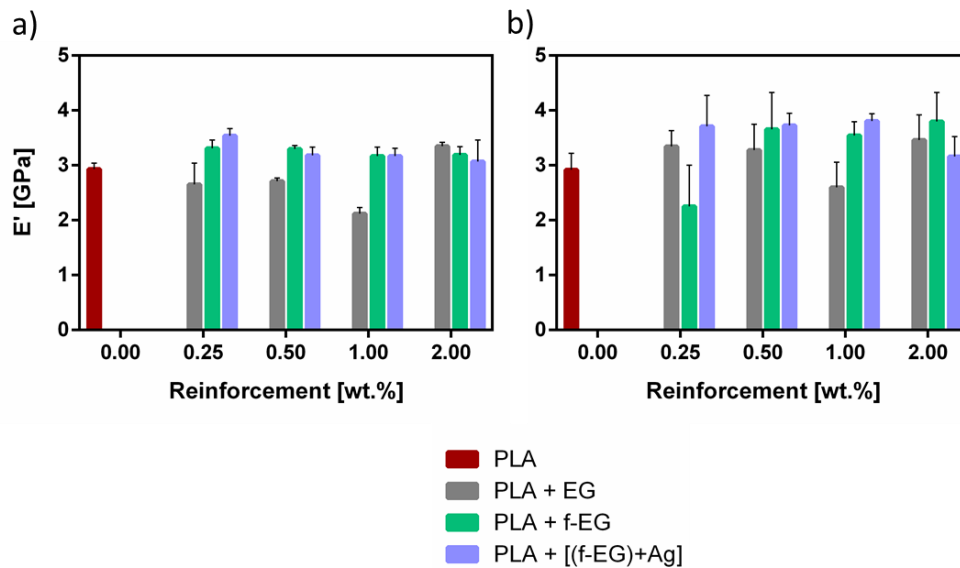
Figure 48 – Storage modulus at 37 °C of (**a**) Fil3D and (**b**) FilText.

3.3.3.8 Electrical resistivity

The electrical properties of materials for TE applications are quite relevant, considering their influence on cell adhesion and growth (288). The application of electrical fields (static and pulsing) has been widely used in orthopedic practices, namely to improve tendon (289) and ligament (290) healing and repair. ACL fibroblasts demonstrated enhanced migration speed and perpendicular alignment to applied electric fields (290).

The homogeneous dispersion of the electrically conductive graphite nanoparticles in PLA is expected to decrease the electrical resistivity of the composite (291). Figure 49 shows the electrical resistivity of the composites as a function of the graphite content for (a) Fil3D and (b) FilText. The electrical resistivity of PLA is in the order of 10^{12} Ω·m, as reported in the literature (275, 292). The electrical resistivity of the composite filaments was determined by measuring the current after applying a voltage of 10 V. It is observed that the electrical resistivity decreases with the incorporation of EG, f-EG and (f-EG)+Ag, as reported in previous studies (263, 291, 293). Although the composite nanoparticle concentrations are far from the electrical percolation threshold, a decrease in electrical resistivity of four orders of magnitude for Fil3D and five orders of magnitude for FilText filaments is observed. The thinner filaments present lower electrical resistivity for all graphite concentrations except for the lower

concentration of pristine EG, showing that the morphology of the nanoparticle distribution was affected by the drawing conditions. The presence of graphite nanoparticles in the composite filaments, even far from the electrical percolation level, may provide a positive effect on the cellular response by allowing localized electron mobility, as re-ported in previous works (236-238).
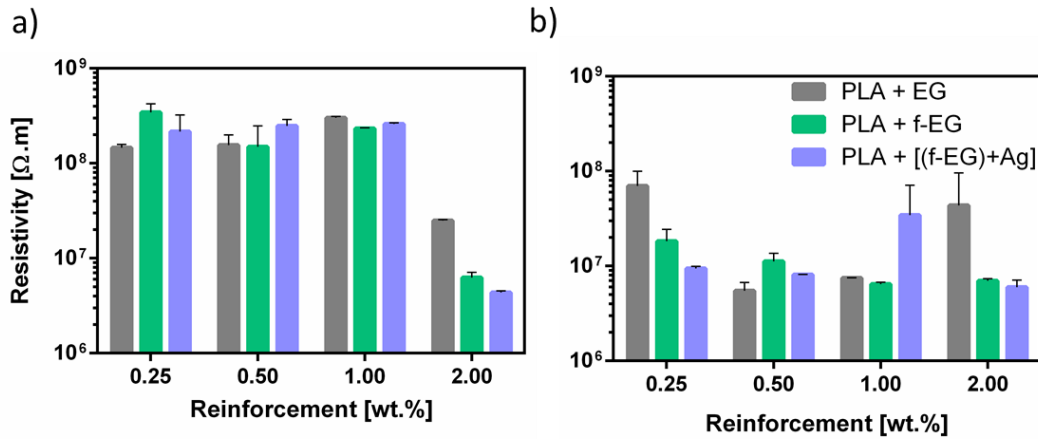
Figure 49 – Electrical resistivity of (a) Fil3D and (b) FilText, as a function of the reinforcement.

3.3.3.9 Monitoring degradation

PLA and all the composite filaments were immersed in a PBS solution at 37 °C, mimicking natural body fluids, for 7, 14, 21, and 28 days. The obtained results are detailed in Supplementary Materials Table 21. PLA did not exhibit any degradation after approximately one month in PBS, and the addition of carbon nanoparticles did not affect its degradation behavior, which is an important feature for the intended application due to the ACL's poor healing capacity and long recovery periods (24), as it takes at least 6–9 months for complete regeneration (9, 10, 41).

3.3.4 Scaffold Production and Characterization

The scaffolds were produced to demonstrate the processability of the composite filaments FilText and Fil3D, their detailed characterization being the focus of future work.

Braided and 3D-printed scaffolds were manufactured using FilText and Fil3D filaments, respectively, as described above. The production of 3D-printed scaffolds was faster, easier, and more reproducible compared to braided scaffolds. While the operating conditions for 3D printing were similar

for both PLA and its composites, obtaining braided scaffolds was lengthier and more difficult for PLA braids, which lacked the flexibility of composite FilText.

Figure 50 illustrates the scaffolds produced by 3D printing and textile engineering, using PLA and PLA+0.5[(f-EG)+Ag] filaments. Observation with a digital microscope shows their porous structure and suitable shape. The composite scaffolds presented a morphology and pore size similar to those of neat PLA scaffolds. A preliminary assessment indicates a porosity greater than 60% for all scaffold compositions, which is appropriate for the intended application.
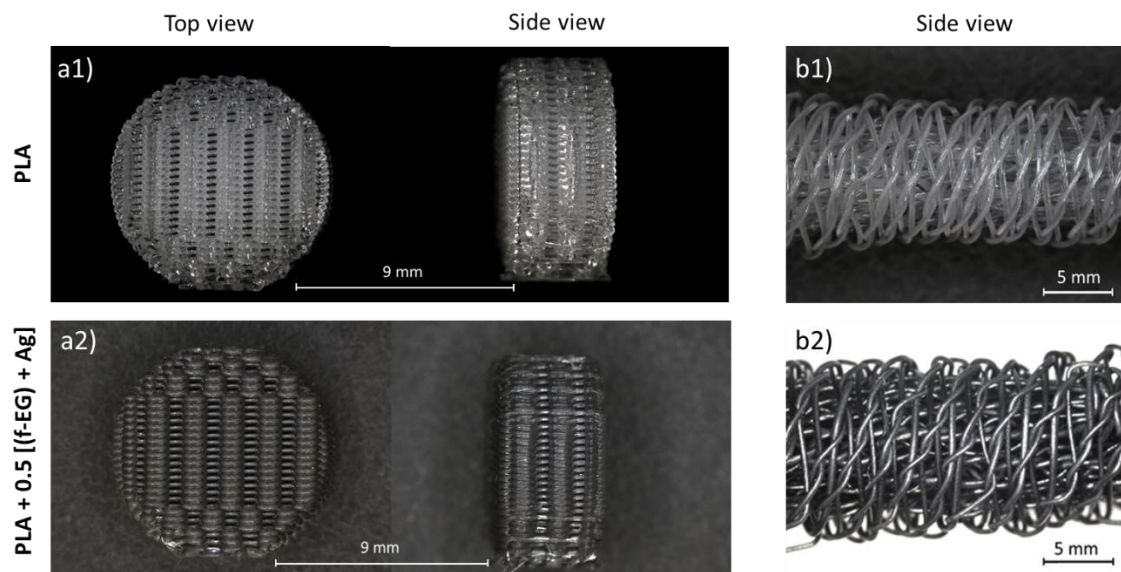
Figure 50 – Stereoscopic magnifying glass images of PLA scaffolds obtained by (**a1**) 3D printing and (**b1**) textile-engineering and of PLA+0.5[(f-EG)+Ag] scaffolds obtained by (**a2**) 3D printing and (**b2**) textile-engineering.

3.3.5 Conclusions

Composite filaments based on PLA reinforced with EG, f-EG, and (f-EG)+Ag were produced by melt processing with diameters of 0.25 and 1.75 mm for the preparation of textile-engineered and 3D-printed scaffolds for ligament application, respectively. All filaments exhibited a good dispersion of the fillers and interaction with the polymeric matrix. The filaments were thermally stable up to 130 °C in the presence of EG and functionalized EG. In general, the storage modulus of the composite filaments is approximately 3 GPa or greater at 37°C, with tan δ values higher than those observed for PLA filaments, indicating that the addition of functionalized graphite increases the stiffness of the composites and provides a higher capacity to dissipate energy and damping. The incorporation of fillers led to a decrease in the electrical resistivity relative to neat PLA up to five orders of magnitude, with the composites with 2 wt.% of reinforcement presenting the lowest values. The degradation rate of PLA and composite filaments

is low, with no significant degradation being observed after 27 days in PBS. Thus, composite filaments based on PLA and thin graphite flakes, functionalized for enhanced interface with PLA and for anchoring a small concentration of Ag as an anti-microbial agent, were produced, presenting good mechanical performance and thermal properties. The composite filaments were successfully processed into three-dimensional scaffolds with finely controlled dimensions using textile-engineered and additive fabrication techniques, demonstrating their potential for ligament TE applications.

3.3.6 Supplementary materials

Table 18 – Operating parameters used for the production of composite filaments

Filament		Fil3D				FilText			
		Barrel 1/Barrel 2/Die Temperature(°C)	Screw speed (rpm)	Roll Speed (mm.s^{-1})		Barrel 1/Barrel 2/Die Temperature(°C)	Screw speed (rpm)	Roll Speed (mm.s^{-1})	
				Roll1	Roll2			Roll1	Roll2
PLA		130/170/160	45	22.8	25.6	130/170/160	15	232.2	233.6
PLA + 0.25		130/170/169	36	24.2	25.6		15	231.5	234.3
PLA + 0.5		130/170/169	36	24.9	27.6	130/170/160	15	232.2	254.3
PLA + 1	EG	135/170/155	45	31.1	33.2		25	228.8	282.7
PLA + 2		135/170/155	65	30.4	32.5		45	228.8	304.8
PLA + 0.25		123/170/160	45	24.9	28.3	123/170/160	25	268.9	270.2
PLA + 0.5		123/170/160	45	25.6	27.6	123/170/160	25	270.9	272.3
PLA + 1	f-EG	135/170/155	65	31.1	34.6	130/170/160	45	246.7	297.2
PLA + 2		135/170/155	65	30.4	32.5	130/170/160	65	228.8	309.6
PLA + 0.25		123/170/160	45	25.6	27.6		25	271.6	273.0
PLA + 0.5		123/170/160	45	25.6	29.7	130/170/160	25	271.6	273.7
PLA + 1	(f-EG)+Ag	125/170/155	65	31.1	34.6		45	246.7	302.7
PLA + 2		125/170/155	80	29.7	31.8		65	228.8	312.4
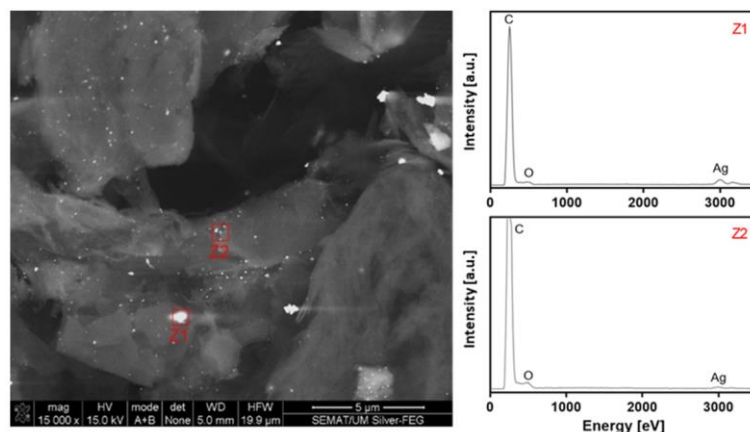
Figure 51 – SEM image and EDS analysis of (f-EG)+ Ag.

EDS tests were performed for (f-EG)+Ag to confirm the presence of silver. Figure 51 presents a backscattered electron image of (f-EG)+Ag with two different zones (Z1 and Z2) analysed through EDS and the Ag signal indicates the presence of silver in this graphite, as expected. The C signal is due to graphite, the O signal may be due to residual oxidation of the pristine EG and also to the presence of some benzyl carbamate and the Ag signal indicates the presence of silver in EG, as expected.
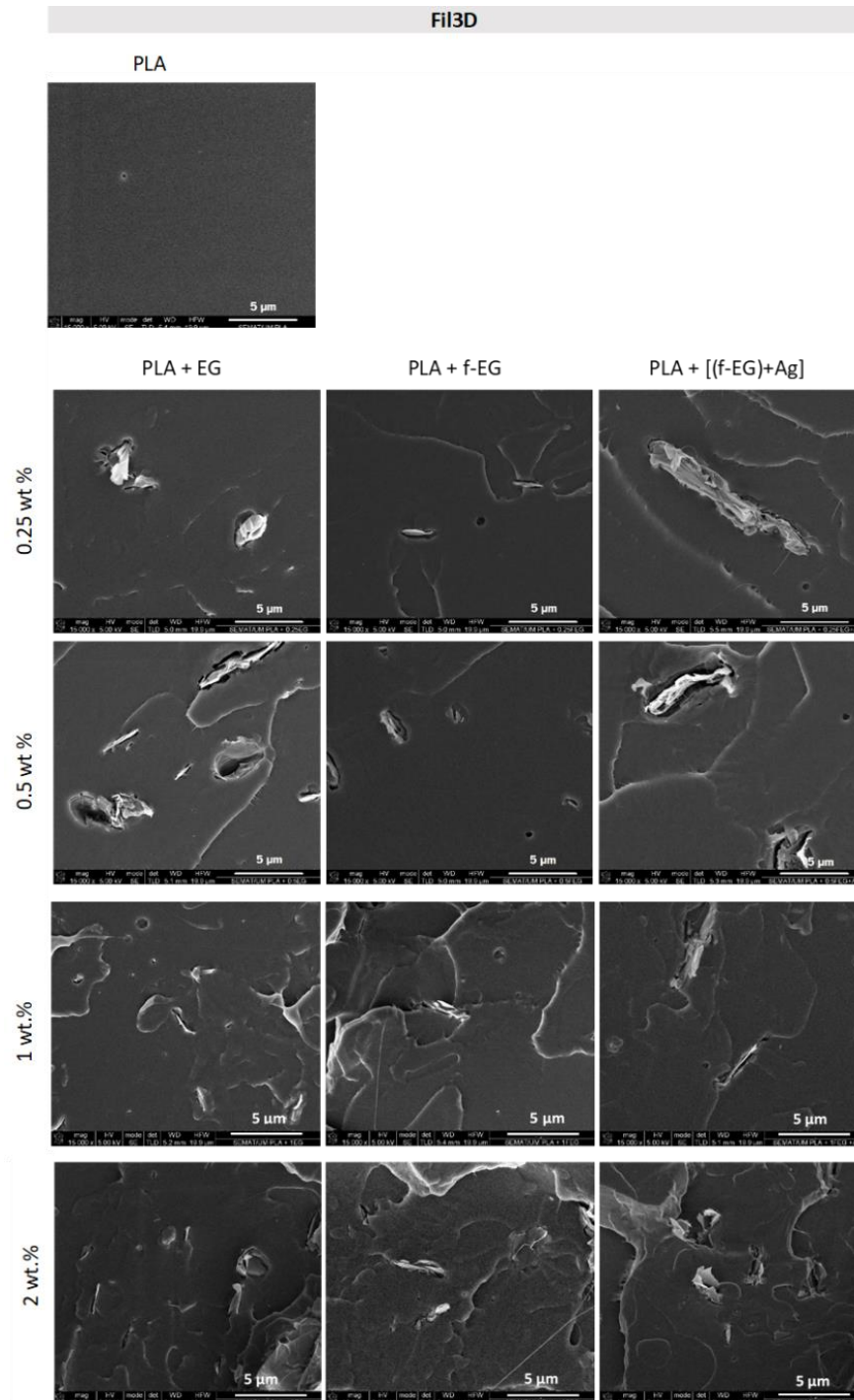
Figure 52 – SEM images of Fil3D: PLA; PLA reinforced with 0.25, 0.5, 1 and 2 wt.% of EG, f-EG and (f-EG)+Ag.
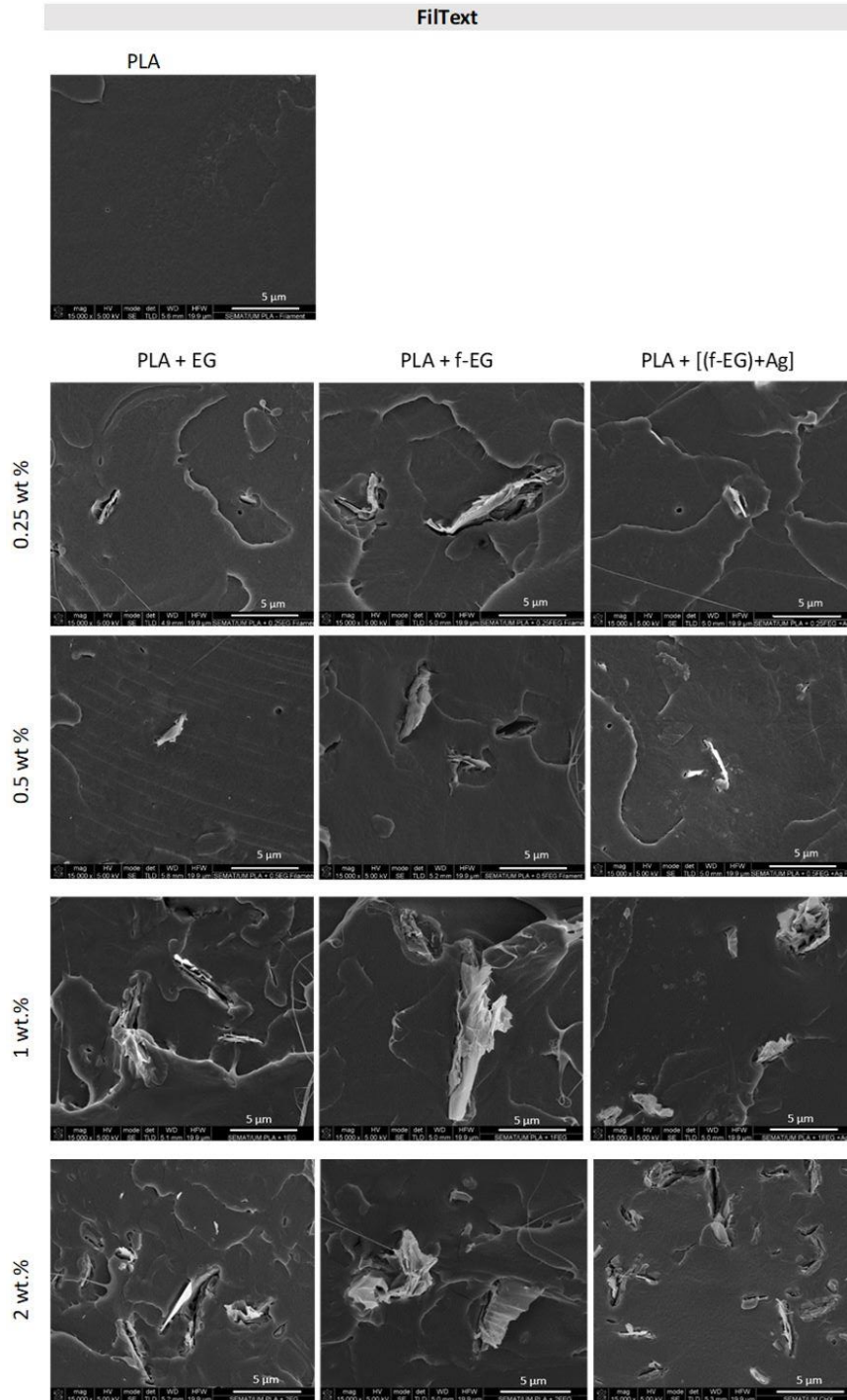
Figure 53 – SEM images of FilText: PLA; PLA reinforced with 0.25, 0.5, 1 and 2 wt.% of EG, f-EG and (f-EG)+Ag.
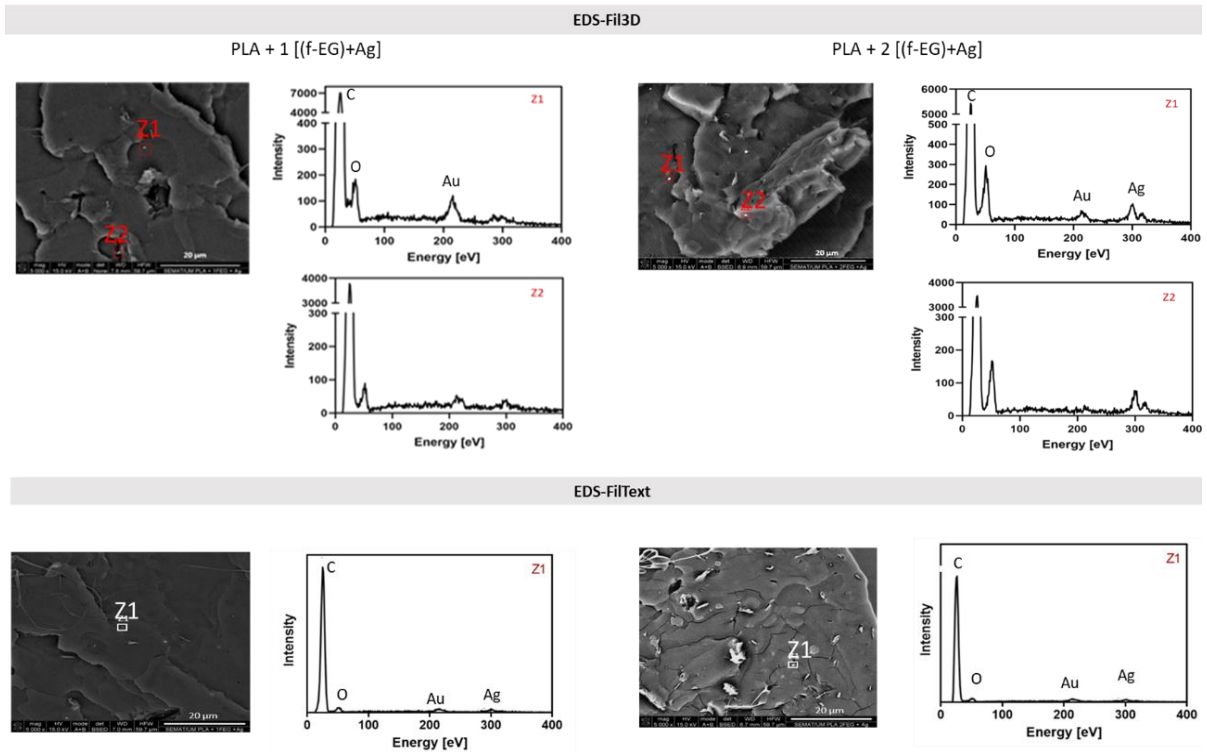
Figure 54 – SEM images and EDS analysis of Fil3D and FilText reinforced with 1 and 2wt.% of (f-EG)+Ag.
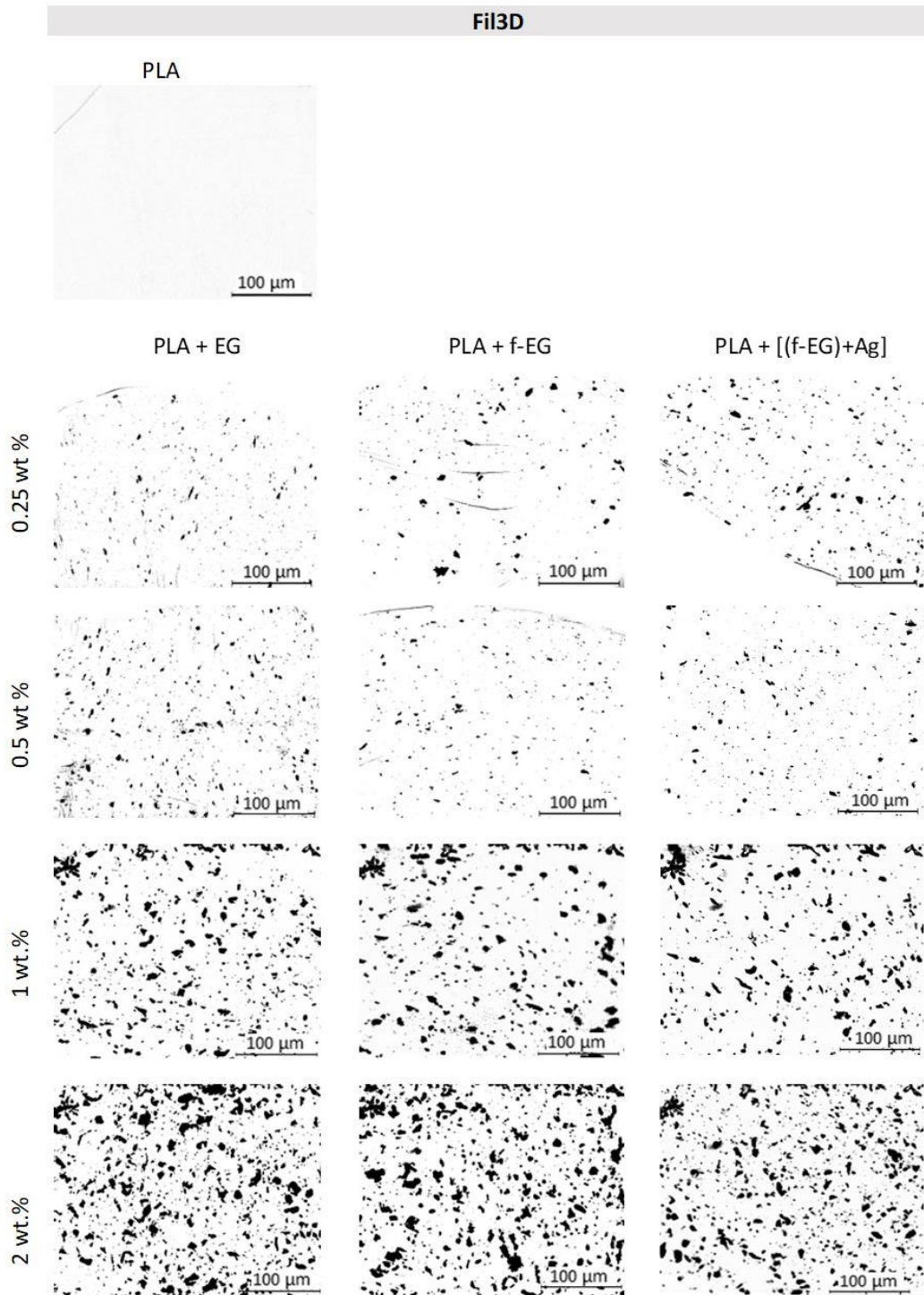
Figure 55 – Optical microscopy images of the Fil3D's cross-section, namely PLA; PLA reinforced with 0.25, 0.5, 1 and 2 wt.% of EG, f-EG and (f-EG)+Ag.
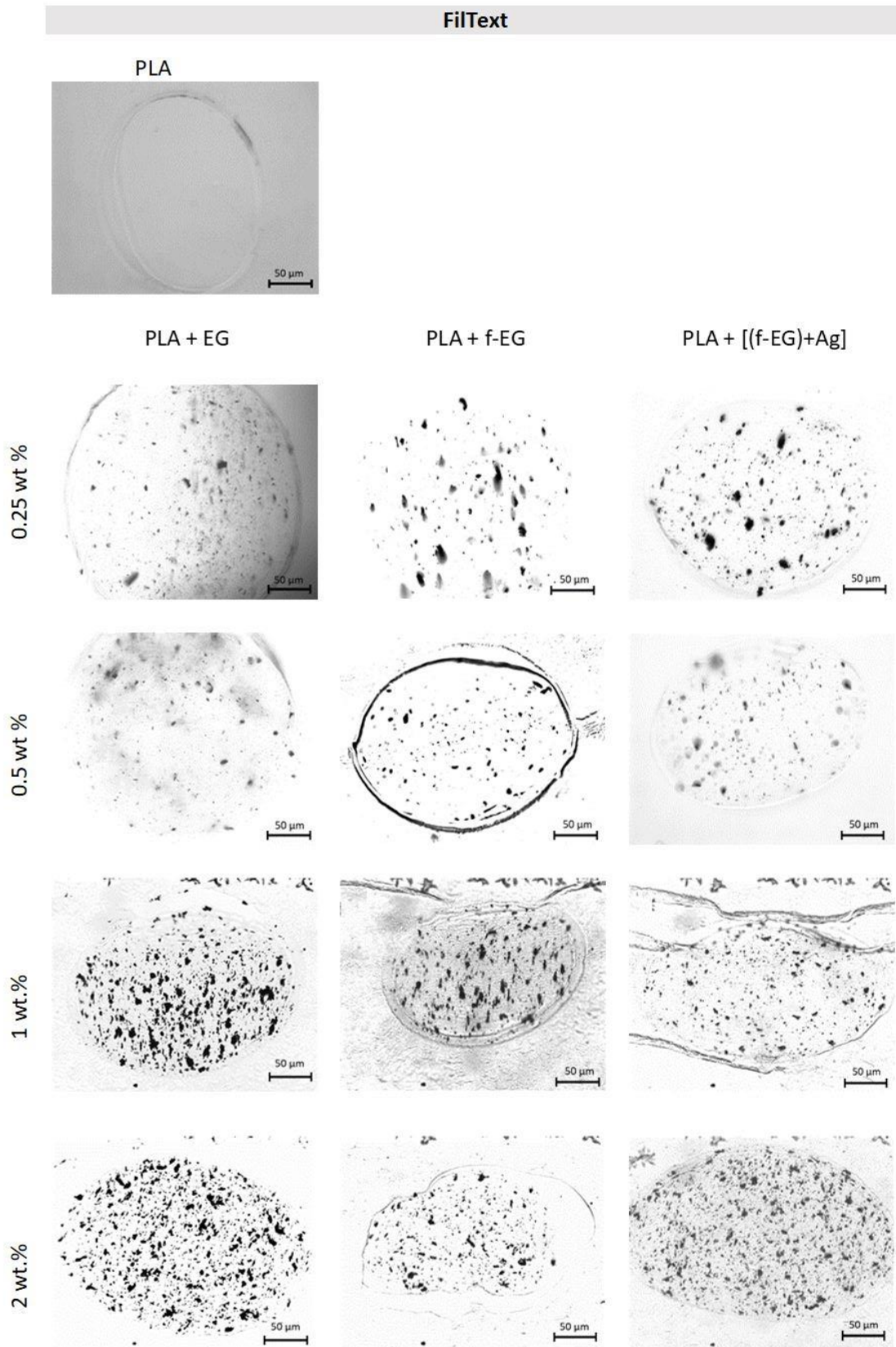
Figure 56 – Optical microscopy images of the FilText's cross-section, namely PLA; PLA reinforced with 0.25, 0.5, 1 and 2 wt.% of EG, f-EG and (f-EG)+Ag.

Table 19 – Summary of the thermal properties of Fil3D and FilText obtained for the 1st heating

Filament		T_g (°C)		T_c (°C)		T_m (°C)		ΔH_c (J/g)		ΔH_m (J/g)		χ_c (%)	
		Fil3D	FilText	Fil3D	FilText	Fil3D	FilText	Fil3D	FilText	Fil3D	FilText	Fil3D	FilText
PLA		57.5	59.2	110	104	162	159.6	30.1	28.9	33.6	29.7	3.7	0.9
0.25	PLA+	57.7	59.8	109	1038	162	158.8	29.4	28.3	31.6	29.7	2.4	1.5
0.5	EG	58.3	59.4	109	104	162	158.8	28.6	27.0	30.8	28.1	2.4	1.2
1		54.7	61.9	118	111	163	160.7	30.0	30.8	35.8	31.4	6.3	0.6
2		55.8	55.7	104	107	163	160.7	26.0	30.4	31.6	30.6	6.1	0.2
0.25	PLA+	58.3	59.5	109	103.	162	158.6	29.4	27.6	32.0	28.6	2.7	1.1
0.5	f-EG	58.2	59.2	108	105	162	159.2	28.2	30.4	31.2	31.0	2.4	0.7
1		55.2	56.3	112	110	162	161.0	28.2	28.3	32.9	28.7	6.3	0.4
2		56.4	57.0	105	108	162	161.1	27.1	28.8	35.5	29.0	6.1	0.2
0.25	PLA+	58.9	59.8	109	104	162	159.2	29.7	25.5	32.7	26.9	3.3	1.5
0.5	(f-	59.4	59.7	109	104	162	159.6	30.4	25.4	32.5	26.8	2.4	1.5
1	EG)+Ag	55.6	54.6	108	112	162	161.0	29.3	29.1	33.7	29.5	6.3	0.5
2		57.1	55.2	108	108	162	160.8	27.2	26.5	34.5	26.8	6.1	0.3

Table 20 – Summary of the thermal properties of Fil3D and FilText obtained for the 2nd heating

Filament		T_g (°C)		T_c (°C)		T_m (°C)		ΔH_c (J/g)		ΔH_m (J/g)		χ_c (%)	
		Fil3D	FilText	Fil3D	FilText	Fil3D	FilText	Fil3D	FilText	Fil3D	FilText	Fil3D	FilText
PLA		60.2	58.5	113	105	161	160	31.9	30.2	34.7	31.5	3.0	1.4
0.25	PLA+	60.7	58.8	117	112	158	159	31.2	30.7	33.7	31.7	2.6	1.1
0.5	EG	60.7	58.4	118	113	155	159	28.0	30.7	32.5	31.4	4.7	0.8
1		59.0	58.7	116	112	161	161	30.3	29.3	37.5	31.6	7.8	2.6
2		59.0	52.0	121	117	156	161	29.3	18.3	36.0	31.6	7.3	14.5
0.25	PLA+	60.8	58.9	121	117	156	157	29.8	28.7	34.1	31.0	4.7	2.4
0.5	f-EG	60.9	59.1	119	118	156	156	29.3	32.6	32.9	33.6	3.9	1.1
1		59.0	59.1	118	114	161	161	29.9	26.2	35.6	28.6	6.3	2.6
2		59.0	58.8	116	111	161	161	33.0	19.4	35.9	28.9	3.2	10.3
0.25	PLA+	60.7	60.1	124	118	157	156	28.9	30.6	31.6	32.1	3.0	1.7
0.5	(f-	60.7	59.6	123	119	157	154	30.9	26.7	32.3	30.5	1.5	4.1
1	EG)+Ag	59.0	60.4	117	116	161	161	33.1	23.4	35.7	30.0	2.8	7.1
2		59.2	58.8	115	113	161	161	31.1	18.9	35.8	26.5	5.1	8.3

Table 21 – Weight loss (%) of Fil3D and FilText

		Weight loss (%)							
		0-7days		0-14 days		0-21 days		0-28 days	
Filament		Fil3D	FilText	Fil3D	FilText	Fil3D	FilText	Fil3D	FilText
PLA		0.00	0.00	0.00	0.00	0.00	0.00	0.00	0.00
PLA+0.25	EG	0.00	0.00	0.00	0.00	0.00	0.00	0.00	0.00
PLA+0.5		0.00	0.00	0.00	0.00	0.00	0.00	1.39	0.00
PLA+0.25	f-EG	0.00	0.00	0.00	0.00	0.00	0.00	0.00	0.00
PLA+0.5		0.00	0.00	1.37	0.00	0.00	0.00	0.00	0.00
PLA+0.25	(f-EG)+Ag	0.00	0.00	1.32	0.00	0.00	0.00	0.00	0.00
PLA+0.5		0.00	0.00	1.24	0.00	0.00	0.00	0.00	0.00

CHAPTER 4

Engineering Ligament Scaffolds Based on PLA/Graphite Nanoplatelet Composites by 3D Printing or Braiding

This chapter is based on the article:

Silva M, Pinho I, Gonçalves H, Vale AC, Paiva MC, Alves NM, Covas JA. Engineering Ligament Scaffolds Based on PLA/Graphite Nanoplatelet Composites by 3D Printing or Braiding. J Compos Sci. 2023, **7**, 104. https://doi.org/10.3390/jcs7030104.

4 Engineering Ligament Scaffolds Based on PLA/Graphite Nanoplatelet Composites by 3D Printing or Braiding

The development of scaffolds for tissue-engineered growth of the anterior cruciate ligament is a promising approach to overcome the limitations of current solutions. This work proposes novel biodegradable and biocompatible scaffolds matching the mechanical characteristics of the native human ligament. PLA scaffolds reinforced with graphite nano-platelets (PLA+EG) as received, chemically functionalized (PLA+f-EG), or functionalized and decorated with silver nanoparticles (PLA+[(f-EG)+Ag]), were fabricated by conventional braiding and using 3D printing technology. The dimensions of both braided and 3D-printed scaffolds were finely controlled. The results showed that the scaffolds exhibited high porosity (> 60 %), pore interconnectivity, and pore size suitable for ligament tissue ingrowth, with no relevant differences between PLA and composite scaffolds. The wet state dynamic mechanical analysis at 37 °C revealed an increase in the storage modulus of the composite constructs, compared to neat PLA scaffolds. Either braided or 3D-printed scaffolds presented storage modulus values similar to those found in soft tissues. The tailorable design of the braided structures, as well as the reproducibility, the high speed, and the simplicity of 3D printing allowed to obtain two different scaffolds suitable for ligament tissue engineering.

4.1 Introduction

Scaffold engineering for ligament tissue regeneration is a promising strategy to heal ligaments with severe injuries, overcoming the inadequacies of current treatments involving auto and allografts (24). The approach consists in incorporating specific cells into a compatible scaffold to be implanted into the lesion site, with combined cell growth and scaffold degradation. Providing the required scaffold morphology and mechanical performance, as well as using the adequate scaffold material and cell type, enables the formation of a new tissue that replaces the damaged one, restoring its functionality (5, 294).

The scaffold properties, such as biocompatibility, biodegradability, and mechanical performance, are directly influenced by the composition of the material used (235). Many biomaterials have been evaluated for ligament TE, including natural materials (e.g., collagen; silk), biodegradable synthetic polymers (e.g. PLA, PLGA), and composites/blends (e.g., PLA-collagen, PCL-collagen, and PLA–PLGA) (17). Among synthetic polymers, formulations based on PLA scaffolds have been widely developed (1, 8,

77), presenting superior mechanical properties and fibroblast proliferation when compared to other biodegradable polymers such as polyglycolic acid (77).

PLA is a biodegradable and biocompatible polymer produced from renewable bio-based resources such as corn or cellulose (235). The median half-life of the polymer is 30 weeks and produces safe hydrolytic degradation products (lactic acid or carbon dioxide and water), naturally metabolized by the human body through the kidneys or breath. PLA-based materials have been routinely used for several medical applications such as drug delivery, TE implants, or sutures (295).

Graphene-based materials such as CNTs and GNPs exhibit unique properties and have been effective as fillers for polymer reinforcement (283), resulting in composites with superior mechanical, thermal, and electrical properties (296, 297). Gonçalves et al. (283) incorporated graphene nanoplatelets in PLA at different loadings (0.1–0.5 wt.%) and observed that the composite with 0.25 wt.% filler presented a 20% increase in tensile strength and a 12% increase in the Young's modulus. Novais et al. showed that the functionalization of graphite nanoparticles through a DCA reaction of an azomethine ylide improved the composite interfacial strength, through covalent bonding of PLA with the pyrrolidine group formed at the graphene surface (263, 267). Moreover, the morphology and metabolic activity of human fibroblasts (HFF-1) were not affected by the presence of graphene (283). The combination of graphene and its derivatives with biocompatible polymeric matrices is also attractive for TE scaffolds because of their high surface area and nanoscale dimension that matches the size of cell surface receptors, and the natural ECM nanotopography (247, 298). Composite scaffolds with low graphene or functionalized graphene content have been considered to reduce the potential cytotoxicity in the human body (247, 298).

An important concern during the implantation of a scaffold is the risk of bacterial infections at implant or device sites, which are frequently difficult to treat due to deep tissue localization and the bacteria involved (299). The incorporation of antibacterial components into scaffolds may aid appropriate postoperative regeneration of the scaffold implantation site (249). Silver nanoparticles have demonstrated interesting activity in tissue regeneration because of their nano-size, high inherent antimicrobial efficiency, and capacity to accelerate the healing process and production of ECM components (272, 300). To facilitate recovery after ACL-reconstructive surgery, the use of electrical stimulation has been recommended (294, 301, 302). As a metallic agent, silver nanoparticles can also change the electrical characteristics of the cells (303). The combination of polymers with metallic nanoparticles, e.g., silver nanoparticles, and carbon fillers, is thus an attractive way to enhance the transmission of an electrical stimulation applied from skin electrodes to the damaged tissue, enhancing its repair (294). A decoration

of functionalized graphene surfaces with silver nanoparticles can be easily obtained through a reaction based on the reduction of silver ions by N,N-dimethylformamide (274, 304).

Current fabrication methods for ligament scaffolds include melt spinning, electro-spinning, freeze-drying, solvent casting, hydrogel solution mixing, and additive manufacturing (305). Fibrous scaffolds have been the preferred choice to mimic the hierarchical organization of native ligaments (18). These structures are based on an assembly of fibers, either random or aligned in parallel, as a rope, or arranged by braiding (8, 77), braid-twisting (1), or knitting (70), as typically performed in the textile industry (18, 120).

Additive manufacturing, also known as 3D printing, has revolutionized the regenerative medicine field due to its capacity of producing customizable scaffolds for tissue engineering (306) with controlled pore size and structure (307). AM enables the production layer by layer of complex and precise structures with high reproducibility (308). Recently, scaffolds have been produced by bioprinting, stereolithography, inkjet printing, selective laser sintering (307), and FDM techniques. FDM is one of the most widespread, simple, and cheap 3D printing methods, whereby a continuous filament of a thermoplastic polymer is extruded through a nozzle and subsequently deposited onto a print bed, creating successive horizontal thin layers of the part in the vertical direction (249, 306). FDM does not require solvents and can use a variety of biodegradable and biocompatible materials, the most common being PLA, to fabricate 3D printed scaffolds (235, 249).

Previously, the authors reported the successful production of PLA/graphite nano-platelet composite filaments with enhanced mechanical and electrical properties (304). Here, those filaments are used to obtain scaffolds for ligament regeneration. Two alternative manufacturing techniques were investigated, one based on braiding, the other using FDM. Braided scaffolds benefit from the tailorable structures that may be obtained by conventional textile techniques to mimic the native ligament morphology. FDM is a simple, fast, and cost-effective technique that, to the best of our knowledge, has not yet been utilized to obtain scaffolds based on PLA/graphene composites for ACL. The present work reports the production, optimization, and characterization of these composite scaffolds based on PLA and micronized graphite nanoplatelets (PLA+EG), functionalized EG (PLA+f-EG) and f-EG with a low concentration of silver nanoparticles anchored at the surface (PLA+[(f-EG)+Ag]). These scaffolds were produced with controlled architecture, adequate porosity, and mechanical properties relevant for the regeneration of the ACL.

4.2 Materials and Methods

4.2.1 Scaffolds Production

4.2.1.1 Materials

PLA filaments and PLA composite filaments with two different diameters (0.26 ± 0.03 mm, designated as FilText, and 1.71 ± 0.07 mm, designated as Fil3D), produced in a previous work (304), were used in the preparation of the textile engineered and 3D printed scaffolds, respectively. The composite filaments were constituted by PLA and EG at weight concentrations of 0.25, 0.5, 1, and 2 wt.%, as determined by thermogravimetric analysis on a TGA Q500 equipment (TA Instruments®, New Castle, DE, USA) at 800 °C, under a nitrogen atmosphere at a flow rate of 50 mL min^{-1} — Table 23 in Supplementary Material. The PLA was the grade Luminy LX175 from Total Corbion, Gorinchem, and the EG were Micrograf HC11 obtained from Nacional de Grafite Lda, Minas Gerais, Brasil. The EG were functionalized by the DCA reaction, and f-EG were decorated with silver nanoparticles, as previously described (304). The melt flow index (MFI) of the filaments containing PLA and PLA reinforced with 0.5 and 2 wt.% of fillers was measured at 185 °C and a load of 2.16 kg on MFI equipment from Daventest (Welwyn Garden City, England).

4.2.1.2 Three-Dimensional Printing

The 3D-printed scaffolds were designed using the Ultimaker Cura (version 4.4, Ultimaker, Geldermalsen, Netherlands) software (Figure 57), with an infill linear pattern (0 and 90 °) and porosity of 50%. The scaffold was printed horizontally using an Ender-3 3D Printer from Creality (London, UK).
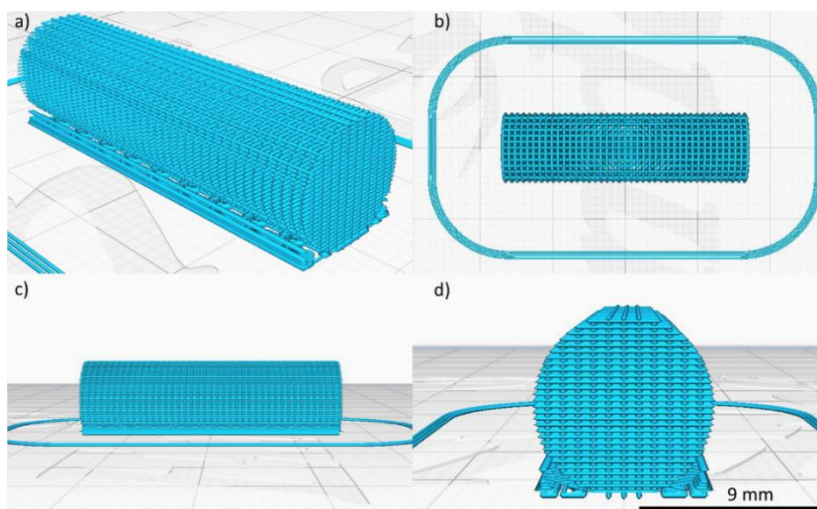
Figure 57 — Three-dimensional-printed scaffolds. (**a**) Isometric view; (**b**) top view; (**c**) lateral view; and (**d**) front view

4.2.1.3 Braiding

Braided scaffolds were manufactured using the FilText filaments reinforced with 0.5 and 1 wt.% of (f-EG)+Ag. The textile-engineered scaffolds made with FilText filaments were produced using a *kumihimo* hand braiding device, with a circular stand (diameter of 12 cm). The *kumihimo* technique and the resulting braided structure (formed by 8 FilText filaments and designated as bundle) are represented in Figure 58a,b, respectively.
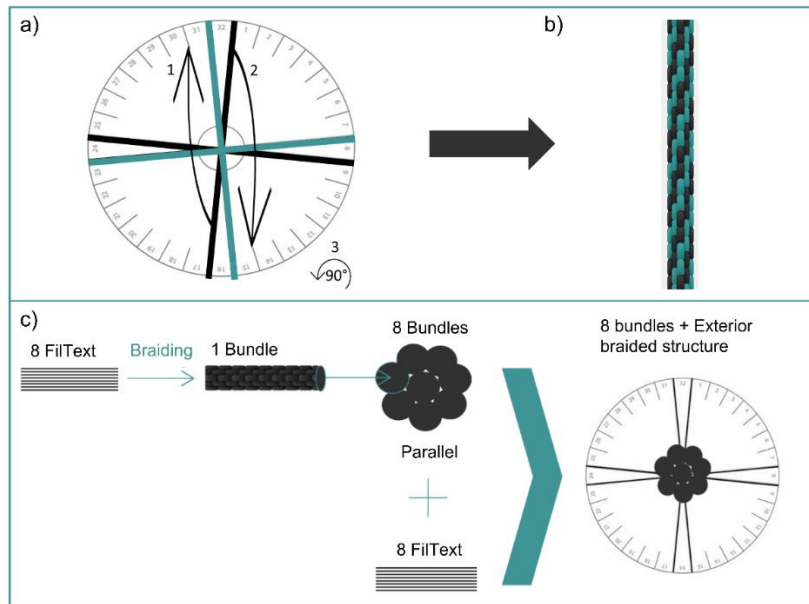
Figure 58 — (**a**) *Kumihimo* technique: slot 32 of the disk is placed in the 12 o'clock position. Eight FilText filaments are tied together, placed in the center of the disk, and the loose ends loaded into slots 31 and 32, 7, and 8, 15 and 16, 23, and 24 on the *kumihimo* disk. Then, FilText filaments are moved from slot 16 to 30 (1) and 32 to 14 (2). Then, the disk is rotated 90 ° counterclockwise (3) and the FilText filaments moved from slot 24 to 6 and slot 8 to 22. This procedure was repeated until the required braid length was reached; (**b**) braided structure obtained after multiple repetitions of (**a**); (**c**) structure of the final braided scaffold.

The number of bundles was optimized to obtain a braided scaffold with a diameter of approximately 9 mm, similar to the native ligament. The resulting scaffold comprises an exterior braided structure formed by 8 FilText filaments and a core containing 8 bundles aligned in parallel and tied together with a suture of the same material (Figure 58 c).

4.2.2. Scaffold Characterization

Both types of scaffolds exhibited a cylindrical shape with a full length of approximately 32 mm and a diameter of 9 mm, which are comparable to the dimensions of the native ACL. Smaller braided

and 3D-printed scaffolds with an approximate length of 25 mm and diameter of 4 mm were also produced for further testing. The morphology and the shape, size, and distribution of the pores of braided and 3D-printed scaffolds were analyzed using a Digital Microscope Leica DMS1000. The scaffolds were imaged by SEM and their cross-sections were observed by SEM/EDS on a FEI Nova 200 FEG-SEM/EDS (FEI Europe Company, Hillsboro, OR, USA). The microstructure of the scaffolds was analyzed by computed micro-tomography (micro-CT) using a high-resolution SkyScan 1272 scan (v1.1.3, Bruker, Boston, USA). Samples were scanned using a pixel size of 21.6 μm, with a voltage of 60kV and a current of 163 μA. The resulting images were reconstructed along the z-axis (software NRecon, SkyScan), then representative images were binarized through a global threshold (value adjusted to the minimum of the global grayscale histogram from each sample) (CTAn software, SkyScan). The reconstructed slice images were processed and through 3D rendering the mean pore size (μm), mean wall thickness (μm), and porosity (%) were determined. Finally, the 3D virtual reconstructions were created using the CTVox software (version 3.3.0 r1412, SkyScan, Boston, USA). At least three samples were analyzed for each condition. Uniaxial compression tests of 3D-printed scaffolds were performed on a Instron 5969 (Norwood, MA, USA), equipped with a 50 kN load cell, setting the initial grip distance at 4 mm and the testing speed at 1 mm/s. At least five samples were analyzed for each condition. The samples were previously soaked overnight in a PBS solution at 37 °C. DMA was performed using a TRITEC2000B equipment (Triton Technology, Grantham, UK) in compressive mode for the 3D-printed scaffolds and in tension mode for the braided scaffolds, with the aim of evaluating their mechanical properties and possible alterations when subjected to cyclic loading and immersed in physiologic fluids. Samples were previously soaked overnight in a PBS solution at 37 °C. DMA spectra were obtained at the same temperature using cycles of increasing frequency from 0.2 to 2 Hz. At least three samples were tested for each composition and scaffold type.

4.3 Results and Discussion

4.3.1 Scaffold Architecture and Morphology

The MFI results obtained for the composites reinforced with 0.5 and 2 wt.% of EG, f-EG and [(f-EG)+Ag]) are summarized in Table 29, ranging from 10 to 14.5 g/10 min, which are adequate for use in extrusion-based processes. The addition of reinforcement did not significantly change the MFI measured for neat PLA. Scaffolds with a porous interconnected network and a pore size greater than 250 μm were

produced, aiming at enabling ligament regeneration (274, 309). As expected, the production of 3D-printed scaffolds was faster, easier, and yielded reproducible samples.

During 3D printing optimization, accumulation of material, deformation of some layers, and/or closing of the pores, were defects observed and related to overheating. The scaffolds printed horizontally with nozzle temperature and printing velocity set at 185 °C and 45 mm.s^{-1}, respectively, the build platform kept at 80 °C, an infill distance of 0.8 mm and layer height of 0.15 mm, and with a substrate of 5° contact angle exhibited well defined pores, with no deformation of layers, as well as no surface distortions. Therefore, these printing conditions were selected to produce all 3D-printed scaffolds. It is worth noting that horizontal printing required the deposition of a support layer. The same material of the scaffold was used, printing at a 5 ° contact angle (see Figure 57), which could be easily removed after cooling. Figure 59 presents the 3D-printed scaffolds of PLA and PLA reinforced with (f-EG)+Ag. A general view is provided in Figure 59a–c).
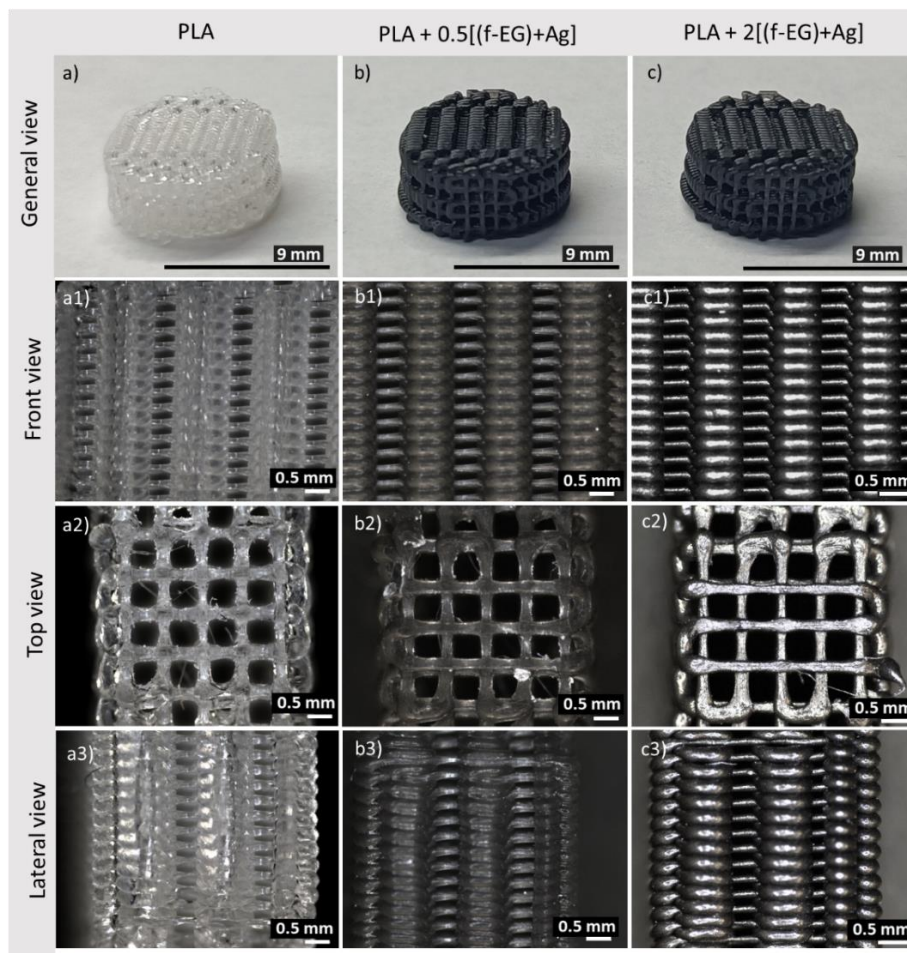
Figure 59 — Three-dimensional-printed scaffolds: general view (**a**—PLA; **b**—PLA+0.5[(f-EG)+Ag]; **c**—PLA+2[(f-EG)+Ag]); higher magnification (**a1–a3**—PLA; **b1–b3**—PLA+0.5[(f-EG)+Ag] and **c1–c3**—PLA+2[(f-EG)+Ag]) from front, top, and side perspectives.

The images obtained at higher magnification in the "front", "top", and "lateral" directions were acquired as indicated in Figure 57. Further images of the 3D-printed scaffolds at all the compositions of EG, f-EG, and (f-EG)+Ag are presented in Figures 69 to 72.

The general architecture of the braided scaffolds containing PLA and PLA reinforced with (f-EG)+Ag is illustrated in Figure 60a–c). The samples had a regular geometry, with large pores regularly distributed with clear pore interconnectivity.
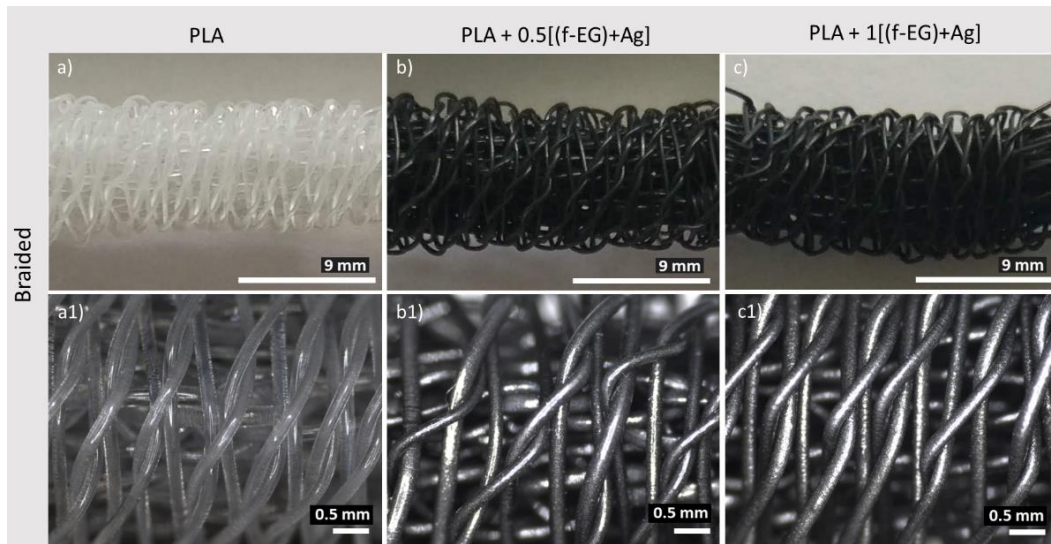
Figure 60 — General view of braided scaffolds (longitudinal direction) containing: (**a**—PLA; **b**—PLA+0.5[(f-EG)+Ag]; **c**—PLA+1[(f-EG)+Ag]) and the corresponding optical images at higher magnification **(a1, b1** and **c1**).

The surface morphology of 3D-printed and braided scaffolds was observed by SEM (Figure 61). A slight roughness may be assigned to the presence of fillers, which may be advantageous for the application. It has been reported that surface roughness at micron and submicron scale may positively affect cell adhesion and proliferation regardless of the cell type and scaffold materials (309). The braided scaffold geometry presents higher pore size compared to the 3D-printed scaffold. The addition of reinforcements did not significantly affect the scaffolds' geometry or pore size, either for braided or 3D-printed scaffolds.

The qualitative and quantitative analysis of porosity, mean pore size, and mean pore thickness of the 3D-printed and braided scaffolds were assessed by micro-CT and are summarized in Table 22. All 3D-printed scaffolds presented uniform pores over the entire surface and a similar structure, regardless of the presence of fillers, as illustrated in Figure 62 by the representative images of 3D-printed scaffolds containing PLA, PLA reinforced with 2 wt.% EG, f-EG and (f-EG)+Ag. Micro-CT cross-section images of the

3D-printed scaffolds produced with the remaining compositions of EG, f-EG and f-EG)+Ag are displayed in Figure 73.
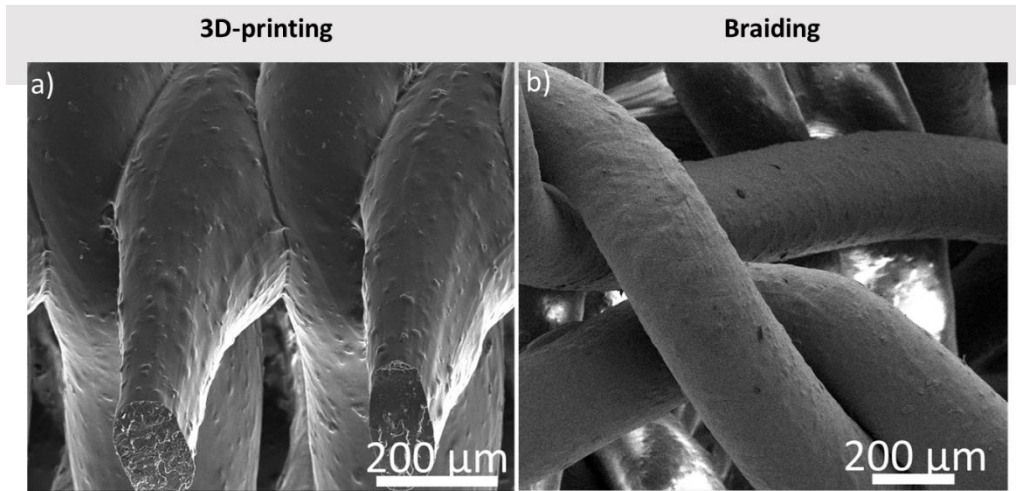
Figure 61 — Morphology of the surface of the (**a**) 3D-printed scaffold containing PLA+2[(f-EG)+Ag], and (**b**) braided scaffold with PLA+1[(f-EG)+Ag].

Table 22 — Mean porosity, pore size, and filament thickness of the 3D-printed and braided scaffolds, calculated from the micro-CT data.

Scaffold			Mean Porosity (%)	Mean filament thickness (µm)	Mean pore size (µm)
3D-printed	PLA		66.8 ± 1.5	240± 3	484 ± 4
	PLA+0.5	(f-EG)+Ag	70.5 ± 1.7	229 ± 8	496 ± 7
	PLA+2		68.9 ± 0.8	236 ± 7	485 ± 17
Braided	PLA		87.6 ± 0.7	264 ± 34	1035 ± 411
	PLA+0.5	(f-EG)+Ag	83.4 ± 2.5	225 ± 33	1154 ± 8
	PLA+1		87.8 ± 3.8	267 ± 33	1164 ± 545

PLA 3D-printed scaffolds exhibited a slightly lower porosity as compared to PLA+0.5[(f-EG)+Ag] and PLA+2[(f-EG)+Ag] 3D-printed scaffolds. Similar results were obtained for all 3D-printed scaffolds with different compositions (see Table 25), indicating that filler addition to the PLA matrix had a slight effect on pore morphology and size, during 3D printing, as reported by other authors (235).

Higher porosity and pore size were observed for braided scaffolds as compared to 3D-printed scaffolds. A large variation of the pore size was observed for the braided scaffolds, characteristic of the braiding design chosen and enhanced by the handcrafted production.
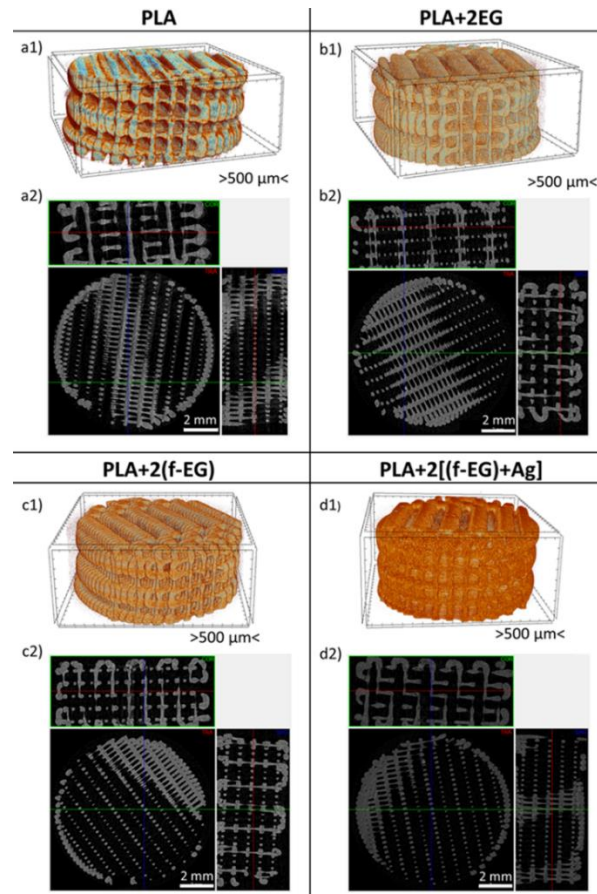
Figure 62 — Representative 3D micro-CT reconstruction and the corresponding micro-CT cross-sections images of the 3D-printed scaffolds containing: (**a1,a2**) PLA; (**b1,b2**) PLA+2EG; (**c1,c2**) PLA+2(f-EG); and (**d1,d2**) PLA+2[(f-EG)+Ag].

The micro-CT images and 3D reconstructions are illustrated in Figure 63. Micro-CT analysis revealed similar porosity and pore size results for the braided scaffolds of PLA and composites with different compositions.
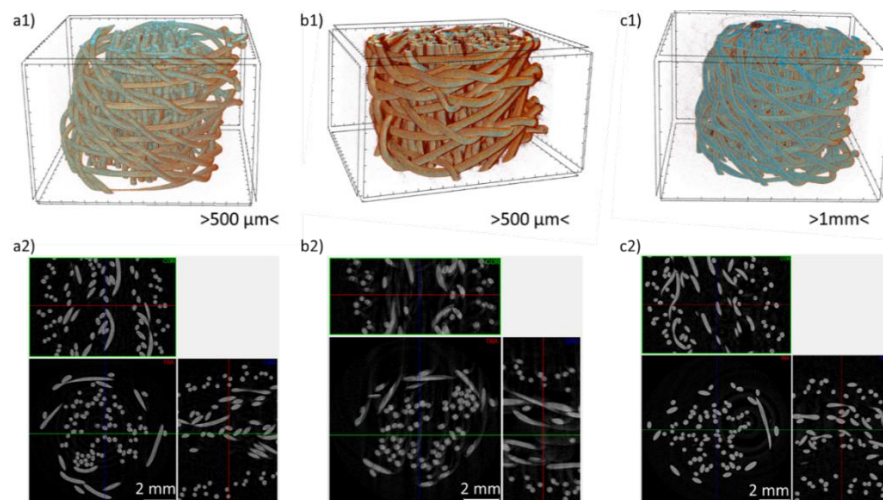
Figure 63 — Representative 3D micro-CT reconstruction and micro-CT cross-sections images of the braided scaffolds containing (**a1,a2**) PLA, (**b1,b2**) PLA+0.5[(f-EG)+Ag], and (**c1,c2**) PLA+1[(f-EG)+Ag].

Pore interconnectivity and high porosity play an important role in the performance of scaffolds, helping the diffusion of nutrients, vascularization, and tissue ingrowth (310, 311). For ACL tissue engineering, it has been recognized that the scaffold should have an overall porosity >50% and exhibit pores with diameters greater than 250 μm (63, 311). Thus, the scaffolds produced in the present work, either 3D-printed or braided, exhibit adequate porosity, pore interconnectivity, and pore size for ACL regeneration. The pore size and morphology of 3D-printed scaffolds are comparable to those reported for other 3D-printed graphene-based scaffolds, such as PLA/GO (235) and polycaprolactone/reduced GO (312). Braided scaffolds also exhibit a pore size similar to that found in other works focused on textile-based scaffolds for ligament regeneration such as knitted scaffolds of PLA/poly lactic-co-glycolic acid (41) and silk/collagen (60).

4.3.2 Morphology of the Nanoparticle Dispersion after 3D Printing

The braiding process does not affect the nanoparticle dispersion morphology since the filaments produced by melt extrusion are only subjected to a textile process. However, 3D Printing involves re-melting and flow, which may affect the dispersion state of the nanoparticles in the composite. In order to evaluate the nanoparticle dispersion morphology after 3D printing, the scaffolds cross-sections were observed by SEM and compared to the morphology of the Fil3D used in the printing process. Figure 64 presents micrographs of the cross-sections of 3D-printed scaffolds containing PLA, PLA+0.5[(f-EG)+Ag], and PLA+2[(f-EG)+Ag] as well as of the Fil3D nanocomposite filaments that originated them.

Figure 64 illustrates the homogenous dispersion and distribution of (f-EG)+Ag in PLA for Fil3D filaments and its preservation after 3D printing. Figure 74 depicts micrographs of the cross-sections of 3D-printed scaffolds produced with composite filaments containing 1 wt.% of EG, f-EG and (f-EG)+Ag, showing similar morphology and good dispersion of the nanoparticles for all compositions.

The EDS elemental analysis of the 3D-printed scaffold containing PLA+2[(f-EG)+Ag] is depicted in Figure 65, confirming the presence of silver nanoparticles anchored on f-EG. The addition of silver nanoparticles onto graphene-based materials was reported to enhance the antimicrobial activity and biocompatibility, depending on its concentration (313, 314). The Au signal is due to the thin Au layer deposition performed to allow the SEM analysis.
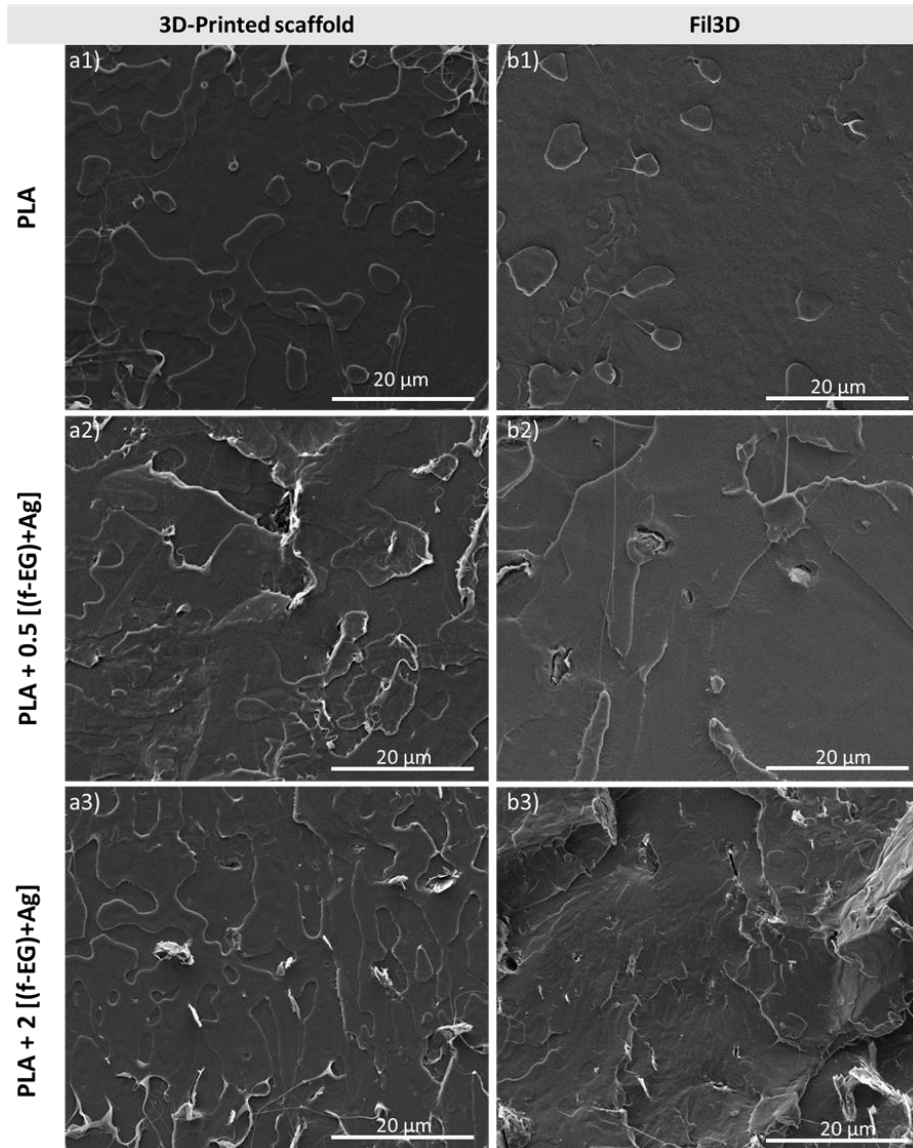
Figure 64 — Morphology of the cross-section of the (**a1–a3**) 3D-printed filament scaffolds and (**b1–b3**) Fil3D containing PLA, PLA+0.5[(f-EG)+Ag], and PLA+2[(f-EG)+Ag], respectively.
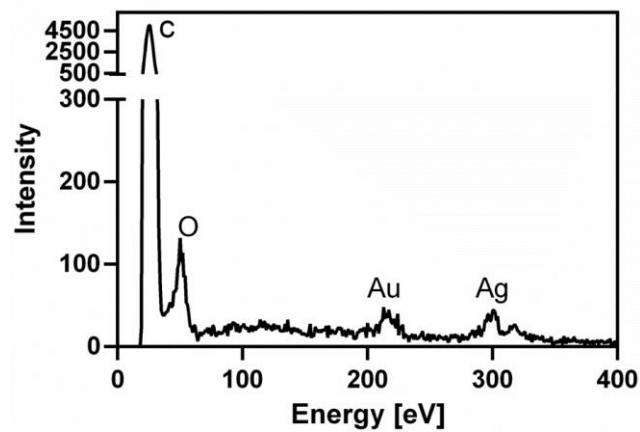
Figure 65 — EDS of the 3D-printed scaffold containing PLA+2[(f-EG)+Ag].

4.3.3 Scaffold Dynamic Mechanical Analysis

The dynamic mechanical properties measured under wet conditions at 37 °C as a function of frequency are displayed in Figures 66 and 67, with Figures 66a1–c1 and 67a1 representing the storage modulus (E') and Figures 66a2–c2 and 67a2 the loss factor (tan δ) of 3D-printed and braided scaffolds, respectively.

Several studies have reported the mechanical improvement of PLA reinforced with graphene-based materials under static loading (315). The mechanical response of knee ligaments, namely ACL, posterior cruciate ligament (pCL), medial collateral ligament (mCL), and lateral collateral ligament (lCL) under static loading is also well documented (18, 267). Values reported for the elastic modulus of ACL, pCL, mCL, and lCL are in the range of 65–447, 150–447, 330, and 245 MPa, respectively. Values reported for the ultimate strain are 14–44% for ACL, 11-19% for pCL, 17% for mCL, and 16% for lCL (18). The ACL is formed by two anatomical bands (anteromedial (AMB) and posterolateral (PLB) bands).
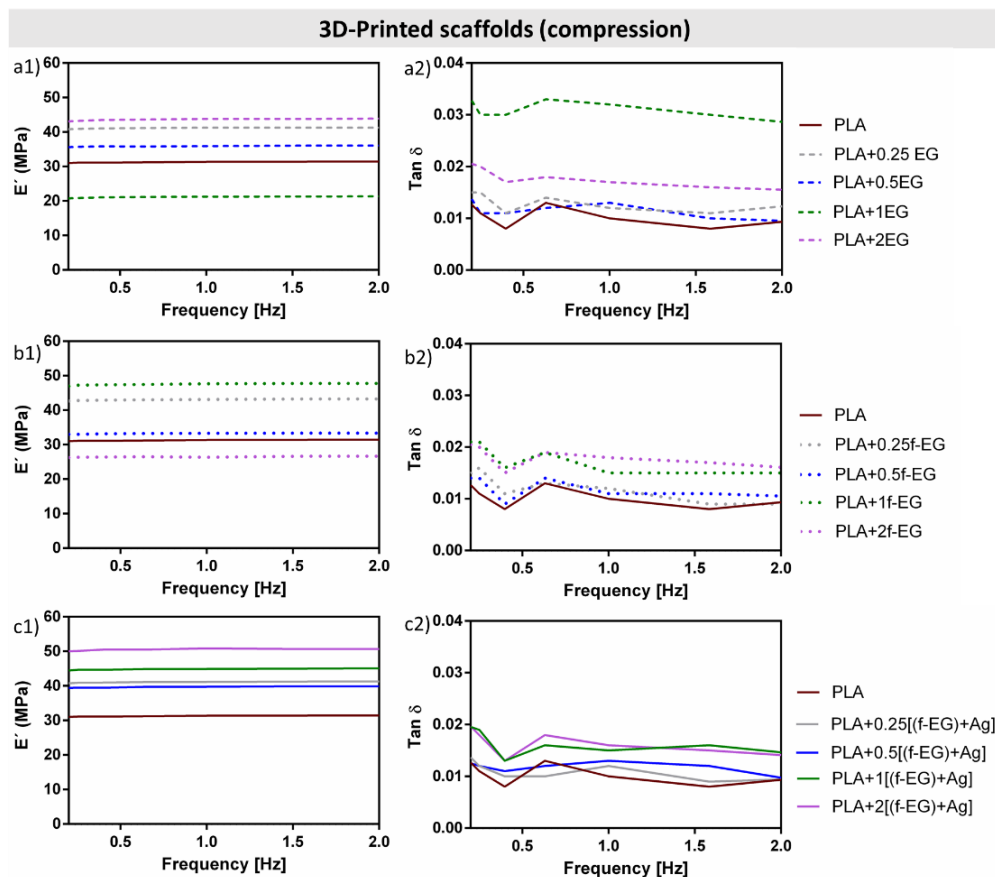
Figure 66 — (**a1–c1**) Storage modulus of 3D-printed scaffolds reinforced with EG, f-EG, and (f-EG)+Ag, respectively, and (**a2–c2**) the corresponding loss factor, as a function of the frequency, ranging from 0.1 to 2 Hz. Three-dimensional printed scaffolds were tested in compression mode.
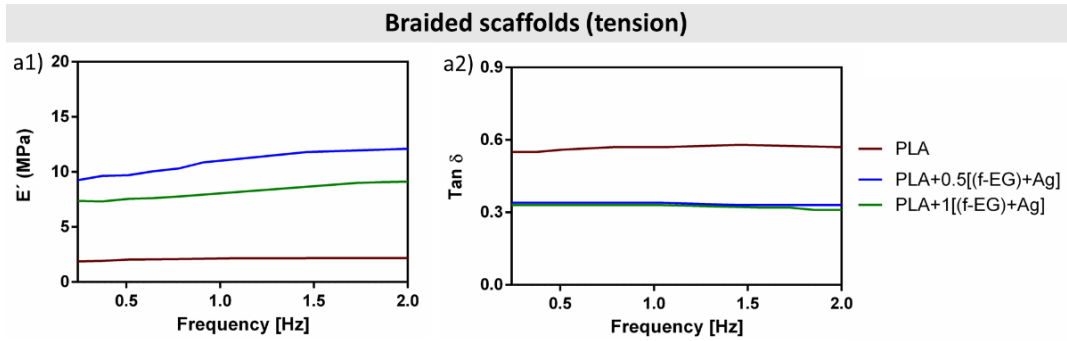
Figure 67 — (**a1**) Storage modulus and (**a2**) loss factor of braided scaffolds, as a function of the frequency, ranging from 0.1 to 2 Hz. Braided scaffolds were tested in tensile mode.

Tensile tests of porcine ACL bundles, similar to human ACL, showed that the stiffness of the PLB was significantly higher than that of the AMB, except for the modulus (111 and 123 MPa, respectively). In fact, no material property of intact ACL, AMB, and PLB specimens was significantly different, including deformation and strain at failure (316). However, ligaments experience dynamic loads during normal locomotion, and their response is influenced by their viscoelastic properties. Thus, it is crucial to confirm the viscoelastic response of the scaffold structure to loading (315). Studies reporting dynamic mechanical tests of PLA/graphene-based composite structures for ligament scaffolds are scarce (285, 317, 318). Pinto et al. (317) produced composites for ACL regeneration based on CNTs functionalized with carboxylic acid (0.3 wt.%) by melt mixing/compression molding and observed an increase of 4% in the storage modulus compared to neat PLA, at 1 Hz and under tension. They also produced composites of PLA/GNPs (2 wt.%) by the same method and observed a decrease (2%) in the storage modulus relative to the neat polymer matrix.

The dynamic mechanical performance of 3D-printed and braided scaffolds may be affected not only by the scaffold's material but also by its structure. Thus, direct comparison of the DMA results obtained for 3D-printed and braided scaffolds is not appropriate. In general, an increase in E' is observed for the composite 3D-printed and braided scaffolds relative to PLA scaffolds, as presented in Figures 66 a1–c1 and 67 a1, respectively. This is a consequence of the addition of high stiffness nanoparticles forming strong/rigid interfaces with the PLA matrix and reducing the polymer mobility near the nanofillers (319), or even to changes in the polymer crystallinity induced by the graphene nanoparticles. Graphene may act as a nucleating agent, restricting the movement of the polymer chains and inducing crystallization (315). These effects may contribute differently to the 3D-printed and braided scaffolds since they were produced from filaments with different diameters and exhibiting distinct structures. Moreover, 3D printing required re-melting of the filament to produce a continuous porous structure.

The DMA of 3D-printed scaffolds was conducted in compression mode, commonly used to mechanically characterize scaffolds obtained by 3D printing (320, 321). The E' of 3D-printed scaffolds was nearly constant for the studied frequency range and, in general, increased with the addition of graphite nanoparticles, as compared to neat PLA, even with the addition of 0.25 wt.% of EG (as received and functionalized). The highest increase in the storage modulus at 37 °C and 1 Hz was observed for PLA+1f-EG and PLA+2[(f-EG)+Ag] exhibiting a storage modulus of 58.4 ± 7 and 61.7 ± 9 MPa, respectively, while the PLA 3D-printed scaffold presented E' = 31.4 ± 10 MPa — Figure 68a, thus representing a 85% and 96% increase, respectively.

Braided scaffolds exhibit a fibrous and more complex geometry, similar to the hierarchical structure of the native ligament (18). Their dynamic mechanical response was tested under tension, as commonly used for testing textile-based scaffolds (11). Composite braided scaffolds possessed higher E' values compared to PLA braided scaffolds, which increased slightly with increasing frequency. An increase in the storage modulus was achieved at 37 °C and 1 Hz for scaffolds reinforced with 0.5 and 1 wt.% of (f-EG)+Ag, reaching 11.1 ± 2 and 7.7 ± 2 MPa, respectively, compared to PLA (2.2 ± 2 MPa), see Figure 68b, representing a 400% and a 250% increase relative to PLA scaffolds, respectively.
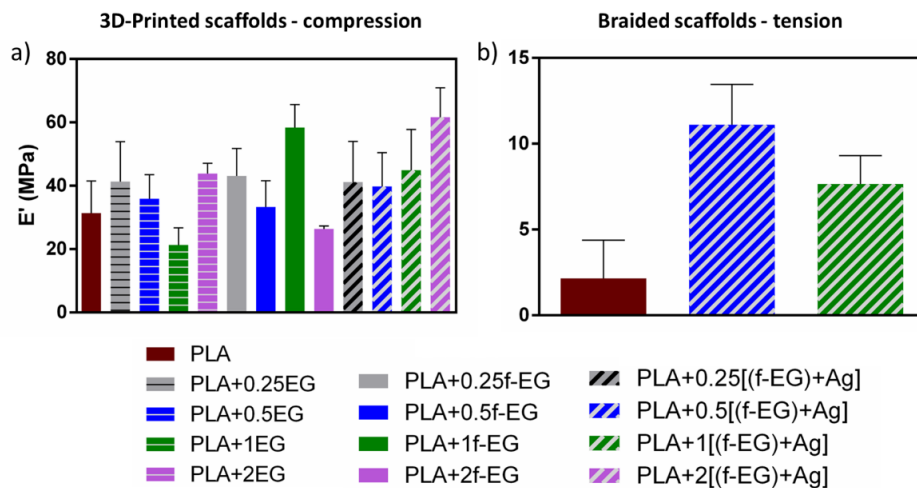
Figure 68 — DMA results for the E' of (**a**) 3D-printed (under compression) and (**b**) braided scaffolds (under tension) at 37 °C and 1 Hz.

The addition of micronized graphite/ few-layer graphene to PLA at low concentrations by melt mixing was reported to produce composites with tensile properties that could be adequate for ligament regeneration applications, without significantly impairing the ductility (322). Similar conclusions were obtained in the present work for compression tests performed on 3D-printed scaffolds about the effect of reinforcement on the composite ductility. The resulting compression stress–strain curves are shown in

Figure 75a1–c1. All scaffolds present an elastic region up to approximately 5% deformation, followed by a plateau region where their load-carrying capacity is maintained and plastic deformation develops as well as structure yielding, followed by a densification region above 40% deformation, similarly to the results described by M. Saleh et al. (323). Thus, from the point of view of ductility and compression strength, the compression test results indicate a similar performance of the 3D printed PLA and composite specimens.

The viscoelastic nature of both 3D-printed and braided scaffolds was also confirmed by the loss factor values of DMA (Figures 66 a2–c2 and 67a2), ranging from 0.02–0.04 and 0.31–0.58, respectively), and suggest that both scaffolds have the capacity to dissipate energy and damping for the tested frequencies (287). The incorporation of fillers also led to a decrease in the damping factor compared to PLA, which is a consequence of the reduced molecular mobility (324).

The storage modulus achieved for the 3D-printed scaffolds is in the same order of magnitude of the dynamic mechanical response reported for ligaments under compression at 1 Hz (325). M. Najafidoust et al. (325) performed dynamic compression mechanical tests in ligaments in a wider range of frequencies (0.01–100 Hz) and at three different preloads (0.25, 0.75, and 2 N). An increase in the storage modulus was observed with increasing preload. At 1 Hz, all samples with different preloads exhibited a storage modulus ranging from approximately 4 to 21 MPa. Other studies measured the viscoelastic properties of ACL (326) and tendons (326, 327) in tension mode, at body temperature and 1 Hz. For instance, J.H. Edwards et al. (327) suggested a xenogeneic tendon intended for ACL replacement and evaluated the dynamic mechanical response of a native and a decellularized tendon. At 1 Hz, the decellularized tendon exhibited a lower storage modulus than the native tendon, but in the same order of magnitude (MPa). The tan delta slightly decreased from 0 to approximately 0.7 Hz and was almost constant from 1 to 2 Hz. These results are similar to those found for the braided scaffolds.

4.4 Conclusions

Composite filaments based on PLA reinforced with EG, f-EG, and (f-EG)+Ag were successfully processed into three-dimensional scaffolds using textile-engineered and 3D printing techniques. The production of 3D-printed scaffolds was faster, easier, and more reproducible compared to braided scaffolds, but all have finely controlled dimensions and geometry. Regardless of the filler, either EG, f-EG or (f-EG)+Ag, a good dispersion and interaction with the polymeric matrix was observed through the cross

section of 3D-printed scaffolds. The anchoring of a small concentration of Ag as an anti-microbial agent was confirmed by EDS on scaffolds reinforced with (f-EG)+Ag. The addition of nanoparticles to the PLA matrix had a very slight effect on pore morphology and size. Three-dimensional-printed scaffolds exhibited a porosity that ranged from 67 to 71% and pore size from 484 to 496 μm. Higher porosity was observed for braided scaffolds compared to 3D-printed scaffolds, ranging from 83–88%, and pore size from 1035 to 1164 μm. Both braided and 3D-printed exhibited a viscoelastic behavior and an increase in the storage modulus for the composite scaffolds compared to neat PLA scaffolds. The highest E' was achieved by the scaffold containing PLA+2[(f-EG)+Ag] (E' = 61.7 ± 9 MPa), among the 3D-printed scaffolds, and the scaffold with PLA+0.5[(f-EG)+Ag] (E' = 11.1 ± 2 MPa), among the braided scaffolds. Both braided and 3D-printed scaffolds exhibited storage modulus values comparable to those measured for ligaments/tendons in tension and compression, as well as high porosity and pore size adequate for ACL regeneration.

4.5 Supplementary materials

Table 23 – Thermogravimetric analysis of composite filaments and the percentage residual weight.

Filament		Fil3D	FilText
		Residue (wt.%)	Residue (wt.%)
PLA		-	-
PLA + 0.25		0.43±0.21	0.20±0.25
PLA + 0.5		0.74±0.22	0.39±0.31
PLA + 1	EG	1.02±0.88	1.14±1.30
PLA + 2		1.44±0.37	2.34±1.74
PLA + 0.25		0.23±0.25	0.48±0.74
PLA + 0.5		0.73±0.16	0.36±0.58
PLA + 1	f-EG	1.13±1.17	1.15±0.26
PLA + 2		2.00±0.96	2.18±1.72
PLA + 0.25		0.26±0.14	0.21±0.85
PLA + 0.5		0.55±0.27	0.53±0.44
PLA + 1	(f-EG)+Ag	1.43±1.40	1.06±1.10
PLA + 2		2.04±0.85	1.02±0.22

Table 24 – MFI of filaments containing PLA and PLA reinforced with 0.5 and 2 wt.% of EG, f-EG and (f-EG)+Ag.

Fil3D		MFI (g/10min)
PLA		14.50 ± 0.86
PLA+0.5	EG	13.22 ± 1.10
PLA+2		15.79 ± 0.89
PLA+0.5	f-EG	10.33 ± 0.73
PLA+2		14.26 ± 1.73
PLA+0.5	(f-EG)+Ag	10.15 ± 0.97
PLA+2		12.09 ± 0.85

Digital microscopy images of the 3D-printed scaffolds at all the compositions of EG, f-EG, and (f-EG)+Ag are displayed in Figure 69-72.
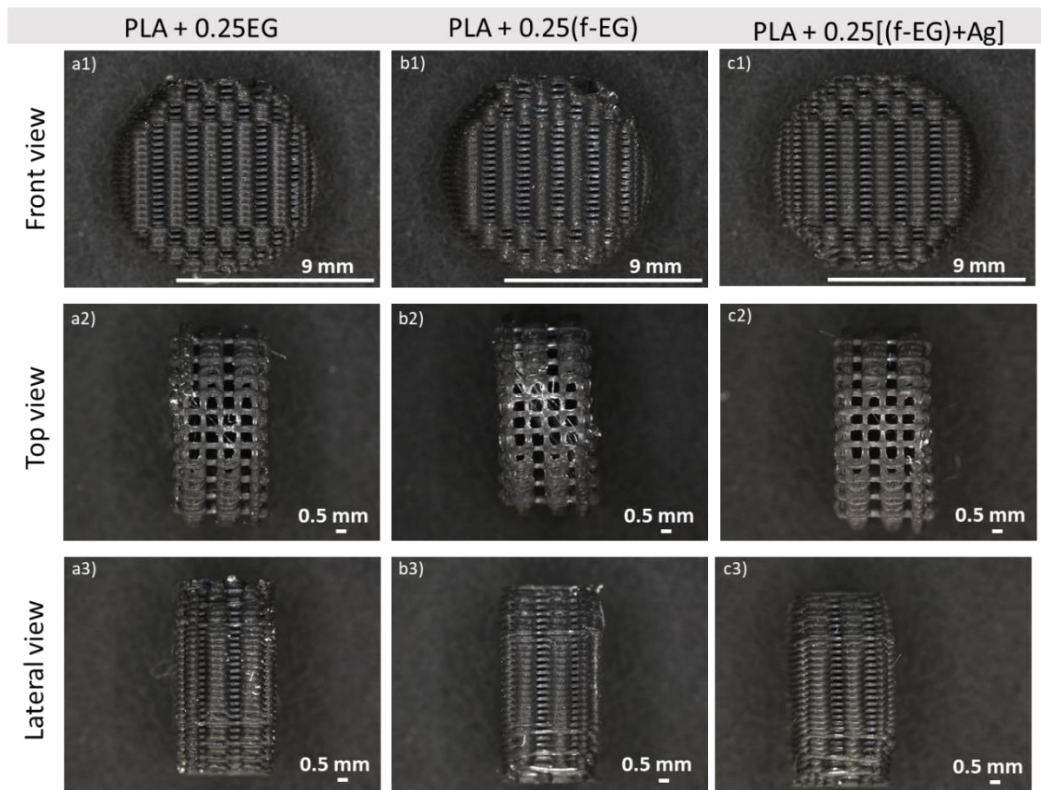
Figure 69– Digital microscopy images of 3D-printed scaffolds containing (a1-a3—PLA+0.25EG; b1-b3—PLA+0.25(f-EG) and c1-c3—PLA+0.25[(f-EG)+Ag]) from a front, top, and side perspectives.
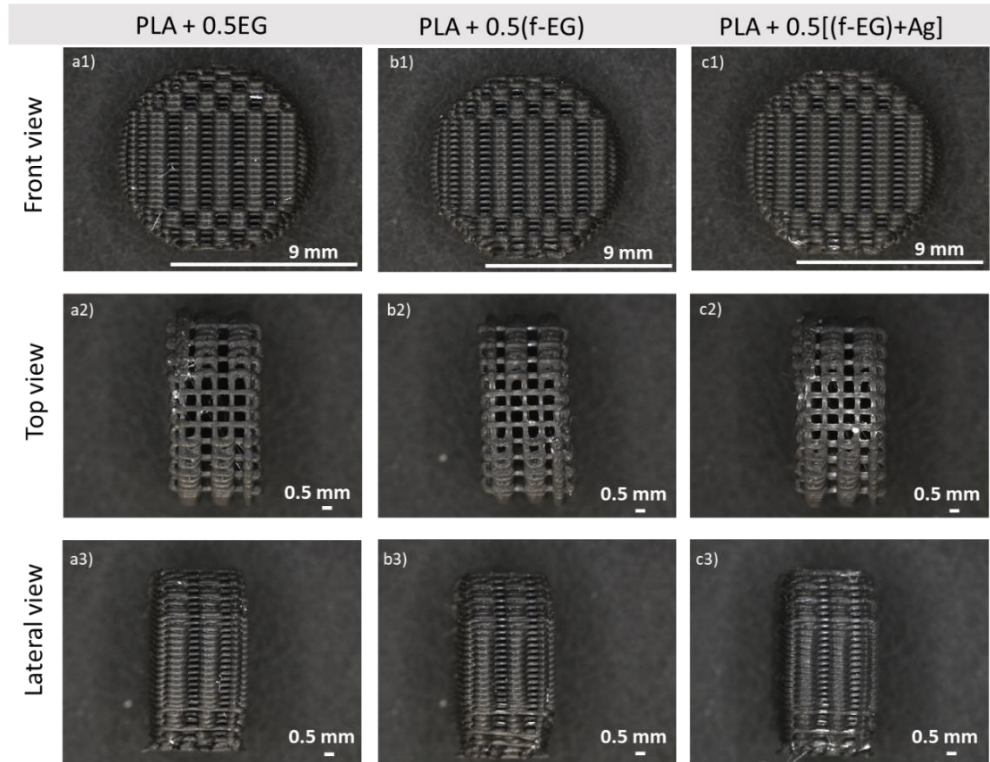
Figure 70 – Digital microscopy images of 3D-printed scaffolds containing (**a1–a3**–PLA+0.5EG; **b1–b3**–PLA+0.5(f-EG) and **c1–c3**–PLA+0.5[(f-EG)+Ag]) from a front, top, and side perspectives.
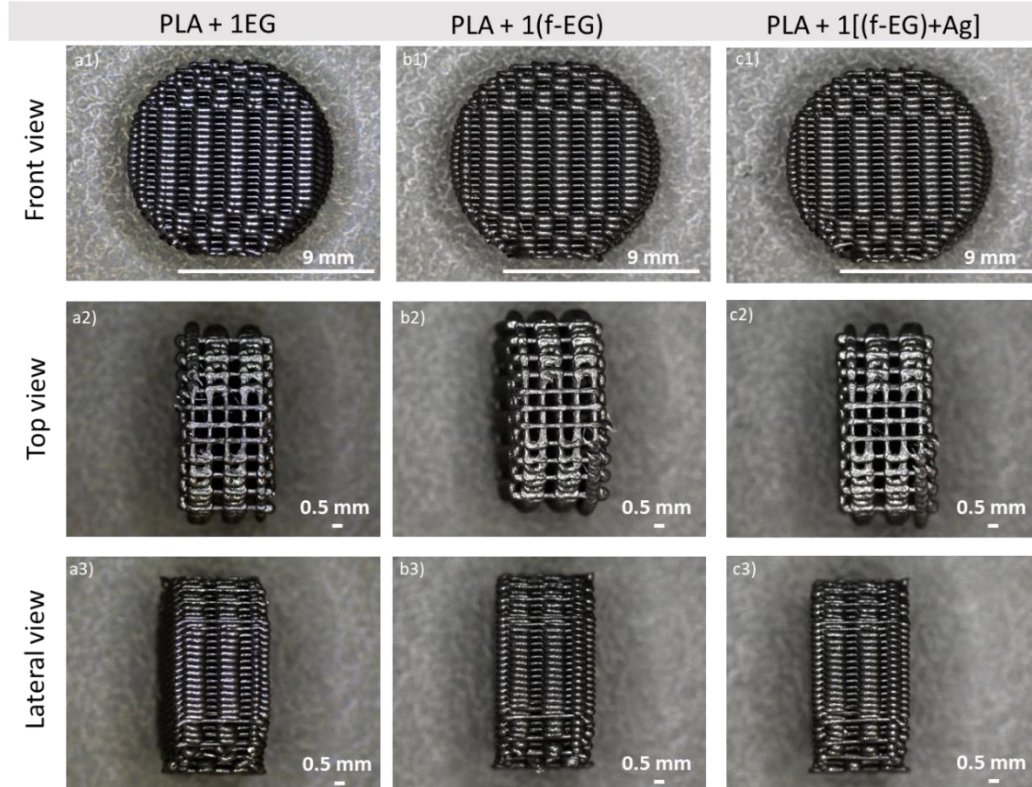
Figure 71 – Digital microscopy images of 3D-printed scaffolds containing (**a1–a3**–PLA+1EG; **b1–b3**–PLA+1(f-EG) and **c1–c3**–PLA+1[(f-EG)+Ag]) from a front, top, and side perspectives.

135
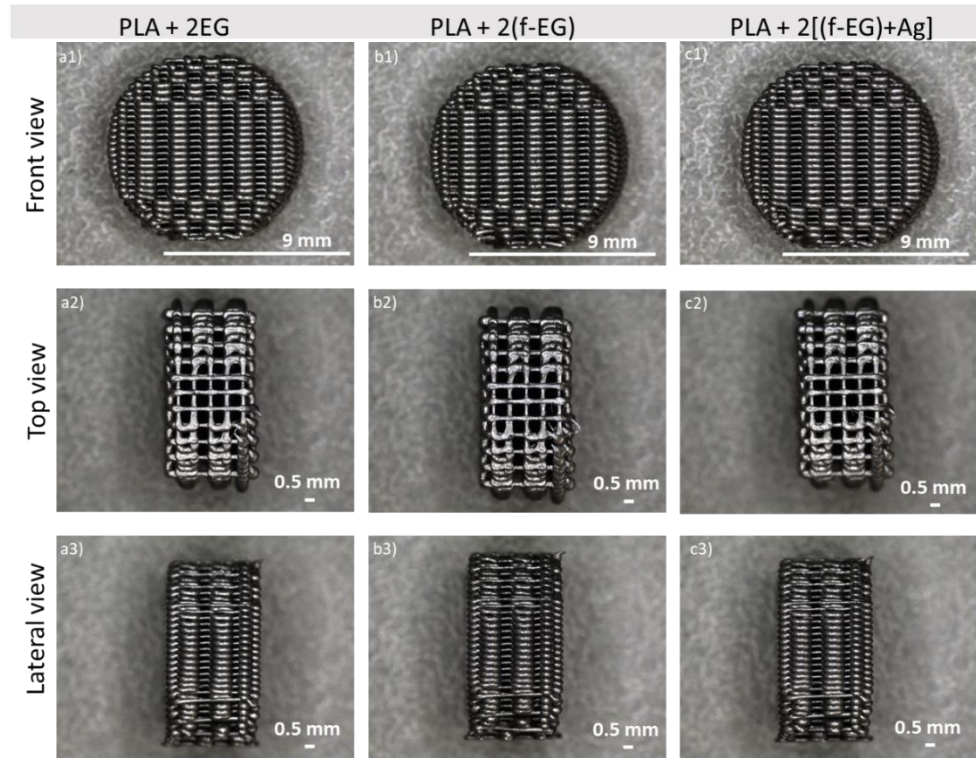
Figure 72 – Digital microscopy images of 3D-printed scaffolds containing: **a1—a3** —PLA+2EG; **b1—b3**—PLA+2(f-EG) and **c1—c3**—PLA+2[(f-EG)+Ag], from a front, top, and side perspectives.

Mean porosity, pore size, and filament thickness of 3D-printed scaffolds containing composites of EG, f-EG, and 0.25–1wt.% of (f-EG)+Ag, calculated from the micro-CT data are presented in Table 25.

Table 25 – Mean porosity, pore size, and filament thickness of 3D-printed scaffolds containing composites of EG, f-EG, and 0.25 and 1wt.% of (f-EG)+Ag, calculated from the micro-CT data.

3D-Printed Scaffold		Mean Porosity (%)	Mean filament thickness (µm)	Mean pore size (µm)
PLA		66.8 ± 1.5	240 ± 3	484 ± 4
PLA+0.25	EG	69.2 ± 0.8	248 ± 17	494 ± 2
PLA+0.5		70.2 ± 2.9	233 ± 5	515 ± 25
PLA+1		69.68 ± 0.9	235 ± 9	492 ± 29
PLA+2		70.29 ± 2.5	228 ± 16	486 ± 44
PLA+0.25	f-EG	75.41 ± 1.5	212 ± 7	539 ± 11
PLA+0.5		73.38 ± 4.3	218 ± 14	517 ± 29
PLA+1		68.73 ± 0.9	249 ± 12	485 ± 2
PLA+2		70.4 ± 1.1	235 ± 10	496 ± 20
PLA+0.25	(f-EG)+Ag	70.5 ± 1.4	234 ± 13	508 ± 10
PLA+1		70.8 ± 3.3	271 ± 7	530 ± 46

Micro-CT cross-section images of the 3D-printed scaffolds containing 0.25, 0.5 and 1 wt.% of EG, f-EG and (f-EG)+Ag are displayed in Figure 73.
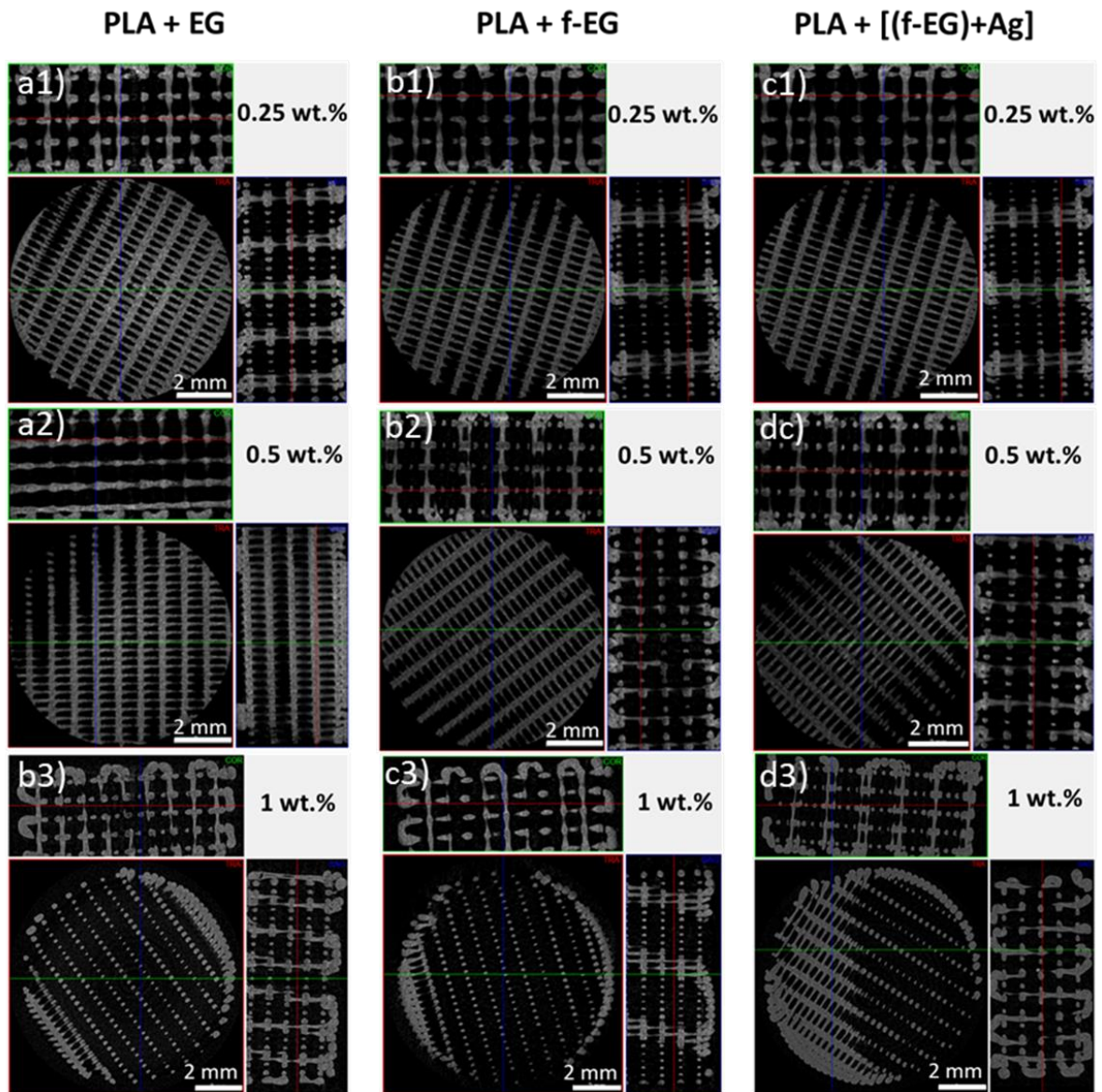
Figure 73 – Representative micro-CT cross-sections images of the 3D-printed scaffolds containing PLA reinforced with 0.25, 0.5, 1 wt.% of EG, f-EG and (f-EG)+Ag.

Micrografs of 3D-printed scaffolds reinforced with 1 wt.% EG, f-EG and (f-EG)+Ag are displayed in Figure 74.
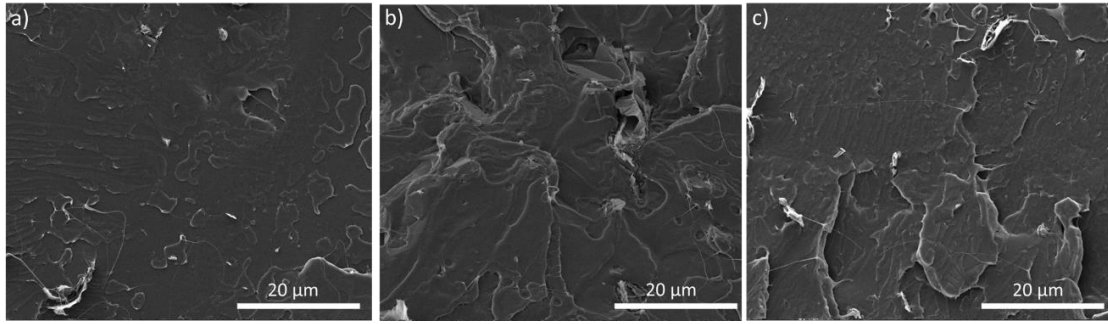
Figure 74 – SEM images of 3D-printed scaffolds: **a**—PLA+1EG; **b**— PLA+1f-EG and **c**— PLA+1[(f-EG)+Ag].

Scaffold stress-strain curve of the 3D-printed scaffolds containing 0.25, 0.5, 1 and 2 wt.% of EG, f-EG and (f-EG)+Ag are displayed in Figure 75.
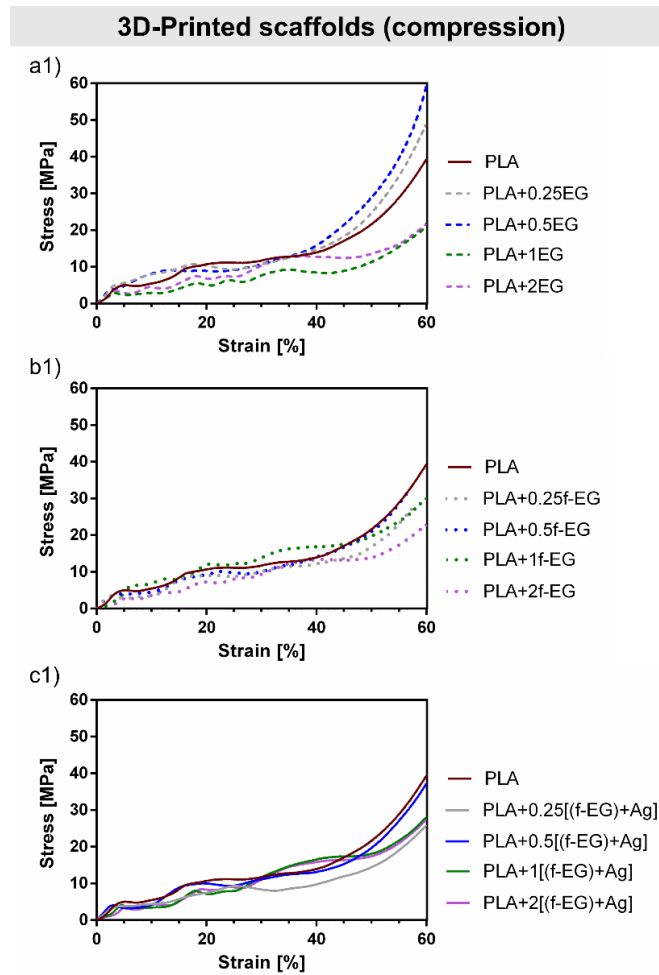
Figure 75 – Compressive tests of 3D-printed scaffolds containing PLA and **a1**— EG, **b1**— f-EG and **c1**— (f-EG)+Ag

CHAPTER **5**

Biocompatible 3D-Printed Tendon/Ligament Scaffolds

Based on Polylactic Acid /Graphite Nanoplatelet

Composites

This chapter is based on the article:

Silva M, Gomes S, Correia C, Peixoto D, Vinhas A, Rodrigues MT, Gomes ME, Covas JA, Paiva MC, Alves NM. Biocompatible 3D-Printed Tendon/Ligament Scaffolds Based on Polylactic Acid/Graphite Nanoplatelet Composites. Nanomaterials. 2023, 13, 2518. https://doi.org/10.3390/nano13182518 .

5 Biocompatible 3D-Printed Tendon/Ligament Scaffolds Based on Polylactic Acid /Graphite Nanoplatelet Composites

3D printing technology has become a popular tool to produce complex structures. It has great potential in the regenerative medicine field to produce customizable and reproducible scaffolds with high control of dimensions and porosity. This study was focused on the investigation of new biocompatible and biodegradable 3D-printed scaffolds with suitable mechanical properties to assist ligament/tendon and ligament regeneration. PLA scaffolds were reinforced with 0.5 wt.% of functionalized graphite nanoplatelets decorated with silver nanoparticles ((f-EG)+Ag). The functionalization of graphene was carried out to strengthen the interface with the polymer. (f-EG)+Ag exhibited antibacterial properties against *Staphylococcus aureus* (*S. aureus*) and *Escherichia coli* (*E. coli*), an important feature for the healing process and prevention of bacterial infections. The scaffolds' structure, biodegradation, and mechanical properties were assessed to confirm their suitability for tendon and ligament/tendon regeneration. All scaffolds exhibited surface nanoroughness created during printing, which was increased by the filler presence. The wet state dynamic mechanical analysis proved that the incorporation of reinforcement led to an increase in the storage modulus, compared with neat PLA. The cytotoxicity assays using L929 fibroblasts showed that the scaffolds were biocompatible. The PLA+[(f-EG)+Ag] scaffolds were also loaded with human tendon-derived cells and showed their capability to maintain the tenogenic commitment with an increase in the gene expression of specific tendon/ligament-related markers. The results demonstrate the potential application of these new 3D-printed nanocomposite scaffolds for tendon and ligament regeneration.

5.1 Introduction

In recent years, 3D printing has emerged as tool for the production of complex and personalized products, built layer-by-layer, and with the advantages of low cost and easy operation (118, 328). Three-dimensional printing finds great potential applications in the medical field, in particular in TE, to produce scaffolds with complex and reproducible geometries, allowing excellent control of porosity and pore size, which is not possible with traditional manufacturing processes. It also provides the possibility to create customized, patient-specific scaffolds (328-331). FDM also known as fused filament fabrication (FFF), is

the most commonly used material extrusion 3D printing method, presenting several advantages compared with other techniques (331). It is reliable, cheap and does not require solvents (235).

Tendon/ligament injuries are one of the most prevailing health problems that affect the adult population worldwide (315). Various materials and strategies have been suggested to find a scaffold that can help the regeneration of these tissues, restoring their function when severely injured (91). It has been reported that highly porous scaffolds with interconnected pores are essential for nutrient and oxygen diffusion, waste removal and cell proliferation (329, 332). In addition, the degradation rate of the implant should match the rate of the new tissue formation, allowing it to receive the appropriate level of mechanical load from the scaffold (332, 333).

PLA is routinely used for medical applications such as sutures or orthopedic fixation devices (235), being slowly degraded and fully reabsorbed (334). It is made from bio-based monomers that are obtained from corn or cellulose (235) with easy modulation of its physical and biochemical features by blending with different nanofillers (334). The mixing or in situ modification with toughening agents, flame retardants, and anti-UV agents have been used to address the unfavorable inherent qualities of PLA (i.e., poor toughness, inflammability, and UV aging) and achieve high-performance PLA composites. However, the addition of these additives may increase the economic cost or even reduce the PLA mechanical properties due their agglomeration (335). A new bio-based porphyrins approach was suggested by Yang and co-workers (335) to improve PLA's overall multifunctional performance. The incorporation of only 3 wt. % of vanillin-based porphyrin (VPR) not only enhanced the anti-UV and flame-retardant properties but also enabled significant toughening of the PLA/VPR composites as well as improvements of elongation at break and impact strength. This strategy greatly increases the versatility of PLA composites (335). Formulations based on PLA have been widely proposed for tendon/ligament regeneration (7, 77), but there are very few studies about the use of material extrusion 3D printing for this application (328, 336, 337), being mainly focused on screw-like scaffolds to help tendon-bone healing after ACL reconstruction (328, 337). This ligament holds a commonly accepted relevance because of the huge related number of injuries and reconstructive surgeries (115).

There has been an increased interest in the use of graphene-based materials such as GNPs and CNTs for different tissue engineering applications such as cardiac, neural and tendon/ligament regeneration, mainly focusing their reinforcing effect on polymer composites (115, 315). For instance, Belaid et al. (235) produced 3D-printed scaffolds based on PLA-GO. Tensile testing demonstrated 30 % increase of the Young's modulus with the incorporation of 0.3 wt.% GO. Composite scaffolds also

promoted bone cell attachment, proliferation, and differentiation (235). In fact, the nanoscale dimension of graphene matches the cell surface receptors and ECM nanotopography, promoting the adhesion and proliferation of various types of cells. In addition, graphene-based scaffolds may also exhibit additional functional properties such as enhanced electrical conductivity, which may be beneficial for the cellular growth and stimulation of the healing process (315, 334). However, each application involving the addition of graphene in the human body should always be carefully investigated because it was observed to have a size, shape, and concentration-time-dependent cytotoxicity (315, 334). It is commonly accepted that using small loadings of graphene materials such as graphene nanoplatelets (composed of single-layer and few-layer graphene) can be effective in the reinforcement of polymeric matrices such as PLA and do not present cytotoxicity (115, 235, 283, 334). When the polymer matrix is a biomaterial, the possibility of a toxic effect of the fillers is even diminished (195). Moreover, the functionalization of graphene is of great importance for the scaffold success. The presence of functional groups may enable stronger interactions with the matrix, thus improving simultaneously the reinforcing ability and biocompatibility (115, 315).

An effective strategy to reduce the risk of infection is to confer antibacterial properties to the implant (338). Silver nanoparticles (AgNPs) have been extensively combined with inorganic materials and biopolymers to produce 3D-printed scaffolds with antibacterial activity (339, 340).

The objective of this work was the production of 3D-printed scaffolds with controllable dimensions and good mechanical properties to help tendon and ligament regeneration, as well as their *in vitro* investigation. We functionalized the GNPs via a DCA reaction of an azomethine ylide, which bonds pyrrolidine groups onto the graphene surface to form amide bonds with the ester groups of PLA under the composite processing conditions (263, 304). Silver nanoparticles were also produced by reducing silver nitrate ($AgNO_3$) in DMF and used to decorate the functionalized graphene (274). A synergetic effect of silver and graphene properties may also occur, such as reported by Kumar S. et al. (341), who produced sheets of reduced GO decorated with silver with improved electrical and antibacterial properties.

Composite filaments based on medical-grade PLA containing a low content (0.5 wt.%) of functionalized and Ag-decorated few-layer graphene were produced and applied to form 3D-printed parts, obtaining porous and reproducible scaffolds. The antibacterial efficiency against Gram-positive and Gram-negative bacteria was confirmed. The mechanical performance and biodegradation of 3D-printed scaffolds were evaluated under physiological conditions, as well as their biocompatibility using L929 cells. The scaffolds were loaded with human tendon-derived stem cells, to investigate the tenogenic commitment

and to analyze gene expression of specific tendon/ligament-related markers. The results are promising and will hopefully widen the application of 3D-printed devices for tissue engineering and demonstrate their potential use in tendon and ligament healing and regeneration.

5.2 Materials and Methods

5.2.1 Materials

Medical-grade PLA pellets (PURASORB® PL10) were purchased from Corbion, Gorinchem, The Netherlands. The PLA exhibited an inherent viscosity in the range 0.9–1.2 dL/g and melting point between 170 and 200 °C. Micrograf HC11, a micronized graphite with a purity of 99.5%, equivalent diameter of approximately 10 μm, and few tens of nanometers of thickness, will be referred, throughout the text, as EG and was purchased from Nacional de Grafite Lda, Itapecerica, MG, Brazil.

EG was functionalized by the DCA reaction as described previously (304) using a functionalization time of 3 h at 250 °C. The decoration of f-EG with silver nanoparticles was achieved by the reduction reaction of silver ions (Ag^+). The detailed procedures and characterization were previously described (304).

5.2.2 Antimicrobial potential of functionalized graphite

The antibacterial properties of different graphite nanoplatelets (EG, f-EG, and (f-EG)+Ag) were evaluated directly against microorganisms of clinical relevance, namely, Gram-positive *Staphylococcus aureus* (*S. aureus*) (ATCC 25923) and Gram-negative *Escherichia coli* (*E.coli*) (ATCC 25922). First, *E. coli* and *S. aureus* strains were cultured on Mueller Hinton Broth (MHB) at 37 °C and 60 rpm, and the microbial suspension was adjusted to 1.0×10^6 CFU/mL. Then, different EGs were sterilized using 1 h of UV lights and dispersed in a sterilized MHB medium to obtain a concentration of 2% *w/v*. The different EG and EG derivatives suspensions were sonicated 1 h before the assay, and then several dilutions were prepared for the tests (1.00, 0.50, 0.25, 0.10, 0.050, and 0.025% *w/v*).

In a 96-well plate, 50 μL of the bacterial suspension was added to 50 μL of the different concentrations of EGs suspensions. The plate was incubated at 37 °C for 24 h. Then, aliquots from each well (10 μL) were added onto the surface of nutrient Mueller Hinton agar (MHA) and incubated at 37 °C for 24 h. The minimal bactericidal concentration (MBC) was determined as the lowest concentration that showed no bacterial growth on the agar plate. Several controls were used: a bacterial suspension without

EGs, a bacterial suspension with Kanamycine (5% *w/v*), and different EGs suspensions without a bacterial suspension. All assays were performed in triplicate. The obtained results allowed the selection of the percentage of EGs for composites' preparation.

5.2.3 Filaments Production and Characterization

According to the literature, low concentrations of GNPs did not present *in vitro* cytotoxicity and may be incorporated safely in PLA to improve aspects relevant for biomedical applications, such as mechanical properties (283, 342). Based on this consideration and the antibacterial results, we fixed the filler content at 0.5 wt.%. To ensure a good dispersion of the reinforcements in the polymer, a pre-mixing of PLA pellets with 0.5 wt.% of EG, f-EG, and (f-EG)+Ag was prepared by manual mixing. The PLA and PLA composite filaments were obtained by using melt extrusion on a co-rotating twin-screw extruder (Microlab Rondol, Nancy, France) equipped with intermeshing screws containing three mixing zones, using a screw speed of 43 rpm and a temperature profile 135/185/$\simeq$160 °C (feed/barrel/die). The extrudate diameter was controlled using two pulling rolls, distanced approximately 25 and 60 cm from the shaping die, respectively. The extrusion process followed the procedure described before (304) under nitrogen atmosphere, as recommended by the polymer manufacturer, to minimize polymer degradation. The detailed processing conditions for each material are presented in Table 28, where pulling roll 1 was located next to the extruder die and allowed to produce filaments with approximately 1.75 ± 0.25 mm, suitable for FDM.

Scanning electron microscopy and energy dispersive spectroscopy (SEM/EDS) were carried out on a FEI Nova 200 FEG-SEM/EDS (FEI Europe Company, Hillsboro, OR, USA) to analyze the coating of the PLA pellets with EG and EG derivatives and to observe the cross-sections of the 3D printing filaments produced. The MFI of all filaments was measured at 190 °C using a load of 2.16 kg on MFI equipment from Daventest (Welwyn Garden City, UK).

High-definition Kelvin force microscopy (HD-KFM) was used to assess the surface electric potential of the PLA+0.5[(f-EG)+Ag] filament, using a Nano-Observer AFM microscope, CSInstruments (Les Ulis, France). The measurements were carried out on longitudinal sections of composite filaments (10 × 10 μm), using a 1V AC signal, at 53 KHz applied to the surface.

5.2.4 Scaffolds Production and Characterization

The 3D-printed scaffolds were designed using the Ultimaker Cura (version 4.4, Ultimaker, Geldermalsen, The Netherlands) software and printed horizontally using an Ender-3 3D Printer from Creality (London, UK). The printing parameters are given in Table 26. The scaffolds exhibited a cylindrical shape with a full length of approximately 32 mm and a diameter of 9 mm, which were comparable to the dimensions of the native ACL. Smaller specimens with an approximate diameter of 9 mm and 4 mm of thickness were also produced for further testing.

Table 26 – Printing settings used for printing PLA and PLA composite scaffolds.

Printing Parameters	
Nozzle diameter	0.4 mm
Nozzle temperature	190 °C
Bed temperature	80 °C
Printing speed	45 mm.s^{-1}
Layer height	0.15 mm
Infill distance	0.8 mm
Infill density	50%
Infill pattern	Lines
Infill lines direction	0°; 90°
Support contact angle	5°

5.2.4.1 Physical and Morphological Analysis of Scaffolds

The scaffolds' morphology as well as the pore size and distribution were analyzed using a Leica DMS1000 digital microscope (Wetzlar, Germany). The average pore size for each scaffold was obtained by running Image J software (version 1.52, National Institutes of Health, Bethesda, MA, USA) on the digital microscopy images. Perpendicular lines at 15 pores from one border of the pore toward the other were measured by the software, at the top, front, and lateral views of the scaffold. Each measurement was taken using the green channel and with improved contrast.

The porosity of the as-prepared 3D scaffolds was determined using the liquid displacement method similar to that reported by Guan et al. (343) and Zhang and Ma (344). Ethanol was chosen as a displacement liquid because it could permeate through the porous scaffolds and did not induce swelling or shrinking of the material. Each scaffold was immersed in a cylinder containing a known volume of ethanol ($V1$). The sample was kept soaked in ethanol for 5 min. Then, the ethanol was pressed to force air from the scaffold and to penetrate and fill the pores. The total volume of ethanol and the ethanol-

impregnated scaffold was recorded as *V2*. The ethanol-impregnated scaffold was removed from the cylinder, and the residual ethanol volume was recorded as *V3*. The porosity of the scaffold (%) was given by

$$Porosity\,(\%) = \left(\frac{V1-V3}{V2-V3}\right) \times 100 \qquad (3)$$

The average of three measurements was taken for each sample. To confirm a homogenous dispersion of EG and EG derivatives on the PLA, the 3D-printed scaffolds were cryo-fractured, and the scaffold cross-sections were sputter-coated with gold and observed by using SEM/EDS on a FEI Nova 200 FEG-SEM/EDS (FEI Europe Company, Hillsboro, OR, USA).

The topography and roughness of the PLA and PLA+[(f-EG)+Ag] scaffolds were determined at the outer layer of the measured scaffolds. The measurements were performed by using a Nano-Observer AFM, CSInstruments (Les Ulis, France), and the operation mode was oscillating, with an amplitude of 5V and automatic frequency around 60 KHz. AFM topography images with dimension (10 × 10) μm^2 were obtained. The root mean square (RMS) surface roughness was calculated by using the statistical tool in the Gwyddion software. This represented the standard deviation of the distribution of surface heights, and it was more sensitive than the arithmetic average height (Ra) to large deviation from the mean line. At least three measurements were performed for each type of scaffold.

5.2.4.2 Mechanical/Viscoelastic Properties

The DMA was carried out to evaluate the mechanical performance and viscoelastic properties of the scaffolds subjected to cyclic loading and immersed in physiologic fluids. The scaffolds were previously soaked overnight in a PBS solution at 37 °C. The DMA analysis was performed using TRITEC2000B equipment (Triton Technology, Grantham, UK) in the compressive mode. The DMA spectra were obtained at the same temperature, applying cycles of increasing frequency from 0.1 to 16 Hz. At least three samples were tested for each composition and scaffold type.

5.2.4.3 Biodegradation

The degradation rates of different scaffolds (9 mm of diameter and 4 mm of thickness) were evaluated *in vitro* by measuring their initial weight and soaking them into PBS (pH = 7.4, Sigma-Aldrich, Saint Louis, MO, USA) at 37 °C. The PBS solution was changed every 3 days. At predefined periods (15 days, 6 weeks, and 12 weeks) the samples were removed from the solution, washed with distilled water

to remove the excess salts, and dried at 37 °C for 2 days. The mass loss was calculated using the following equation:

$$Weight\ loss(\%) = \left(\frac{M_i - M_f}{M_i}\right) \times 100 \qquad (4)$$

where M_i and M_f are the weights of the scaffolds before and after degradation, respectively. Three replicates per composition were analyzed, and the results are presented as an averaged value ± standard deviation.

Specimens of PLA and PLA+0.5EG/f-EG/(f-EG)+Ag were also observed by SEM and compared with images of non-degraded samples, to identify the surface erosion after 12 weeks of hydrolytic degradation. To evaluate the changes in the mechanical properties after the complete degradation period, the scaffolds (n = 3 or 4 per scaffold composition per time point) were immersed in 1 mL of PBS (pH = 7.4) at 37 °C overnight and tested by dynamical mechanical analysis, using the method described above.

5.2.4.4 Biological Assays—L929 Cell Line

Cell seeding. For the *in vitro* cell studies, L929 mouse fibroblast-like cells (NCTC clone 929, ATCC® CCL-1™, acquired from ATCC® (Manassas, VA, USA), passage P26) were cultured in Dulbecco's modified minimum essential medium (low glucose DMEM, Sigma-Aldrich, Saint Louis, MO, USA) supplemented with 10% fetal bovine serum (FBS, Life Technologies, Paisley, UK) and 1% of an Antibiotic-Antimycotic (A/A) solution (Life Technologies, Paisley, UK), in 150 cm^2 tissue culture flasks. The cells were maintained in a humidified air atmosphere containing 5% CO_2 at 37 °C to grow, and the medium was replaced every 3 days until a 90% confluence was reached. Then, the cells were washed with Dulbecco's phosphate buffered saline (DPBS, Life technologies, Carlsbad, CA, USA) and detached with 5 mL of trypLE™ express solution (Life technologies, Paisley, UK) for 5 min at 37 °C. An amount of 10 mL of culture medium was added to inactivate the trypLE™. The cells were centrifuged at 300 rcf for 5 min, and the obtained pellet was resuspended in the culture medium.

Before the cell seeding, the scaffolds (diameter = 9 mm, thickness = 4 mm) were sterilized by immersion in 70% ethanol (*v/v*) for 1 h and by exposition to UV light, for 30 min on both sides.

The sterile scaffolds were placed in a 24-wells suspension culture plate, and 200 µL of a cell suspension in DMEM culture medium (2 × 10^5) was added to each well. The samples were then incubated at 37 °C in a humidified air atmosphere of 5% CO_2. After 4 h of seeding, fresh culture medium was added

to each well until reaching 1 mL of volume. The seeding procedure was also applied on tissue culture polystyrene (TCPS, Sarstedt, Singapore) to be used as a positive control.

Live/Dead staining. The viability of the L929 cells was evaluated by Calcein AM (ThermoFisher Scientific, Bleiswijk, The Netherlands) and Propidium Iodide (PI) (ThermoFisher Scientific, Bleiswijk, The Netherlands) staining. Before staining, at each time point (1, 3, 7, and 14 days of culture), the culture medium was removed, and each sample was immersed with 1 mL of DMEM medium supplemented with 2 μg Calcein AM and 1 μg PI, for 30 min, in the dark. After that, the samples were washed with PBS and analyzed using an inverted confocal microscope with incubation (TCS SP8, Leica, Germany). All experiments were performed in triplicate.

SEM. The attachment and morphology of L929 cells were analyzed by SEM. The scaffolds were removed from the wells after 1, 3, 7, and 14 days of culture; washed with PBS; and then fixed with 2.5% glutaraldehyde (Sigma-Aldrich, Saint Louis, MO, USA) for 2 h. After dehydration in a graded series of ethanol (50%, 70%, 80%, 90%, and 100%) and thermostatic drying, the scaffolds were gold sputtered for analysis.

DAPI-Phalloidin staining. The morphology and cytoskeletal organization of the cells was visualized by fluorescent microscopy after staining with phalloidin tetramethylrhodamine and 4′,6-diami-dino-2-phenylindole (DAPI, Sigma-Aldrich, Saint Louis, MO, USA). After 1, 3, 7, and 14 days of culture, the medium was removed and washed with PBS fixed by using neutral buffered formalin (10%, ThermoFisher Scientific, Waltham, MA, USA) for 30 min. Then, the fixed samples were permeabilized using Triton X-100 (0.2% v/v in PBS, Sigma-Aldrich, Saint Louis, MO, USA) for 5 min and immersed in bovine serum albumin (BSA, 3% w/v in PBS, Sigma-Aldrich, Saint Louis, MO, USA) for 30 min. The seeded scaffolds were stained with DAPI (1:1000 in PBS, pH = 7.4) for 5 min and rhodamine-phalloidin (1:100 in PBS, pH = 7.4, Sigma Aldrich, Saint Louis, MO, USA) for 30 min. The samples were extensively washed with PBS and analyzed using an AiryScan 2 confocal microscope (LSM 980, Zeiss, Germany).

Alamar blue. The metabolic activity of the cells was determined by using the Alamar blue method for 1, 3, 7, and 14 days of culture. After each time point, the culture medium was removed, and a fresh medium supplemented with 20% of Alamar blue reagent (Bio-Rad, Hercules, CA, USA) was added to the cultured scaffolds. The samples were incubated in the dark, for 4 h, at 37 °C, in a humidified air atmosphere of 5% CO_2. Following this, 100 μL of each solution was transferred to a 96-well black plate to measure the fluorescence at the 590 nm emission wavelength and the 530 nm excitation wavelength using a microplate reader (BIO-TEK Instruments, Winooski, VT, USA).

5.2.4.5 Biological Assays—Human Tendon-Derived Cells

Human tendon-derived cells (hTDCs)—Isolation and Culture. The hTDCs were isolated from tendon surplus samples under established protocols with Hospital da Prelada (Porto, Portugal). The samples were provided with the informed consent of the patients, and the procedures were reviewed and approved by the Hospital Ethics Committee (P.I. No. 005/2019). The hTDCs were isolated and cultured as previously described (345-348). First, the tissue explants were dropwise rinsed in a sterile solution of PBS. The excess of PBS was eliminated using a filtration system for 50 mL tubes (Falcon). The tissue samples were mechanically minced and placed into a 50 mL tube with an enzymatic solution consisting of collagenase (0.1%, Sigma-Aldrich, C6885, Saint Louis, MO, USA), 2 M $CaCl_2$ (1:1000, VWR, Darmstadt, Germany), and 1% BSA (Sigma-Aldrich, Saint Louis, MO, USA), followed by a 1 h incubation at 37 °C under agitation. The digested tissue was centrifuged three times at 290 g for 5 min. The pellet of hTDCs was then expanded in a complete culture medium consisting of a medium essential alpha (α-MEM, Invitrogen, Life Technologies Limited, Paisley, UK) supplemented with 10% FBS (Life Technologies) and 1% A/A in humidified 5% CO_2 atmosphere and used at passage 1–3.

Cell culture on PLA and PLA+0.5[(f-EG)+Ag] scaffolds. The hTDCs were seeded at a density of 1.2×10^5 cells per scaffold and cultured in α-MEM medium for 7 and 14 days in humidified 5% CO_2 atmosphere. Two experimental conditions were considered in which the hTDCs were seeded on i) PLA scaffolds or ii) PLA+0.5[(f-EG)+Ag] scaffolds to investigate the potential of these scaffolds for tendon/ligament applications. The hTDCs' response was investigated by assessing tendon-associated markers at the gene and protein levels.

RNA Extraction and Real-Time RT-qPCR. The total ribonucleic acid (RNA) was extracted using the RNeasy Mini Kit (Qiagen, Hilden, Germany) following the manufacturer's instructions and was quantified using a Nanodrop® ND-1000 spectrophotometer (ThermoFisher Scientific, Wilmington, NC, USA) at 260/280 nm. Complementary DNA was synthesized from 1 μg of RNA of each sample using a qScript™ cDNA Synthesis Kit (Quanta Biosciences, Gaithersburg, MD, USA) according to the manufacturer's protocol using a Mastercycler® Realplex (Eppendorf, Hamburg, Germany). The transcripts quantification presented in Table 29 was carried out via quantitative polymerase chain reaction (qPCR) using the PerfeCTA SYBR Green FastMix Kit (Quanta Biosciences, Gaithersburg, MD, USA) according to the kit instructions in a Real-Time Mastercycler ep realplex thermocycler (Eppendorf, Hamburg, Germany). Glyceraldehyde-3-phosphate dehydrogenase (GAPDH) was used as reference genes. The relative expression level was calculated using the $2^{-\Delta\Delta Ct}$ method for each target gene (349).

Immunofluorescence of tendon-related markers in 3D scaffolds. The hTDCs cultured on the 3D scaffolds were fixed with 10% (v/v) neutral buffered formalin (ThermoFisher Scientific, Waltham, MA, USA) and permeabilized with 0.025% (v/v) Triton X-100 (Sigma-Aldrich, Saint Louis, MO, USA) in PBS for 10 min. Afterward, the samples were washed three times with PBS, blocked with Normal Horse Serum (RTU Vectastin Kit, PK-7200, Vector, Burlingame, CA, USA), and incubated overnight at 4 °C with antibodies against Tenomodulin (TNMD, Rabbit anti-human, ab81328, 1:100, Abcam, Cambridge, UK), Scleraxis (SCX, Rabbit polyclonal anti-SCX, ab58655, 1:100, Abcam, Cambridge, UK), and Collagen type I (COL1, Rabbit polyclonal anti-COL1, 47972, 1:100, Novus Biologicals™, ThermoFisher Scientific, Waltham, MA, USA). Subsequently, the samples were washed in PBS and incubated with anti-rabbit Alexa Fluor 488-fluorescent secondary antibody or anti-rabbit Alexa Fluor 594 antibodies (ThermoFisher Scientific, Waltham, MA, USA) for 1 h at RT. All antibodies were diluted in 0.1% BSA/PBS. The samples were rinsed with PBS and stained with DAPI (5 mg/mL, D9564, Sigma-Aldrich, Saint Louis, MO, USA) for 10 min. The immunolabeled samples were observed by confocal laser scanning microscopy (CLSM, TCS SP8, Leica, Wetzlar, Germany).

5.2.5 Statistical Analysis

The presented data were expressed as the mean ± standard deviation (SD) of at least three replicates, except for RT-PCR analysis, which was expressed as the mean ± standard error of the mean of two independent experiments (n = 2). The error bars presented in the graphs denote the SD. The statistical analysis was performed using the GraphPad Prism6 software from Windows. The statistical significance was evaluated by one-way ANOVA after performing the Shapiro–Wilk test for normal distribution and by two-away ANOVA followed by Bonferroni post hoc test multiple comparison tests for RT-PCR. A difference was considered significant with a confidence interval of 95% for different degrees of confidence, $p < 0.05$ (*), $p < 0.01$ (**), $p < 0.001$ (***), and $p < 0.0001$ (****).

5.3 Results and Discussion

5.3.1 Antimicrobial Potential

The potential antimicrobial activity of EG and EG derivatives against *E. coli* and *S. aureus* was tested, and the results obtained after 24 h are presented in Table 27. Soft agar plates incubated with the

suspensions of bacteria and different concentrations of EG and EG derivatives observed after 24 h, as well as positive and negative controls, are shown in Figure 86.

Table 27 – Presence (+) or absence (−) of E. coli and S. aureus at concentrations (0.025–1%) of different EGs.

	Concentration (%)	*E. coli*	*S. aureus*
EG	1	+	+
	0.5	+	+
	0.25	+	+
	0.1	+	+
	0.05	+	+
	0.025	+	+
f-EG	1	+	+
	0.5	+	+
	0.25	+	+
	0.1	+	+
	0.05	+	+
	0.025	+	+
(f-EG)+Ag	1	−	−
	0.5	−	−
	0.25	−	−
	0.1	−	+
	0.05	+	+
	0.025	+	+

Bacterial colonies of both *E. coli* and *S. aureus* were found in the presence of EG and f-EG, at different concentrations. However, no bacterial growth of *S. aureus* or *E. coli* was observed for 0.25 up to 1% of (f-EG)+Ag. The MBC of (f-EG)+Ag was 0.25% for *S. aureus*, while for *E. coli* it was only 0.1%. These results provided evidence that the presence of silver nanoparticles conferred antimicrobial properties against these two bacteria strains. This is in agreement with the literature that reports the antibacterial efficacy of silver-containing materials such as PLA fibrous membranes for tendon repair (270) and even composite mats of PLA-GO with antibacterial effects against *E. coli* and *S. aureus* (350). Although the mechanism of the antibacterial action of AgNPs is not fully understood, it is suggested that silver ions could interact with bacterial cells in several ways (338), such as disturbing the permeability of the cells wall or even penetrating them, causing damage and changing the microbial DNA and proteins (338).

5.3.2 Filaments' Production and Characterization

A pre-coating of the PLA pellets with EG and EG derivatives was applied before the filament extrusion process. Figure 87 shows a uniform distribution of the EG flakes onto the surface of the PLA pellets. The filament cross-sections were observed by using SEM (Figure 88a–d) and revealed a homogenous dispersion of the fillers in the PLA matrix. The MFI of the filaments was measured to evaluate

their potential printability. The MFI values were similar for the PLA and composite filaments, ranging from 24 to 26 g/10 min, which were adequate for use in 3D printing (Figure 88e) (351).

The incorporation of conductive particles in a polymer matrix reduces the electrical resistivity of the latter and allows electronic transport/mobility. Considering the envisaged application, it may have a positive effect on the cellular adhesion and growth (237, 288). In addition, the rate of wound healing *in vivo* is closely correlated with changes in the electrical current generated from the wound site (290, 352). We used high-definition Kelvin force microscopy to obtain a map of the variation in the surface potential of the PLA+0.5[(f-EG)+Ag] filaments (Figure 76).
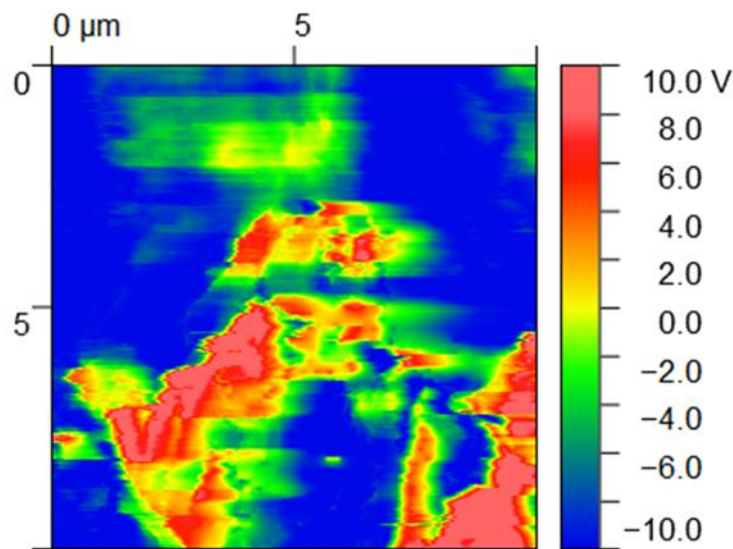
Figure 76 – Maps of surface potential (V) obtained from HDKFM potential for composites containing PLA+0.5[(f-EG)+Ag].

EG and EG derivatives are conductive particles (red regions) and thus show a contrasting surface potential relative to the polymer matrix (dark blue regions), presenting high relative potential values (10V) (353). A charge outflow from the graphene flakes can be seen around these particles since EGs have low electron affinity, as observed in other works (353).

5.3.3 Scaffolds' Characterization

5.3.3.1 Physical and Morphological Analysis

The 3D printing process was easy to set up and fast to carry out, taking 7 min to print a scaffold with dimensions equivalent to those of the average ACL. This process yielded reproducible samples with high structural homogeneity and controlled geometry, indicating that the printing parameters could be

easily adjusted according to the shape and location of the injured tissue (354). Figure 77 illustrates the 3D-printed PLA (a1–a4) and PLA+0.5[(f-EG)+Ag] scaffolds (b1–b4), at the top, front, and lateral views, at increasing magnifications of their porous morphology.
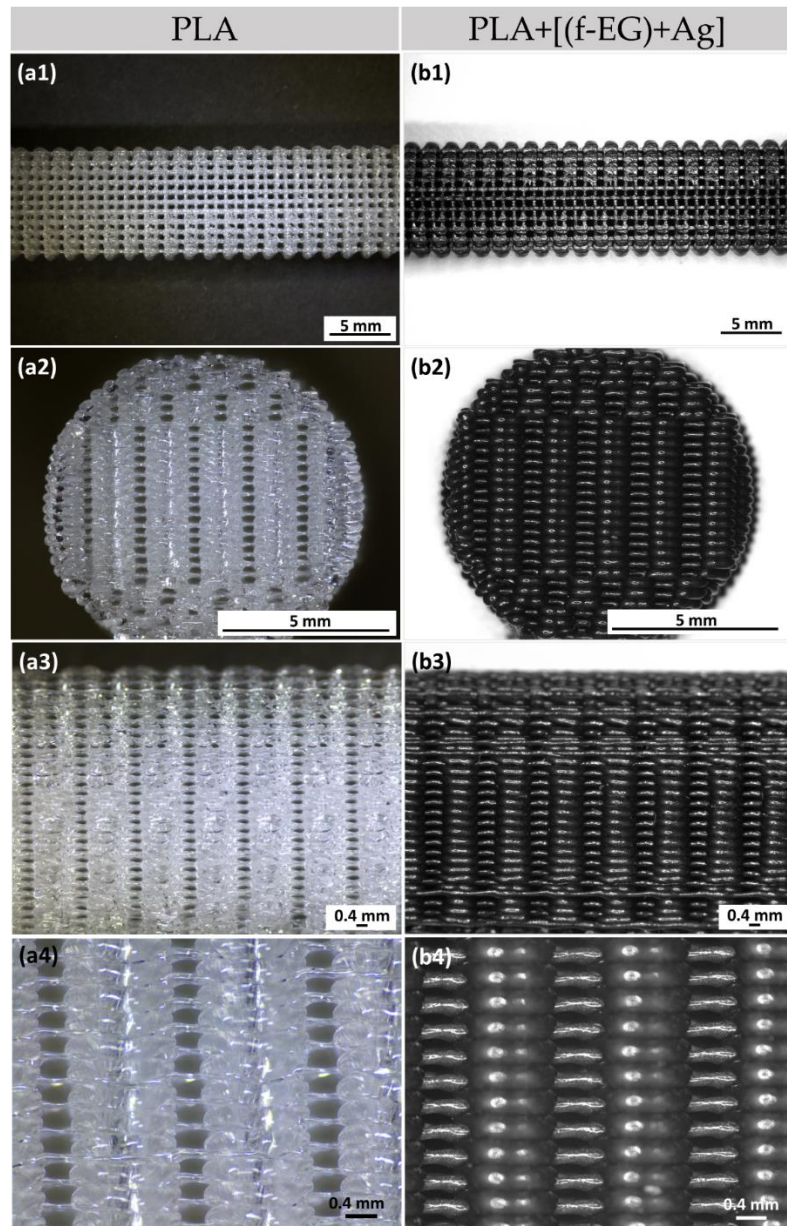
Figure 77 – Three-dimensional-printed scaffolds of (**a1–a3**) PLA and (**b1–b3**) PLA+0.5[(f-EG)+Ag] from the top, front, and side views. Magnification of the (**a4**) PLA and (**b4**) PLA+0.5[(f-EG)+Ag] scaffold structure.

The 3D-printed scaffolds presented well-defined pores and interconnectivity. The pore sizes of the PLA and PLA+[(f-EG)+Ag] scaffolds were similar: 430 ± 130 μm and 430 ± 0.100 μm, respectively. Comparable pore sizes were found for scaffolds with other compositions, with no statistically significant differences ($p < 0.05$) (Table 30). The porosity of all scaffolds was measured by the liquid displacement

method yielding results from 64 to 71% as observed in Figure 78, with no significant impact caused by the presence of EGs.
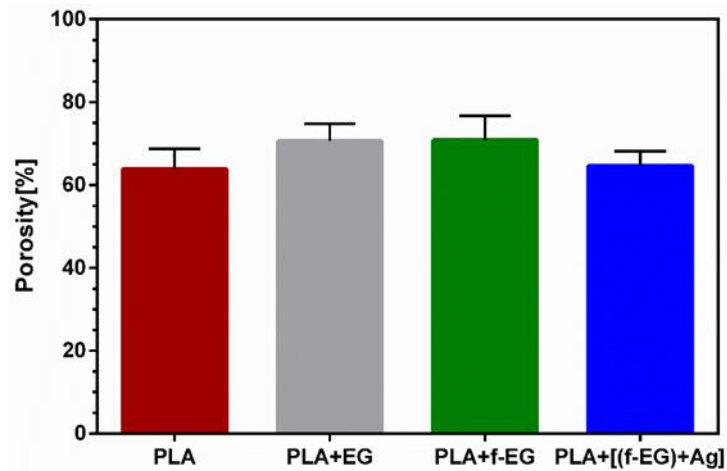
Figure 78 – Mean porosity of 3D-printed scaffolds obtained by the liquid displacement method.

The scaffolds for tendon/ligament regeneration should offer a high porosity (ranging from 50 to 85%) and large interconnected pores, with diameters ranging from approximately 250 to 500 μm, to enable cell ingrowth and the flow of nutrients and waste products (311, 355). Thus, the general structural parameters found in the 3D-printed scaffolds enable their use in cell seeding. The scaffold morphologies obtained in this study were in accordance with other studies about 3D-printed scaffolds filled with carbon-based materials, which reported pore sizes ranging from approximately 300 to 500 μm (235, 312).

Collagen, silk, PLA, PCL, PGA, and PLGA, as well as their composites, have been used as scaffold materials for tendon/ligament replacements, mainly in the form of fibrous scaffolds engineered with textile-based techniques (120). Different solutions have demonstrated adequate mechanical properties, as well as the ability to sustain cell adhesion and proliferation under satisfactory conditions (7, 41, 111). For instance, Sahoo et al. (109) produced a complex hybrid scaffold system by coating bFGF-releasing PLGA fibers onto the surfaces of a knitted silk scaffold. Rabbit bone-marrow-derived mesenchymal stem cells grew on PLGA fibers and silk microfibers and exhibited good viability. The release of bFGF stimulated cell proliferation and the gene expression of tendon/ligament-specific ECM proteins increased the collagen production and, hence, the mechanical properties of the scaffold (109). Despite the significant advancements in the tendon/ligament TE, the current solutions have not yet reached the clinic or even the pre-clinic due to some drawbacks in the application including poor mechanical strength and quick degradability or insufficient biological activity (315). Another remaining problem is the lack of reproducibility and ability to precisely control the pore size and interconnectivity, as well as the scaffolds'

structure and mechanical properties (120). Some of the major advantages of the proposed scaffolds are their simplicity and controlled architecture and porosity. The scaffolds' polymer matrix based on PLA provides the possibility to produce scaffolds easily and cost-effectively by 3D printing. The 3D technology was also suggested by Jiang et al. (336) to produce PLGA scaffolds with collagen-fibronectin hydrogels for rotator cuff tendon regeneration. This composite scaffold promoted the proliferation and tenogenic differentiation of ADSCs.

The cryo-fractured cross-sections of all 3D-printed scaffolds were observed by SEM, as illustrated in Figures 79 and 89, to evaluate if the re-melting of composite filaments led to the re-agglomeration of EG. The presence of silver nanoparticles was confirmed by EDS analysis (Figure 90). The obtained images illustrate a homogenous dispersion of EGs after 3D printing. When well dispersed, the large surface area of EGs maximizes the interfacial area, which results in an enhanced load transfer ability (315). The smoothness of the external surface can also be observed, the composite scaffolds showing a slightly rougher surface due to the EG nanoparticles.
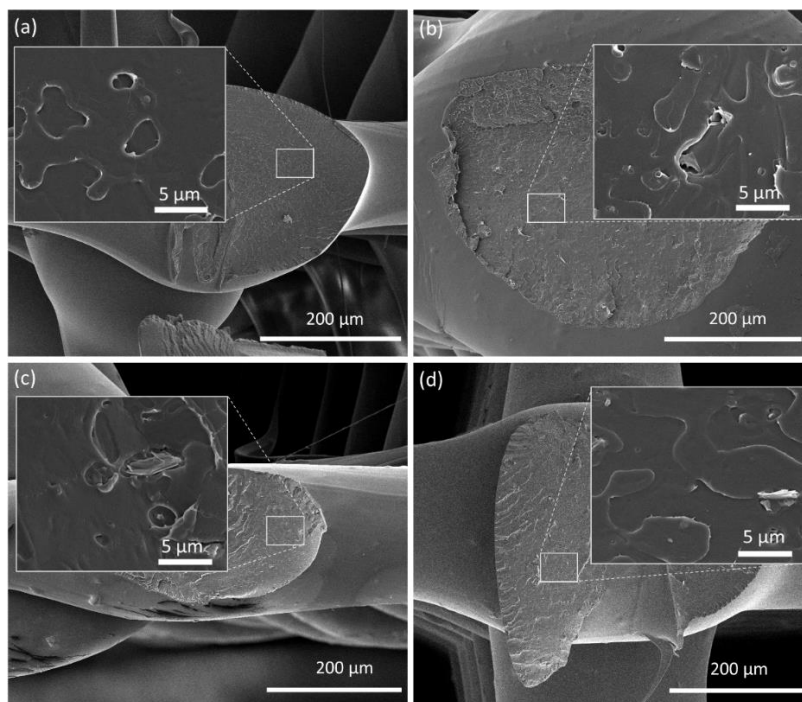
Figure 79 – SEM images of the cross-section of 3D-printed scaffolds formed by (**a**) PLA, (**b**) PLA+0.5EG, (**c**) PLA+0.5f-EG, and (**d**) PLA+0.5[(f-EG)+Ag]. The insets represent a higher magnification.

The surface morphology of the 3D-printed PLA and PLA+0.5[(f-EG)+Ag] scaffolds was analyzed by AFM (Figure 80) and SEM (Figure 91a,d), respectively. The average roughness (Ra) and the root-mean-square (RMS) of the surfaces are represented in Figure 5c.

Both scaffolds exhibited a surface roughness at the nanoscale, which increased with the presence of (f-EG)+Ag. In consonance with these observations, the composite scaffolds also presented higher Ra values. This was consistent with the observations of other works concerning 3D-printed PLA scaffolds reinforced with GO (235) and films of PLA reinforced with GNPs (342). Nanoscale topography has been receiving great attention because of its potential to influence cellular response and its similarity to *in vivo* surroundings (288). As a comparison, Wu et al. (356) used a coating of PLGA fibers on PLA microfiber yarns to provide topological cues to guide the behavior of human ADSCs in terms of proliferation, migration, collagen secretion, and tenogenic differentiation (356).
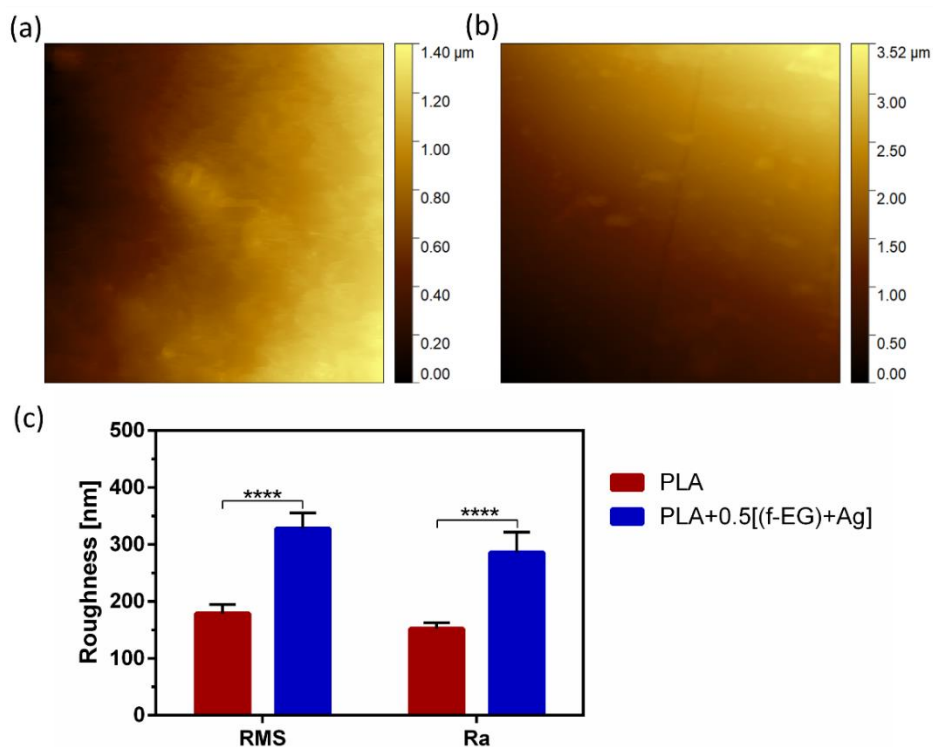
Figure 80 – Surface topography of (**a**) PLA and (**b**) PLA+0.5[(f-EG)+Ag] scaffolds as well as (**c**) RMS and Ra of both scaffolds. Significant differences were stated for $p < 0.0001$ (****).

5.3.3.2 Mechanical Properties of Scaffolds

The mechanical properties of composites based on PLA reinforced with graphene-based materials are often measured under static loading. Composites of PLA and low concentrations of EG/few-layer graphene, produced by melt mixing, were reported to exhibit tensile properties that could be adequate for tendon and ligament regeneration applications, without significantly impairing the ductility (322). Similar conclusions were obtained in our preliminary work (357) performed on 3D-printed composite

scaffolds based on a non-medical-grade PLA reinforced with (f-EG)+Ag. The resulting stress–strain curves of compression tests as a function of the filler content illustrated that the reinforcement did not significantly affect the ductility, even with a filler content of 2 wt.% (357). However, ligaments experience dynamic loads during normal locomotion, and their response was influenced by their viscoelastic properties. The viscoelastic properties of the 3D-printed scaffolds of PLA and composites were assessed by using DMA under dynamic conditions after immersion in physiological media overnight, to mimic the physiological conditions. Figure 81a,b show the storage modulus (E') and the loss factor (tan δ) of the scaffolds as a function of frequency at 37 °C.
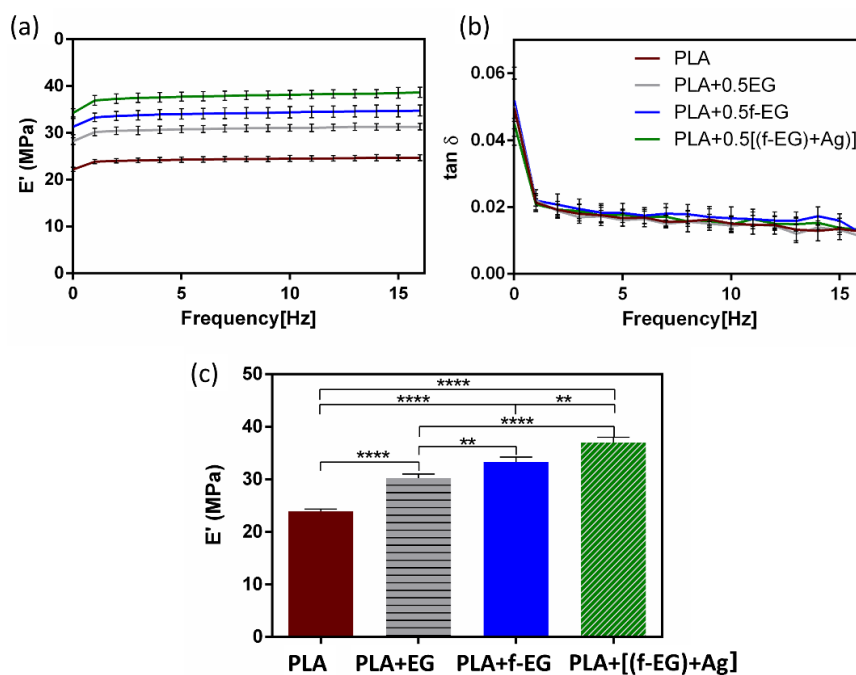
Figure 81 – (**a**) Storage modulus and (**b**) the loss factor obtained for 3D-printed PLA scaffolds and scaffolds reinforced with 0.5 wt.% of EG, f-EG, and (f-EG)+Ag, as a function of the frequency, ranging from 0.01 to 16 Hz. (**c**) Storage modulus of 3D-printed scaffolds at 37 °C and 1 Hz. Significant differences were stated for $p < 0.01$ (**) and $p < 0.0001$ (****).

For all formulations, the storage modulus slightly increased while the tan δ decreased with increasing frequency, as commonly observed in viscoelastic materials (286, 327). This viscoelastic characteristic was extremely important since native tendons and ligaments also exhibited viscoelastic behavior (315). No significant differences were found for the damping ability between the PLA and composite scaffolds. The incorporation of EGs in the composites led to an increase in the storage modulus, typical in graphene-reinforced PLA materials (319, 358). At 1 Hz, the PLA scaffolds had the lowest E' ($\simeq$24 MPa). As observed in Figure 6c, for the scaffolds containing PLA+EG and PLA+f-EG, the storage modulus increased approximately 27% and 40%, respectively. Since fillers are stiffer than PLA,

that may produce rigid interfaces with PLA and restrict the mobility of polymer chains, resulting in an increased modulus of the composites (319). The highest increase in the storage modulus was observed for the scaffolds with PLA+[(f-EG)+Ag], which represents an improvement of $\simeq 55\%$ compared with the PLA scaffolds. Here the AgNPs seem to act as a filler increasing the stiffness, as observed by other authors (339, 359). These 3D-printed scaffolds present a storage modulus comparable to values reported in the literature for ligaments/tendons at 1 Hz (325, 327), which supports their suitability for the envisaged application. Another strategy to develop scaffolds with a viscoelasticity suitable for ACL regeneration involves the incorporation of a hydrogel in a scaffold, as reported by Freeman et al. (122), which combined 10% of poly(ethylene glycol) (PEG) diacrylate hydrogel with a poly-l-lactic acid scaffold (122).

The incorporation of the different EGs had a significant impact on the viscoelastic/mechanical properties of PLA when compared with other works. For instance, Pinto et al. (317) produced composites of PLA/GNPs (2 wt.%) and PLA/CNTs functionalized with carboxylic acid (0.3 wt.%) by melt mixing/compression molding. The authors observed an increase (4%) in the storage modulus of PLA/CNTs composite relative to the neat PLA matrix, while for the PLA/GNPs composite, they found a decrease of 2%, at 1 Hz and under tension (317). The existing PLA hybrids/composites for tendon/ligament TE include PLA or poly-L-lactic acid/hydroxyapatite (Hap) (118, 337, 360), PLA/PEG/Hap (361), PLA/Col (362), or PLA/PLGA (356). The suggestion of PLA–ceramic composites has been a choice for tissue interfaces between the tendon/ligament and bone (360). Our scaffolds benefit from the electrically conductive character of (f-EG) and the antibacterial properties of AgNPs, which is a relevant advancement relative to current solutions. The presence of silver nanoparticles also accelerates the tendon healing process, by boosting cell proliferation, and modulates the ECM composition (more and better quality of collagen fibrils) (273).

5.3.3.3 Biodegradation of Scaffolds

A biodegradable scaffold should preserve at least half of its structural and mechanical integrity for a minimum of 3–6 months (for tendon/ligament recovery) and then should degrade gradually (315). Approximately 6 weeks after the initial injury, remodeling begins and will eventually yield a slightly disorganized ECM (333). The stability behavior of 3D-printed scaffolds was assessed over a period of 12 weeks and is presented in Figure 82a. After 3 months, a very short reduction from the initial mass (<1%)

was verified. Independently of the composition, the degradation was more pronounced between the first 2 and 6 weeks. It has been suggested that during hydrolytic degradation, PLA breaks into lactic acid or into carbon dioxide and water, naturally excreted from the body (295). Even though there were no statistically significant differences, these results seem to indicate that the incorporation of EG and EG derivatives slightly induced a higher resistance to degradation. This behavior may be related to the nucleation effect induced by EGs, increasing the crystallization of the polymer (317). Pinto et al. (317) also assessed the hydrolytic degradation of composites based on PLA and (1 wt.%) GNPs over 16 weeks and found a maximum weight loss of 5% and a comparable behavior of PLA and its composites (317). By analyzing Figure 91, it is possible to compare the surface images of non-degraded and degraded (after 12 weeks) 3D-printed scaffolds that illustrate these conclusions. After 3 months of hydrolytic degradation, some surface erosion and the existence of pores on the surface of degraded scaffolds were visible, being more pronounced in neat PLA and PLA+0.5EG scaffolds. In addition, as expected, the storage modulus of the degraded samples at 37 °C and 1 Hz decreased when compared with non-degraded samples, remaining in the same order of magnitude (MPa) (Figure 82b).
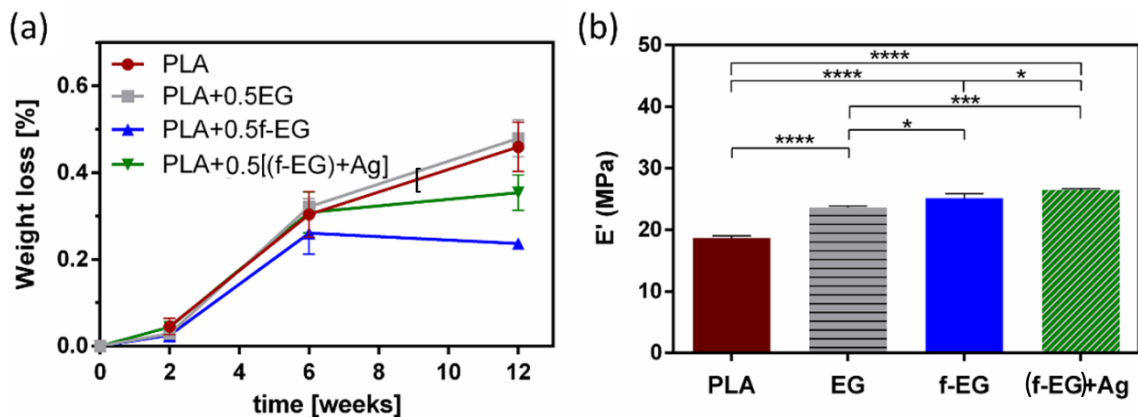
Figure 82 – (**a**) Weight loss (%) of 3D-printed scaffolds and (**b**) storage modulus of degraded scaffolds (after 12 weeks), at 37 °C and 1 Hz. Significant differences were stated for $p < 0.05$ (*), $p < 0.001$ (***), and $p < 0.0001$ (****).

5.3.3.4 Biological Assays

L929. The cytocompatibility of the produced scaffolds was evaluated through the *in vitro* culture of L929 fibroblast cells in direct contact with the scaffolds. The scaffolds must be able to withstand sterilization without physical, chemical, and biological change. Their metabolic activity and viability were assessed after 1, 3, 7, and 14 days of culture (Figure 83a,b). The L929 morphology and cytoskeleton organization were investigated by using SEM (Figure 92) and a DAPI-phalloidin test (Figure 83c).

As observed in Figure 83a, at early stages of culture (days 1 and 3) the metabolic activity of cells on composites exhibited values around 70% relative to those of PLA. After 14 days, their metabolic activity increased and became similar to that of the PLA scaffolds, with the cells on PLA+EG scaffolds exhibiting the highest value ($\simeq$91%), followed by PLA+ f-EG ($\simeq$84%) and PLA+[(f-EG)+Ag] ($\simeq$83%). As illustrated in the live/dead images (Figure 83b), none or almost none dead cells (red) were found in composite scaffolds. Such features suggest that the addition of EG and EG derivatives did not affect the metabolic activity of the fibroblasts or their cellular viability, discarding the potential toxic effects of EGs. Thus, all studied scaffolds can be considered non-cytotoxic. Other authors also obtained biocompatible composites of PLA reinforced with a low content (0.4 wt.%) of GNPs or GO (283, 342). In a period of 3 days of culture, Gonçalves et al. (283) also found high metabolic activity of fibroblasts in PLA–GNPs, never below 97% when compared with PLA (283).

After 24 h of incubation, cells adhered well on 3D-printed scaffolds, although presenting a rounder shape in the composite scaffolds than on the PLA (Figure 83c). Fine filopodial extensions were also visible. On the third day, an elongated spindle-like morphology was observed for all compositions, with higher surface attachment than on the control. A higher increase in the cell density was observed at the 7th up to the 14th day, reaching confluency for all studied conditions. The proliferation was even more pronounced than on the control, with the cells covering large areas of the scaffolds' surfaces. The nanoroughness caused by FDM and by the presence of nanoparticles increased the surface area, and this was shown to positively influence the attachment, migration, and orientation of various cell lines including fibroblasts, which play a critical role in the healing process (334, 342).

161
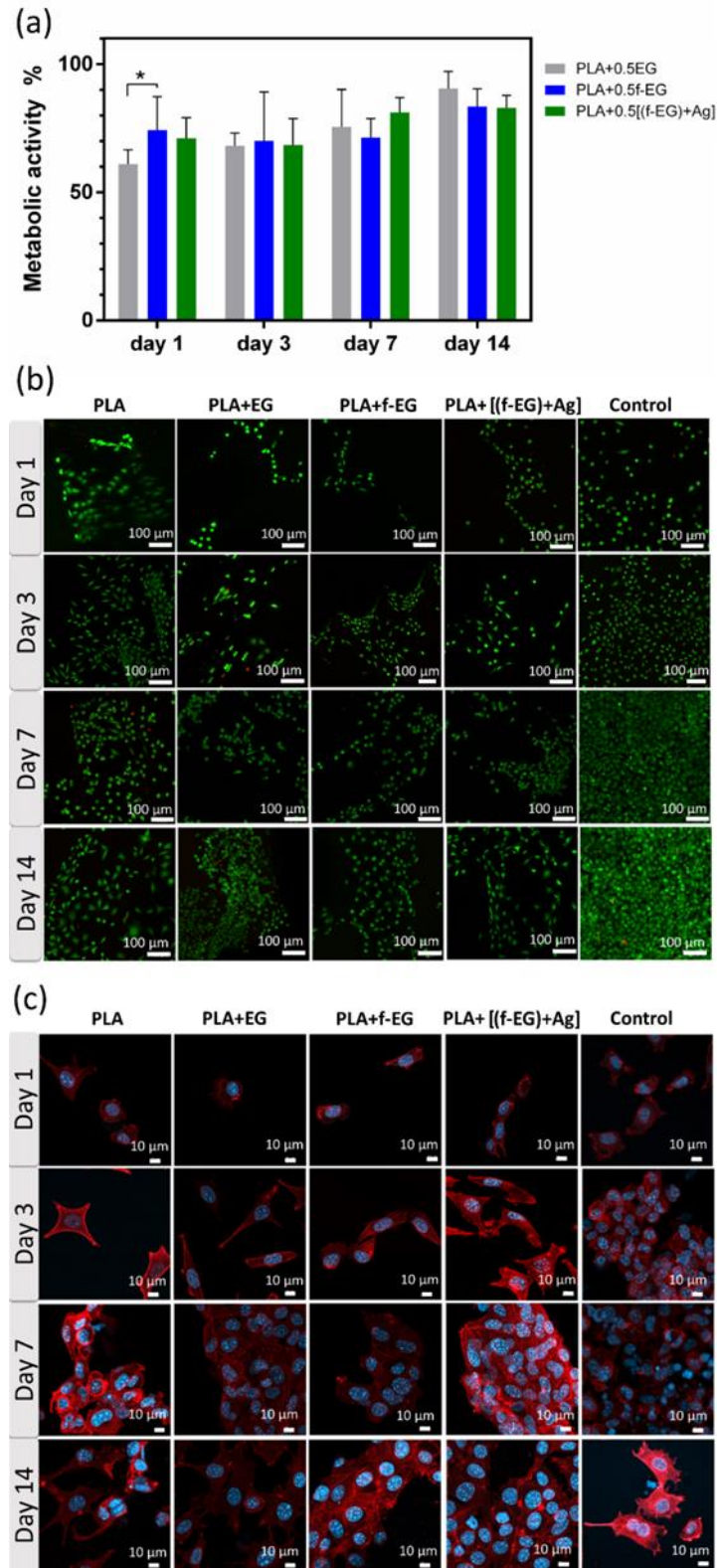
Figure 83 – *In vitro* cell culture on the scaffolds. (**a**) Metabolic activity of L929 cells determined by Alamar blue cell viability assay. Data normalized to PLA (100% metabolic activity). Significant differences, effect of the material: $p < 0.05$ (*). (**b**) Representative fluorescent images of live (green)/dead (red) cells seeded on the scaffolds. (**c**) Fluorescence image of L929 cells seeded on 3D-printed scaffolds and TCPS. Cells were immunostained for F-actin with phalloidin (red), and cell nuclei were stained with DAPI (blue).

Human tendon-derived cells in PLA and PLA+0.5[(f-EG)+Ag] scaffolds—Expression of tendon-related markers. Due to the similarities among tissues and to the expression of common markers such as TNMD and SCX (346, 363), engineering tendons and ligaments have been pursued with common strategies. In this work, the potential of PLA+0.5[(f-EG)+Ag] scaffolds to support the tenogenic/ligamentogenic phenotype was assessed in hTDCs through gene expression analysis (Figure 84). The resident cell populations including stem/progenitor cells subsets have an epigenetic commitment to respond to tendon and ligament-specific requirements and a natural role in the renewal and maintenance and of tissue composition and properties, with impact on the healing process and its outcomes (346, 363). These cells exhibit clonogenicity, self-renewal, and multipotency, as well as a high expression of scleraxis (SCX), tenomodulin (TNMD), and collagen type I (COL1) (346).
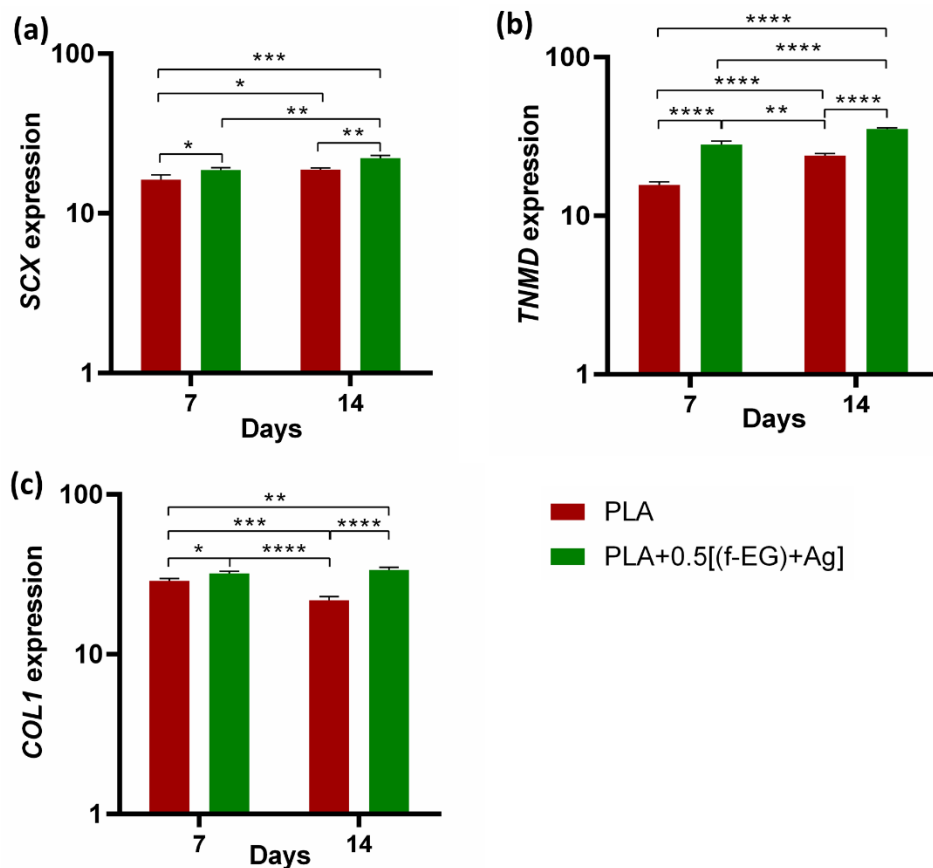
Figure 84 – Assessment of the genetic expression of tenogenic markers of hTDCs in 3D scaffolds after 7 and 14 days of culture. Relative gene expression of (**a**) SCX, (**b**) TNMD, and (**c**) COL1. Symbols denote statistical differences: * for p < 0.05, ** for p < 0.01, *** for p < 0.001, and **** for p < 0.0001.

Cells cultured on both types of scaffolds showed increased expression of tendon/ligament markers, namely, *SCX*, *TNMD*, and *COL1*, during the experimental setup. *SCX, TNMD*, and *COL1*

163

evidenced an upregulation from day 7 to day 14, suggesting that the 3D-printed scaffolds assisted the maintenance of the hTDCs' phenotype (364). In addition, the gene expression levels of SCX, TNMD, and COL1 were significantly increased by the presence of (f-EG)+Ag, suggesting that the composite scaffolds supported the tenogenic phenotype (345). In accordance, the expressions of *SCX* and *COL1* were significantly increased in hTDCs cultured on the composites (*SCX*: at day 7, $p < 0.05$, and at day 14, $p < 0.01$, and *COL1*: at day 7, $p < 0.05$, and at day 14, $p < 0.0001$), relative to hTDCs on the PLA scaffolds. The levels of TNMD showed a significant increase in composite scaffolds when compared with PLA, at each and every time point ($p < 0.0001$). We further investigated the locations of the tendon-related proteins in the scaffolds, which were analyzed by immunofluorescence (Figure 85a,b). SCX, TNMD, and COL1 were observed over time in cells cultured on both types of scaffolds. The cells were homogenously distributed, evidencing a dense colonization of the scaffolds' structures. Moreover, seeded cells exhibit a fusiform morphology and a tendency to organize themselves into parallel alignment on the surface of the scaffolds, which is typically observed in tendon cells in native tissues. The obtained results support that 3D-printed scaffolds encourage the colonization of hTDCs and the expression of genes and proteins associated to the tenogenic/ligamentogenic phenotype and, therefore, hold the potential to sustain healing strategies aiming to regenerate tendons and ligaments. Similar results were found for other graphene-based polymer scaffolds (365, 366). These are encouraging results for further *in vivo* experiments.

The 3D-printed scaffold developed could be further explored both as an acellular and cell-laden scaffold. As a promising tendon and ligament TE product, the inclusion of cells as a component introduces risks, and for that reason the selection for an acellular scaffold as medical device should be less time-consuming and face less regulatory scrutiny. In EU, medical devices are strictly regulated both by national competent authorities and by the EMA, while in the USA the extensive regulatory requirements are defined by the FDA.
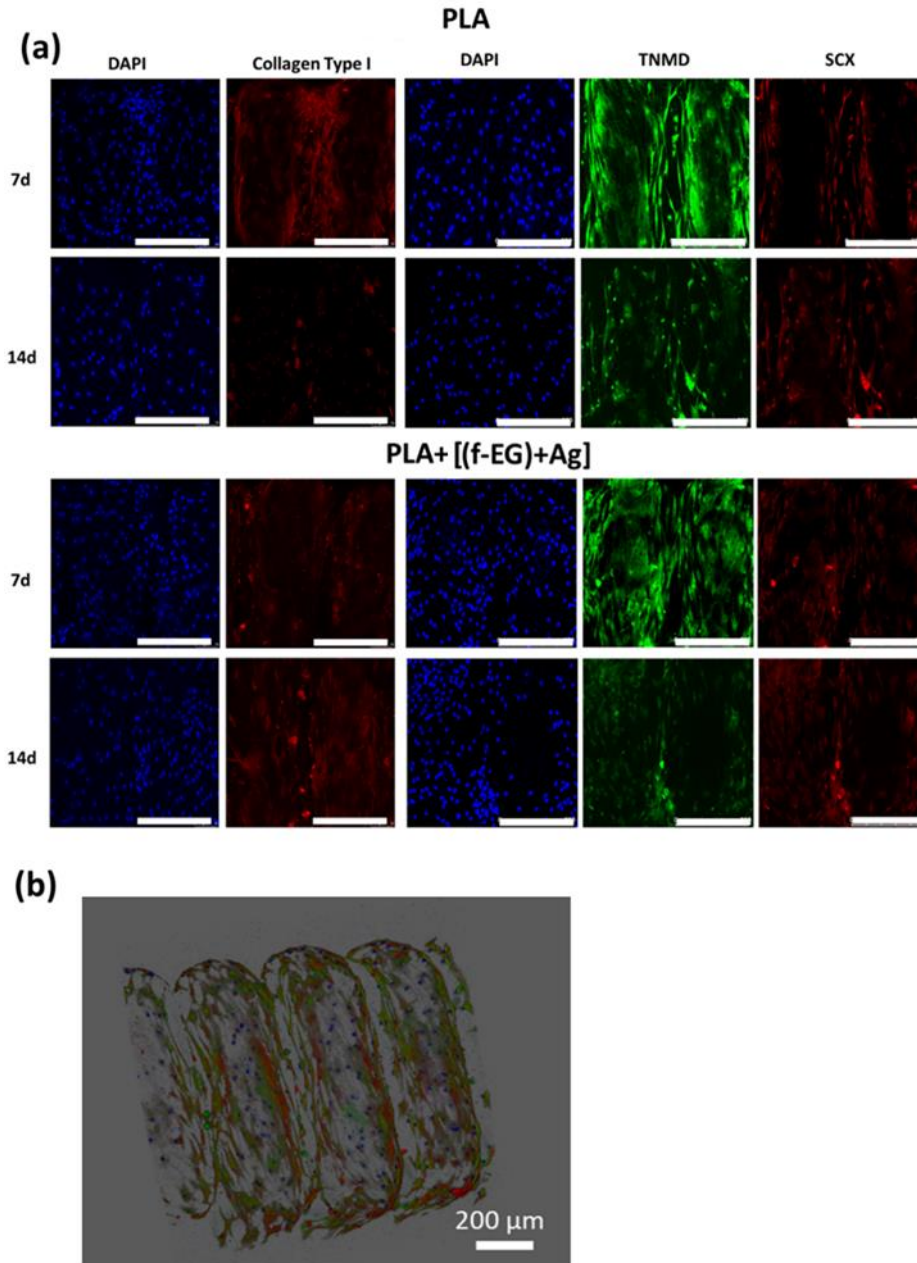
Figure 85 – Immune-location of (**a**) COL1 (red), SCX (red), and TNMD (green) in hTDCs-laden scaffolds after 7 and 14 days of culture (20×, scale bar 250 μm). Nuclei were stained with DAPI (blue). (**b**) A 3D image reconstruction of the z-stacks collected from the hTDCs-laden PLA+[0.5(f-EG)+Ag] scaffold, evidencing scaffold structure and distribution of TNMD (green).

5.4 Conclusions and Future Work

The 3D-printed scaffolds based on medical-grade PLA reinforced with 0.5 wt.% of EG, f-EG, and (f-EG)+Ag were successfully produced and characterized. EG was organically functionalized and decorated with silver nanoparticles. The aim of the organic functionalization of EG was to strengthen the interface with the polymer and to provide anchoring sites for Ag, allowing the inclusion of a small concentration of

Ag. The Ag anchored on EG acted as an anti-microbial agent, as confirmed against microorganisms of clinical relevance *S. aureus* and *E. coli*, an important feature for the healing process and prevention of bacterial infections. PLA composite filaments were melt-extruded with a good filler dispersion and used for the fabrication of customized 3D porous scaffolds. Highly reproducible scaffolds were obtained with a porosity of 64–71% and a network of interconnected pores of around 400 μm. The scaffolds' biodegradation and mechanical properties were evaluated. All scaffolds exhibited high stability and surface nanoroughness, which was increased by the fillers' presence. The wet state dynamic mechanical analysis proved that the addition of reinforcements led to a significant increase in the storage modulus, being mechanically adequate for tendon and ligament applications. The highest increase was observed for scaffolds with PLA+0.5[(f-EG)+Ag], which represents an increase of ≃55% compared with PLA scaffolds. Similar to native living tissues, the scaffolds exhibited a viscoelastic behavior. The PLA+[(f-EG)+Ag] scaffolds were non-toxic and showed capability to maintain the tenogenic commitment of human tendon-derived cells, with an increase in the gene expression of specific tendon/ligament-related markers. The results demonstrate the possibility for easy, cost-effective, and personalized 3D-printed scaffolds with great potential applications for tendon and ligament regeneration. We believe that this article presents compelling *in vitro* results for further *in vivo* experiments. Some strategies may be considered for future directions of this research, to improve the scaffolds' overall performance and clinical applications, namely, their capability to inhibit mycobacteria (367) or even adapt and change over time (368).

5.5 Supplementary Materials

Table 28 – Operating parameters used for the production of composite filaments.

Filament	Feed/Barrel/Die Temperature (°C)	Feed rate (g.min^{-1})	Pulling rolls	
			R1(mm.s^{-1})	R2(mm.s^{-1})
PLA	135-185-170	4.2	27.84	31.64
PLA+0.5EG	135-185-168		45.70	47.87
PLA+0.5f-EG	135-185-163		34.50	35.50
PLA+0.5[(f-EG)+Ag]	135-185-155		32.81	35.85

Table 29 – Primers used for real-time quantitative RT-PCR analysis.

	Primer Sequence	Accession number
Human Glyceraldehyde 3-phosphate dehydrogenase (*GAPDH*)	F - TGTACCACCAACTGCTTAGC R - GGCATGGACTGTGGTCATGAG	NM_002046.4
Scleraxis (SCX)	F – CGAGAACACCCAGCCCAAAC R – CTCCGAATCGCAGTCTTTCTGTC	XM_001717912
Collagen, Type I, alpha 1 (COL1A1)	F – CGAAGACATCCCACCAATCAC R – GTCACAGATCACGTCATCGC	NM_000088.3
Tenomodulin (TNMD)	F – CCGCGTCTGTGAACCTTTAC R – CACCCACCAGTTACAAGGCA	NM_022144.2
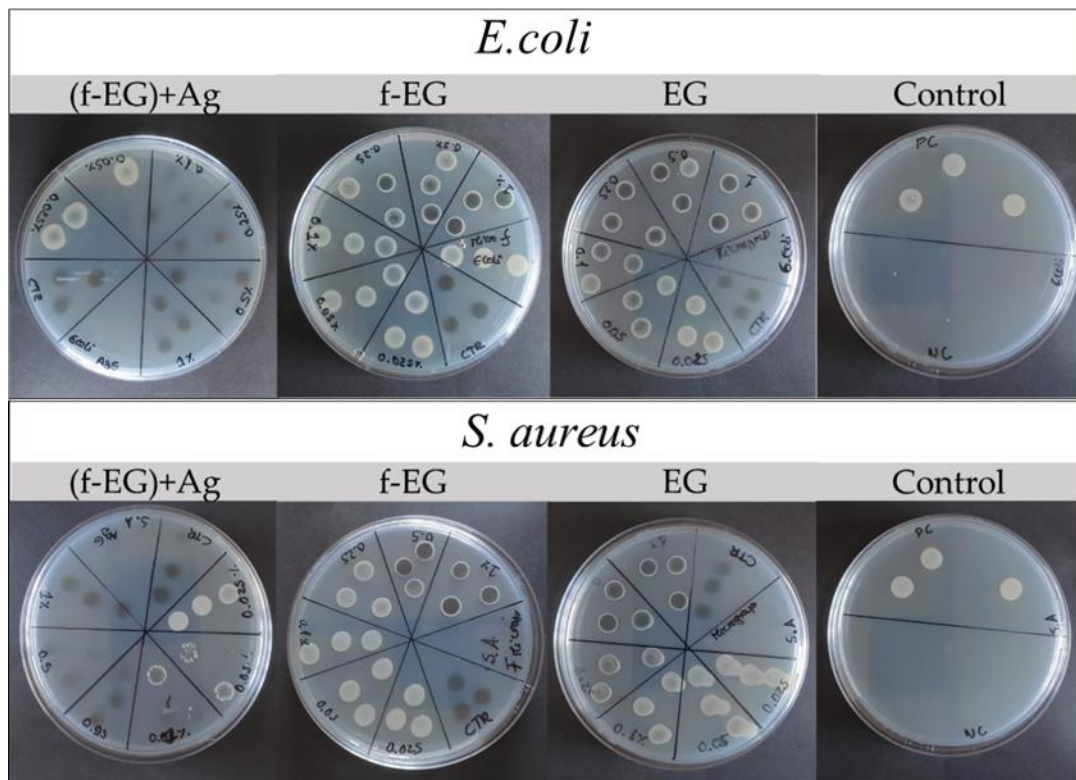
Figure 86 – Minimum bactericidal concentration of different EGs (EG, f-EG, and (f-EG)+Ag) against *E.coli* and *S. aureus*.
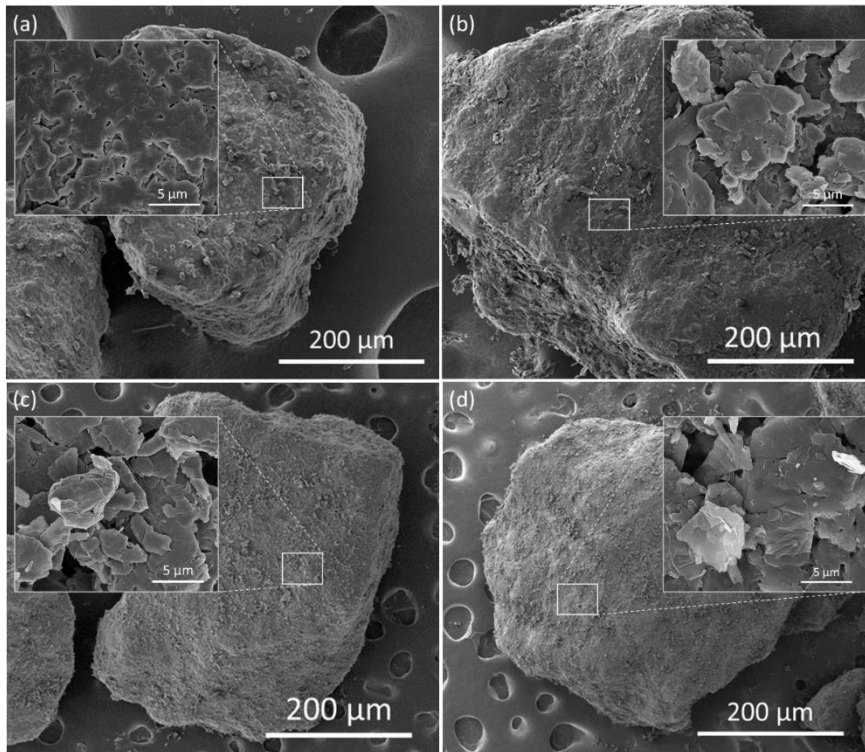
Figure 87 – SEM images of (**a**) PLA pellet and PLA pellet coated with 0.5 wt.% of (**b**) pristine EG, (**c**) f-EG, and (**d**) (f-EG)+Ag powder. The insets represent different magnifications.
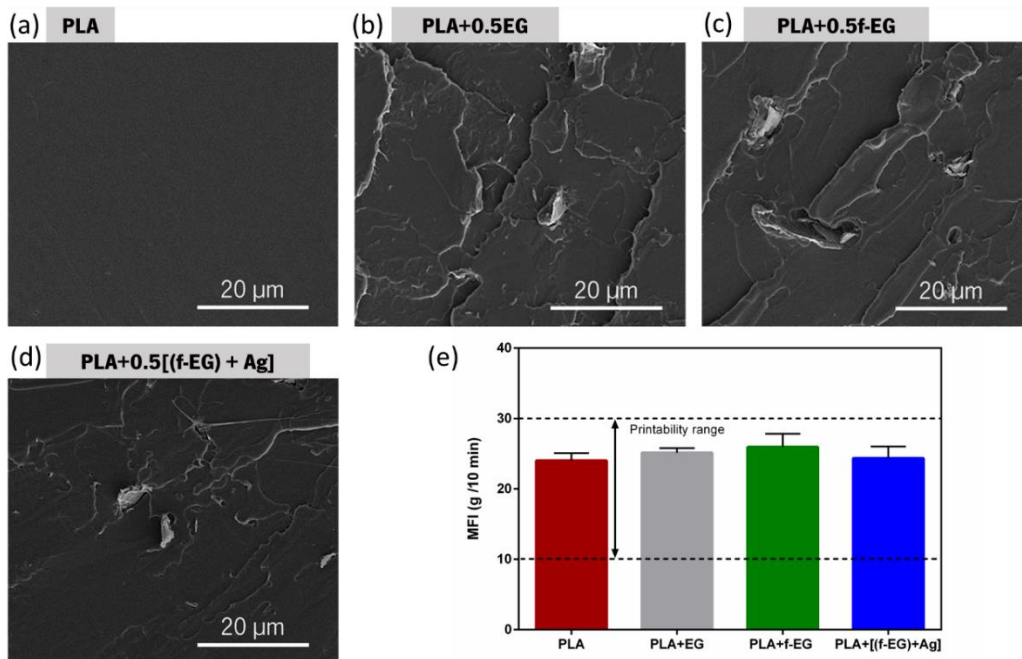
Figure 88 – SEM images of filaments' cross-sections: (**a**) PLA, (**b**) PLA+0.5EG, (**c**) PLA+0.5f-EG, and (**d**) PLA+0.5[(f-EG)+Ag]; (**e**) MFI values of filaments.

Table 30 – Mean pore size of the 3D-printed scaffolds.

Scaffold		Pore size (mm)
PLA		0.43 ± 0.13
PLA+0.5	EG	0.45 ± 0.11
PLA+0.5	f-EG	0.42 ± 0.13
PLA+0.5	(f-EG)+Ag	0.43 ± 0.10
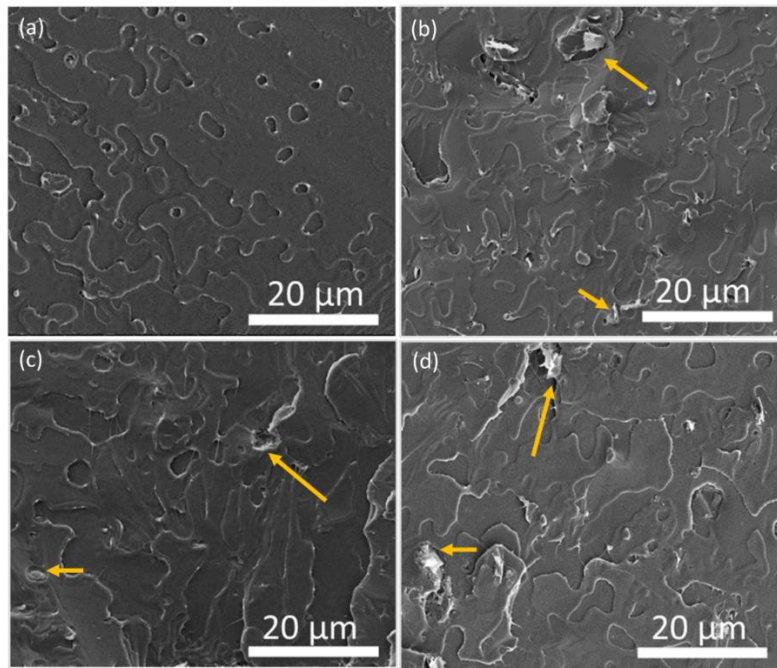
Figure 89 – SEM images of the cross-section of 3D printed scaffolds formed by (**a**) PLA, (**b**) PLA+0.5EG, (**c**) PLA+0.5f-EG, and (**d**) PLA+0.5[(f-EG)+Ag].
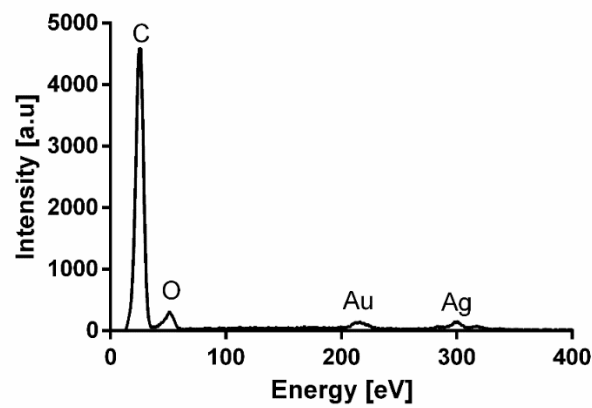
Figure 90 – EDS of PLA+0.5[(f-EG)+Ag] scaffolds.

169
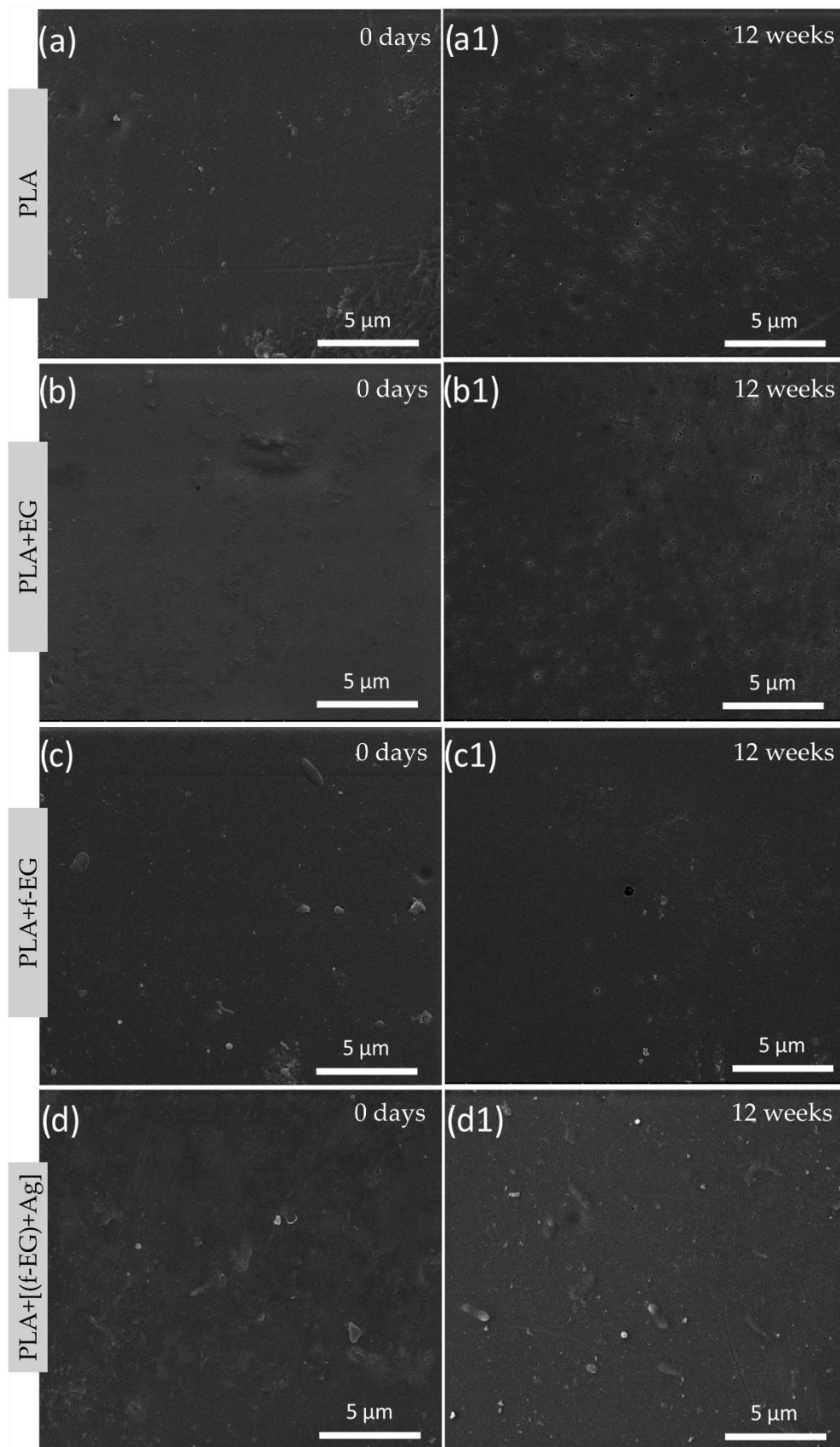
Figure 91 – SEM images of the surface of (**a,a1**) PLA, (**b,b1**) PLA+0.5EG, (**c,c1**) PLA+0.5f-EG, and (**d,d1**)PLA+0.5[(f-EG)+Ag] scaffolds at stage 0 and after 12 weeks of degradation, respectively.
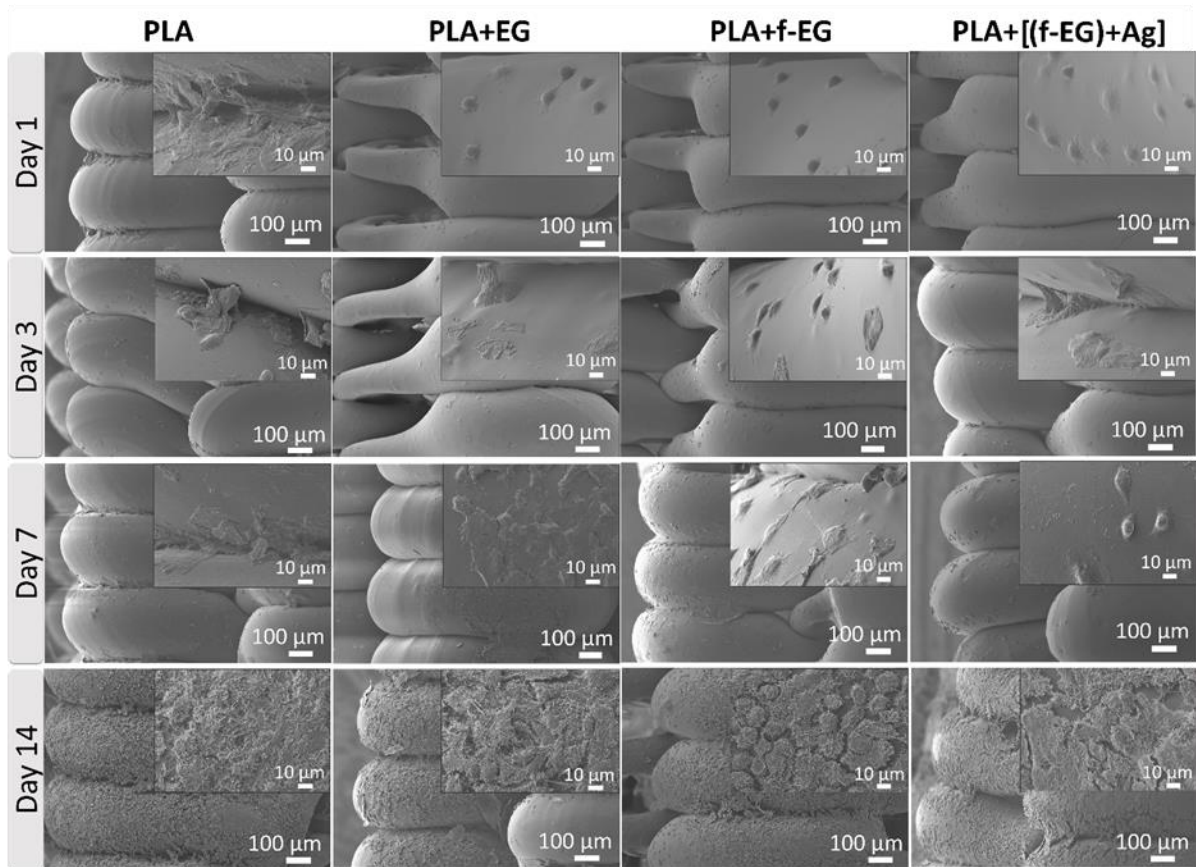
Figure 92 – SEM images of the L929 cells seeded on PLA, PLA+EG, PLA+f-EG and PLA+[(f-EG)+Ag] scaffolds, after 1, 3, 7, and 14 days. Magnifications for closer observation of L929 cells.

CHAPTER **6**

Conclusions and future work

6 Conclusions and future work

6.1 General conclusions

The focus of this thesis was the production of novel biodegradable graphene-based scaffolds for ligament regeneration.

An extensive review on the state of art of this work was crucial to understand the current solutions for tendon/ligament injuries as well as the developments achieved in the production of biodegradable polymer composites for ligament/tendon regeneration. Despite the remarkable progress made in this field, the current tissue engineering approaches on fibrous scaffolds still present limitations in terms of mechanical properties, degradation rate and biological response that are necessary to overcome. 3D printing has been a rapid and promising solution for the production of graphene/polymer scaffolds for different biomedical applications, using different additive manufacturing techniques.

Graphite nanoplatelets were functionalized to strengthen the interface with the polymer and to provide anchoring sites for Ag, allowing the inclusion of a low concentration of Ag. Composite filaments based on a commercial grade PLA reinforced with EG, f-EG, and (f-EG)+Ag were successfully produced by melt processing with diameters of 0.25 and 1.75 mm for the preparation of both textile-engineered and 3D-printed scaffolds, respectively. All filaments exhibited a good dispersion of the fillers and interaction with the polymeric matrix. The filaments were thermally stable up to 130 °C in the presence of EG and functionalized EG. In general, the storage modulus of the composite filaments was approximately 3 GPa or higher at 37°C, with tan δ values also higher than those observed for PLA filaments, indicating that the addition of functionalized graphite increases the stiffness of the composites and provides a higher capacity to dissipate energy and damping. The incorporation of fillers led to a decrease in the electrical resistivity relative to neat PLA up to five orders of magnitude, with the composites with 2 wt.% of reinforcement presenting the lowest values. The degradation rate of PLA and composite filaments is low, with no significant degradation being observed after 27 days in PBS. These results demonstrated that the composite filaments can be successfully processed into three-dimensional scaffolds using additive manufacturing as well as textile-engineered techniques.

The production of scaffolds for tendon/ligament tissue engineering was successfully attained by conventional braiding and 3D printing (using FDM technology). The production of 3D-printed scaffolds was faster, easier, and more reproducible compared to braided scaffolds, but all have finely controlled dimensions and geometry. Regardless of the filler, either EG, f-EG or (f-EG)+Ag, a good dispersion and

interaction with the polymeric matrix was observed through the cross section of 3D-printed scaffolds. The anchoring of a small concentration of Ag as an anti-microbial agent was confirmed by EDS on scaffolds reinforced with (f-EG)+Ag. The addition of nanoparticles to the PLA matrix had a very slight effect on pore morphology and size. 3D-printed scaffolds exhibited a porosity that ranged from 67 to 71% and pore size from 484 to 496 µm. Higher porosity was observed for braided scaffolds compared to 3D-printed scaffolds, ranging from 83–88%, and pore size from 1035 to 1164 µm. Both braided and 3D-printed exhibited a viscoelastic behavior and an increase in the storage modulus for the composite scaffolds compared to neat PLA scaffolds. The highest E' was achieved by the scaffold containing PLA+2[(f-EG)+Ag] (E' = 61.7 ± 9 MPa), among the 3D-printed scaffolds, and the scaffold with PLA+0.5[(f-EG)+Ag] (E' =11.1 ± 2 MPa), among the braided scaffolds. Both braided and 3D-printed scaffolds exhibited storage modulus values comparable to those measured for ligaments/tendons in tension and compression, as well as high porosity and pore size adequate for ACL regeneration.

3D-printed scaffolds based on medical-grade PLA reinforced with 0.5 wt.% of EG, f-EG, and (f-EG)+Ag were successfully produced and characterized. The Ag anchored on f-EG acted as an anti-microbial agent, as confirmed against the microorganisms of clinical relevance *S. aureus* and *E. coli*, an important feature for the healing process and prevention of bacterial infections. PLA composite filaments were melt-extruded with a good filler dispersion and used for the fabrication of customized 3D porous scaffolds. Highly reproducible scaffolds were obtained with a porosity of 64–71% and a network of interconnected pores of around 400 µm. The scaffolds' biodegradation and mechanical properties were evaluated. All scaffolds exhibited high stability and surface nanoroughness, which was increased by the fillers' presence. The wet state dynamic mechanical analysis proved that the addition of reinforcements led to a significant increase in the storage modulus, being mechanically adequate for tendon and ligament applications. The highest increase was observed for scaffolds with PLA+0.5[(f-EG)+Ag], which represents an increase of ≃55% compared with PLA scaffolds. Similar to native living tissues, the scaffolds exhibited a viscoelastic behavior. The PLA+[(f-EG)+Ag] scaffolds were non-toxic and showed capability to maintain the tenogenic commitment of human tendon-derived cells, with an increase in the gene expression of specific tendon/ligament-related markers.

The results demonstrate the possibility for easy, cost-effective, and personalized 3D-printed scaffolds with great potential applications for tendon and ligament regeneration.

6.2 Future Work

In this research, the use of PLA reinforced with (f-EG)+Ag and its associated antibacterial properties demonstrated promising results regarding the mechanical properties, biocompatibility, and cells tenogenic commitment maintenance of 3D-printed scaffolds. Thus, this work provides new considerations and motivations for future work, to improve the scaffolds' overall performance and clinical applications:

The mechanical stability over time and long-term biodegradability could be explored over extended periods in order to ensure that the scaffolds' degradation aligns with the complete tissue's regeneration and remodelling processes, retaining the mechanical integrity throughout the whole regeneration process.

Considering the prevalence of antibiotic-resistant bacteria, evaluating the scaffolds' effectiveness against other strains would also be relevant.

In addition, this work presents compelling *in vitro* results for further *in vivo* experiments to understand how the scaffolds interact with the host tissue in a living organism, the immune response, and the overall effectiveness of the regeneration process.

References

1.   Freeman JW, Woods MD, Laurencin CT. Tissue engineering of the anterior cruciate ligament using a braid-twist scaffold design. J Biomech 2007;40:2029-36.

2.   Yilgor C, Huri PY, Huri G. Tissue Engineering Strategies in Ligament Regeneration. Stem Cells International. 2012;2012:9.

3.   Yates EW, Rupani A, Foley GT, Khan WS, Cartmell S, Anand SJ. Ligament Tissue Engineering and Its Potential Role in Anterior Cruciate Ligament Reconstruction. Stem Cells International 2012;2012.

4.   Nau T, Teuschl A. Regeneration of the anterior cruciate ligament: Current strategies in tissue engineering. World J Orthop. 2015;6(1):127-36.

5.   Kuo CK, Marturano JE, Tuan RS. Novel strategies in tendon and ligament tissue engineering: Advanced biomaterials and regeneration motifs. Sports Med Arthros Rehab Ther Tech. 2010;2(1):20.

6.   Tovar N, Bourke S, Jaffe M, Murthy NS, Kohn J, Gatt C, et al. A comparison of degradable synthetic polymer fibers for anterior cruciate ligament reconstruction. J Biomed Mater Res A. 2010;93(2):738-47.

7.   Cooper JA, Lu HH, Ko FK, Freeman JW, Laurencin CT. Fiber-based tissue-engineered scaffold for ligament replacement: design considerations and in vitro evaluation. Biomaterials. 2005;26:1523–32.

8.   Laurencin CT, Freeman JW. Ligament tissue engineering: An evolutionary materials science approach. Biomaterials. 2005;26:7530–6.

9.   Leong NL, Petrigliano FA, McAllister DR. Current tissue engineering strategies in anterior cruciate ligament reconstruction. J Biomed Mater Res A. 2014;102(5):1614-24.

10.   Vieira AC, Guedes RM, Marques AT. Development of Ligament Tissue Biodegradable Devices: A Review. J Biomech. 2009;13:2421-30.

11.   Almeida LR, Martins AR, Fernandes EM, Oliveira MB, Correlo VM, Pashkuleva I, et al. New biotextiles for tissue engineering: Development, characterization and in vitro cellular viability. Acta Biomaterialia. 2013;9(9):98167–8181.

12.   Lui H, Vaquette C, Bindra R. Tissue Engineering in Hand Surgery: A Technology Update. J Hand Surg Am. 2017;42(9):727-35.

13.   Singh S, Ramakrishna S. Biomedical applications of additive manufacturing: Present and future. . Current Opinion in Biomedical Engineering. 2017;2:105-15.

14.   Quan Z, Wu A, Keefe M, Qin X, Yu J, Suhr J, et al. Additive manufacturing of multidirectional preforms for composites: opportunities and challenges. Materials Today. 2015;18(8):503-12.

15.   Peltola SM, Melchels F.P.W., Grijpma DW, Kellomäki M. A review of rapid prototyping techniques for tissue engineering purposes. Annals of Medicine. 2008;40:268-80.

16.   Rodrigues MT, Reis RL, Gomes ME. Engineering tendon and ligament tissues: present developments towards successful clinical products. J Tissue Eng Regen Med 2013;7:673–86.

17.   Ge Z, Yang F, Goh JC, Ramakrishna S, Lee EH. Biomaterials and scaffolds for ligament tissue engineering. J Biomed Mater Res A. 2006;77(3):639-52.

18.   Santos ML, Rodrigues MT, Domingues RMA, Reis RL, Gomes ME. Biomaterials as Tendon and Ligament Substitutes: Current Development. Regenerative Strategies for the Treatment of Knee Joint Disabilities: Springer; 2017. p. 349-71.

19.   Batty LM, Norsworthy CJ, Lash NJ, Wasiak J, Richmond AK, Feller JA. Synthetic devices for reconstructive surgery of the cruciate ligaments: a systematic review. Arthroscopy 2015;31(5):957–68.

20.   Francois E, Dorcemus D, Nukavarapu S. 1 - Biomaterials and scaffolds for musculoskeletal tissue engineering. In: Nukavarapu SP, Freeman JW, Laurencin CT, editors. Regenerative Engineering of Musculoskeletal Tissues and Interfaces: Woodhead Publishing; 2015. p. 3-23.

21.   Petrigliano FA, McAllister DR, Wu BM. Tissue Engineering for Anterior Cruciate Ligament Reconstruction: A Review of Current Strategies. Arthroscopy: The Journal of Arthroscopic & Related Surgery. 2006;22(4):441–51.

22.   Goh JCH, Sahoo S. Scaffolds for tendon and ligament tissue engineering. Regenerative Medicine and Biomaterials for the Repair of Connective Tissues. In: In: Archer C RJ, editors, editor. Regenerative Medicine and Biomaterials for the Repair of Connective Tissues. Cambridge, England: Woodhead Publishing; 2010. p. 452-68.

23.   Li W-J, Laurencin CT, Caterson E, Tuan R, S.,, Ko FK. Electrospun nanofibrous structure: A novel scaffold for tissue engineering. Journal of Biomedical Materials Research. 2002;60(4):613–21.

24.   Altman GH, Horan RL, Lu HH, Moreau J, Martin I, Richmond JC, et al. Silk matrix for tissue engineered anterior cruciate ligaments. Biomaterials. 2002;23(20):4131-41.

25.   Smith BD, Grande DA. The current state of scaffolds for musculoskeletal regenerative applications. Nature Reviews Rheumatology. 2015;11(4):213–22.

26.   Gil PR, Yang F, Thomas H, Li L, Terfort A, Parak WJ. Development of an assay based on cell counting with quantum dot labels for comparing cell adhesion within cocultures. Nano Today 2011;6:20—7.

27.   Qiu J, Li D, Mou X, Li J, Guo W, Wang S, et al. Effects of Graphene Quantum Dots on the Self-Renewal and Differentiation of Mesenchymal Stem Cells. Adv Healthc Mater. 2016;5(6):702-10.

28.   Kwansa AL, Empson YM, Ekwueme EC, Walters VI, Freeman JW, Laurencin CT. Novel matrix based anterior cruciate ligament (ACL) Regeneration. Soft Matter. 2010;6:5016-25.

29.   Nair LS, C. L. Biodegradable polymers as biomaterials. Progress in Polymer Science. 2007;32(8-9):762-98.

30.   Williams DF. On the mechanisms of biocompatibility. Biomaterials. 2008;29(20):2941–53.

31.   Goonoo N, Bhaw-Luximon A. Mimicking growth factors: role of small molecule scaffold additives in promoting tissue regeneration and repair. RSC Adv. 2019;9:18124-46.

32.   Hellman KB. Tissue Engineering: Translating Science to Product 2008.

33.   Mano JF, Silva GA, Azevedo HS, Malafaya PB, Sousa RA, Silva SS, et al. Natural origin biodegradable systems in tissue engineering and regenerative medicine: present status and some moving trends. J R Soc Interface. 2007;4:999–1030.

34.   Ulery BD, Nair LS, Laurencin CT. Biomedical Applications of Biodegradable Polymers. J Polym Sci B Polym Phys. 2011;49(12):832–64.

35.   Middleton JC, Tipton AJ. Synthetic biodegradable polymers as orthopedic devices. . Biomaterials 2000;21:. 2000;21:2335-46.

36.   Azevedo HS, Reis RL. Understanding the enzymatic degradation of biodegradable polymers and strategies to control their degradation rate. . Biodegradable Systems in Tissue Engineering and Regenerative Medicine2005. p. 177–201

37.   Engineer C, Parikh JK, Raval A. Review on Hydrolytic Degradation Behavior of Biodegradable Polymers from Controlled Drug Delivery System. Trends in Biomaterials and Artificial Organs. 2011;25(2):79-85.

38.   Van Dijkhuizen-Radersma R, Moroni L, van Apeldoorn A, Zhang Z, Grijpma D. Degradable polymers for tissue engineering. In: Van Blitterswijk C, Thomsen P, Lindahl A, Hubbell J, Williams D, Cancedda R, et al., editors. Tissue engineering. Burlington, MA: Academic Press; 2008. p. 193-221.

39.   Gomes ME, Reis RL. Biodegradable polymers and composites in biomedical applications: from catgut to tissue engineering, Part1-Available systems and their properties. International Materials Reviews. 2004;49(5):261-73.

40.   Reis RL, Neves N, Mano J, Gomes M, Marques AP. Natural-based polymers for biomedical applications. . Boca Raton: CRC Press,; 2008.

41.   Ge Z, Goh JC, Wang L, Tan EP, Lee EH. Characterization of knitted polymeric scaffolds for potential use in ligament tissue engineering. J Biomater Sci Polym Ed 2005;16(9):1179-92.

42.   Wu L, Ding J. In vitro degradation of three-dimensional porous poly(d,l-lactide-co-glycolide) scaffolds for tissue engineering. Biomaterials. 2004;25(27):5821–30.

43.   Beldjilali-Labro M, Garcia Garcia A, Farhat F, Bedoui F, Grosset J-F, Dufresne M, et al. Biomaterials in Tendon and Skeletal Muscle Tissue Engineering: Current Trends and Challenges. Materials. 2018;11(7):1116.

44.   Kimura Y, Hokugo A, Takamoto T, Tabata Y, Kurosawa H. Regeneration of anterior cruciate ligament by biodegradable scaffold combined with local controlled release of basic fibroblast growth factor and collagen wrapping. Tissue Eng Part C Methods. 2008;14:47–57.

45.   Narayanan N, Kuang L, Del Ponte M, Chain C, Deng M. Design and fabrication of nanocomposites for musculoskeletal tissue regeneration. In: H L, editor. Nanocomposites for Musculoskeletal Tissue Regeneration. 3–29. Amsterdam,Boston, Cambridge,Heidelberg, London, New York, Oxford, Paris, San Deigo, San Francisco, Singapore, Sidney, Tokyo: Woodhead Publishing; 2016.

46.   Sionkowska A. Current research on the blends of natural and synthetic polymers as new biomaterials: Review. Progress in Polymer Science 2011;36(9):1254-76.

47.   Blitterswijk CV, Boer JD, Thomsen P, Hubbell J, Cancedda R, Bruijn JDd, et al. Tissue Engineering. 1st ed. San Diego: Academic Press; 2008.

48.   Tangsadthakun C, Kanokpanont S, Sanchavanakit N, Banaprasert T, Damrongsakkul S. Properties of Collagen/Chitosan Scaffolds for Skin Tissue Engineering. Journal of Metals, Materials and Minerals. 2006;16(1):37-44.

49.   Cristino S, Grassi F, Toneguzzi S, Piacentini A, Grigolo B, Santi S, et al. Analysis of mesenchymal stem cells grown on a three-dimensional HYAFF 11- based prototype ligament scaffold. J Biomed Mater Res A. 2005;73:275–83.

50.   Kosuge D, Khan WS, Haddad B, Marsh D. Biomaterials and scaffolds in bone and musculoskeletal engineering. Curr Stem Cell Res Ther. 2013;8:185–91.

51.   Gentleman E, Lay AN, Dickerson DA, Nauman EA, Livesay GA, Dee KC. Mechanical characterization of collagen fibers and scaffolds for tissue engineering. Biomaterials. 2003;24:3805–13.

52.   Dunn MG, Liesch JB, Tiku ML, Zawadsky JP. Development of fibroblast-seeded ligament analogs for ACL reconstruction. J Biomed Mater Res A. 1995;29:1363–71.

53.   Bellincampi LD, Closkey RF, Prasad R, Zawadsky JP, Dunn MG. Viability of fibroblast-seeded ligament analogs after autogenous implantation. J Orthop Res 1998;16:414–20.

54.   Walters VI, Kwansa AL, Freeman JW. Design and analysis of braid-twist collagen scaffolds. Connective Tissue Research. 2012;53:255–66.

55.   Noyes FR, Grood ES. The strength of the anterior cruciate ligament in humans and Rhesus monkeys. J Bone Joint Surg. 1976;58:1074–82.

56.   Fan H, Liu H, Toh SL, Goh JC. Anterior cruciate ligament regeneration using mesenchymal stem cells and silk scaffold in large animal model. Biomaterials 2009;30(28):4967-77.

57.   Teh TK, Toh SL, Goh JC. Aligned hybrid silk scaffold for enhanced differentiation of mesenchymal stem cells into ligament fibroblasts. Tissue Eng Part C Methods. 2011;17(6):687-703.

58.   Horan RL, Collette AL, Lee C, Antle K, Chen J, Altman GH. Yarn design for functional tissue engineering. Journal of Biomechanics. 2006;39:2232–40.

59.   Teuschl A, Heimel P, Nürnberger S, van Griensven M, Redl H, Nau T. A Novel Silk Fiber–Based Scaffold for Regeneration of the Anterior Cruciate Ligament. Am J Sports Med. 2016;44(6):1547-57.

60.   Chen X, Qi YY, Wang LL, Yin Z, Yin GL, Zou XH, et al. Ligament regeneration using a knitted silk scaffold combined with collagen matrix. Biomaterials. 2008;29:3683–92.

61.   Chen J, Altman GH, Karageorgiou V, Horan R, Collette A, Volloch V, et al. Human bone marrow stromal cell and ligament fibroblast responses on RGD-modified silk fibers. Journal of Biomedical Materials Research. 2003;67A(2):559–70.

62.   Liu H, Fan H, Toh SL, Goh JCH. A comparison of rabbit mesenchymal stem cells and anterior cruciate ligament fibroblasts responses on combined silk scaffolds. Biomaterials. 2008;29(10):1443–53.

63.   Mengsteab PY, Nair LS, Laurencin CT. The past, present and future of ligament regenerative engineering. Regen Med. 2016;11(8):871-81.

64.   Vepari C, Kaplan DL. Silk as a Biomaterial. Prog Polym Sci. 2007;32(8-9):991–1007.

65.   Tuzlakoğlu T, Reis RL. Biodegradable Polymeric Fiber Structures in Tissue Engineering. Tissue Engineering Part B 2009;15(1):17-27.

66.   Majima T, Irie T, Sawaguchi N, Funakoshi T, Iwasaki N, Harada K, et al. Chitosan-based hyaluronan hybrid polymer fibre scaffold for ligament and tendon tissue engineering. Proc Inst Mech Eng H. 2007;221(5):537-46.

67.   Majima T, Funakosi T, Iwasaki N, Yamane ST, Harada K, Nonaka S, et al. Alginate and chitosan polyion complex hybrid fibers for scaffolds in ligament and tendon tissue engineering. J Orthop Sci. 2005;10(3):302-7.

68.   Younesi M, Islam A, Kishore V, Anderson JM, Akkus O. Tenogenic Induction of Human MSCs by Anisotropically Aligned Collagen Biotextiles. Adv Funct Mater. 2014;24(36):5762-70.

69.   Juncosa-Melvin N, Shearn JT, Boivin GP, Gooch C, Galloway MT, West JR, et al. Effects of mechanical stimulation on the biomechanics and histology of stem cell-collagen sponge constructs for rabbit patellar tendon repair. Tissue Eng. 2006;12(8):2291-300.

70.   Liu H, Fan H, Wang Y, Toh SL, Goh JC. The interaction between a combined knitted silk scaffold and microporous silk sponge with human mesenchymal stem cells for ligament tissue engineering. Biomaterials 2008;29(6):662-74.

71.   Li X, Snedeker JG. Wired silk architectures provide a biomimetic ACL tissue engineering scaffold. Journal of the Mechanical Behavior of Biomedical Materials. 2013;22:30-40.

72.   Sun H, Mei L, Song C, Cui X, Wang P. The in vivo degradation, absorption and excretion of PCL-based implant. Biomaterials. 2006;27(9):1735-40.

73.   Liao S, Chan CK, Ramakrishna S. Stem cells and biomimetic materials strategies for tissue engineering. Materials Science and Engineering: C. 2008;28(8):1189-202.

74.   Liu X, Laurent C, Du Q, Targa L, Cauchois G, Chen Y, et al. Mesenchymal stem cell interacted with PLCL braided scaffold coated with poly-L-lysine/hyaluronic acid for ligament tissue engineering. . J Biomed Mater Res Part A. 2018;9999:1–11.

75.   Moffat KL, Kwei AS, Spalazzi JP, Doty SB, Levine WN, Lu HH. Novel Nanofiber-Based Scaffold for Rotator Cuff Repair and Augmentation. Tissue Engineering Part A. 2009;15(1):115–26.

76.   Sahoo S, Ouyang H, Goh JC, Tay TE, Toh SL. Characterization of a novel polymeric scaffold for potential application in tendon/ligament tissue engineering. Tissue Eng. 2006;12(1):91-9.

77.   Lu HH, Cooper JA, Manuel S, Freeman JW, Attawia MA, Ko FK, et al. Anterior cruciate ligament regeneration using braided biodegradable scaffolds: in vitro optimization studies. Biomaterials. 2005;26:4805-16.

78.   Dürselen L, Dauner M, Hierlemann H, Planck H, Claes LE, Ignatius A. Resorbable polymer fibers for ligament augmentation. Journal of Biomedical Materials Research. 2001;58(6):666–72.

79.   Cooper JA, Bailey LO, Carter JN, Castiglioni CE, Kofron MD, Koc FK, et al. Evaluation of the anterior cruciate ligament, medial collateral ligament, achilles tendon and patellar tendon as cell sources for tissue-engineered ligament. Biomaterials. 2006;27:2747-54.

80.   Cooper JA, Sahota JS, Gorum WJ, Carter J, Doty SB, Laurencin CT. Biomimetic tissue-engineered anterior cruciate ligament replacement. Proceedings of the National Academy of Sciences. 2007;104(9):3049–54.

81.   Laitinen O, Törmälä P, Taurio R, Skutnabb K, Saarelainen K, Iivonen T, et al. Mechanical properties of biodegradable ligament augmentation device of poly(L-lactide) in vitro and in vivo. Biomaterials. 1992;13(14):1012-6.

82.   Agrawal CM, Ray RB. Biodegradable polymeric scaffolds for musculoskeletal tissue engineering. J Biomed Mater Res. 2001;55(2):141-50.

83.   Chen CC, Chueh JY, Tseng H, Huang HM, Lee SY. Preparation and characterization of biodegradable PLA polymeric blends. Biomaterials. 2003;24:1167–73.

84.   Leong NL, Kabir N, Arshi A, Nazemi A, Wu B, Petrigliano FA, et al. Evaluation of Polycaprolactone Scaffold with Basic Fibroblast Growth Factor and Fibroblasts in an Athymic Rat Model for Anterior Cruciate Ligament Reconstruction. Tissue Engineering Part A. 2015;21(11-12):1859–68.

85.   Sahoo S, Cho-Hong JG, Siew-Lok T. Development of hybrid polymer scaffolds for potential applications in ligament and tendon tissue engineering. Biomed Mater 2007;2(3):169-73.

86.   Leung M, Jana S, Tsao C-T, Zhang M. Tenogenic differentiation of human bone marrow stem cells via a combinatory effect of aligned chitosan–poly-caprolactone nanofibers and TGF-β3. Journal of Materials Chemistry B. 2013;1(47):6516.

87.   Domingues RMA, Chiera S, Gershovich P, Motta A, Reis RL, Gomes ME. Enhancing the Biomechanical Performance of Anisotropic Nanofibrous Scaffolds in Tendon Tissue Engineering: Reinforcement with Cellulose Nanocrystals. Advanced Healthcare Materials. 2016;5(11):1364–75.

88.   Petrigliano FA, English CS, Barba D, Esmende S, Wu BM, Mcallister DR. The Effects of Local bFGF Release and Uniaxial Strain on Cellular Adaptation and Gene Expression in a 3D Environment: Implications for Ligament Tissue Engineering. Tissue Engineering. 2007;13(11):2721–31.

89.   Cao H, McHugh K, Chew SY, Anderson JM. The topographical effect of electrospun nanofibrous scaffolds on the in vivo and in vitro foreign body reaction. J Biomed Mater Res A 2010;93(3):1151-9.

90.   Wagner ER, Bravo D, Dadsetan M, Riester SM, Chase S, Westendorf JJ, et al. Ligament Tissue Engineering Using a Novel Porous Polycaprolactone Fumarate Scaffold and Adipose Tissue-Derived Mesenchymal Stem Cells Grown in Platelet Lysate. Tissue Eng Part A. 2015;21(21-22):2703-13.

91.   Alshomer F, Chaves C, Kalaskar DM. Advances in Tendon and Ligament Tissue Engineering: Materials Perspective. Journal of Materials. 2018;2018:17.

92.   Mishra R, Militky J. Nanocomposites. In: Mishra R, Militky J, editors. Nanotechnology in Textiles: Woodhead Publishing; 2019. p. 263-310.

93.   Armentano I, Puglia D, Luzi F, Arciola CR, Morena F, Martino S, et al. Nanocomposites Based on Biodegradable Polymers. Materials (Basel). 2018;11(5):795.

94.   Hasnain MS, Nayak AK. Nanocomposites for improved orthopedic and bone tissue engineering applications. In: Inamuddin AA, Mohammad A, editor. Applications of Nanocomposite Materials in Orthopedics: Woodhead Publishing; 2019. p. 145-77.

95.   Erisken C, Zhang X, Moffat KL, Levine WN, Lu HH. Scaffold Fiber Diameter Regulates Human Tendon Fibroblast Growth and Differentiation. Tissue Engineering Part A. 2013;19(3-4):519-28.

96.   Barber JG, Handorf AM, Allee TJ, Li WJ. Braided nanofibrous scaffold for tendon and ligament tissue engineering. Tissue Eng Part A. 2013;19:1265-74.

97.   Freeman JW, Woods MD, Cromer DA, Wright LD, Laurencin CT. Tissue engineering of the anterior cruciate ligament: The viscoelastic behavior and cell viability of a novel braid-twist scaffold. J Biomater Sci Polym 2009;20:1709–28.

98.   Yin Z, Chen X, Chen JL, Shen WL, Nguyen TMH, Gao L, et al. The regulation of tendon stem cell differentiation by the alignment of nanofibers. Biomaterials. 2010;31(8):2163-75.

99.   Bosworth LA, Rathbone SR, Bradley RS, Cartmell SH. Dynamic loading of electrospun yarns guides mesenchymal stem cells towards a tendon lineage. J Mech Behav Biomed Mater. 2014;39:175-83.

100.   Gunatillake PA, Adhikari R. Biodegradable synthetic polymers for tissue engineering. Eur Cell Mater. 2003;20(5):1-16.

101.   Vunjak-Novakovic G, Altman G, Horan R, Kaplan DL. Tissue engineering of ligaments. Annual Review of Biomedical Engineering. 2004;6:131–56.

102.   Chen JL, Yin Z, Shen WL, Chen X, Heng BC, Zou XH, et al. Efficacy of hESC-MSCs in knitted silk-collagen scaffold for tendon tissue engineering and their roles. Biomaterials. 2010;31(36):9438–51.

103.   Shen W, Chen X, Chen J, Yin Z, Heng BC, Chen W, et al. The effect of incorporation of exogenous stromal cell-derived factor-1 alpha within a knitted silk-collagen sponge scaffold on tendon regeneration. Biomaterials. 2010;31(28):7239-49.

104.   Zheng Z, Ran J, Chen W, Hu Y, Zhu T, Chen X, et al. Alignment of collagen fiber in knitted silk scaffold for functional massive rotator cuff repair. Acta Biomater. 2017;51:317-29.

105.   Ran J, Hu Y, Le H, Chen Y, Zheng Z, Chen X, et al. Ectopic tissue engineered ligament with silk collagen scaffold for ACL regeneration: A preliminary study. Acta Biomater. 2017;53:307-17.

106.   Bi F, Shi Z, Liu A, Guo P, Yan S. Anterior Cruciate Ligament Reconstruction in a Rabbit Model Using Silk-Collagen Scaffold and Comparison with Autograft. PLoS One. 2015;10(5):0125900.

107.   Seo YK, Yoon HH, Song KY, Kwon SY, Lee HS, Park YS, et al. Increase in cell migration and angiogenesis in a composite silk scaffold for tissue-engineered ligaments J Orthop Res. 2009;27(4):495-503.

108.   Sensini A, Gualandi C, Cristofolini L, Tozzi G, Dicarlo M, Teti G, et al. Biofabrication of bundles of poly(lactic acid)-collagen blends mimicking the fascicles of the human Achille tendon. Biofabrication. 2017;9(1):015025

109.   Sahoo S, Toh SL, Goh JCH. A bFGF-releasing silk/PLGA-based biohybrid scaffold for ligament/tendon tissue engineering using mesenchymal progenitor cells. Biomaterials. 2010;31(11):2990–8

110.   Yang C, Deng G, Chen W, Ye X, Mo X. A novel electrospun-aligned nanoyarn-reinforced nanofibrous scaffold for tendon tissue engineering. Colloids and Surfaces B: Biointerfaces. 2014;122:270–6.

111.   Xu Y, Wu J, Wang H, Li H, Di N, Song L, et al. Fabrication of electrospun poly(L-lactide-co-ε-caprolactone)/collagen nanoyarn network as a novel, three-dimensional, macroporous, aligned scaffold for tendon tissue engineering. Tissue Eng Part C Methods. 2013;19(12):925-36.

112.   Ladd MR, Lee SJ, Stitzel JD, Atala A, Yoo JJ. Co-electrospun dual scaffolding system with potential for muscle-tendon junction tissue engineering. Biomaterials. 2011;32(6):1549-59.

113. Green EC, Zhang Y, Li H, Minus ML. Gel-spinning of mimetic collagen and collagen/nano-carbon fibers: Understanding multi-scale influences on molecular ordering and fibril alignment. J Mech Behav Biomed Mater. 2017;65:552-64.

114. Ge Z, Goh JCH, Lee EH. The Effects of Bone Marrow-Derived Mesenchymal Stem Cells and Fascia Wrap Application to Anterior Cruciate Ligament Tissue Engineering. Cell Transplantation. 2005;15:763–73.

115. Pinto VC, Costa RA, Rodrigues I, Guardão L, Soares R, Miranda GR. Exploring the in vitro and in vivo compatibility of PLA, PLA/GNP and PLA/CNT-COOH biodegradable nanocomposites: Prospects for tendon and ligament applications. Journal of Biomedical Materials Research Part A. 2017;105(8):2182–90.

116. Pinto VC, Ramos T, Alves ASF, Xavier J, Tavares PJ, Moreira PMGP, et al. Dispersion and failure analysis of PLA, PLA/GNP and PLA/CNT-COOH biodegradable nanocomposites by SEM and DIC inspection. Engineering Failure Analysis. 2016;71:63-71.

117. LaCroix AS, Duenwald-Kuehl SE, Lakes RS, Vanderby RJ. Relationship between tendon stiffness and failure: a metaanalysis. J Appl Physiol. 2013;115:43-51.

118. Liu A, Xue G-h, Sun M, Shao H-f, Ma C-y, Gao Q, et al. 3D Printing Surgical Implants at the clinic: A Experimental Study on Anterior Cruciate Ligament Reconstruction. Scientific Reports. 2016;6: 21704.

119. Deng D, Wang W, Wang B, Zhang P, Zhou G, Zhang WJ, et al. Repair of Achilles tendon defect with autologous ASCs engineered tendon in a rabbit model. Biomaterials 2014;35(31):8801-9.

120. Akbari M, Tamayol A, Bagherifard S, Serex L, Mostafalu P, Faramarzi N, et al. Textile Technologies and Tissue Engineering: A Path Towards Organ Weaving. Adv Healthc Mater. 2016;5(7):751–66.

121. Sawaguchi N, Majima T, Funakoshi T, Shimode K, Harada K, Minami A, et al. Effect of cyclic three-dimensional strain on cell proliferation and collagen synthesis of fibroblast-seeded chitosan-hyaluronan hybrid polymer fiber. J Orthop Sci. 2010;15(4):569-77.

122. Freeman JW, Woods MD, Cromer DA, Ekwueme EC, Andric T, Atiemo EA, et al. Evaluation of a hydrogel–fiber composite for ACL tissue engineering. Journal of Biomechanics. 2011;44:694–9.

123. Oryan A, Moshiri A, Parizi AM, Maffulli N. Implantation of a novel biologic and hybridized tissue engineered bioimplant in large tendon defect: an in vivo investigation. Tissue Eng Part A. 2014;3-4:447-65.

124. Sahoo S, Toh SL, Goh JC. PLGA nanofiber-coated silk microfibrous scaffold for connective tissue engineering. J Biomed Mater Res B Appl Biomater. 2010;95(1):19-28.

125. Naghashzargar E, Farè S, Catto V, Bertoldi S, Semnani D, Karbasi S, et al. Nano/micro hybrid scaffold of PCL or P3HB nanofibers combined with silk fibroin for tendon and ligament tissue engineering. J Appl Biomater Funct Mater. 2015;13(2):156-68.

126. Gurkan UA, Cheng X, Kishore V, Uquillas JA, Akkus O. Comparison of morphology, orientation, and migration of tendon derived fibroblasts and bone marrow stromal cells on electrochemically aligned collagen constructs. Jounal of biomedical materials research, Part A. 2010;94(4):1070–9.

127. Leroy A, Nottelet B, Bony C, Pinese C, Charlot B, Garric X, et al. PLA-poloxamer/poloxamine copolymers for ligament tissue engineering: Sound macromolecular design for degradable scaffolds and MSC differentiation. Biomater Sci. 2015;3:617.

128. Rider P, Kačarević ŽP, Alkildani S, Retnasingh S, Barbeck M. Bioprinting of tissue engineering scaffolds. J Tissue Eng. 2018;9:2041731418802090.

129. Parry JA, Oltho GL, Shogren KM, Dadsetan M, Wijnen AV, Yaszemski M, et al. 3D-Printed Porous Poly(propylene fumarate) Scaffolds with Delayed rhBMP-2 Release for ACL Graft Fixation. Tissue engineering Part A. 2016;23:9.

130. Hull E, Grove W, Zhang M, Song X, Pei ZJ, Cong W. Effects of Process Variables on Extrusion of Carbon Fiber Reinforced ABS Filament for Additive Manufacturing. In: ASME, editor. International Manufacturing Science and Engineering Conference; North Carolina, USA2015.

131. Zhang D, Chi B, Li B, Gao Z, Du Y, Guo J, et al. Fabrication of highly conductive graphene flexible circuits by 3D printing. Synthetic Metals. 2016;217:79-86.

132. Alafaghani A, Qattawi A, Alrawi B, Guzman A. Experimental Optimization of Fused Deposition Modelling Processing Parameters: A Design-for-Manufacturing Approach. Procedia Manufacturing. 2017;10:791-803.

133. Bishop ES, Mostafa S, Pakvasa M, Luu HH, Lee MJ, Wolf JM, et al. 3-D bioprinting technologies in tissue engineering and regenerative medicine: Current and future trends. Genes Dis. 2017;4(4):185-95.

134. Derakhshanfar S, Mbeleck R, Xu K, Zhang X, Zhong W, Xing M. 3D bioprinting for biomedical devices and tissue engineering: A review of recent trends and advances. Bioactive Materials. 2018;3(2):144-56.

135. Popov A, Malferrari S, Kalaska DM. 3D bioprinting for musculoskeletal application. J 3D Print Med. 2017;1(3):191–211.

136. Park SH, Choi Y-J, Moon SW, Lee BH, Shim J-H, Cho D-W, et al. Three-Dimensional Bio-Printed Scaffold Sleeves With Mesenchymal Stem Cells for Enhancement of Tendon-to-Bone Healing in Anterior Cruciate Ligament Reconstruction Using Soft-Tissue Tendon Graft. Arthroscopy: The Journal of Arthroscopic & Related Surgery. 2018;34(1):166-79.

137. Itapu B, Jayatissa A. A Review in Graphene/Polymer Composites. Chem Sci Int J. 2018;23(3):1-16.

138. Hales S, Tokita E, Neupane R, Ghosh U, Elder B, Wirthlin D, et al. 3D printed nanomaterial-based electronic, biomedical, and bioelectronic devices. Nanotechnology. 2020;31(17):172001.

139. Sayyar S, Officer DL, Wallace GG. Fabrication of 3D structures from graphene-based biocomposites. J Mater Chem B. 2017;5(19):3462-82.

140. Rajesh R, Ravichandran Y, Shanmugharaj A, Hariharasubramanian A. Advances in Polymer Materials and Technology. Srinivasan A, Bandyopadhyay S, editors. Boca Raton London New York: CRC Press; 2016. 657–90 p.

141. Silva M, Alves NM, Paiva MC. Graphene-polymer nanocomposites for biomedical applications. Polymers for Advanced Technologies. 2018;29(2):687-700.

142. Li J, Liu X, Crook JM, Wallace GG. Development of a porous 3D graphene-PDMS scaffold for improved osseointegration. Colloids and Surfaces B: Biointerfaces. 2017;159:386-93.

143. Pinto AM, Cabral J, Tanaka DAP, Mendes AM, Magalhães FD. Effect of incorporation of graphene oxide and graphene nanoplatelets on mechanical and gas permeability properties of poly(lactic acid) films: Incorporation of GO and GNP in PLA films. Polymer International. 2013;62(1):33-40.

144. Valencia C, Valencia C, Zuluaga F, Valencia M, Mina J, Grande-Tovar CD. Synthesis and Application of Scaffolds of Chitosan-Graphene Oxide by the Freeze-Drying Method for Tissue Regeneration. Molecules. 2018;23(10):2651.

145. Ghoshal S. Polymer/Carbon Nanotubes (CNT) Nanocomposites Processing Using Additive Manufacturing (Three-Dimensional Printing) Technique: An Overview. Fibers. 2017;5(4):40.

146. Javaid M, Haleem A. Additive manufacturing applications in medical cases: A literature based review. Alexandria Journal of Medicine. 2018;54(4):411-22.

147. Culmone C, Smit G, Breedveld P. Additive manufacturing of medical instruments: A state-of-the-art review. Additive Manufacturing. 2019;27:461-73.

148.   Donate R, Monzón M, Ortega Z, Wang L, Ribeiro V, Pestana D, et al. Comparison between calcium carbonate and β-tricalcium phosphate as additives of 3D printed scaffolds with polylactic acid matrix. Journal of Tissue Engineering and Regenerative Medicine. 2020;14(2):272-83.

149.   Saroia J, Wang Y, Wei Q, Lei M, Li X, Guo Y, et al. A review on 3D printed matrix polymer composites: its potential and future challenges. The International Journal of Advanced Manufacturing Technology. 2020;106(5-6):1695-721.

150.   Ventola CL. Medical Applications for 3D Printing: Current and Projected Uses. PT. 2014;39:704.

151.   Dumitrescu IB, Lupuliasa D, Drăgoi CM, Nicolae AC, Pop A, Şaramet G, et al. The Age of Pharmaceutical 3D Printing. Technological and Therapeutical Implications of Additive Manufacturing. Farmacia. 2018;66(3):365-89

152.   Guo H, Lv R, Bai S. Recent advances on 3D printing graphene-based composites. Nano Materials Science. 2019;1(2):101-15.

153.   Costa SF, Duarte FM, Covas JA. Thermal conditions affecting heat transfer in FDM/FFE: a contribution towards the numerical modelling of the process: This paper investigates convection, conduction and radiation phenomena in the filament deposition process. Virtual and Physical Prototyping. 2015;10(1):35-46.

154.   Phan DD, Swain ZR, Mackay ME. Rheological and heat transfer effects in fused filament fabrication. Journal of Rheology. 2018;62(5):1097-107.

155.   Costa SF, Duarte FM, Covas JA. Estimation of filament temperature and adhesion development in fused deposition techniques. Journal of Materials Processing Technology. 2017;245:167-79.

156.   Silva M. Freestanding Multilayered Films based on Functionalized Graphene and Natural Polymers for Biomedical Applications. In: Minho Uo, editor. 2016. p. 148.

157.   Liu J, Yan C. 3D printing. Cvetković D, editor: IntechOpen; 2018.

158.   Ghosh S, ., Parker ST, Wang X, Kaplan DL, Lewis JA. Direct-Write Assembly of Microperiodic Silk Fibroin Scaffolds for Tissue Engineering Applications. Advanced Functional Materials. 2008;18(13):1883-9

159.   Nara S, Chameettachal S, Ghosh S. Precise patterning of biopolymers and cells by direct write technique. Materials Technology. 2014;29(1):B10-B4

160.   Xu W, Wang X, Sandler N, Willför S, Xu C. Three-Dimensional Printing of Wood-Derived Biopolymers: A Review Focused on Biomedical Applications. ACS Sustainable Chemistry & Engineering. 2018;6(5):5663-80.

161.   Zhang B, Chung SH, Barker S, Craig D, Narayan RJ, Huang J. Direct ink writing of polycaprolactone / polyethylene oxide based 3D constructs. Progress in Natural Science: Materials International. 2020;31(2):180-91.

162.   Jiang P, Yan C, Guo Y, Zhang X, Cai M, Jia X, et al. Direct ink writing with high-strength and swelling-resistant biocompatible physically crosslinked hydrogels. Biomaterials Science. 2019;7(5):1805-14.

163.   Karis DG, Ono RJ, Zhang M, Vora A, Storti D, Ganter MA, et al. Cross-linkable multi-stimuli responsive hydrogel inks for direct-write 3D printing. Polymer Chemistry. 2017;8(29):4199-206.

164.   Li L, ., Lin Q, Tang M, Duncan AJE, Ke C. Advanced Polymer Designs for Direct-Ink-Write 3D Printing. Chemistry – A European Journal. 2019;25(46):10768-81.

165.   Wan X, Lou L, Liu Y, Leng J. Direct Ink Writing Based 4D Printing of Materials and Their Applications. Advance Science. 2020;7(16):001000.

166.   Pinargote NWS, Smirnov A, Peretyagin N, Seleznev A, Peretyagin P. Direct Ink Writing Technology (3D Printing) of Graphene-based Ceramic Nanocomposites: A Review Nanomaterials. 2020;10(7).

167.   Román-Manso B, Figueiredo FM, Achiaga B, Barea R, Pérez-Coll D, Morelos-Gómez A, et al. Electrically functional 3D-architectured graphene/SiC composites. Carbon. 2016;100:318-28.

168.   You X, Yang J, Feng Q, Huang K, Zhou H, Hu J, et al. Three-dimensional graphene-based materials by direct ink writing method for lightweight application. International Journal of Lightweight Materials and Manufacture. 2018;1(2):96-101

169.   Studart AR. Additive manufacturing of biologically-inspired materials. Chemical Society Reviews. 2016;45(2):359-76.

170.   Wang X, Jiang M, Zhou Z, Gou J, Hui D. 3D printing of polymer matrix composites: A review and prospective. Composites Part B: Engineering. 2017;110:442-58.

171.   Chin SY, Dikshit V, Pryadarshini BM, Zhang Y. Powder-Based 3D Printing for the Fabrication of Device with Micro and Mesoscale Features. Micromachines. 2020;11(7):658.

172.   Yap CY, Chua CK, Dong ZL, Liu ZH, Zhang DQ, Loh LE, et al. Review of selective laser melting: Materials and applications. Applied Physics Reviews. 2015;2(4):041101.

173.   Lamikiz A, Sánchez JA, López De Lacalle LN, Arana JL. Laser polishing of parts built up by selective laser sintering. International Journal of Machine Tools and Manufacture. 2007;47(12-13):2040-50.

174.   Deshmukh K, Muzaffar A, Kovářík T, Křenek T, Ahamed MB, Pasha SKK. Fundamentals and applications of 3D and 4D printing of polymers: Challenges in polymer processing and prospects of future research. In: Sadasivuni KK, Deshmukh K, Almaadeed MA, editors. 3D and 4D Printing of Polymer Nanocomposite Materials. Amsterdam: Elsevier; 2020. p. 527-60.

175.   Gul JZ, Sajid M, Rehman MM, Siddiqui GU, Shah I, Kim K-H, et al. 3D printing for soft robotics – a review. Science and Technology of Advanced Materials. 2018;19(1):243-62.

176.   Gardan J. Additive manufacturing technologies: state of the art and trends. International Journal of Production Research. 2016;54(10):3118-32.

177.   Singh S, Ramakrishna S, Berto F. 3D Printing of polymer composites: A short review. Material Design & Processing Communications. 2020;2:e97.

178.   Ahangar P, Cooke ME, Weber MH, Rosenzweig DH. Current Biomedical Applications of 3D Printing and Additive Manufacturing. Applied Sciences. 2019;9(8):1713.

179.   Sur UK. Graphene: A Rising Star on the Horizon of Materials Science. International Journal of Electrochemistry. 2012;2012:1-12.

180.   Zhu Y, Murali S, Cai W, Li X, Suk JW, Potts JR, et al. Graphene and graphene oxide: synthesis, properties, and applications. Adv Mater. 2010;22(35):3906-24.

181.   Hernandez Y, Nicolosi V, Lotya M, Blighe FM, Sun Z, De S, et al. High-yield production of graphene by liquid-phase exfoliation of graphite. Nature Nanotechnology. 2008;3(9):563-8.

182.   Sengupta R, Bhattacharya M, Bandyopadhyay S, Bhowmick AK. A review on the mechanical and electrical properties of graphite and modified graphite reinforced polymer composites. Progress in Polymer Science. 2011;36(5):638-70.

183.   Du W, Jiang X, Zhu L. From graphite to graphene: direct liquid-phase exfoliation of graphite to produce single- and few-layered pristine graphene. Journal of Materials Chemistry A. 2013;1(36):10592.

184.   Cataldi P, Athanassiou A, Bayer I. Graphene Nanoplatelets-Based Advanced Materials and Recent Progress in Sustainable Applications. Applied Sciences. 2018;8(9):1438.

185.   Shtein M, Pri-Bar I, Varenik M, Regev O. Characterization of Graphene-Nanoplatelets Structure via Thermogravimetry. Analytical Chemistry. 2015;87(8):4076-80.

186.   Rasheed AK, Khalid M, Rashmi W, Gupta TCSM, Chan A. Graphene based nanofluids and nanolubricants – Review of recent developments. Renewable and Sustainable Energy Reviews. 2016;63:346-62.

185

187.   Safaei MR, Goshayeshi HR, Chaer I. Solar Still Efficiency Enhancement by Using Graphene Oxide/Paraffin Nano-PCM. Energies. 2019;12(10).

188.   Dasari BL, Nouri JM, Brabazon D, Naher S. Graphene and derivatives – Synthesis techniques, properties and their energy applications. Energy. 2017;140:766-78.

189.   Caradonna A, Badini C, Padovano E, Pietroluongo M. Electrical and thermal conductivity of epoxy-carbon filler composites processed by calendaring. Materials. 2019;12(9):1522.

190.   Perreault F, de Faria AF, Elimelech M. Environmental applications of graphene-based nanomaterials. Chemical Society Reviews. 2015;44(16):5861-96.

191.   Yuvaraj G, Bhuvaneswari V, Vignesh G, Vairamuthu L. Mechanical properties of aluminium alloy AA2219 reinforced with graphite. First International Conference on Recent Advances in Aerospace Engineering (ICRAAE); Coimbatore: ICRAAE; 2017. p. 1-6.

192.   Shen M-Y, Chang T-Y, Hsieh T-H, Li Y-L, Chiang C-L, Yang H, et al. Mechanical Properties and Tensile Fatigue of Graphene Nanoplatelets Reinforced Polymer Nanocomposites. Journal of Nanomaterials. 2013;2013:1-9.

193.   Zhen Z, Zhu H. Graphene: Fabrication, Characterizations, Properties and Applications. Amsterdam: Elsevier; 2017.

194.   Zhang Y, Nayak TR, Hong H, Cai W. Graphene: a versatile nanoplatform for biomedical applications. Nanoscale. 2012;4(13):3833.

195.   Pinto AM, Gonçalves IC, Magalhães FD. Graphene-based materials biocompatibility: A review. Colloids and Surfaces B: Biointerfaces. 2013;111:188-202.

196.   Zhang B, Wang Y, Zhai G. Biomedical applications of the graphene-based materials. Materials Science and Engineering: C. 2016;61:953-64.

197.   Qu Y, He F, Yu C, Liang X, Liang D, Ma L, et al. Advances on graphene-based nanomaterials for biomedical applications. Materials Science and Engineering: C. 2018;90:764-80.

198.   Zhang S, Yang K, Feng L, Liu Z. In vitro and in vivo behaviors of dextran functionalized graphene. Carbon. 2011;49(12):4040-9.

199.   Erol O, Uyan I, Hatip M, Yilmaz C, Tekinay AB, Guler MO. Recent advances in bioactive 1D and 2D carbon nanomaterials for biomedical applications. Nanomedicine: Nanotechnology, Biology and Medicine. 2018;14(7):2433-54.

200.   Gurunathan S, Kim J-H. Synthesis, toxicity, biocompatibility, and biomedical applications of graphene and graphene-related materials. International Journal of Nanomedicine. 2016;11:1927.

201.   Syama S, Mohanan PV. Comprehensive Application of Graphene: Emphasis on Biomedical Concerns. Nano-Micro Letters. 2019;11(1):6.

202.   Syama S, Mohanan PV. Safety and biocompatibility of graphene: A new generation nanomaterial for biomedical application. International Journal of Biological Macromolecules. 2016;86:546-55.

203.   Wei C, Liu Z, Jiang F, Zeng B, Huang M, Yu D. Cellular Behaviours of bone marrow-derived mesenchymal stem cells towards pristine graphene oxide nanosheets. Cell Prolif. 2017;50(5):e12367.

204.   Zhang X, Wei C, Li Y, Li Y, Chen G, He Y, et al. Dose-dependent cytotoxicity induced by pristine graphene oxide nanosheets for potential bone tissue regeneration. Journal of Biomedical Materials Research Part A. 2020;108(3):614-24.

205.   Ou L, Song B, Liang H, Liu J, Feng X, Deng B, et al. Toxicity of graphene-family nanoparticles: a general review of the origins and mechanisms. Particle and Fibre Toxicology. 2016;13(1):57

206.   Chen GY, Pang DWP, Hwang SM, Tuan HY, Hu YC. A graphene-based platform for induced pluripotent stem cells culture and differentiation. Biomaterials. 2012;33(2):418-27.

207.   Gurunathan S, Han JW, Eppakayala V, Dayem AA, Kwon D-N, Kim J-H. Biocompatibility effects of biologically synthesized graphene in primary mouse embryonic fibroblast cells. Nanoscale Research Letters. 2013;8(1):393.

208.   Kim Y-K, Kim M-H, Min D-H. Biocompatible reduced graphene oxide prepared by using dextran as a multifunctional reducing agent. Chemical Communications. 2011;47(11):3195.

209.   Miao W, Shim G, Kang CM, Lee S, Choe YS, Choi H-G, et al. Cholesteryl hyaluronic acid-coated, reduced graphene oxide nanosheets for anti-cancer drug delivery. Biomaterials. 2013;34(37):9638-47.

210.   Shi S, Yang K, Hong H, Chen F, Valdovinos HF, Goel S, et al. VEGFR targeting leads to significantly enhanced tumor uptake of nanographene oxide in vivo. Biomaterials. 2015;39:39-46.

211.   Wang G, Qian F, Saltikov CW, Jiao Y, Li Y. Microbial reduction of graphene oxide by Shewanella. Nano Research. 2011;4(6):563-70.

212.   Duch MC, Budinger GRS, Liang YT, Soberanes S, Urich D, Chiarella SE, et al. Minimizing Oxidation and Stable Nanoscale Dispersion Improves the Biocompatibility of Graphene in the Lung. Nano Letters. 2011;11(12):5201-7.

213.   Zhang Y, Ali SF, Dervishi E, Xu Y, Li Z, Casciano D, et al. Cytotoxicity Effects of Graphene and Single-Wall Carbon Nanotubes in Neural Phaeochromocytoma-Derived PC12 Cells. ACS Nano. 2010;4(6):3181-6.

214.   Li B, Zhang X-Y, Yang J-Z, Zhang Y-J, Li W, Fan C-H, et al. Influence of polyethylene glycol coating on biodistribution and toxicity of nanoscale graphene oxide in mice after intravenous injection. International Journal of Nanomedicine. 2014;9:4697.

215.   Rodrigues AF, Newman L, Jasim DA, Vacchi IA, Ménard-Moyon C, Crica LE, et al. Immunological impact of graphene oxide sheets in the abdominal cavity is governed by surface reactivity. Archives of Toxicology. 2018;92(11):3359-79.

216.   Schinwald A, Murphy FA, Jones A, MacNee W, Donaldson K. Graphene-Based Nanoplatelets: A New Risk to the Respiratory System as a Consequence of Their Unusual Aerodynamic Properties. ACS Nano. 2012;6(1):736-46.

217.   Wang X, Podila R, Shannahan JH, Rao AM, Brown JM. Intravenously delivered graphene Nanosheets and multiwalled carbon nanotubes induce site-specific Th2 inflammatory responses via the IL-33/ST2 Axis. Int J Nanomedicine 2013;8:1733-48.

218.   Potts JR, Dreyer DR, Bielawski CW, Ruoff RS. Graphene-based polymer nanocomposites. Polymer. 2011;52(1):5-25.

219.   Rane AV, Kanny K, Abitha VK, Thomas S. Methods for Synthesis of Nanoparticles and Fabrication of Nanocomposites. Synthesis of Inorganic Nanomaterials. Sawston: WoodheadPublishing Company; 2018. p. 121-39.

220.   Mirabedini A, Ang A, Nikzad M, Fox B, Lau KT, Hameed N. Evolving Strategies for Producing Multiscale Graphene-Enhanced Fiber-Reinforced Polymer Composites for Smart Structural Applications. Advanced Science. 2020;7(11):1903501.

221.   Beyou E, Akbar S, Chaumont P, Cassagnau P. Polymer Nanocomposites Containing Functionalised Multiwalled Carbon NanoTubes: a Particular Attention to Polyolefin Based Materials. In: Suzuki S, editor. Syntheses and Applications of Carbon Nanotubes and Their Composites: IntechOpen; 2013. p. 77–115.

222.   Texter J. Graphene Science Handbook: Electrical and Optical Properties. Aliofkhazraei, M., Ali, N., Milne, W., Ozkan, C., Mitura, S., Gervasoni, J. ed. Boca Raton: CRC Press Taylor & Francis Group; 2016.

223.   Singh V, ., Joung D, Zhai L, Das S, Khondaker SI, Seal S. Graphene based materials: Past, present and future. Progress in Materials Science. 2011;56(8):1178-271.

224. Tang L, Zhao L. Advanced Composite Materials: Properties and Applications. Warsaw: De Gruyter; 2017.

225. Deshmukh K, Ahamed M, B., Deshmukh RR, Pasha SKK, Bhagat PR, Chidambaram K. Biopolymer Composites With High Dielectric Performance: Interface Engineering. In: Sadasivuni KK, Ponnamma D, Kim, Cabibihan J-J, AlMaadeed MA, editors. Biopolymer Composites in Electronics. Amsterdam: Elsevier inc; 2018. p. 27-128.

226. Kim H, Miura Y, Macosko CW. Graphene/Polyurethane Nanocomposites for Improved Gas Barrier and Electrical Conductivity. Chemistry of Materials. 2010;22(11):3441-50.

227. Hu K, Kulkarni DD, Choi I, Tsukruk VV. Graphene-polymer nanocomposites for structural and functional applications. Progress in Polymer Science. 2014;39(11):1934-72.

228. Galpaya D, Wang M, Liu M, Motta N, Waclawik E, Yan C. Recent Advances in Fabrication and Characterization of Graphene-Polymer Nanocomposites. Graphene. 2012;1(2):30-49.

229. Wang J, Liu Y, Fan Z, Wang W, Wang B, Guo Z. Ink-based 3D printing technologies for graphene-based materials: a review. Advanced Composites and Hybrid Materials. 2019;2(1):1-33.

230. Fonseca DR, Sobreiro-Almeida R, Sol PC, Neves NM. Development of non-orthogonal 3D-printed scaffolds to enhance their osteogenic performance. Biomaterials Science. 2018;6(6):1569-79.

231. Costa JB, Silva-Correia J, Reis RL, Oliveira JM. Recent advances on 3D printing of patient-specific implants for fibrocartilage tissue regeneration. Journal of 3D Printing in Medicine. 2018;2(3):129-40.

232. Moroni L, Boland T, Burdick JA, De Maria C, Derby B, Forgacs G, et al. Biofabrication: A Guide to Technology and Terminology. Trends in Biotechnology. 2018;36(4):384-402.

233. Costa JB, Park J, Jorgensen AM, Silva-Correia J, Reis RL, Oliveira JM, et al. 3D Bioprinted Highly Elastic Hybrid Constructs for Advanced Fibrocartilaginous Tissue Regeneration. Chemistry of Materials. 2020;32(19):8733-46.

234. Hollister SJ. Porous scaffold design for tissue engineering. Nature Materials. 2005;4(7):518-24.

235. Belaid H, Nagarajan S, Teyssier C, Barou C, Barés J, Balme S, et al. Development of new biocompatible 3D printed graphene oxide-based scaffolds. Materials Science and Engineering: C. 2020;110:110595.

236. Sayyar S, Bjorninen M, Haimi S, ., Miettinen S, Gilmore K, Grijpma D, et al. UV Cross-Linkable Graphene/Poly(trimethylene Carbonate) Composites for 3D Printing of Electrically Conductive Scaffolds. ACS Applied Materials & Interfaces. 2016;8(46):31916-25.

237. Gonçalves EM, Oliveira FJ, Silva RF, Neto MA, Fernandes MH, Amaral M, et al. Three-dimensional printed PCL-hydroxyapatite scaffolds filled with CNTs for bone cell growth stimulation. Journal of Biomedical Materials Research Part B: Applied Biomaterials. 2016;104(6):1210-9.

238. Wang W, Junior JRP, Nalesso PRL, Musson D, Cornish J, Mendonça F, et al. Engineered 3D printed poly(ε-caprolactone)/graphene scaffolds for bone tissue engineering. Materials Science and Engineering: C. 2019;100:759-70.

239. Jakus AE, Secor EB, Rutz AL, Jordan SW, Hersam MC, Shah RN. Three-Dimensional Printing of High-Content Graphene Scaffolds for Electronic and Biomedical Applications. ACS Nano. 2015;9(4):4636-48.

240. Sayyar S, Murray E, Thompson BC, Chung J, Officer DL, Gambhir S, et al. Processable conducting graphene/chitosan hydrogels for tissue engineering. Journal of Materials Chemistry B. 2015;3(3):481-90.

241. Feng P, ., Jia J, Peng S, Yang W, Bin S, Shuai C. Graphene oxide-driven interfacial coupling in laser 3D printed PEEK/PVA scaffolds for bone regeneration. Virtual and Physical Prototyping. 2020;15(2):211-26.

242. Angulo-Pineda C, ., Srirussamee K, Palma P, Fuenzalida VM, Cartmell SH, Palza H. Electroactive 3D Printed Scaffolds Based on Percolated Composites of Polycaprolactone with Thermally Reduced Graphene Oxide for Antibacterial and Tissue Engineering Applications. Nanomaterials. 2020;10(3):428.

243. Zhang Y, Zhai D, Xu M, ., Yao Q, Zhu H, Chang J, et al. 3D-printed bioceramic scaffolds with antibacterial and osteogenic activity. Biofabrication. 2017;9(2):025037.

244. Cabral CSD, Miguel SP, De Melo-Diogo D, Louro RO, Correia IJ. Green reduced graphene oxide functionalized 3D printed scaffolds for bone tissue regeneration. Carbon. 2019;146:513-23.

245. Bendtsen ST, Quinnell SP, Wei M. Development of a novel alginate–polyvinyl alcohol-hydroxyapatite hydrogel for 3D bioprinting bone tissue engineered scaffolds. Journal of Biomedical Materials Research Part A. 2017;105(5):1457-68.

246. Zhang Y, Wang C, Fu L, Ye S, Wang M, Zhou Y. Fabrication and Application of Novel Porous Scaffold in Situ-Loaded Graphene Oxide and Osteogenic Peptide by cryogenic 3D Printing for Repairing Critical-Sized Bone Defect. Molecules. 2019;24(9):1669.

247. Caetano GF, Wang W, Chiang W-H, Cooper G, Diver C, Blaker JJ, et al. 3D-Printed Poly(ε-caprolactone)/Graphene Scaffolds Activated with P1-Latex Protein for Bone Regeneration. 3D Printing and Additive Manufacturing. 2018;5(2):127-37.

248. Wang W, Caetano G, Ambler W, Blaker J, Frade M, Mandal P, et al. Enhancing the Hydrophilicity and Cell Attachment of 3D Printed PCL/Graphene Scaffolds for Bone Tissue Engineering. Materials (Basel). 2016;9(12):992.

249. Rajzer I, Kurowska A, Jabłoński A, Kwiatkowski R, Piekarczyk W, Hajduga MB, et al. Scaffolds modified with graphene as future implants for nasal cartilage. Journal of Materials Science. 2020;55(9):4030-42.

250. Unagolla JM, Jayasuriya AC. Enhanced cell functions on graphene oxide incorporated 3D printed polycaprolactone scaffolds. Materials Science and Engineering: C. 2019;102:1-11.

251. Chen Q, ., Mangadlao JD, Wallat J, De Leon A, l, Pokorski JK, Advincula RC. 3D Printing Biocompatible Polyurethane/Poly(lactic acid)/Graphene Oxide Nanocomposites: Anisotropic Properties. ACS Applied Materials & Interfaces. 2017;9(4):4015-23.

252. Olate-Moya F, ., Arens L, Wilhelm M, Mateos-Timoneda MA, Engel E, Palza H. Chondroinductive Alginate-Based Hydrogels Having Graphene Oxide for 3D Printed Scaffold Fabrication. ACS Applied Materials & Interfaces. 2020;12(4):4343-57.

253. Feng Z, Li Y, Hao L, Yang Y, Tang T, Tang D, et al. Graphene-Reinforced Biodegradable Resin Composites for Stereolithographic 3D Printing of Bone Structure Scaffolds. Journal of Nanomaterials. 2019;2019:1-13.

254. Shuai C, Feng P, Gao C, Shuai X, Xiao T, Peng S. Graphene oxide reinforced poly(vinyl alcohol): nanocomposite scaffolds for tissue engineering applications. RSC Advances. 2015;5(32):25416-23.

255. Sharafeldin M, Jones A, Rusling JF. 3D Printed Biosensor Arrays for Medical Diagnostics. Micromachines (Basel). 2018;9(8):394.

256. Palenzuela CLM, Novotný F, Krupička P, Sofer Z, Pumera M. 3D-Printed Graphene/Polylactic Acid Electrodes Promise High Sensitivity in Electroanalysis. Analytical Chemistry. 2018;90(9):5753-7.

257. Cardoso RM, Silva PRL, Lima AP, Rocha DP, Oliveira TC, Do Prado TM, et al. 3D-Printed graphene/polylactic acid electrode for bioanalysis: Biosensing of glucose and simultaneous determination of uric acid and nitrite in biological fluids. Sensors and Actuators B: Chemical. 2020;307:127621.

258. Marzo AML, Mayorga-Martinez CC, Pumera M. 3D-printed graphene direct electron transfer enzyme biosensors. Biosensors and Bioelectronics. 2020;151:111980.

259. Leigh SJ, Bradley RJ, Purssell CP, Billson DR, Hutchins DA. A Simple, Low-Cost Conductive Composite Material for 3D Printing of Electronic Sensors. PLoS ONE. 2012;7(11):e49365.

260.   Kadimisetty K, ., Mosa IM, Malla S, Satterwhite-Warden JE, Kuhns TM, Faria RC, et al. 3D-printed supercapacitor-powered electrochemiluminescent protein immunoarray. Biosensors and Bioelectronics. 2016;77:188-93.

261.   Tyler B, Gullotti D, Mangraviti A, Utsuki T, Brem H. Polylactic acid (PLA) controlled delivery carriers for biomedical applications. Advanced Drug Delivery Reviews. 2016;107:163-75.

262.   Gonçalves C, Gonçalves I, Magalhães F, Pinto AM. Poly(lactic acid) composites containing carbon-based nanomaterials: a review. Polymers. 2017;9(12):269.

263.   Novais RM, Simon F, Pötschke P, Villmow T, Covas JA, Paiva MC. Poly(lactic acid) Composites with Poly(lactic acid)-Modified Carbon Nanotubes. J Polym Sci Part A: Polym Chem. 2013;51:3740–50.

264.   Goenka S, Sant V, Sant S. Graphene-based nanomaterials for drug delivery and tissue engineering. Journal of Controlled Release. 2014;173:75-88.

265.   Silva M, Alves NM, Paiva MC. Graphene-polymer nanocomposites for biomedical applications. Polym Adv Technol. 2017;29:687– 700.

266.   Silva M, Caridade SG, Vale AC, Cunha E, Sousa MP, Mano JF, et al. Biomedical films of graphene nanoribbons and nanoflakes with natural polymers. RSC Adv. 2017;7:27578.

267.   Paiva MC, Simon F, Novais RM, Ferreira T, Proença MF, Xu W, et al. Controlled Functionalization of Carbon Nanotubes by a Solvent-free Multicomponent Approach. ACS Nano. 2010;4(12):7379-86.

268.   Georgakilas V, Kordatos K, Prato M, Guldi DM, Holzinger M, A H. Organic functionalization of carbon nanotubes. J Am Chem Soc. 2002;124:760–1.

269.   Georgakilas V, Otyepka M, Bourlinos AB, Chandra V, Kim N, Kemp KC, et al. Functionalization of graphene: covalent and non-covalent approaches, derivatives and applications. Chem Rev. 2012;112(11):6156-214.

270.   Liu S, Zhao J, Ruan H, Wang W, Wu T, Cui W, et al. Antibacterial and anti-adhesion effects of the silver nanoparticles-loaded poly (L-lactide) fibrous membrane. . Mater Sci Eng C Mater Biol App. 2013;33:1176–82.

271.   Fathi-Achachelouei M, Knopf-Marques H, Ribeiro da Silva CE, Barthès J, Bat E, Tezcaner A, et al. Use of Nanoparticles in Tissue Engineering and Regenerative Medicine. Front Bioeng Biotechnol. 2019;7:113.

272.   Parchi PD, Vittorio O, Andreani L, Battistini P, Piolanti N, Marchetti S, et al. Nanoparticles for Tendon Healing and Regeneration: Literature Review. Front Aging Neurosci. 2016;8:202.

273.   Kwan KH, Yeung KW, Liu X, Wong KK, Shum HC, Lam YW, et al. Silver nanoparticles alter proteoglycan expression in the promotion of tendon repair. Nanomed Nanotechnol Biol Med. 2014;10(7):1375–83.

274.   Silva M, Ribeiro D, Cunha E, Proença MF, Young RJ, MC P. A Simple Method for Anchoring Silver and Copper Nanoparticles on Single Wall Carbon Nanotubes. Nanomaterials (Basel). 2019;9:1416.

275.   Guo R, Ren Z, Bi H, Xu M, Cai L. Electrical and Thermal Conductivity of Polylactic Acid (PLA)-Based Biocomposites by Incorporation of Nano-Graphite Fabricated with Fused Deposition Modeling. Polymers. 2019;11(3):549.

276.   Menczel J, Prime RB. Thermal analysis of polymers : fundamentals and applications. Materials Today. 2009;12(6):46.

277.   Bokobza L, Zhang J. Raman spectroscopic characterization of multiwall carbon nanotubes and of composites eXPRESS Polymer Letters 2012;6(7):601–8.

278.   Ni Z, Wang Y, Yu T, Shen Z. Raman Spectroscopy and Imaging of Graphene. Nano Res. 2008;1(4):273-91.

279.   Quintana M, Spyrou K, Grzelczak M, Browne WR, Rudolf P, Prato M. Functionalization of Graphene via 1,3- Dipolar Cycloaddition. Am Chem Soc. 2010;4(6):3527–33.

280.   Ferrari AC, Meyer JC, Scardaci V, Casiraghi C, Lazzeri M, Mauri F, et al. Raman spectrum of graphene and graphene layers. Phys Rev Lett. 2006;97(18):187401.

281.   Alimohammadi F, Gashti MP, Shamei A, Kiumarsi A. Deposition of silver nanoparticles on carbon nanotube by chemical reduction method: Evaluation of surface, thermal and optical properties. Superlattices and Microstructures. 2012;52(1):50-62.

282.   Wu D, Cheng Y, Feng S, Yao Z, Zhang M. Crystallization Behavior of Polylactide/Graphene Composites. Industrial & Engineering Chemistry Research. 2013;52(20):6731–9.

283.   Gonçalves C, Pinto A, Machado AV, Moreira J, Gonçalves IC, Magalhães F. Biocompatible reinforcement of poly(Lactic acid) with graphene nanoplatelets. Polymer Composites. 2016;39:E308–E20.

284.   Valapa RB, Pugazhenthi G, Katiyar V. Effect of graphene content on the properties of poly(lactic acid) nanocomposites. RSC Adv. 2015;5:28410.

285.   Murariu M, Dechief AL, Bonnaud L, Paint Y, Gallos A, Fontaine G, et al. The Production and Properties of Polylactide Composites Filled with Expanded Graphite. Polym Degrad Stab. 200;95:889.

286.   Caridade SG, Merino EG, Alves NM, Bermudez VZ, Boccaccino AR, Mano JF. Chitosan membranes containing micro or nano-size bioactive glass particles: evolution of biomineralization followed by in situ dynamic mechanical analysis. J Mech Behav Biomed Mater. 2013;20:173-83.

287.   Shearer T, Parnell WJ, Lynch B, Screen HRC, Abrahams D. A Recruitment Model of Tendon Viscoelasticity That Incorporates Fibril Creep and Explains Strain-Dependent Relaxation. ASME J Biomech Eng. 2020;142(7):071003.

288.   Armentano I, Bitinis N, Fortunati E, Mattioli S, Rescignano N, Verdejo R, et al. Multifunctional Nanostructured PLA Materials for Packaging and Tissue Engineering. Prog Polym Sci 2013;38:1720.

289.   Ahmed AF, Abdelgayed SS, Ibrahim IM. Polarity effect of microcurrent electrical stimulation on tendon healing: Biomechanical and histopathological studies. Journal of Advanced Research. 2012;3:109-17.

290.   Chao P-HG, Lu HH, Hung CT, Nicoll SB, Bulinski JC. Effects of Applied DC Electric Field on Ligament Fibroblast Migration and Wound Healing. Connective Tissue Research. 2007;48(4):188-97.

291.   Qi XY, Yan D, Jiang Z, Cao YK, Yu ZZ, Yavari F, et al. Enhanced Electrical Conductivity in Polystyrene Nanocomposites at Ultra-Low Graphene Content. ACS Appl Mater Interface. 2011;3:3130.

292.   Lamberti P, Spinelli G, Kuzhir PP, Guadagno L, Naddeo C, Romano V, et al. Evaluation of thermal and electrical conductivity of carbon-based PLA nanocomposites for 3D printing. 2018;1981:020158.

293.   Zhou TN, Qi XD, Fu Q. The Preparation of the Poly(Vinyl Alcohol)/Graphene Nanocomposites with Low Percolation Threshold and High Electrical Conductivity by Using the Large-Area Reduced Graphene Oxide Sheets. Express Polym Lett. 2013;7:747-55.

294.   Ferrigno B, Bordett R, Duraisamy N, Moskow J, Arul MR, Rudraiah S, et al. Bioactive polymeric materials and electrical stimulation strategies for musculoskeletal tissue repair and regeneration. Bioact Mater. 2020;5(3):468-85.

295.   da Silva D, Kaduri M, Poley M, Adir O, Krinsky N, Shainsky-Roitman J, et al. Biocompatibility, biodegradation and excretion of polylactic acid (PLA) in medical implants and theranostic systems. Chem Eng J. 2018;340:9-14.

296.   Kim I-H, Jeong YG. Polylactide/exfoliated graphite nanocomposites with enhanced thermal stability, mechanical modulus, and electrical conductivity. . J Polym Sci B Polym Phys. 2010;48:850-8.

297.   Lawal AT. Graphene-based nano composites and their applications. A review. Biosensors and Bioelectronics. 2019;141:111384.

298.   Bellet P, Gasparotto M, Pressi S, Fortunato A, Scapin G, Mba M, et al. Graphene-Based Scaffolds for Regenerative Medicine. Nanomaterials (Basel). 2021;11(2):404.

299.   Godoy-Gallardo M, Eckhard U, Delgado LM, de Roo Puente YJD, Hoyos-Nogués M, Gil FJ, et al. Antibacterial approaches in tissue engineering using metal ions and nanoparticles: from mechanisms to applications. Bioact Mater. 2021;6:4470-449.

300.   Burduşel AC, Gherasim O, Grumezescu AM, Mogoantă L, Ficai A, Andronescu E. Biomedical Applications of Silver Nanoparticles: An Up-to-Date Overview. Nanomaterials (Basel). 2018;8(9):681.

301.   Buckthorpe M, La Rosa G, Villa FD. Restoring knee extensor strength after anterior cruciate ligament reconstruction: a clinical commentary. Int J Sports Phys Ther. 2019;14(1):159-72.

302.   Imoto AM, Peccin S, Almeida GJ, Saconato H, Atallah ÁN. Effectiveness of electrical stimulation on rehabilitation after ligament and meniscal injuries: a systematic review. Sao Paulo Med J. 2011;129(6):414-23.

303.   Yadegari-Dehkordi S, Sadeghi HR, Attaran-Kakhki N, Shokouhi M, Sazgarnia A. Silver nanoparticles increase cytotoxicity induced by intermediate frequency low voltages. Electromagn Biol Med. 2015;34(4):317–21.

304.   Silva M, Gomes C, Pinho I, Gonçalves H, Vale AC, Covas JA, et al. Poly(Lactic Acid)/Graphite Nanoplatelet Nanocomposite Filaments for Ligament Scaffolds. Nanomaterials. 2021;11(11):2796.

305.   Oluwadamilola A, Yousaf S, Zare M, Mozafari M, Youseffi M, Twigg P, et al. Scaffolds for ligament tissue engineering. In: Mozafari M, Sefat F, Atala A, editors. Handbook of Tissue Engineering Scaffolds: Volume One. 1. Amsterdam (The Netherlands): Woodhead Publishing Series in Biomaterials; 2019. p. 299–327.

306.   Chung JJ, Im H, Kim SH, Park JW, Jung Y. Toward Biomimetic Scaffolds for Tissue Engineering: 3D Printing Techniques in Regenerative Medicine. . Front Bioeng Biotechnol. 2020;8:586406.

307.   An J, Teoh JEM, Suntornnond R, Chua CK. Design and 3D Printing of Scaffolds and Tissues. Engineering. 2015;1(2):261-8.

308.   Ghilan A, Chiriac AP, Nita LE, Rusu AG, Neamtu I, Chiriac VM. Trends in 3D Printing Processes for Biomedical Field: Opportunities and Challenges. J Polym Environ. 2020;28:1345–67.

309.   Cai S, Wu C, Yang W, Liang W, Yu H, Liu L. Recent advance in surface modification for regulating cell adhesion and behaviors. Nanotechnology Reviews. 2020;9(1):971-89.

310.   Cengiz IF, Oliveira JM, Reis RL. A Digital 3D Microstructural Voyage into Scaffolds: A Systematic Review of the Reported Methods and Results. Biomater Res. 2018;22:26.

311.   Laurent C, Liu X, De Isla N, Wang X, Rahouadj R. Defining a scaffold for ligament tissue engineering: What has been done, and what still needs to be done. Journal of Cellular Immunotherapy. 2018;4(1):4-9.

312.   Seyedsalehi A, Daneshmandi L, Barajaa M, Riordan J, Laurencin CT. Fabrication and characterization of mechanically competent 3D printed polycaprolactone-reduced graphene oxide scaffolds. . Sci Rep. 2020;10(1):22210.

313.   De Faria AF, Martinez DST, Meira SMM, de Moraes ACM, Brandelli A, Filho AGS, et al. Anti-adhesion and antibacterial activity of silver nanoparticles supported on graphene oxide sheets. Colloids Surf B Biointerfaces. 2014;113:115–24.

314.   Khalil WA, Sherif HHA, Hemdan BA, Khalil SKH, Hotaby WE. Biocompatibility enhancement of graphene ox-ide-silver nanocomposite by functionalisation with polyvinylpyrrolidone. IET Nanobiotechnol. 2019;13:816–23.

315.   Peixoto T, Paiva MC, Marques AT, Lopes MA. Potential of Graphene–Polymer Composites for Ligament and Tendon Repair: A Review. Adv Eng Mater 2020;22:2000492.

316.   Zhou T, Grimshaw PN, Jones C. A biomechanical investigation of the anteromedial and posterolateral bands of the porcine anterior cruciate ligament. Proc Inst Mech Eng H. 2009;223:767–75.

317. Pinto VMOC. Biodegradable polymer nanocomposites reinforced with carbon nanostructures, PLA/CNT-COOH and PLA/GNP, for augmentation ligament devices: production and characterization [Thesis on the Doctoral Program of Physics Engineering]. Porto: Faculdade de Engenharia da Universidade do Porto; 2016.

318. Cao Y, Feng J, Wu P. Preparation of organically dispersible graphene nanosheet powders through a lyophilization method and their poly (lactic acid) composites. . Carbon. 2010;48(13):3834-9.

319. Li X, Xiao Y, Bergeret A, Longerey M, Che J. Preparation of polylactide/graphene composites from liquid-phase exfoliated graphite sheets. Polymer Composites. 2014;35(2):396-403.

320. Sharma A, Gupta S, Sampathkumar TS, Verma RS. Modified graphene oxide nanoplates reinforced 3D printed multifunctional scaffold for bone tissue engineering. Biomaterials Advances. 2022;134:112587.

321. Gunes OC, Kara A, Baysan G, Husemoglu RB, Akokay P, Albayrak AZ, et al. Fabrication of 3D Printed poly(lactic acid) strut and wet-electrospun cellulose nano fiber reinforced chitosan-collagen hydrogel composite scaffolds for meniscus tissue engineering. Journal of Biomaterials Applications. 2022;37(4):683-97.

322. Peixoto T, Nunes J, Lopes MA, Marinho E, Proença MF, Lopes PE, et al. Poly(lactic acid) composites with few layer graphene produced by noncovalent chemistry. Polym Compos. 2022;43:8409–25.

323. Saleh M, Anwar S, Al-Ahmari AM, Alfaify A. Compression Performance and Failure Analysis of 3D-Printed Carbon Fiber/PLA Composite TPMS Lattice Structures. Polymers. 2022;14:4595.

324. Costa UO, Nascimento LFC, Almeida Bezerra WB, de Oliveira Aguiar V, Pereira AC, Monteiro SN, et al. Dynamic Mechanical Behavior of Graphene Oxide Functionalized Curaua Fiber-Reinforced Epoxy Composites: A Brief Report. Polymers. 2021;13:1897.

325. Najafidoust M, Hashemi A, Oskui IZ. Dynamic viscoelastic behavior of bovine periodontal ligament in compression. J Periodont Res. 2020;55(5):651-9.

326. Netti P, D'Amore A, Ronca D, Ambrosio L, Nicolais L. Structure-mechanical properties relationship of natural tendons and ligaments. . Journal of Materials Science: Materials in Medicine. 1996;7:525–30.

327. Edwards JH, Ingham E, Herbert A. Decellularisation affects the strain rate dependent and dynamic mechanical properties of a xenogeneic tendon intended for anterior cruciate ligament replacement. J Mech Behav Biomed Mater. 2019;91:18-23.

328. Pitaru AA, Lacombe JG, Cooke ME, Beckman L, Steffen T, Weber MH, et al. Investigating Commercial Filaments for 3D Printing of Stiff and Elastic Constructs with Ligament-Like Mechanics. Micromachines (Basel). 2020;11(9):846.

329. Loh QL, Choong C. Three-dimensional scaffolds for tissue engineering applications: role of porosity and pore size. Tissue Eng Part B Rev. 2013;19(6):485-502.

330. Fazeli N, Arefian E, Irani S, Ardeshirylajimi A, Seyedjafari E. 3D-Printed PCL Scaffolds Coated with Nanobioceramics Enhance Osteogenic Differentiation of Stem Cells. ACS Omega. 2021;6(51):35284-96.

331. Kantaros A. 3D Printing in Regenerative Medicine: Technologies and Resources Utilized. Int J Mol Sci. 2022;23(23):14621.

332. O'Brien FJ. Biomaterials & scaffolds for tissue engineering. Materials Today. 2011;14(3):88-95.

333. Walters MA, Chambers M.C., Karki R, Knox E, Levengood G, El-Amin SF. Anterior Cruciate Ligament Tissue Engineering: A Review of Current Investigations. J Nanotechnol Mater Sci. 2016;3:3-9.

334. Gasparotto M, Bellet P, Scapin G, Busetto R, Rampazzo C, Vitiello L, et al. 3D Printed Graphene-PLA Scaffolds Promote Cell Alignment and Differentiation. Int J Mol Sci 2022;23(3):1736.

335. Yang W, Zhou Q, Pan W, Zhu S, Wei C, Lu H, et al. Synthesis of vanillin-based porphyrin for remarkably enhancing the toughness, UV-resistance and self-extinguishing properties of polylactic acid. Chemical Engineering Journal. 2023;469:143935.

336. Jiang X, Wu S, Kuss M, Kong Y, Shi W, Streubel PN, et al. 3D printing of multilayered scaffolds for rotator cuff tendon regeneration. Bioact Mater. 2020;5(3):636-43.

337. Wang Y, Ren C, Bi F, Li P, Tian K. The hydroxyapatite modified 3D printed poly L-lactic acid porous screw in reconstruction of anterior cruciate ligament of rabbit knee joint: a histological and biomechanical study. BMC Musculoskelet Disord. 2023;24:151.

338. Lim PN, Chang L, Thian ES. Development of nanosized silver-substituted apatite for biomedical applications: A review. Nanomedicine. 2015;11(6):1331-44.

339. Radhakrishnan S, Nagarajan S, Belaid H, Farha C, Iatsunskyi I, Coy E, et al. Fabrication of 3D printed antimicrobial polycaprolactone scaffolds for tissue engineering applications. Mater Sci Eng C Mater Biol Appl. 2021;118:111525.

340. Correia TR, Figueira DR, de Sá KD, Miguel SP, Fradique RG, Mendonça AG, et al. 3D Printed scaffolds with bactericidal activity aimed for bone tissue regeneration. Int J Biol Macromol. 2016;93(Pt B):1432-45.

341. Kumar S, Raj S, Jain S, Chatterjee K. Multifunctional biodegradable polymer nanocomposite incorporating graphene-silver hybrid for biomedical applications. Mater Des. 2016;108:319–32.

342. Pinto AM, Moreira S, Gonçalves IC, Gama FM, Mendes AM, F.D. M. Biocompatibility of poly(lactic acid) with incorporated graphene-based materials. Colloids and Surfaces B: Biointerfaces. 2013;104:229-38.

343. Guan J, Fujimoto KL, Sacks MS, Wagner WR. Preparation and characterization of highly porous, biodegradable polyurethane scaffolds for soft tissue applications. Biomaterials. 2005;26(18):3961-71.

344. Zhang RY, Ma PX. Poly(α-hydroxyl acids)/hydroxyapatite porous composites for bone-tissue engineering. I. Preparation and morphology. J Biomed Mater Res. 1999;44:446-55.

345. Vinhas A, Rodrigues MT, Gonçalves AI, Reis RL, Gomes ME. Magnetic responsive materials modulate the inflammatory profile of IL-1β conditioned tendon cells. Acta Biomater. 2020;117:235-45.

346. Gonçalves AI, Vinhas A, Rodrigues MT, Gomes ME. The impact of cryopreservation in signature markers and immunomodulatory profile of tendon and ligament derived cells. J Cell Physiol. 2022;237(1):675-86.

347. Vinhas A, Goncalves AI, Rodrigues MT, Gomes ME. Human tendon-derived cell sheets created by magnetic force-based tissue engineering hold tenogenic and immunomodulatory potential. Acta Biomater. 2021;131:236-47.

348. Vinhas A, Rodrigues MT, Goncalves AI, Reis RL, Gomes ME. Pulsed Electromagnetic Field Modulates Tendon Cells Response in IL-1beta-Conditioned Environment. J Orthop Res. 2019;38(1):160-72.

349. Livak KJ, Schmittgen TD. Analysis of relative gene expression data using re- al-time quantitative PCR and the 2(-Delta Delta C(T)) Method. Methods. 2001;25(4):402–8.

350. Liu C, Shen J, Yeung KWK, Tjong SC. Development and Antibacterial Performance of Novel Polylactic Acid-Graphene Oxide-Silver Nanoparticle Hybrid Nanocomposite Mats Prepared By Electrospinning. ACS Biomater Sci Eng. 2017;3(3):471–86.

351. Pascual-González C, de la Vega J, Thompson C, Fernández-Blázquez JP, Herráez-Molinero D, Biurrun N, et al. Processing and mechanical properties of novel biodegradable poly-lactic acid/Zn 3D printed scaffolds for application in tissue regeneration. Journal of the Mechanical Behavior of Biomedical Materials. 2022;132:105290.

352.   Akai M, Oda H, Shirasaki Y, Tateishi T. Electrical stimulation of ligament healing. An experimental study of the patellar ligament of rabbits. Clin Orthop Relat Res. 1988;235:296-301.

353.   Cadena MJ, Misiego R, Smith KC, Avila A, Pipes B, Reifenberger R, et al. Sub-surface imaging of carbon nanotube–polymer composites using dynamic AFM methods. Nanotechnology. 2013;24(13):135706.

354.   Chen F, Han J, Guo Z, Mu C, Yu C, Ji Z, et al. Antibacterial 3D-Printed Silver Nanoparticle/Poly Lactic-Co-Glycolic Acid (PLGA) Scaffolds for Bone Tissue Engineering. Materials. 2023;16(11):3895.

355.   Zheng Y, Han Q, Li D, Sheng F, Song Z, Wang J. Promotion of tendon growth into implant through pore-size design of a Ti-6Al-4 V porous scaffold prepared by 3D printing. Materials & Design. 2021;197:109219.

356.   Wu S, Zhou R, Zhou F, Streubel PN, Chen S, Duan B. Electrospun thymosin Beta-4 loaded PLGA/PLA nanofiber/ microfiber hybrid yarns for tendon tissue engineering application. Mater Sci Eng C 2019;106:110268.

357.   Silva M, Pinho I, Gonçalves H, Vale AC, Paiva MC, Alves NM, et al. Engineering Ligament Scaffolds Based on PLA/Graphite Nanoplatelet Composites by 3D Printing or Braiding. J Compos Sci. 2023;7:104.

358.   Wei X, Li D, Jiang W, Gu Z, Wang X, Zhang Z, et al. 3D Printable Graphene Composite. Sci Rep. 2015;5:11181.

359.   Gonzalez-Campos JB, Prokhorov E, Sanchez IC, Luna-Bárcenas JG, Manzano-Ramírez A, González-Hernández J, et al. Molecular dynamics analysis of PVA-AgnP composites by dielectric spectroscopy. J Nanomater. 2012;925750:1-11.

360.   Li X, Cheng R, Sun Z, Su W, Pan G, Zhao S, et al. Flexible bipolar nanofibrous membranes for improving gradient microstructure in tendon-to-bone healing. Acta Biomater. 2017;61:204–16.

361.   Nedaipour F, Bagheri H, Mohammadi S. Polylactic acid-polyethylene glycol-hydroxyapatite composite" an efficient composition for interference screws. Nanocomposites. 2020;6(3):99-110.

362.   Sensini A, Gualandi C, Zucchelli A, Boyle LA, Kao AP, Reilly GC, et al. Tendon Fascicle-Inspired Nanofibrous Scaffold of Polylactic acid/Collagen with Enhanced 3D-Structure and Biomechanical Properties. Sci Rep. 2018;8(1):17167.

363.   Ning C, Li P, Gao C, Fu L, Liao Z, Tian G, et al. Recent advances in tendon tissue engineering strategy. Frontiers in Bioengineering and Biotechnology. 2023;11.

364.   Calejo I, Labrador-Rached CJ, Gomez-Florit M, Docheva D, Reis RL, Domingues RMA, et al. Bioengineered 3D Living Fibers as In Vitro Human Tissue Models of Tendon Physiology and Pathology. Adv Healthcare Mater. 2022;11:2102863.

365.   Rodríguez-Lozano FJ, García-Bernal D, Aznar-Cervantes S, Ros-Roca MA, Algueró MC, Atucha NM, et al. Effects of composite films of silk fibroin and graphene oxide on the proliferation, cell viability and mesenchymal phenotype of periodontal ligament stem cells. J Mater Sci Mater Med. 2014;25(12):2731-41.

366.   Su W, Wang Z, Jiang J, Liu X, Zhao J, Zhang Z. Promoting tendon to bone integration using graphene oxide-doped electrospun poly(lactic-co-glycolic acid) nanofibrous membrane. Int J Nanomedicine. 2019;14:1835-47.

367.   García-García Á, Julián-Ortiz JVd, Gálvez J, Font D, Ayats C, Guna Serrano MdR, et al. Similarity-Based Virtual Screening to Find Antituberculosis Agents Based on Novel Scaffolds: Design, Syntheses and Pharmacological Assays. Int J Mol Sci. 2022;23:15057.

368.   Kantaros A, Ganetsos T, Piromalis D. 3D and 4D Printing as Integrated Manufacturing Methods of Industry 4.0. American Journal of Engineering and Applied Sciences. 2023;16(1):12-22.